Electron Spin Resonance Analysis of Cu(II) Coordination in Alzheimer's Disease-Related Peptides

by

Byong-kyu Shin

B.S., Seoul National University, Republic of Korea, 1998

M.S., Seoul National University, Republic of Korea, 2003

Submitted to the Graduate Faculty of

School of Arts and Sciences in partial fulfillment

of the requirements for the degree of

Doctor of Philosophy

University of Pittsburgh

2011

UNIVERSITY OF PITTSBURGH

SCHOOL OF ARTS AND SCIENCES

This dissertation was presented

by

Byong-kyu Shin

It was defended on

July 20, 2011

and approved by

David H. Waldeck, Ph.D., Professor, Department of Chemistry, School of Arts and Sciences

Stephen G. Weber, Ph.D., Professor, Department of Chemistry, School of Arts and Sciences

Rieko Ishima, Ph.D., Assistant Professor, Department of Structural Biology, School of Medicine

Dissertation Advisor: Sunil K. Saxena, Ph.D., Associate Professor, Department of Chemistry, School of Arts and Sciences

Electron Spin Resonance Analysis of Cu(II) Coordination in Alzheimer's Disease-Related Peptides

Byong-kyu Shin, Ph.D.

University of Pittsburgh, 2011

We exploit electron spin resonance (ESR) to understand the Cu(II) coordination of Alzheimer's disease-related peptides. It has been observed that at a low level of Cu(II), the amyloid-β (Aβ) peptide forms fibrillar aggregates, whereas amorphous aggregates are dominant at a high level of Cu(II). Three histidine residues, His6, His13, and His14, are believed to be important to the interaction between Aβ and the metal ion. The role of each histidine residue in binding to Cu(II) has been controversial mainly due to the difficulty in elucidating the coordination environment of Cu(II) at physiological pH. Using pulsed ESR, we precisely examine the multiple histidine coordination in the Cu(II)–Aβ complex. For the first time, we provide direct evidence that all the three histidine residues coordinate to Cu(II) at physiological pH. Also, the relative contribution of the imidazole ring of each histidine residue to the Cu(II) coordination is quantified. To establish the relative contribution, we have developed a method that examines the effects of multiple histidine coordination on electron spin-echo modulation. The ESR results reveal that His13 and His14 simultaneously coordinate to Cu(II) in a significant fraction of the Cu(II)–Aβ complex at physiological pH. A broad interpretation of this result leads to the hypothesis that the simultaneous Cu(II)-coordination by the two adjacent residues retards the formation of the β-sheet structure and enables a substantial amount of amorphous aggregates to form.

Next, we propose potential Cu(II)-binding motifs in tau protein based on the ESR spectra of some tau fragments. In tau protein, there are four pseudorepeats, each of which has a highly

conserved 18-amino-acid segment. The ESR results show that the 18-amino-acid sequence in each pseudorepeat has a good binding affinity for Cu(II). In particular, pulsed ESR spectra reveal that a histidine residue and a backbone amide group are involved in the Cu(II) coordination and the presence of the intact N-terminus is essential for the stability of the complex. Also, given that the reported dissociation constants of some Cu(II)–peptide complexes vary by several orders of magnitude, we have developed a simple method to precisely compare the dissociation constants at physiological pH.

TABLE OF CONTENTS

LIST OF FIGURES

PREFACE

First, I would like to thank my advisor, Prof. Sunil Saxena, for letting me be who I am today. It has been a great honor for me to work under his supervision. Had it not been for his timely guidance, help, and encouragement, this dissertation would not have been possible.

I am also indebted to Profs. David Waldeck, Stephen Weber, and Rieko Ishima for their service on my dissertation committee. Their comments and suggestions have enabled further improvements to be made through my work.

Next, I am grateful to the Saxena group for its sincere support and warm wishes. In particular, much of my knowledge on spectroscopy is attributed to Dr. Soraya Pornsuwan and Dr. Zhongyu Yang, both of whom were always willing to have discussions about the theoretical aspects of magnetic resonance with me. Dr. Sharon Ruthstein, Dr. Katherine Stone, Dr. Sangmi Jun, Jessica Sarver, Ming Ji, Timothy Cunningham, Kulakulasooriyagei Ishara Silva, and Gayathri Rajapakse were decent collaborators. I would like to give thanks to Dr. Ronny Ribeiro, Emily Wheeler, Drew Kise, and Marshall McGoff even though I did not spend much time with them.

Also, it was a pleasure for me to work with Prof. Peter Wipf and Dr. Maciej Walczak. They led and helped me in several ways when I was an immature graduate student.

Finally, I would like to appreciate the staff of the department, including David Emala, Lori Neu, Darlene Lanz, Toni Weber, and Fran Nagy, for their support.

1.0 INTRODUCTION

Electron spin resonance (ESR) is a powerful tool to investigate the structure of a complex in which a transition metal ion is coordinated by several ligands. Although also useful in small complexes, the specificity of ESR to paramagnetic species is especially important for relatively large systems such as metal-containing biomolecules. In fact, a number of proteins and nucleic acids either contain metal ions in their regular structures or have potential binding site(s) to accommodate metal ions. In particular, Cu(II), a paramagnetic ion, serves as a cofactor in numerous enzymes and plays a significant role in physiological or pathological processes. In a number of biological systems, Cu(II) tends to coordinate to one or more histidine residues.[1] In this context, we have sought a better way to resolve the ESR signatures of multiple histidine coordination of Cu(II). To this end, we use conventional continuous-wave (CW) ESR as well as more advanced pulsed methods such as electron spin-echo envelope modulation (ESEEM) and hyperfine sublevel correlation (HYSCORE) spectroscopy. Combining the pulsed ESR techniques with residue-specific ^{15}N-labeling, we have designed a method to examine the magnetic interaction between Cu(II), the central ion, and the non-coordinating imidazole nitrogen of each equatorially bound histidine residue. Using the method, we have found direct evidence that three histidine residues coordinate to Cu(II) in the equimolar mixture of Cu(II) and a fragmented amyloid-β (Aβ) peptide. More details are provided in Chapter 2 of this dissertation. With more precise analysis, we have quantified the relative contribution of each histidine residue to the

Cu(II) coordination in Aβ(1–16) at physiological pH. Detailed results are presented in Chapter 3. Our approach is unique because the Cu(II)–peptide system is examined without any side-chain modification or change in pH. Also, our findings are informative in that they confirm the probable Cu(II)-binding site near the N-terminus and the type of coordinating residues. More importantly, they suggest a mechanism by which changes in Cu(II) coordination affect the overall morphology of Aβ aggregates. The toxicity of the aggregates has been found to be intimately linked to the overall morphology.[2-3]

In Chapter 4, potential Cu(II) binding motifs of tau protein, another possible causative agent of Alzheimer's disease, are suggested. Tau protein has four pseudorepeat regions, each of which contains an 18-amino-acid segment with a high homology. The CW-ESR results reveal that the highly conserved 18-amino-acid segment in each pseudorepeat has a good Cu(II)-binding affinity. The pulsed ESR results reveal that a histidine residue and a backbone amide group are involved in the Cu(II) coordination. The ESR data also suggest that the Cu(II)-coordination by a backbone amide and the presence of the intact N-terminus are essential for the stability of the Cu(II)–peptide complex. Interestingly, our ESR experiments on a longer tau fragment imply that even the full-length tau protein may not have a stable structure to accommodate more than one equivalent of Cu(II).

In the next chapter, we turn our attention to the Cu(II)-binding affinities of biomolecules. The reported dissociation constants of some Cu(II)–peptide complexes at physiological pH vary by several orders of magnitude depending upon buffer conditions. For instance, dissociation constants ranging from picomolar to micromolar have been reported for the Cu(II)–Aβ complex.[4-8] Such variation makes it difficult to assess the biological importance of the complexation of the metal ion by biomolecules. To compare the Cu(II)-binding affinities of

peptides at physiological pH in a buffer-independent manner, we have introduced a simple ESR-based method where the solubility equilibria of practically insoluble Cu(II) salts are exploited. The method is explained in detail in Chapter 5.

In subsequent sections of this chapter, we detail the basic concepts of ESR used in this dissertation.

1.1 FUNDAMENTAL INTERACTIONS IN ESR SPECTROSCOPY ON A Cu(II) COMPLEX

Electron spin resonance is currently widely used to investigate paramagnetic species, which range from small metal ions to macromolecules such as proteins and nucleic acids. While various microwave frequencies, including, albeit not limited to, L-band (1–2 GHz), S-band (2–4 GHz), X-band (8–12 GHz), Q-band (33–50 GHz), and W-band (76–110 GHz), are currently available for ESR spectroscopy, ESR spectrometers operating at X-band are most common.

Figure 1-1 illustrates the general coordination sphere of a type II Cu(II) complex. Given the focus of this dissertation, we specifically illustrate the case of multiple histidine coordination in Cu(II) complexes. In general, the Cu(II) ion is coordinated by four atoms located in a plane. In addition, there may exist up to two more electron-pair donors along the axis perpendicular to the plane. The inner sphere, that is, the primary coordination sphere, contains the central ion, Cu(II), and the directly coordinating atoms, which are generally nitrogen, oxygen, and, less frequently, sulfur.

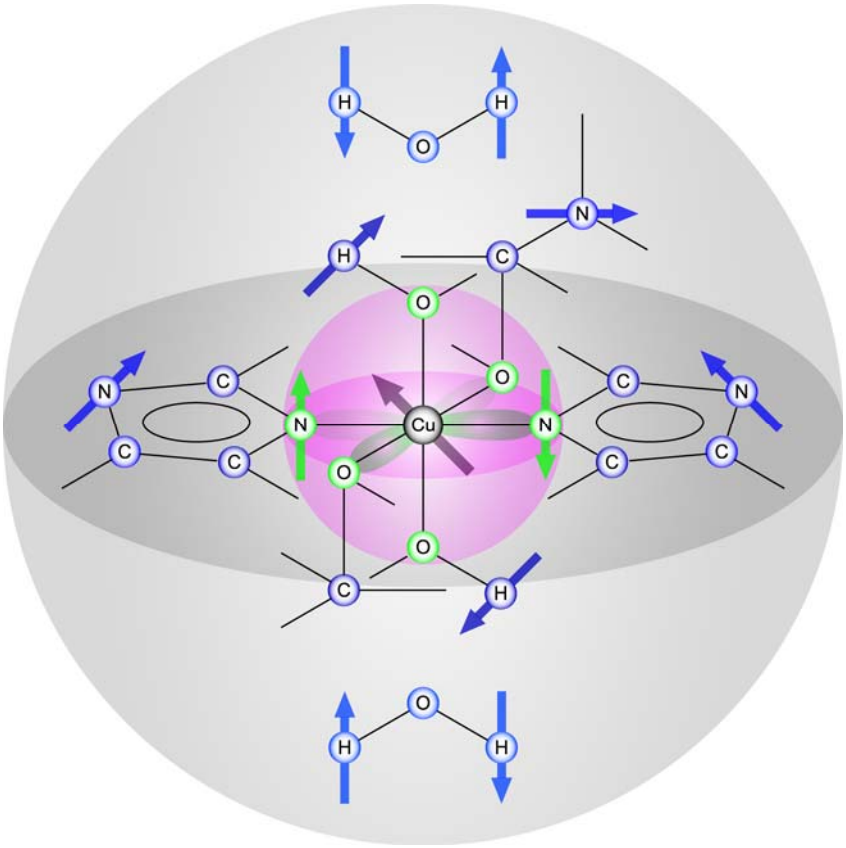

Figure 1-1. Coordination sphere of a type II Cu(II) complex. In the equatorial plane, Cu(II) is coordinated by four atoms, forming a square-planar structure. There may be up to two electron-pair donors in the axis perpendicular to the plane. The inner sphere (purple), i.e., the primary coordination sphere, contains the central ion, Cu(II), (gray) and directly coordinating atoms (green). Some of the orbitals of the equatorially coordinating atoms interact with the $3d_{x^2-y^2}$ orbital of the Cu(II) ion, which changes CW-ESR parameters such as $g_{||}$ and $A_{||}$. The interactions between the axially coordinating atoms and the central ion are relatively weak. The outer sphere (gray), i.e., the secondary coordination sphere, includes non-coordinating atoms (dark blue), which are linked to the central atoms by multiple chemical bonds, and ambient water or solvent molecules (light blue). The interactions between the central ion and an atom with a non-zero spin in the outer sphere may be observed in pulsed ESR spectroscopy.

CW-ESR spectroscopy is sensitive to the identity and the number of the equatorially coordinating atoms as the interactions between the orbitals of the central ion, Cu(II), and those of the equatorially coordinating atoms are reflected in some ESR parameters.[9] On the other hand, the orbital interactions between the central ion and the axially coordinating atoms are relatively too weak to affect ESR parameters. The outer sphere includes non-coordinating atoms and ambient water or solvent molecules. The interactions between Cu(II) and some nuclei with a non-zero spin in the outer sphere may be detected by ESEEM and HYSCORE spectroscopy. In particular, the non-coordinating imidazole nitrogen of histidine bound to Cu(II) and hydrogen of coordinating and ambient water molecules are often examined with the pulsed techniques. The nuclei of such non-coordinating atoms are hereafter referred to as remote nuclei. In brief, the CW-ESR parameters change with the orbitals of the coordinating atoms, while the magnetic interactions between the electron spin of Cu(II) and the nuclear spins of some non-coordinating atoms may be detected in ESEEM and HYSCORE.

The spin Hamiltonian operator that describes an electron spin coupled to k nuclei with a non-zero spin is made up of the terms for the electron Zeeman (ez) interaction, the nuclear Zeeman (nz) interaction, the electron–nuclear hyperfine (hf) interaction, and the nuclear quadrupole (nq) interaction, respectively. The Hamiltonian operator is given by:[10]

$$\begin{aligned}\hat{\mathcal{H}} &= \hat{\mathcal{H}}_{\mathrm{ez}} + \hat{\mathcal{H}}_{\mathrm{nz}} + \hat{\mathcal{H}}_{\mathrm{hf}} + \hat{\mathcal{H}}_{\mathrm{nq}} \\ &= \beta_e \mathbf{B}_0 \cdot \tilde{\mathbf{g}} \cdot \hat{\mathbf{S}} - \beta_n \sum_{i=1}^{k} \left(\mathbf{B}_0 \cdot \tilde{\mathbf{g}}_{in} \cdot \hat{\mathbf{I}}_i \right) + \hbar \sum_{i=1}^{k} \left(\hat{\mathbf{S}} \cdot \tilde{\mathbf{A}}_i \cdot \hat{\mathbf{I}}_i \right) + \hbar \sum_{i=1}^{k} \left(\hat{\mathbf{I}}_i \cdot \tilde{\mathbf{Q}}_i \cdot \hat{\mathbf{I}}_i \right)\end{aligned} \tag{1-1}$$

where β_e is the Bohr magneton, β_n is the nuclear magneton, $\mathbf{B}_0$ is the external magnetic field, $\hbar$ is the reduced Planck constant, $\tilde{\mathbf{g}}$ and $\tilde{\mathbf{g}}_{in}$ are the g-tensor of the electron spin and the *i*th nuclear spin, respectively, $\tilde{\mathbf{A}}_i$ is the *i*th electron–nuclear hyperfine tensor, $\tilde{\mathbf{Q}}_i$ is the *i*th nuclear

quadrupole tensor, and $\hat{\mathbf{S}}$ and $\hat{\mathbf{I}}_i$ are the (dimensionless) electron and the *i*th nuclear spin angular momentum operator, respectively. For a Cu(II) complex such as the one shown in Figure 1-1, we will refer to the nucleus of the central ion as $i = 1$ and use an i greater than 1 ($i > 1$) to describe other nuclei with a non-zero spin, including those of directly coordinating atom(s) and remote atoms.

- **Electron Zeeman Interaction**

The first term describes the electron Zeeman interaction and its anisotropic property. In the case of Cu(II) species, three different interactions mainly contribute to the first term, and they are given by:[11]

$$\hat{\mathcal{H}}_{\mathrm{ez}} = g_e\beta_e\mathbf{B}_0 \cdot \hat{\mathbf{S}} + \beta_e\mathbf{B}_0 \cdot \hat{\mathbf{L}} + \lambda\hat{\mathbf{S}} \cdot \hat{\mathbf{L}} \tag{1-2}$$

where g_e is the g-value of the free electron, $\hat{\mathbf{L}}$ is the (dimensionless) orbital angular momentum operator, and λ is the spin–orbit coupling constant. In eq (1-2), the interactions between the electron spin and the external magnetic field, between the orbital and the external magnetic field, and between the electron spin and the orbital are included. The net magnetic moment associated with the intrinsic electron spin angular momentum, $\hat{\boldsymbol{\mu}}_S$, is aligned with the external magnetic field. On the other hand, the magnetic moment associated with the orbital motion of the electron, $\hat{\boldsymbol{\mu}}_L$, which is represented by the orbital angular momentum, is locked to the molecular wavefunction, which depends on the orbital shapes and molecular structures.

Figure 1-2 illustrates the orientation of the magnetic moments with the two different physical causes, that is, $\hat{\boldsymbol{\mu}}_S$ and $\hat{\boldsymbol{\mu}}_L$, with respect to the external magnetic field.

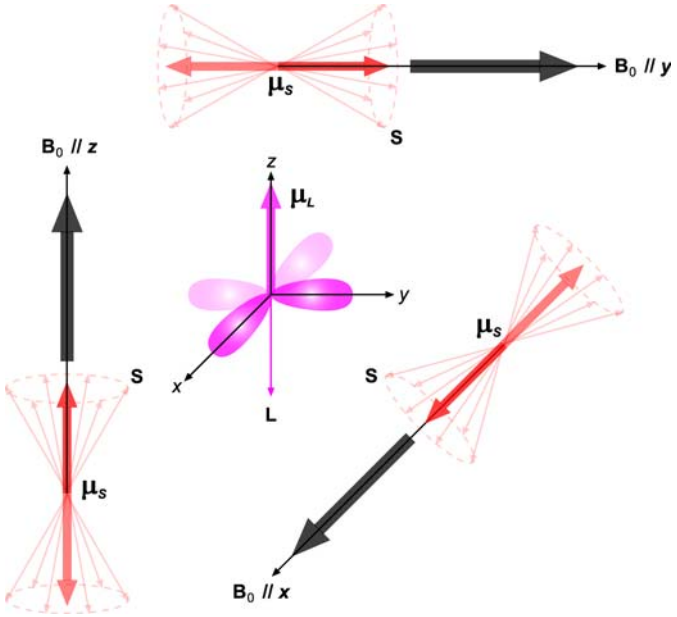

Figure 1-2. Orientation of the magnetic moments associated with the spin angular momentum and the orbital angular momentum. The net moment associated with the spin, $\hat{\boldsymbol{\mu}}_S$, is aligned with the external magnetic field whereas the orientation of the moment associated with the orbital angular momentum, $\hat{\boldsymbol{\mu}}_L$, is locked to the molecular wavefunction.

When the external magnetic field is parallel to $\hat{\boldsymbol{\mu}}_L$, the magnetic moments with the two different physical causes are parallel to each other as well as the external magnetic field. However, when the external magnetic field is perpendicular to $\hat{\boldsymbol{\mu}}_L$, only $\hat{\boldsymbol{\mu}}_S$ contributes to the Zeeman energy. In general, the net effect of all the three terms in eq (1-2) can be incorporated into the first term in eq (1-1), that is, $\hat{\mathcal{H}}_{\mathrm{ez}} = \beta_e \mathbf{B}_0 \cdot \tilde{\mathbf{g}} \cdot \hat{\mathbf{S}}$. In eq (1-1), $\tilde{\mathbf{g}}$ is a tensor that is diagonal in its principal axis system, which is defined in the molecular frame. More detailed information is provided in Appendix A. In fact, eq (1-2) may not be a good approximation for a heavy atom whose atomic number is more than 57. For such an atom, the J–J coupling between two or more angular momenta is a better approximation than the simple spin–orbit coupling scheme.[12] Nevertheless, the equation is reasonable for Cu(II) species where there is no heavy atom.

- **Nuclear Zeeman Interaction**

The second term in eq (1-1) details the nuclear Zeeman interactions of the central nucleus ($i = 1$) and nearby nuclei ($i > 1$), which include those of directly coordinating atom(s) in the inner sphere and remote nuclei in the outer sphere. The nuclear Zeeman term of the central nucleus such as Cu(II) in a complex may be neglected in CW-ESR spectroscopy because the nuclear spin state does not change in the ESR transition. Also, the nuclear Zeeman interactions of nearby nuclei are usually ignored in X-band CW-ESR mainly because the magnitude of the interactions is so small that the line splittings due to the interactions are not resolved in the ESR spectrum. Typically, the splittings are ~1 MHz for ^{14}N and ~14 MHz for ^{1}H in X-band ESR, where the magnitude of the electron Zeeman interaction corresponds to ~10 GHz. However, the Zeeman terms of some remote atoms in the outer sphere may be important in pulsed ESR such as ESEEM spectroscopy. More detailed information is presented in the third section of this chapter, **1.3**.

Also, the tensor $\tilde{\mathbf{g}}_{in}$ can, to a good approximation, be assumed to be isotropic and replaced with g_{in}.

- **Hyperfine Interaction**

The third term in eq (1-1) describes the electron–nuclear hyperfine interactions with the central nucleus and nearby nuclei. The hyperfine term of the central nucleus (i = 1) is usually significant: ~400 MHz for ^{63}Cu and ^{65}Cu in a Cu(II) complex. The hyperfine tensor of the central nucleus may be defined in the same frame as the g-tensor. For example, the ^{63}Cu or ^{65}Cu nucleus in a Cu(II) complex or the ^{14}N nucleus of a nitroxide moiety are defined in the same frame as the g-tensor frame. Indeed, the principal axes of the g-tensor coincide with those of the hyperfine tensor in most cases. Unlike the case of the central nucleus, the magnitude of the hyperfine interactions with nearby nuclei depends on several factors such as the interspin distance and the molecular structure.

In fact, the hyperfine terms can be further divided into two terms describing different interactions, which are given by:[13]

$$\begin{aligned}\hat{\mathcal{H}}_{\mathrm{hf}} &= \hat{\mathcal{H}}_{\mathrm{fc}} + \hat{\mathcal{H}}_{\mathrm{dip}} \\ &= \sum_{i=1}^{k}\left(\frac{2\mu_0 g\beta_e g_{in}\beta_n|\psi_i(0)|^2}{3}\hat{\mathbf{S}}\cdot\hat{\mathbf{I}}_i\right) - \sum_{i=1}^{k}\left\{\frac{\mu_0 g\beta_e g_{in}\beta_n}{4\pi {r_i}^3}\left[\hat{\mathbf{S}}\cdot\hat{\mathbf{I}}_i - 3\frac{(\hat{\mathbf{S}}\cdot\mathbf{r}_i)(\hat{\mathbf{I}}_i\cdot\mathbf{r}_i)}{{r_i}^2}\right]\right\}\end{aligned} \quad (1\text{-}3)$$

where μ_0 is the permeability of vacuum, $|\psi_i(0)|^2$ is the electron density at the ith nucleus, $\mathbf{r}_i$ is the electron–nuclear interspin vector for the ith nucleus, and r_i is its absolute value, that is, the interspin distance. The first term in eq (1-3) is the Fermi contact (fc) and dependent on the electron density at the nucleus, $|\psi_i(0)|^2$. The second term is the electron–nuclear dipolar interaction (dip), which is inversely proportional to the cube of the interspin distance, r_i.

In a Cu(II) complex, the Fermi contact is especially significant for the nuclear spins of the central ion and the directly coordinating nitrogen atoms because the unpaired electron is delocalized through the chemical bonds between Cu(II) and the coordinating atoms. Also, an increase in the number of equatorially coordinating oxygen atoms in a type II Cu(II) complex leads to a decrease in the magnitude of the Fermi contact at or around the nucleus of the central ion because the electron density at the central ion decreases due to the larger electronegativity of oxygen.

In general, the hyperfine interaction becomes less significant as the interspin distance increases due to the dependence of the dipolar term on the distance. For example, the hyperfine interaction with a directly coordinating ^{14}N nucleus in a Cu(II) complex may correspond to a frequency of ~40 MHz, whereas the magnitude is typically ~2 MHz for a non-coordinating ^{14}N nucleus such as the remote ^{14}N of a Cu(II)-coordinating imidazole ring illustrated in Figure 1-1. The hyperfine interactions with remote nuclei in the outer sphere are often too small to be resolved in the CW-ESR spectrum of a Cu(II) complex due to a large inhomogeneously broadened linewidth of ~20 MHz. However, the interactions with the nuclear spins of directly coordinating nitrogen atoms, also known as the superhyperfine interactions that are principally the Fermi contact due to the delocalization of the unpaired electron, are often detected in S-band ESR and may be detected in X-band as well. Nevertheless, the parameters related to the electron Zeeman and the hyperfine interaction with the central nucleus, Cu(II), are mainly observed in X-band and reported for a CW-ESR spectrum of a Cu(II) complex in a number of cases.

- **Nuclear Quadrupole Interaction**

The fourth term in eq (1-1) describes the electrical nuclear quadrupole interactions for coupled nuclei. Only a nucleus with a spin of 1 or greater has an electrical quadrupole moment, Q, which is due to the asymmetric charge distribution. In general, the nuclear quadrupole interactions are neglected in CW-ESR spectroscopy because their magnitude corresponds to a frequency lower than 3 MHz, which is rarely resolved in a CW-ESR spectrum. Nevertheless, the nuclear quadrupole interaction of a non-coordinating ^{14}N nucleus such as the remote ^{14}N of a Cu(II)-coordinating imidazole ring is often important and may be clearly observed in ESEEM spectroscopy. More detailed information is provided in the third and fourth section, **1.3** and **1.4**.

1.2 SPECTRAL FEATURES IN CW-ESR

If the central nucleus is considered to be the only coupled one, with the nuclear Zeeman term and the nuclear quadrupole term neglected, eq (1-1) can be simplified to:

$$\begin{aligned}\hat{\mathcal{H}} &= \hat{\mathcal{H}}_{\mathrm{ez}} + \hat{\mathcal{H}}_{\mathrm{hf}} \\ &= \beta_e \mathbf{B}_0 \cdot \tilde{\mathbf{g}} \cdot \hat{\mathbf{S}} \; + \; \hbar \hat{\mathbf{S}} \cdot \tilde{\mathbf{A}} \cdot \hat{\mathbf{I}}\end{aligned} \tag{1-4}$$

where $\tilde{\mathbf{A}}$ and $\hat{\mathbf{I}}$ are the hyperfine tensor, $\tilde{\mathbf{A}}_1$, and the nuclear spin angular momentum, $\hat{\mathbf{I}}_1$, for the central nucleus, respectively. Then, in the principal axis system of the g-tensor, which is defined in the molecular frame and assumed to be also the principal axis system of the hyperfine tensor, eq (1-4) becomes:

$$\hat{\mathcal{H}} = \beta_e(g_{xx}B_x\hat{S}_x + g_{yy}B_y\hat{S}_y + g_{zz}B_z\hat{S}_z) + \hbar(A_{xx}\hat{S}_x\hat{I}_x + A_{yy}\hat{S}_y\hat{I}_y + A_{zz}\hat{S}_z\hat{I}_z) \tag{1-5}$$

where the subscripts x, y, and z denote the *x*-, *y*-, and *z*-component of the vector, respectively, and the subscripts xx, yy, and zz denote the *xx*-, *yy*-, and *zz*-component of the tensor, respectively. For instance, B_x, B_y, and B_z are the three components of the external magnetic field in the molecular frame.

In a special case where the external magnetic field is aligned with the *z*-axis, eq (1-5) is simplified to:

$$\hat{\mathcal{H}} = g_{zz}\beta_e B_z \hat{S}_z + \hbar(A_{xx}\hat{S}_x\hat{I}_x + A_{yy}\hat{S}_y\hat{I}_y + A_{zz}\hat{S}_z\hat{I}_z) \tag{1-6}$$

Under the high-field approximation, where the electron Zeeman term is about three or more orders of magnitude greater than the hyperfine term, only the component that is parallel to the external magnetic field is important for the electron spin. Then, the equation above is further simplified to:

$$\hat{\mathcal{H}} = g_{zz}\beta_e B_z \hat{S}_z + \hbar A_{zz}\hat{S}_z\hat{I}_z \tag{1-7}$$

In a similar way, the Hamiltonian operator can be simplified when the external magnetic field is aligned with the *x*-axis or *y*-axis.

$$\hat{\mathcal{H}} = g_{xx}\beta_e B_x \hat{S}_x + \hbar A_{xx}\hat{S}_x\hat{I}_x \tag{1-8}$$

$$\hat{\mathcal{H}} = g_{yy}\beta_e B_y \hat{S}_y + \hbar A_{yy}\hat{S}_y\hat{I}_y \tag{1-9}$$

In fact, eqs (1-7), (1-8), and (1-9) show only three special cases of all possible orientations. In numerous cases, the three components of the g-tensor, g_{xx}, g_{yy}, and g_{zz}, may not be identical to one another, and a similar anisotropy is observed for the A-tensor. For instance, the *xx*- and *yy*-component of the tensors for a type II Cu(II) complex are identical to each other, while the *zz*-component is much greater. Thus, the molecules aligned with the external magnetic field

resonate at a frequency different from that of the molecules perpendicular to the field. More details of the CW-ESR spectra of Cu(II) complexes are explained in the next part of this section.

At low temperature, the rotational motion of molecules is generally slow enough to be detected in the ESR timescale. Then, the ESR spectrum of a sample with all possible orientations is the superposition of the spectrum corresponding to each orientation with respect to the external magnetic field. As a result, the ESR spectrum spans a broad range of frequencies. Also, the possible slight difference in the magnetic field felt by individual spins leads to inhomogeneously broadened lines. Similar spectral patterns are observed when the molecule is relatively rigid or a powder sample is used.

On the other hand, when the rotational motion is too rapid on the ESR timescale, the orientation dependence is averaged out. Accordingly, the three g-tensor components and the three hyperfine components collapse to the isotropic g-value, g_{iso}, and A-value, A_{iso}, respectively. Then, in the lab frame where the *z*-axis is designated as the direction of the external magnetic field, the Hamiltonian operator becomes:

$$\hat{\mathcal{H}} = g_{\mathrm{iso}}\beta_e B_z \hat{S}_z + \hbar A_{\mathrm{iso}} \hat{S}_z \hat{I}_z \tag{1-10}$$

where

$$g_{\mathrm{iso}} = \frac{g_{xx} + g_{yy} + g_{zz}}{3} \quad ; \quad A_{\mathrm{iso}} = \frac{A_{xx} + A_{yy} + A_{zz}}{3} \tag{1-11}$$

The relatively fast rotational motion also significantly reduces the inhomogenous broadening, and the ESR linewidth is mainly determined by the homogeneous broadening, which is characterized by the phase memory time T_{m}.

- **Samples Containing a Cu(II) Ion**

Numerous chemical species have ESR-active transition metal ions. In particular, Cu(II) ions are often found in biomolecules and synthetic substances. The relatively simple spectral shape of Cu(II) complexes allows for various applications of ESR. A paramagnetic ion with an electron spin of 1/2, Cu(II) has interesting properties, especially when it forms a complex with ligand(s). Aside from the electron Zeeman interaction, the hyperfine interaction with the nuclear spin of Cu(II) essentially determines the ESR spectroscopic features of Cu(II) species. The two naturally abundant isotopes of copper, ^{63}Cu and ^{65}Cu, have a nuclear spin of 3/2, which leads to four possible ESR transitions. Therefore, the ESR spectrum of a Cu(II) species with the isotropic g- and A-value is characterized by four distinguishable absorptive lines.

Interestingly, the rigid-limit or low-temperature spectrum of a Cu(II) complex provides useful information about the coordination environment. Figure 1-3 shows the CW-ESR spectrum of a type II Cu(II) complex obtained at 80 K. First, the coordination geometry is identified by the overall spectral shape such as the relative position of the peaks with respect to the given magnetic field strength and the splitting between two adjacent peaks. If the geometry is trigonal-planar or tetrahedral, that is, type I Cu(II) complex, g_{xx} and g_{yy} may be different by up to 0.06, and A_{zz} is smaller than 100 G.[14] On the other hand, the spectrum of a type II Cu(II) complex with a square-planar geometry is featured by identical g_{xx} and g_{yy} values, identical A_{xx} and A_{yy} values, and a large A_{zz} value, which is greater than 140 G.[14]

Figure 1-4 shows the orientation of the g-tensor of a type II Cu(II) complex. The molecular frame of type II Cu(II) complexes is defined by designating the *z*-axis as the direction of the normal of the equatorial plane on which the $3d_{x^2-y^2}$ orbital lies.

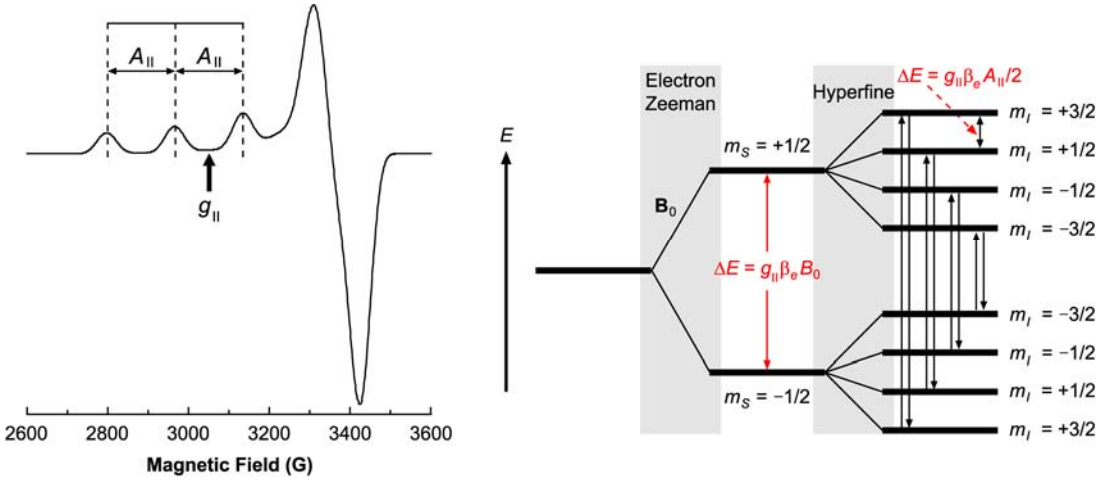

Figure 1-3. Magnetic field position corresponding to the $g_{||}$ value and the splitting due to the $A_{||}$ value in the spectrum of a type II Cu(II) complex. The two parameters are usually clear enough to be directly determined from the spectrum. For an S=1/2, I=3/2 system, each of the two Zeeman eigenstates is further split into four due to the hyperfine interaction.

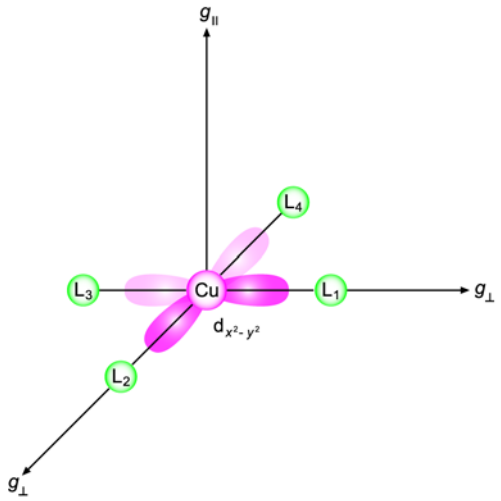

Figure 1-4. Orientation of the g-tensor of a type II Cu(II) complex. The molecular frame of the Cu(II) complex is defined with respect to the equatorial plane on which the $d_{x^2-y^2}$ orbital is located.

When the normal is aligned with the external magnetic field, the g- and A-value are denoted as $g_{||}$ and $A_{||}$, respectively: $g_{||} = g_{zz}$ and $A_{||} = A_{zz}$. When the external magnetic field is placed on the plane, the g- and A-value are denoted as $g_{\perp}$ and $A_{\perp}$, respectively: $g_{\perp} = g_{xx} = g_{yy}$ and $A_{\perp} = A_{xx} = A_{yy}$. Since g_{xx} and g_{yy} are identical, and therefore any orientation on the equatorial plane has the same g-value, $g_{\perp}$, the spectral intensity is higher around the magnetic field that corresponds to $g_{\perp}$. Therefore, the spectrum is intrinsically asymmetric and becomes more complicated due to the hyperfine interaction with the Cu(II) nuclear spin. The $g_{||}$ value is typically greater than the $g_{\perp}$ value by 0.2, and the $A_{\perp}$ value is smaller than 30 G. In spite of the complication by several parameters, the $g_{||}$ and $A_{||}$ value can be easily determined directly from the spectrum.[14] Figure 1-3 also shows the magnetic field strength corresponding to the $g_{||}$ value and the splitting due to the $A_{||}$ value in the spectrum of a type II Cu(II) complex. Other parameters are usually determined by spectral simulations.

More intriguingly, it has been found that the $g_{||}$ and $A_{||}$ value of the central nucleus are dependent on the type of equatorially coordinating atoms whose orbitals interact with the $3d_{x^2-y^2}$ orbital of the central atom, as illustrated in Figure 1-1. In particular, Peisach and Blumberg[9] have shown that the $g_{||}$ and $A_{||}$ value vary with the number of nitrogen and oxygen atoms that equatorially coordinate to Cu(II). While the parameters for the central ion, Cu(II), are mainly observed, the electronegativity of the equatorially coordinating atoms alters the electron density of the central ion, which leads to changes in the parameters regarding the hyperfine interaction. Also, the splittings due to the superhyperfine interactions with the coordinating nitrogen nuclei may be directly observed in the CW-ESR spectrum. Figure 1-5 illustrates the dependence of the ESR parameters on the type of ligands.

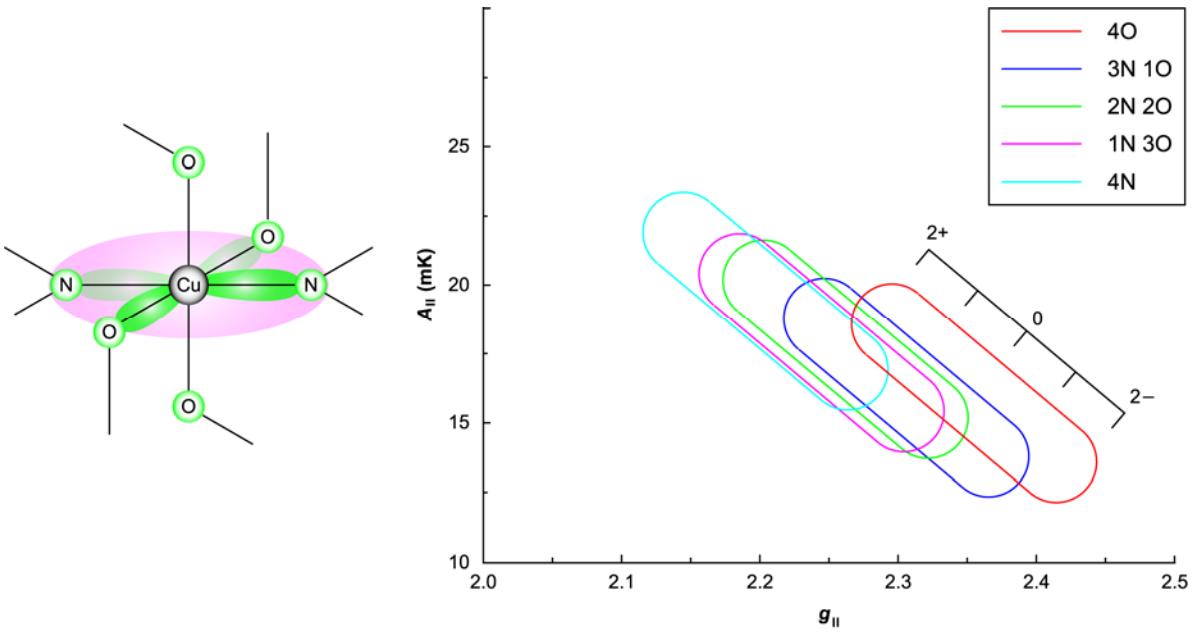

Figure 1-5. Peisach–Blumberg plot showing the correlation between equatorially coordinating atoms and ESR parameters such as $g_{||}$ and $A_{||}$ (Taken from Peisach, J. and Blumerg, W. E. (1974) *Arch. Biochem. Biophys.* 165, 691–708 with permission of Elsevier). As the number of nitrogen atoms increases, the $g_{||}$ value and $A_{||}$ value tend to decrease and increase, respectively. The number in the diagonal axis indicates the total charge of the Cu(II) complex. The $A_{||}$ values are in millikaisers. They are converted to those in Gauss by the equation, $A_{||}(\mathrm{mK}) = 0.046686\, g A_{||}(\mathrm{G})$, where g is the g-value.

Even though there are overlapped regions in the diagram, the relationship is widely used in order to determine the type of coordinating ligands.

If there are two or more species with different chemical structures in a sample, they may appear in the CW-ESR spectrum as two or more components, each of which has a distinguishable $g_{||}$ value and/or $A_{||}$ value. Furthermore, using spectral simulations, one can calculate the ratio of the components present in the sample. If there is another Cu(II) complex whose concentration is known, the concentration of the unknown sample can be estimated based on the fact that the integrated intensity of the ESR absorption signal is a function of the Cu(II) complex concentration irrespective of the structure of the Cu(II) complex.

1.3 ECHO-BASED PULSED ESR TECHNIQUES TO INTERROGATE REMOTE NUCLEI

In pulsed ESR spectroscopy, a short and intense microwave pulse is applied at a fixed magnetic field. The excitation bandwidth of the pulse is much broader than that of the microwave used in CW-ESR. Therefore, spins with different precession frequencies can be examined in a shorter time. In a pulsed ESR experiment, one or more pulses are applied to the ESR sample, and the signal from the detector is digitized in the time domain. Then, the digitized signal is Fourier-transformed into the frequency domain. After a single microwave pulse is applied, the magnetization on the plane perpendicular to the external magnetic field may be detected. As the magnetization decays with time, a free induction decay (FID) signal is observed. While the FID signal is generally useful, it decays too quickly to be meaningful data in many cases. Using a multiple-pulse sequence, one can recover the decaying signal by producing an echo. Echo-based

ESR experiments are particularly advantageous when the corresponding CW-ESR spectrum displays inhomogeneously broadened lineshapes. Currently, a number of commonly used pulsed ESR experiments are echo-based.

- **Geometric View of ESEEM**

Modulations at nuclear frequencies are often observed in the time-domain signal of echo-based ESR experiments. The nuclear modulations, also known as electron spin-echo envelope modulation (ESEEM) phenomena, are attributed to the interaction between the electron spin and nearby nuclear spin(s). Interestingly, however, not all nearby nuclei lead to detectable ESEEM. In a type II Cu(II) complex in which imidazole ring(s) coordinate to Cu(II), the magnitude of the interaction between the electron spin of the Cu(II) ion and the nuclear spin of the coordinating nitrogen atom(s) corresponds to ~40 MHz. Because of the limited excitation bandwidth of an ESEEM experiment, modulations due to this interaction are usually not detected. Moreover, the interaction with the nuclear spin of the central ion is even larger in magnitude. On the other hand, the frequency corresponding to the interaction with the remote nitrogen is approximately 1–2 MHz, which is within the excitation bandwith and therefore detected in an ESEEM experiment. The interaction with some nearby hydrogen may be detected for the same reason.

Figure 1-6 shows the energy levels and the ESR transitions for a system with S=1/2 and I=1/2. In the absence of an external magnetic field, the energy levels are degenerate with respect to the electron spin quantum number m_S. When a static magnetic field is applied along the z-axis, the electron spin has two eigenstates, $|\alpha_e\rangle$ and $|\beta_e\rangle$, which correspond to m_S = 1/2 and m_S = –1/2, respectively.

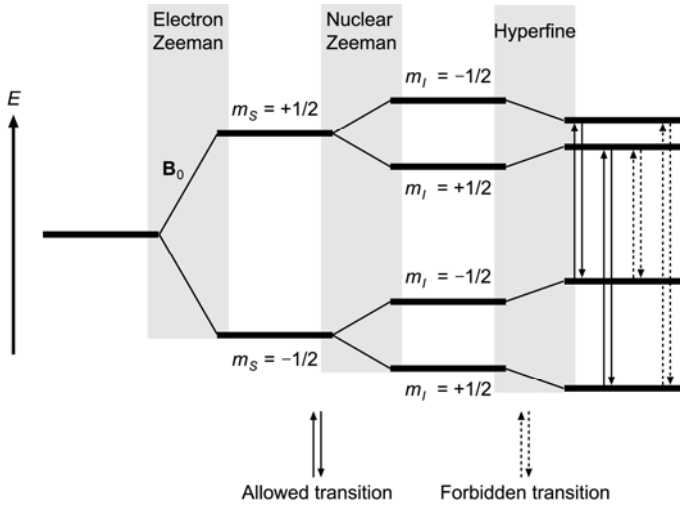

Figure 1-6. Allowed transitions and forbidden transitions for an S =1/2, I=1/2 system. There exist four eigenstates. Accordingly, four different ESR transitions can be considered. Two of them meet the selection rule for ESR (i.e., $\Delta m_S = \pm 1$ and $\Delta m_I = 0$) and are allowed whereas the other two do not meet the selection rule and are forbidden.

Each state is further split into two due to the existence of two different nuclear spin eigenstates, which depend on the nuclear Zeeman interaction, the electron–nuclear hyperfine interaction, and the electron spin state. Then, one can consider four different states, $|\alpha_e \alpha_n\rangle$, $|\alpha_e \beta_n\rangle$, $|\beta_e \alpha_n\rangle$, and $|\beta_e \beta_n\rangle$.

In ESR, the electromagnetic radiation is resonant with the electron spin but not with the nuclear spin. Therefore, the transition moment operator is then the raising/lowering operator for the electron spin angular momentum, $\hat{S}^{\pm} = \hat{S}_x \pm i\hat{S}_y$. If the wavefunctions of the two states involved in the transition are such that the transition moment integral is non-zero, the transition is allowed. On the other hand, the transition is forbidden in the case that the transition moment integral is zero. When the external magnetic field is dominant, the selection rule for ESR is Δm_S = ±1 and Δm_I = 0. The transitions between $|\alpha_e \alpha_n\rangle$ and $|\beta_e \alpha_n\rangle$ or between $|\alpha_e \beta_n\rangle$ and $|\beta_e \beta_n\rangle$ meet the selection rule. On the contrary, those between $|\alpha_e \alpha_n\rangle$ and $|\beta_e \beta_n\rangle$ or between $|\alpha_e \beta_n\rangle$ and $|\beta_e \alpha_n\rangle$ are considered to be forbidden by the rule because the nuclear spin quantum number m_I changes during the transitions.

However, the rule is based on the condition that the axis along which the nuclear spin eigenstates are aligned is the same for both electron spin manifolds. When the nuclear spin quantization axes are significantly different between the two electron spin manifolds, the forbidden transitions become weakly allowed. Typically, such forbidden transitions occur at a low external magnetic field. Since the nuclear eigenstates and their quantization axes are significantly affected by the hyperfine interaction, the magnitude and direction of the interaction are critical factors for the forbidden transitions. The eigenstates of the nuclear spins can be explained from a geometric point of view.

In general, the Hamiltonian that describes the magnetic interaction between a magnetic moment, $\hat{\boldsymbol{\mu}}$, and a magnetic field, $\mathbf{B}$, is given by:

$$\hat{\mathcal{H}} = -\mathbf{B} \cdot \hat{\boldsymbol{\mu}} \tag{1-12}$$

where the negative sign denotes that the energy is a minimum when the two vectors are parallel to each other. In particular, when a nuclear spin is situated in an external magnetic field, eq (1-12) can be rewritten as:

$$\hat{\mathcal{H}}_{\mathrm{nz}} = -\mathbf{B}_0 \cdot \hat{\boldsymbol{\mu}}_n = -g_n \beta_n \mathbf{B}_0 \cdot \hat{\mathbf{I}} \tag{1-13}$$

where the subscript nz denotes the nuclear Zeeman interaction, the subscript n denotes that the nuclear spin is considered, and $\mathbf{B}_0$ is the external magnetic field whose magnitude is B_0. If the nuclear spin is coupled with a nearby electron spin, the effective magnetic field at the nuclear spin is the vector sum of the external magnetic field and the local magnetic field generated by the electron spin. Then, the nuclear Hamiltonian is given by:

$$\begin{aligned} \hat{\mathcal{H}}_n = \hat{\mathcal{H}}_{\mathrm{nz}} + \hat{\mathcal{H}}_{\mathrm{hf}} = -\mathbf{B}_{\mathrm{ef}} \cdot \hat{\boldsymbol{\mu}}_n &= -(\mathbf{B}_0 + \mathbf{B}_{\mathrm{hf}}) \cdot \hat{\boldsymbol{\mu}}_n \\ &= -g_n \beta_n \mathbf{B}_0 \cdot \hat{\mathbf{I}} - g_n \beta_n \mathbf{B}_{\mathrm{hf}} \cdot \hat{\mathbf{I}} \end{aligned} \tag{1-14}$$

where the subscript hf denotes the hyperfine interaction, $\mathbf{B}_{\mathrm{ef}}$ is the effective magnetic field at the nuclear spin, and $\mathbf{B}_{\mathrm{hf}}$ is the local magnetic field generated by the electron spin at the nuclear spin. The hyperfine term of the Hamiltonian in eq (1-14) can be further divided into the isotropic component and the dipolar, that is, anisotropic, component.

$$\begin{aligned} \hat{\mathcal{H}}_{\mathrm{hf}} &= \hat{\mathcal{H}}_{\mathrm{iso}} + \hat{\mathcal{H}}_{\mathrm{dip}} \\ &= \hbar A_{\mathrm{iso}} \hat{\mathbf{S}} \cdot \hat{\mathbf{I}} + \hbar T_{\mathrm{dip}} \left[\hat{\mathbf{S}} \cdot \hat{\mathbf{I}} - 3 \frac{(\hat{\mathbf{S}} \cdot \mathbf{r})(\hat{\mathbf{I}} \cdot \mathbf{r})}{r^2} \right] \end{aligned} \tag{1-15}$$

where $\mathbf{r}$ is the electron–nuclear interspin vector, r is its absolute value, that is, the interspin distance, and

$$A_{\mathrm{iso}} = \frac{2\mu_0 g\beta_e g_n\beta_n|\psi(0)|^2}{3\hbar} \;;\; T_{\mathrm{dip}} = -\frac{\mu_0 g\beta_e g_n\beta_n}{4\hbar\pi r^3} \tag{1-16}$$

In eq (1-16), μ_0 is the permeability of vacuum, g and g_n are the g-value of the electron spin and the nuclear spin, respectively, β_e is the Bohr magneton, β_n is the nuclear magneton, and $|\psi(0)|^2$ is the electron density at the nucleus. Under the high-field approximation, only the *z*-component of the electron spin, $\hat{S}_z$, is considered while the *x*- and *y*-component are ignored. Then, introducing $\mathbf{m}$ and $\mathbf{n}$, the unit vector along the direction of the external magnetic field and interspin vector, respectively, one can rewrite eq (1-15) as:

$$\hat{\mathcal{H}}_{\mathrm{hf}} = \hbar A_{\mathrm{iso}}\hat{S}_z\mathbf{m}\cdot\hat{\mathbf{I}} + \hbar T_{\mathrm{dip}}\hat{S}_z[\mathbf{m}\cdot\hat{\mathbf{I}} - 3(\mathbf{m}\cdot\mathbf{n})(\hat{\mathbf{I}}\cdot\mathbf{n})] \tag{1-17}$$

Comparison of eq (1-14) and eq (1-17) leads to the following equation, which reveals the direction of the local magnetic field at the nuclear spin.

$$-g_n\beta_n\mathbf{B}_{\mathrm{hf}} = \hbar A_{\mathrm{iso}}\langle\hat{S}_z\rangle\mathbf{m} + \hbar T_{\mathrm{dip}}\langle\hat{S}_z\rangle[\mathbf{m} - 3(\mathbf{m}\cdot\mathbf{n})\mathbf{n}] \tag{1-18}$$

In the lab frame, the vector $\mathbf{m}$ is parallel to the *z*-axis, and the vector $\mathbf{n}$ can be expressed in terms of the colatitude, θ, and the azimuthal angle, ϕ: $\mathbf{m} = (0,\, 0,\, 1)$ and $\mathbf{n} = (\sin\theta\cos\phi,\, \sin\theta\sin\phi,\, \cos\theta)$. Then eq (1-18) can be explicitly written as:

$$-g_n\beta_n\mathbf{B}_{\mathrm{hf}} = \hbar\langle\hat{S}_z\rangle(-3T_{\mathrm{dip}}\sin\theta\cos\theta\cos\phi,\; -3T_{\mathrm{dip}}\sin\theta\cos\theta\sin\phi,\; A_{\mathrm{iso}} + T_{\mathrm{dip}}(1 - 3\cos^2\theta)) \tag{1-19}$$

In fact, the three components in the parentheses correspond to the three third-row elements of the 3 × 3 hyperfine tensor matrix, A_{zx}, A_{zy}, and A_{zz}, respectively. In a manner similar to the

hyperfine term of the Hamiltonian, the nuclear Zeeman term can be expressed in terms of the vector $\mathbf{m}$.

$$\hat{\mathcal{H}}_{\mathrm{nz}} = -g_n\beta_n\mathbf{B}_0 \cdot \hat{\mathbf{I}} = -\hbar\omega_I\mathbf{m} \cdot \hat{\mathbf{I}} \tag{1-20}$$

where ω_I is the Larmor frequency of the nuclear spin. Finally, the effective magnetic field is expressed as:

$$\mathbf{B}_{\mathrm{ef}} = \mathbf{B}_0 + \mathbf{B}_{\mathrm{hf}} = \frac{\hbar}{g_n\beta_n}\left[(0,\, 0,\, \omega_I) - \langle\hat{S}_z\rangle(A_{zx},\, A_{zy},\, A_{zz})\right] \tag{1-21}$$

Figure 1-7 illustrates the quantization axes and precessions of the electron spin and the nuclear spin in the lab frame where the *z*-axis is parallel to the external magnetic field. It is evident from eq (1-21) that the effective magnetic field and the corresponding angular frequency depend on the electron spin quantum number m_S, that is, whether the electron spin state is α or β. The angular frequencies in the two manifolds, ω_α and ω_β are:[10,15-16]

$$\omega_\alpha = \sqrt{\left(\omega_I - \frac{A}{2}\right)^2 + \left(\frac{B}{2}\right)^2}\ ;\ \omega_\beta = \sqrt{\left(\omega_I + \frac{A}{2}\right)^2 + \left(\frac{B}{2}\right)^2} \tag{1-22}$$

where

$$A = A_{zz}\ ;\ B = \sqrt{A_{zx}^2 + A_{zy}^2} \tag{1-23}$$

Since the effective magnetic field, about which the nuclear spin precesses, may be different between the two electron manifolds, it is possible that the nuclear spin quantum number changes while the electron spin flips.

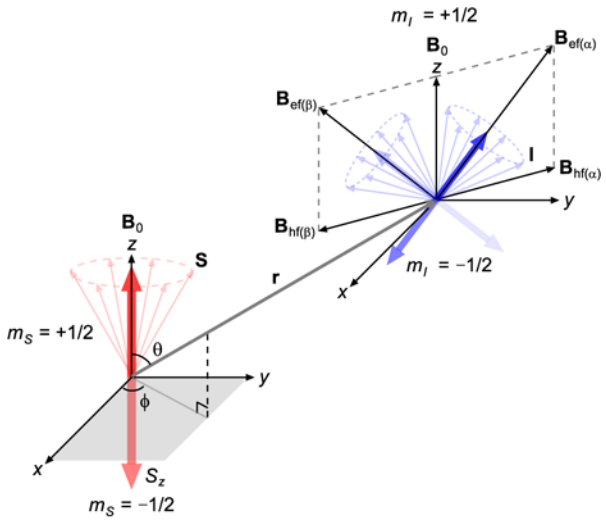

Figure 1-7. Quantization axes of the electron spin and the nuclear spin. The axis about which the electron spin precesses is parallel to the external magnetic field. However, the nuclear spin precesses about the direction of the effective magnetic field, which is the vector sum of the external magnetic field and the magnetic field induced by the electron spin at the nucleus. As the direction of the induced magnetic field depends on the electron spin quantum number m_S, the quantization axis of the nuclear spin may be different between two electron manifolds.

The probability of a change in the nuclear spin quantum number depends on the angle between the two effective magnetic fields, that is, the two quantization axes. If the angle is 0, no ESEEM effect is observed because the selection rule during the electron spin flip is obeyed. If the two axes are far from being parallel to each other, some forbidden transitions occur, which leads to ESEEM phenomena.

In fact, the forbidden transitions can be explained by applying the selection rule in a more rigorous manner. Even though the notations $|\alpha_e\alpha_n\rangle$, $|\alpha_e\beta_n\rangle$, $|\beta_e\alpha_n\rangle$, and $|\beta_e\beta_n\rangle$, are the commonly accepted forms describing the four different states and the corresponding wavefunctions, $|\alpha_n\rangle$ and $|\beta_n\rangle$ in the α-electron spin manifold may be different from those in the the β-electron spin manifold. The wavefunctions for the two nuclear spin eigenstates in the the α-electron spin manifold and the β-electron spin manifold are expressed as:

$$|\alpha_n\rangle(\alpha) = \cos\frac{\eta_\alpha}{2}|\alpha_n\rangle + \sin\frac{\eta_\alpha}{2}|\beta_n\rangle \;\; ; \;\; |\beta_n\rangle(\alpha) = -\sin\frac{\eta_\alpha}{2}|\alpha_n\rangle + \cos\frac{\eta_\alpha}{2}|\beta_n\rangle \qquad (1\text{-}24)$$

$$|\alpha_n\rangle(\beta) = \cos\frac{\eta_\beta}{2}|\alpha_n\rangle + \sin\frac{\eta_\beta}{2}|\beta_n\rangle \;\; ; \;\; |\beta_n\rangle(\beta) = -\sin\frac{\eta_\beta}{2}|\alpha_n\rangle + \cos\frac{\eta_\beta}{2}|\beta_n\rangle \qquad (1\text{-}25)$$

where η_α and η_β are the angle between the external magnetic field and the quatization axis of the nuclear spin in the α- and β-electron spin manifold, respectively. It is evident from eqs (1-24) and (1-25) that $|\alpha_n\rangle(\alpha)$ and $|\beta_n\rangle(\alpha)$ are orthogonal to each other, and $|\alpha_n\rangle(\beta)$ and $|\beta_n\rangle(\beta)$ are also orthogonal. If the two angles η_α and η_β are identical, the transitions between the two electron manifolds meet the selection rule for ESR as $|\alpha_n\rangle(\alpha)$ is the same as $|\alpha_n\rangle(\beta)$ and $|\beta_n\rangle(\alpha)$ is the same as $|\beta_n\rangle(\beta)$. However, if the two angles are different from each other, the transitions between $|\alpha_n\rangle(\alpha)$ and $|\beta_n\rangle(\beta)$ and between $|\beta_n\rangle(\alpha)$ and $|\alpha_n\rangle(\beta)$ may occur because the transition moment integral is non-zero.

In the case of the ^{1}H nuclei of ambient water, the nuclear spins are weakly coupled to the electron spin: the magnitude of the hyperfine interaction is much smaller than that of the nuclear Zeeman interaction, that is, $A, B \ll \omega_I$.[17] Thus, the two angular frequencies, ω_α and ω_β, converge to each other and to the Larmor frequency, ω_I. Typically, the small difference between the two angular frequencies is not resolved in X-band ESR. However, two distinguishable peaks may be observed if the spectral resolution is enhanced.

- **Electron Spin-Echo Detection Pulse Sequence and ESEEM**

Figure 1-8 shows the two-pulse electron spin-echo detection sequence, which is composed of a $\pi/2$ pulse and a π pulse separated by time t. At thermal equilibrium, the net magnetization is aligned with the *z*-axis, the direction of the external magnetic field $\mathbf{B}_0$. The magnetization is flipped into the *xy*-plane by the $\pi/2$ microwave pulse. If the microwave-induced magnetic field $\mathbf{B}_1$ is parallel to the *x*-axis, the magnetization is rotated from the +*z* direction to the –*y* direction. However, since the magnetization precesses about the *z*-axis and the magnetic field $\mathbf{B}_1$ is oscillating, the description in the lab frame is complicated. In a rotating frame with a microwave frequency of ω_{mw}, the $\mathbf{B}_1$ field becomes static, and a spin precessing at a frequency of ω_L can be considered to have a resonance offset of $\omega_L - \omega_{\mathrm{mw}}$. It is often assumed that the effect of the resonance offset on the rotation about the *x*-axis due to the $\mathbf{B}_1$ field is negligible. Then, the description of the magnetization being flipped into the –*y* direction is valid in the rotating frame.

Once the magnetization is located on the *xy*-plane, each spin precesses at its offset frequency during the first time interval t, which leads to the dephasing of the net magnetization. Then, the π pulse rotates each spin by 180° about the *x*-axis.

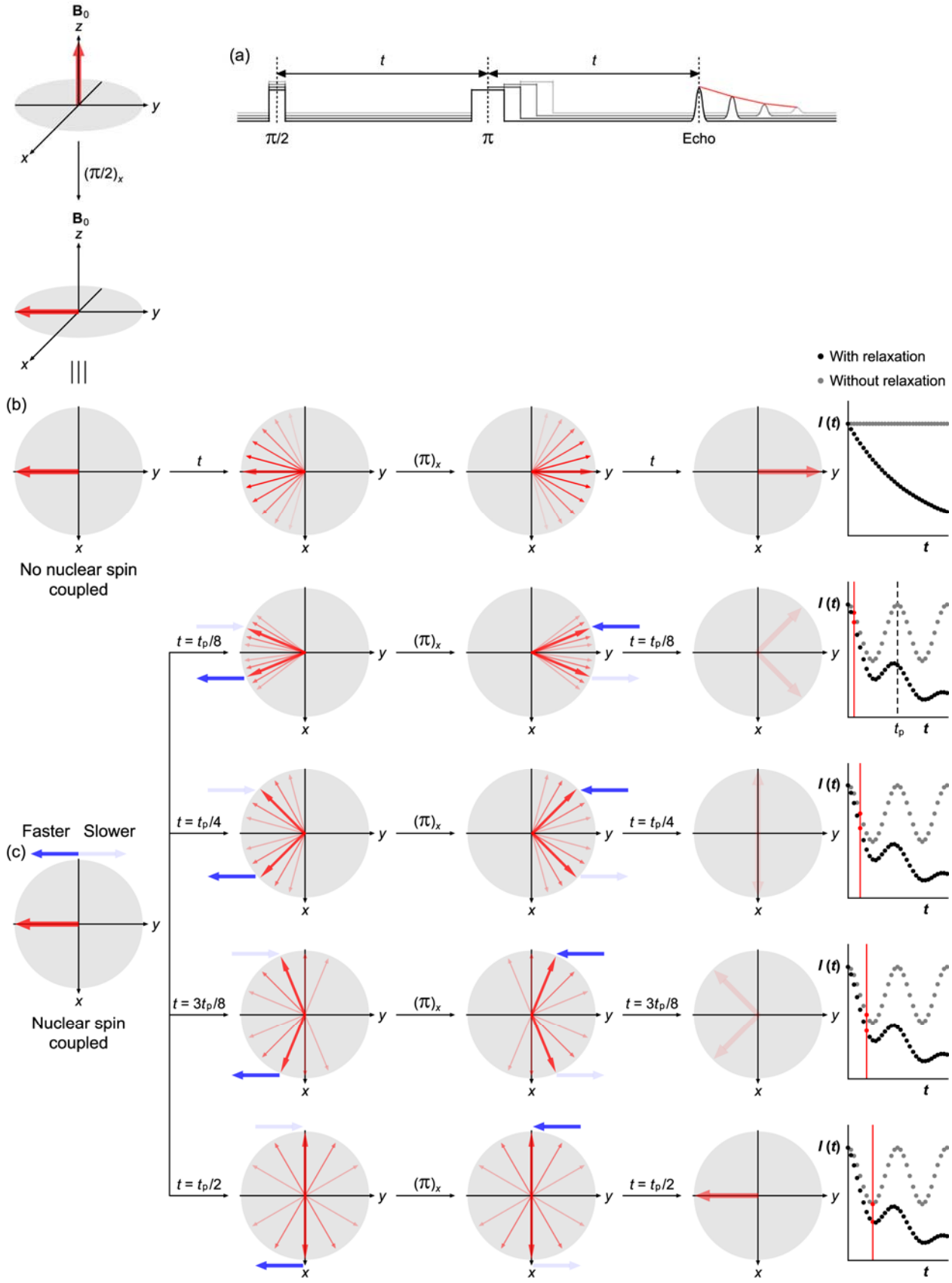
B0
z
y
x
(π/2)x
(a)
t
t
π/2
π
Echo
With relaxation
Without relaxation
(b)
t
(π)x
t
I (t)
No nuclear spin coupled
t = tp/8
(π)x
t = tp/8
tp
t = tp/4
(π)x
t = tp/4
Faster Slower
(c)
t = 3tp/8
(π)x
t = 3tp/8
Nuclear spin coupled
t = tp/2
(π)x
t = tp/2

Figure 1-8. Two-pulse electron spin-echo detection pulse sequence and ESEEM: (a) two-pulse detection sequence, (b) refocusing of the net magnetization, and (c) partial refocusing of the net magnetization in the presence of a nearby nuclear spin. Since each spin precesses at its offset frequency, the net magnetization on the *xy*-plane is defocused during the first time interval t. The defocused net magnetization is refocused during the second time interval. Nevertheless, in the presence of a nearby nuclear spin, the net magnetization is only partially refocused because the precession frequency before and after the π pulse may be different from each other.

During the second time interval t, each spin precesses in a manner that compensates for its phase difference introduced in the first time interval. As a result, an echo is formed when all the spins are in the same phase in the +*y* direction. The echo formed by two pulses is particularly called a Hahn echo or a primary echo.

Nevertheless, the amplitude of the magnetization refocused in the +*y* direction is not the same as the initial amplitude but dependent on the time t. In fact, the dephasing of the net magnetization is also affected by relaxation processes, which are irreversible. Thus, the echo amplitude decays as a function of t. While a number of relaxation processes may contribute to the phase memory time, the transverse relaxation between electron spins, the cross relaxation between the electron spin and a nuclear spin, and the spectral diffusion are usually significant.

When a nearby nuclear spin is coupled to the electron spin system, the electron spins can be grouped by their precession frequencies. In particular, a coupled nucleus with a spin of 1/2 splits the electron spins into four groups. If an electron spin belongs to different groups before and after the π pulse, the net magnetization may not be completely aligned with the *y*-axis when the echo is formed. Then, the echo amplitude is modulated as a function of t, and the period, denoted as t_{p}, depends on the precession frequencies of the groups the spin belongs to.

The final amplitude at the echo is expressed as a damped oscillatory function, which accounts for both the modulation due to the nuclear spin and the decay due to the relaxation processes. In fact, the modulations occur at the NMR transition frequencies in the two electron spin manifolds, ω_α and ω_β, and their sum or difference. In Figure 1-8, the effect of the nuclear spin on the electron spin-echo and the dependence of the echo intensity on the time interval are illustrated. For a system with S=1/2 and I=1/2, the modulation in the echo intensity is given by:[10]

$$V_{2p}(t) = 1 - \frac{k}{2}(1 - \cos\omega_\alpha t)(1 - \cos\omega_\beta t)$$
$$= 1 - \frac{k}{4}[2 - 2\cos\omega_\alpha t - 2\cos\omega_\beta t + \cos(\omega_\alpha + \omega_\beta)t + \cos(\omega_\alpha - \omega_\beta)t] \quad (1\text{-}26)$$

where k is the modulation depth parameter. More detailed information about eq (1-26) is presented in Appendix B.

- **Stimulated Echo Sequence and Three-Pulse ESEEM**

In the two-pulse electron spin-echo detection sequence, the pulse separation t is primarily limited by the phase memory time, T_m, which is usually on the order of microseconds. If the π pulse is split into two $\pi/2$ pulses separated by time T, the relaxation processes during the time T is mainly dependent on the phase memory time of coupled nuclear spins, which is much longer than that of the electron spin. The refocusing of the magnetization at time t after the third $\pi/2$ pulse is called a stimulated echo.

Figure 1-9 shows the three-pulse sequence for the generation of a stimulated echo, which is composed of three $\pi/2$ pulses. As the time interval T is incremented, the amplitude of the magnetization at the echo top decays as an exponential function of T, and the decay is characterized by the nuclear phase memory time, which is normally on the order of the longitudinal relaxation time of the electron spin, T_1.

In the three-pulse sequence, an echo envelope modulation may be still observed as in the two-pulse sequence. The modulation in the echo intensity for a system with S=1/2 and I=1/2 is given by:[10]

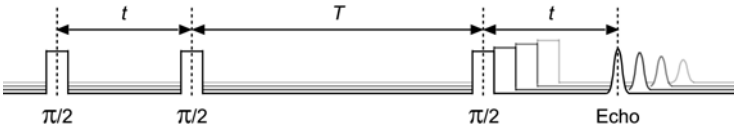

Figure 1-9. Three-pulse stimulated echo sequence. Three $\pi/2$ pulses are applied in the sequence. The first time interval t is fixed while the second pulse interval T is varied.

$$V_{3p}(t, T) = 1 - \frac{k}{4}\{(1 - \cos\omega_\alpha t)[1 - \cos\omega_\beta(T + t)] + (1 - \cos\omega_\beta t)[1 - \cos\omega_\alpha(T + t)]\} \quad (1\text{-}27)$$

In fact, the intensity of the stimulated echo is only half as much as that of the primary echo as the magnetization is partially refocused along the +*y*-direction. However, the slower decay of the stimulated echo enables the Fourier transform of the time-domain signal to have narrower linewidths. Also, in the three-pulse sequence, the modulations occur at only two nuclear frequencies, ω_α and ω_β, which is often advantageous in analyzing the spectrum. More detailed information about eq (1-27) is presented in Appendices B and C.

- **Two-Dimensional ESEEM and HYSCORE**

In the conventional one-dimensional three-pulse ESEEM experiment, the second time interval T is incremented while the first time interval t is fixed. When the signal is a function of T, the modulation depth of one frequency depends on a term containing the other frequency. In an extreme case where $\cos\omega_\alpha t$ or $\cos\omega_\beta t$ is 1, the modulation at the frequency of ω_β or ω_α cannot be observed. This blind-spot effect often requires more experiments with a different t value.

One way to overcome problems from the blind-spot effect is a two-dimensional experiment where each of the time intervals t and T is incremented in a separate dimension. Nevertheless, when the time interval t is varied, the decay is characterized by the phase memory time of the electron spin, which dilutes the advantage of exploiting the three-pulse sequence. If the time interval T is divided into two parts, t_1 and t_2, by a π pulse and the two intervals are independently incremented, the signal in either dimension has the features of the three-pulse sequence. The π pulse for the four-pulse experiment called hyperfine sublevel correlation

(HYSCORE) allows the nuclear coherence to be transferred between the two electron spin manifolds.[18-20] Figure 1-10 illustrates the HYSCORE pulse sequence and the way t_1 and t_2 are varied.

The two-dimensional HYSCORE spectrum is intrinsically symmetric with respect to the diagonal axis on which some peaks appear. Besides the diagonal peaks, cross-peaks are also observed due to the correlation between the two electron spin manifolds. The existence of such cross-peaks provides further information about the nuclear frequencies obtained in the one-dimensional ESEEM experiment. Moreover, the two frequencies of some cross-peaks may not be observed in the corresponding one-dimensional ESEEM spectrum if the modulations are too shallow.[21-22] For these reasons, the HYSCORE experiment is performed in a number of cases along with the ESEEM experiment. The equation that explains the modulations in a HYSCORE experiment is presented in Appendix B.

- **Nuclear Quadrupole Interaction for a System with *I* > 1/2 in ESEEM / HYSCORE**

Because nuclear frequencies are observed in ESEEM and HYSCORE experiments, non-magnetic interactions due to a nuclear spin are considered at times. For a nucleus with a spin of 1 or greater, the electrical nuclear quadrupole interaction is the dominant non-magnetic interaction. Furthermore, the nuclear quadrupole term in the Hamiltonian may be a major contributor to the off-diagonal elements.[23] Detailed information about the importance of the off-diagonal elements in ESEEM is provided in Appendices B and E. A nucleus with a spin of 1 or greater has an electric quadrupole moment, Q, which is due to the non-spherical, that is, asymmetric, charge distribution. The quadrupole moment interacts, at the nucleus, with the electric field gradient, which depends on the local environment around the nucleus.

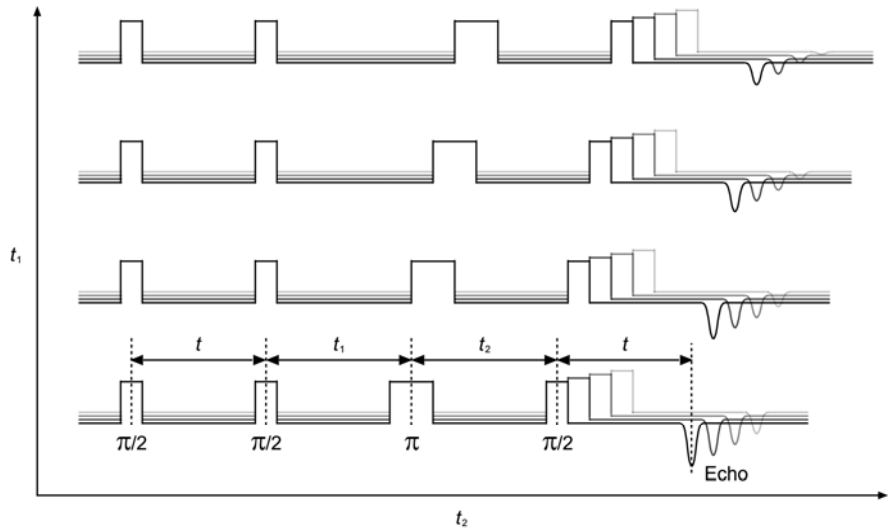

Figure 1-10. Four-pulse HYSCORE sequence. The π pulse allows the nuclear coherence to be transferred between the two electron spin manifolds. The first time interval t is fixed while the second time interval t_1 and the third time interval t_2 are independently varied, which results in a two-dimensional signal.

The anisotropy of the gradient yields different energy levels for nuclear spins with different orientations. Then, the spin Hamiltonian that describes the interaction is given by:[23]

$$\hat{\mathcal{H}}_{\mathrm{nq}} = \hbar \hat{\mathbf{I}} \cdot \tilde{\mathbf{Q}} \cdot \hat{\mathbf{I}} \tag{1-28}$$

where $\tilde{\mathbf{Q}}$ is the nuclear quadrupole tensor. In the simplest case where the nucleus has a spin of 1, the *x*-, *y*-, and *z*-component of the (traceless) tensor in the principal axis system are given by:

$$Q_{xx} = \frac{e^2 q Q(1-\eta)}{4\hbar} \;;\; Q_{yy} = \frac{e^2 q Q(1+\eta)}{4\hbar} \;;\; Q_{zz} = -\frac{e^2 q Q}{2\hbar} \tag{1-29}$$

where e is the elementary charge, q is the *z*-component of the electric field gradient across the nucleus, and η is the asymmetry parameter, which relates the three components of the tensor and is defined by the following equation.

$$\eta = \frac{Q_{xx} - Q_{yy}}{Q_{zz}} \;;\; |Q_{xx}| \geqq |Q_{yy}| \geqq |Q_{zz}| \;;\; 0 \leqq \eta \leqq 1 \tag{1-30}$$

In the pure nuclear quadrupole eigenbasis, $|T_x\rangle$, $|T_y\rangle$, and $|T_z\rangle$, there exist three energy levels that correspond to the three component of the tensor. Accordingly, the transition frequencies between two of the three energy levels are given by:[24]

$$\omega_+ = \frac{e^2 q Q(3+\eta)}{4\hbar} \;;\; \omega_- = \frac{e^2 q Q(3-\eta)}{4\hbar} \;;\; \omega_0 = \frac{e^2 q Q \eta}{2\hbar} \tag{1-31}$$

In eq (1-31), the sum of the lower two frequencies coincides with the highest one, because the nuclear quadrupole tensor is traceless. For a specific nucleus, the quadrupole interaction is characterized by the q and η values in its principal axis system. However, the Euler angles are also required in order to define the orientation of the tensor with respect to another axis system.

1.4 USE OF ESEEM AND HYSOCRE FOR THE CHARACTERIZATION OF Cu(II)-BINDING SITES

As shown in Figure 1-1, the local magnetic interactions between Cu(II) and nearby atoms, which are normally non-coordinating, in a Cu(II)–peptide complex can be detected by ESEEM and/or HYSCORE experiments. In particular, modulations due to ^{1}H and/or ^{14}N are frequently observed in ESEEM and HYSCORE spectra because of their natural abundance and ubiquity in a number of biological systems.

When an ^{14}N nucleus is present within a certain range (ca. 3–8 Å for X-band ESR) of distances from the Cu(II) ion, the magnitude of the hyperfine interaction between the electron spin and the nuclear spin is similar to that of the nuclear Zeeman interaction. Then, the two interactions cancel each other in one electron spin manifold, whereas in the other manifold, they act on each other in a reinforcing manner. Since the nuclear electric quadrupole moment of ^{14}N is not negligibe (0.019×10^{-24} cm^2), the nuclear quadrupole interaction (NQI) accounts for the transitions between the nuclear spin states in the electron spin manifold with the cancellation condition. Therefore, the three transition frequencies between the nuclear quadrupole energy levels, ω_+, ω_-, and ω_0, are observed in the electron spin manifold. From the three frequencies, the nuclear quadrupole parameters, q and η, can be determined. In the other manifold, the double quantum transition frequency is usually observed because of its less orientation-dependent nature, while the peaks due to the single quantum transitions are broadened out beyond detection. The double quantum transition frequency is given by:[25]

$$\omega_{\mathrm{dq}} = 2\sqrt{\omega_\beta^2 + \left(\frac{e^2qQ}{4\hbar}\right)^2(3+\eta^2)} \tag{1-32}$$

While the double quantum transition frequency is dependent on the external magnetic field strength, the three nuclear quadrupole frequencies are not affected by a change of the external magnetic field. Thus, the peaks corresponding to the nuclear quadrupole frequencies can be distinguished from others by a series of ESEEM experiments at different magnetic fields. Also, the relationship between the three nuclear quadrupole frequencies, that is, $\omega_+ = \omega_- + \omega_0$, may be used in order to reaffirm the identity of the peaks. On the other hand, the relationship between the three frequencies and the double quantum frequency can be observed in the corresponding HYSCORE spectrum, in which the cross-peaks at (ω_+, ω_{dq}) and (ω_{dq}, ω_+) usually appear. The hyperfine coupling constants, the nuclear quadrupole parameters, the double quantum transition frequency, and the Euler angles, combined together, can be used as fingerprints in order to characterize the environment around the ^{14}N nucleus interacting with Cu(II). The hyperfine coupling constants and the Euler angles are often estimated by spectral simulations.

As a prominent illustration of the usefulness of ^{14}N-ESEEM, deep modulations are observed when Cu(II) is coordinated by imidazole or its derivatives.[23] It has been revealed that the interaction between the Cu(II) ion and the remote, that is, non-coordinating, nitrogen of the imidazole ring gives rise to the modulations.[26-28] Figure 1-11 illustrates the nuclear quadrupole interaction of the remote ^{14}N of a Cu(II)-coordinating imidazole ring. In the ESEEM spectrum, three narrow lines due to the transitions between different nuclear quadrupole energy levels are observed. Also, a broad line appears as the double quantum transition occurs in the other electron spin manifold. On the other hand, the interaction between the Cu(II) ion and the coordinating nitrogen is unlikely to be detected because the frequency corresponding to the interaction is out of the excitation bandwidth of the pulses.

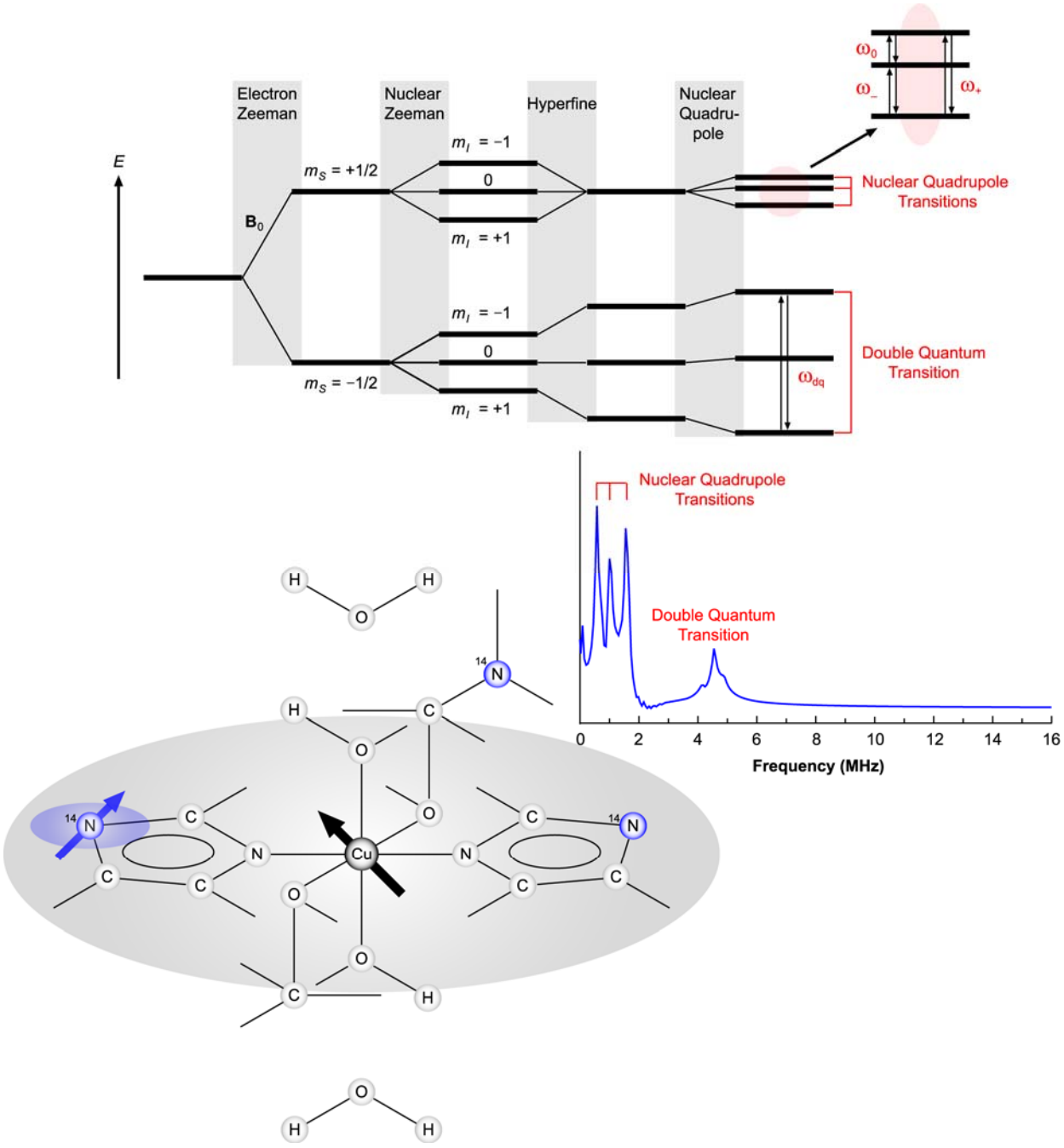

Figure 1-11. Interactions of the electron spin of the Cu(II) ion and the nuclear spin of the remote ^{14}N of a Cu(II)-coordinating imidazole. The nuclear spin transition frequencies due to the nuclear quadrupole interaction of the remote ^{14}N nucleus are observed in the ESEEM spectrum as the nuclear Zeeman interaction and the hyperfine interaction cancel each other.

Fortunately, the typical ranges of the three transition frequencies, ω_+, ω_-, and ω_0, and the nuclear quadrupole parameters for a number of Cu(II)–peptide and Cu(II)–imidazole derivative complexes have been reported; the frequencies are generally below 2 MHz. Thus, the emergence of peaks that fall into this category in ESEEM or HYSCORE spectra provides the evidence of Cu(II)–imidazole coordination, which, in turn, may indicate histidine residue(s) involved in the Cu(II) coordination. If multiple hisitidine residues simultaneously coordinate to Cu(II), harmonic or combination peaks might appear between 2 and 3.5 MHz.[29] Also, as the number of Cu(II)-coordinating histidine residues increases, the peak due to the double quantum transition becomes more prominent.[30-33] These features may be exploited in order to precisely analyze the Cu(II)–histidine coordination. More detailed information is provided in Appendix D. Besides Cu(II)–imidazole coordination, the interaction between Cu(II) and a backbone amide group can be detected by ESEEM or HYSCORE experiments. It has been shown that an amide nitrogen interacting with Cu(II) generates conspicuous modulations when the nearest carbonyl oxygen coordinates to Cu(II).[17] The interaction is characterized by the appearance of peaks around 2 MHz and 3 MHz.

When ^{1}H nuclei are present near the Cu(II) ion, modulations due to the nuclei are seen in most cases. The two fundamental frequencies, ω_α and ω_β, often converge to the Larmor frequency of ^{1}H, because the magnitude of the hyperfine interaction is much smaller than that of the nuclear Zeeman interaction in X-band ESR: the Larmor frequency at a magnetic field strength of 3360 G is 14.3 MHz. Since samples of Cu(II)–peptide complexes are generally prepared in an aqueous buffer system, ^{1}H nuclei in water molecules are one of the most probable causes of the modulation at the ^{1}H Larmor frequency.

The utility and effectiveness of ESEEM and HYSCORE can be improved by introduction of some isotopes. Even though the low natural abundance of ^{15}N (ca. 0.37%) prevents the isotope from being commonly utilized, enrichment of ^{15}N at a specific atom allows new information to be obtained.

A nucleus with a spin of 1/2, ^{15}N displays a spectroscopic feature completely different from that of ^{14}N. Since there is no quadrupole moment of ^{15}N, the ^{15}N-ESEEM spectrum is much simpler than the corresponding ^{14}N-ESEEM spectrum. Also, the modulation depths of the ^{15}N transition frequencies are usually shallower than those of the ^{14}N transition frequencies. In most cases, the modulations due to ^{15}N are not clearly seen in the one-dimensional ESEEM spectrum.[17] Figure 1-12 illustrates the interactions regarding the electron spin of Cu(II) and the remote ^{15}N and the corresponding energy diagram and ESEEM spectrum. Unlike the case of ^{14}N, the modulations in the echo intensity due to ^{15}N are shallow, which leads to relatively low intensity in the corresponding spectrum. Based on the difference between the two isotopes, one can compare the ESEEM and HYSCORE spectra of several samples that are either natural or ^{15}N-labeled in a distinguishable fashion. Eventually, the analysis of the ESEEM and HYSCORE spectra provides information about which ^{14}N nuclei in the natural sample indeed interact with Cu(II).

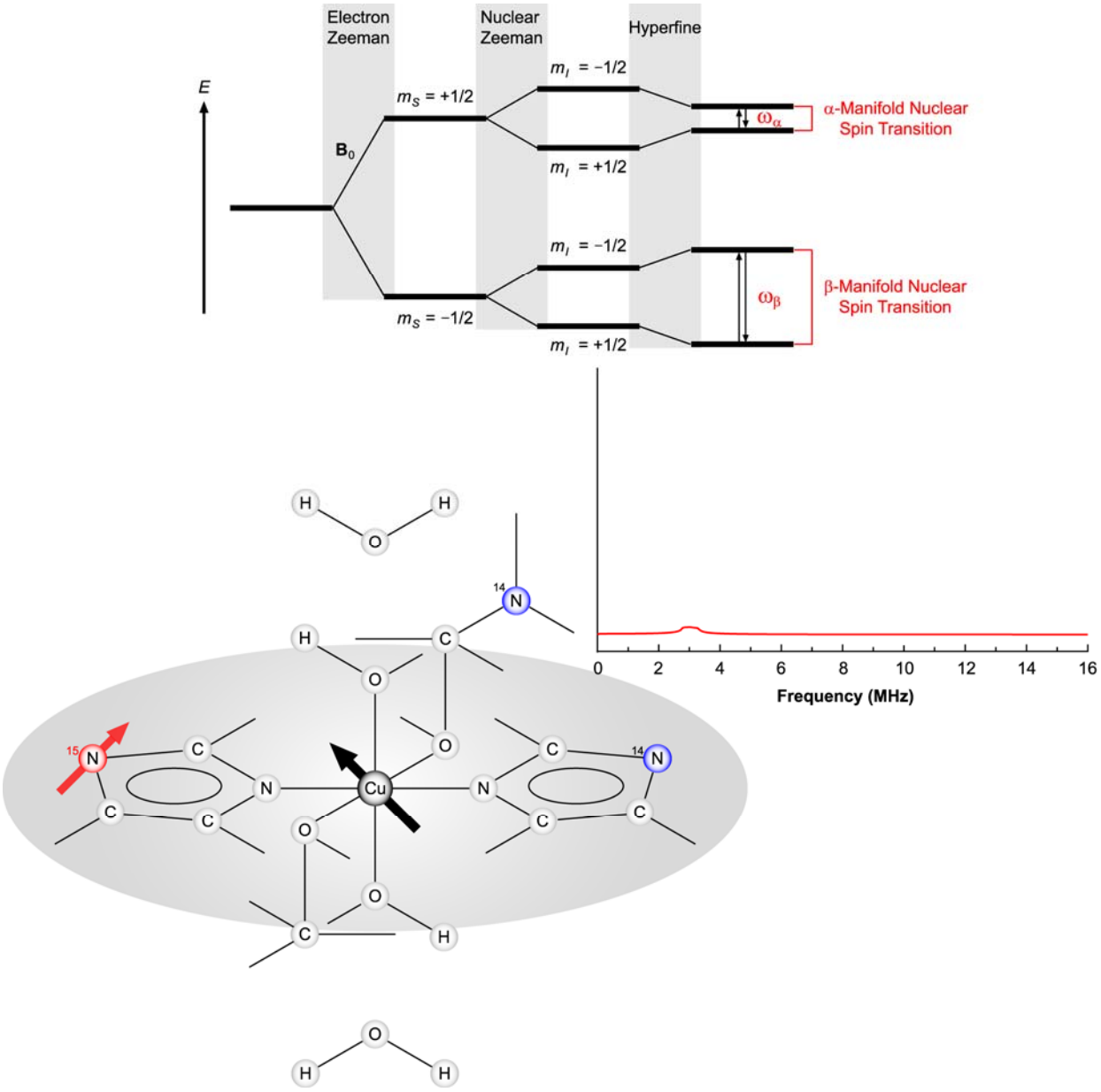

Figure 1-12. Interactions of the electron spin of the Cu(II) ion and the nuclear spin of the remote ^{15}N of a Cu(II)-coordinating imidazole. Unlike the case of ^{14}N, the interaction between the electron spin of Cu(II) and the nuclear spin of the remote ^{15}N leads to relatively weak intensity in the ESEEM spectrum.

2.0 DIRECT EVIDENCE THAT ALL THREE HISTIDINE RESIDUES COORDINATE TO Cu(II) IN AMYLOID-β(1–16)

This work, written in collaboration with Sunil Saxena, has been published in Biochemistry, 2008, V. 47, pages 9117–9123.

2.1 ABSTRACT

We provide direct evidence that all three histidine residues in amyloid-β(1–16) [Aβ(1–16)] coordinate to Cu(II). In our approach, we generate Aβ(1–16) analogues, in each of which a selected histidine residue is isotopically enriched with ^{15}N. Pulsed ESR experiments such as ESEEM and HYSCORE spectroscopy clearly show that all three histidine imidazole rings at positions 6, 13, and 14 in Aβ(1–16) bind to Cu(II). The method employed here does not require either chemical side chain modification or amino acid residue replacement, each of which is traditionally used to determine whether an amino acid residue in a protein binds to a metal ion. We find that the histidine coordination in the Aβ(1–16) peptide is independent of the Cu(II)-to-peptide ratio, which is in contrast to the Aβ(1–40) peptide. The ESR results also suggest tight binding between the histidine residues and the Cu(II) ion, which is likely the reason for the high binding affinity of the Aβ peptide for Cu(II).

2.2 INTRODUCTION

Amyloid-β (Aβ) is a naturally occurring peptide with 39–43 amino acid residues. The aggregation of Aβ is deeply associated with the onset of Alzheimer's disease, the most common form of dementia. The intermediates in the aggregation process have been suggested to play a major role in the toxicity of the disease.[34-38] It is believed that transition metal ions such as Cu(II) and Zn(II) stabilize the toxic intermediates by coordinating with the Aβ peptide.[39-43] Also, the in vitro misfolding mechanism of Aβ peptide is found to be governed by the concentration of Cu(II) ions.[44] The role of Cu(II) ions in Aβ peptide aggregation has, therefore, aroused recent scientific interest.

From a molecular point of view, however, some uncertainty about the Cu(II)-coordination site, which constitutes a fundamental determinant of the metal–peptide interaction, still exists. The work performed by Karr et al.[4,45-46] suggests that the two main forms, Aβ(1–40) and Aβ(1–42), have essentially the same Cu(II)-binding site as shorter Aβ peptides, Aβ(1–16) and Aβ(1–28). They also argue that one of the three histidine residues, presumably His14, is unlikely to be bound to Cu(II) because their CW-ESR data are consistent with 3N1O coordination and one of the nitrogen ligands is located in the N-terminus.[4,9] On the other hand, potentiometric titrations performed by Kowalik-Jankowska et al.[47] suggest that two histidine residues, His13 and His14, coordinate to Cu(II) in Aβ(1–16) and Aβ(1–28) at physiological pH. However, NMR experiments performed with Aβ(1–28) analogues by Syme et al.[48] indicate that His6, His13, and His14 as well as the N-terminus are the ligands that coordinate to Cu(II). Indeed, the Cu(II) coordination of each histidine residue has remained unresolved until lately, as seen in the three different coordination models for Cu(II)–Aβ(1–42) complexes proposed by

Raffa et al.[49] In this context, we have sought to find a way to unequivocally determine which histidine residues coordinate to Cu(II).

We have used the approach of Burns et al.[17,50-51] to investigate Cu(II)–peptide complexes. Using pulsed ESR techniques and ^{15}N-enriched peptides, they successfully identified the Cu(II) coordination site in the prion protein to be a short sequence, PHGGGW.[17,52-54] In this article, we assess the Cu(II) coordination of the three histidine residues in the Cu(II)–Aβ(1–16) complex by pulsed ESR spectroscopy. To observe the interaction between the Cu(II) ion and each histidine residue, we designed three different ^{15}N-labeled Aβ(1–16) peptide analogues, in each of which only one of the three histidine residues is isotopically ^{15}N-enriched. Pulsed ESR experiments such as ESEEM and HYSCORE on the ^{15}N-labeled peptide analogues reveal that all three histidine residues, His6, His13, and His14, bind to Cu(II). This approach does not require either amino acid side-chain modification or replacement of specific amino acid residue(s), each of which is a traditional way of determining whether an amino acid residue coordinates to a metal ion. Our experiments also indicate very little dependence of Cu(II)–histidine coordination on the molar ratio of Cu(II) to Aβ(1–16) peptide. This result is contrasted with the case of Aβ(1–40).[44] In addition, we observe a strong hyperfine interaction between the Cu(II) ion and the remote nitrogen of histidine imidazole by analysis of HYSCORE spectra. The strong interaction suggests a tight binding of histidine to Cu(II), which is likely the reason for the high affinity of the Aβ peptide to Cu(II).[48,55]

2.3 EXPERIMENTAL SECTION

- **Peptide Synthesis and Cu(II)–Peptide Complex Preparation**

Three different analogues of the Aβ(1–16) peptide, DAEFRHDSGYEVHHQK, with an ^{15}N-labeled histidine residue at either position 6 (Aβ(1–16)H6[^{15}N]), position 13 (Aβ(1–16)H13[^{15}N]), or position 14 (Aβ(1–16)H14[^{15}N]) were synthesized at the Peptide Synthesis Facility of the University of Pittsburgh. Isotopically enriched [G-^{15}N]-N_{α}-Fmoc-N_{τ}-trityl-L-histidine, in which all nitrogen atoms are enriched with ^{15}N, was purchased from Cambridge Isotope Laboratory (Andover, MA). Each of the analogues was characterized by high-performance liquid chromatography and mass spectrometry. Nonlabeled Aβ(1–16) peptide was purchased from rPeptide (Bogart, GA).

Isotopically enriched [^{63}Cu]Cl_2 was purchased from Cambridge Isotope Laboratory. A 100 mM *N*-ethylmorpholine (NEM) buffer with a pH of 7.4 was prepared by mixing NEM and hydrochloric acid in 50% glycerol. Then, 2.5 mM solutions of Aβ(1–16), Aβ(1–16)H6[^{15}N], Aβ(1–16)H13[^{15}N], and Aβ(1–16)H14[^{15}N] were prepared in the 100 mM NEM buffer. Separately, a 10 mM Cu(II) stock solution was prepared in the same buffer. For the nonlabeled Aβ(1–16) peptide and each of the three ^{15}N-labeled analogues, 1:1 and 0.25:1 Cu(II)-to-peptide molar ratio mixtures were prepared with a final concentration of 1.25 mM in the peptide. For the nonlabeled Aβ(1–16) peptide, a 4:1 mixture was additionally prepared.

- **Electron Spin Resonance Spectroscopy**

For ESR experiments, 200 μL of each Cu(II)–peptide mixture solution was transferred into a quartz tube with an inner diameter of 3 mm. ESR experiments were carried out on a Bruker ElexSys E580 FT/CW X-band spectrometer equipped with a Bruker ER 4118X-MD5

dielectric ring resonator. The temperature was adjusted with an Oxford ITC503 temperature controller and an Oxford CF935 dynamic continuous flow cryostat.

Three-pulse ESEEM experiments were performed on all of the sample solutions at 20 K with a stimulated echo pulse sequence of $\pi/2 - t - \pi/2 - T - \pi/2 - t -$ echo. The first pulse separation, t, was set at 200 ns and the second pulse separation, T, was varied from 400 ns with a step size of 16 ns for a total of 1024 points. The pulse length was 16 ns for $\pi/2$ and the magnetic field strength was fixed at approximately 3360 G, where the echo intensity was a maximum. In addition, a four-step phase cycle was employed to eliminate unwanted signals.[56-57] The maximum intensity of the data was normalized to 1, and the baseline decay was subtracted before Fourier transformation.

Four-pulse HYSCORE experiments were performed on all of the 1:1 mixture solutions at 20 K with a pulse sequence of $\pi/2 - t - \pi/2 - t_1 - \pi - t_2 - \pi/2 - t -$ echo. The first pulse separation, t, was set at 200 ns and both of the second pulse separation, t_1, and the third pulse separation, t_2, were varied from 200 ns with a step size of 16 ns for a total of 256 points. The maximum intensity of the data was normalized to 1, and the baseline decay was subtracted. Then, the data were zero-filled to 1024 points before Fourier transformation. The pulse lengths were 16 ns and 32 ns for $\pi/2$ and π pulse, respectively, and the magnetic field strength was fixed at approximately 3360 G, where the echo intensity was a maximum. In addition, a four-step phase cycle was employed to eliminate unwanted signals.

2.4 RESULTS AND DISCUSSION

All ESR experiments were carried out on the nonlabeled Aβ(1–16) peptide and three labeled Aβ(1–16) analogues. Each of the three labeled analogues has one ^{15}N-labeled histidine residue at either His6, His13, or His14. These ^{15}N-labeled peptide analogues are termed Aβ(1–16)H6[^{15}N], Aβ(1–16)H13[^{15}N], and Aβ(1–16)H14[^{15}N], respectively.

- **Evidence of Cu(II)–Histidine Coordination in Aβ(1–16) Peptide**

Three pulse ESEEM experiments were performed on the mixtures of Cu(II) and the non-labeled Aβ(1–16) with three different Cu(II)-to-peptide ratios of 4:1, 1:1, and 0.25:1. Figure 2-1 illustrates the ESEEM spectra of the three mixtures. Each of the spectra has three peaks at or around 0.55, 1.04, and 1.53 MHz. The sum of the lower two frequencies is almost equal to the highest one within the resolution error range of ±0.03 MHz, which indicates that the three peaks are presumably due to the nuclear quadrupole interaction (NQI).[58] The three ESEEM frequencies, ν_0, ν_- and ν_+, for the ^{14}N (I = 1) NQI transitions are given by:[58]

$$\nu_+ = \frac{e^2qQ(3+\eta)}{4h} \;;\; \nu_- = \frac{e^2qQ(3-\eta)}{4h} \;;\; \nu_0 = \frac{e^2qQ\eta}{2h} \qquad (2\text{-}1)$$

which is essentially the same as eq (1-29). In eq (2-1), h is Planck's constant. With these frequencies, the nuclear quadrupole parameters, e^2qQ/h and η, are determined to be 1.71 ± 0.03 MHz and 0.64 ± 0.02, respectively. All of these values, including the three frequencies and the two calculated parameters, are comparable to those for many Cu(II)–imidazole complexes that were determined by McCracken et al.[28,30,32]

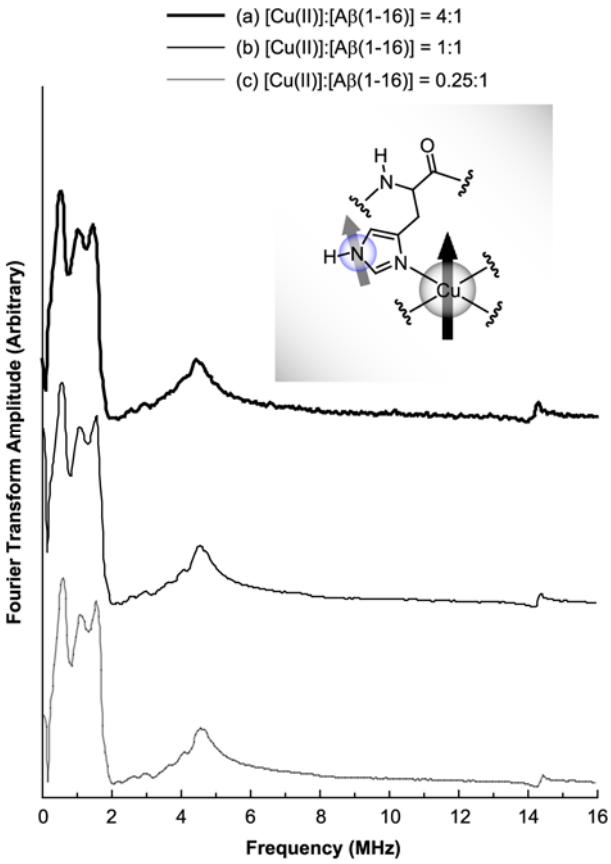

Figure 2-1. ESEEM spectra of the nonlabeled Aβ(1–16) peptide mixed with Cu(II) at different molar ratios. The three sharp peaks (0–2 MHz) and one broad peak (~4.5 MHz) are unique to the Cu(II) bound to imidazole ring(s). No significant difference in the spectra indicates little effect of the Cu(II) level on the binding environment.

Their research has shown that the interaction between the Cu(II) and the remote nitrogen of the coordinated imidazole ring causes three different nuclear quadrupole frequencies. In their experiments, the three frequencies, ν_0, ν_- and ν_+, range from 0.45 to 0.70 MHz, from 0.70 to 1.10 MHz, and from 1.40 to 1.55 MHz, respectively, and the calculated e^2qQ/h and η values were between 1.44 and 1.73 MHz and between 0.48 and 0.98, respectively.[32]

In addition, the appearance of the broad peak around 4.5 MHz is due to the ^{14}N double-quantum transition. The theoretical frequency is given by:[25]

$$\nu_{\mathrm{dq}} = 2\sqrt{\nu_\beta^2 + \left(\frac{e^2qQ}{4h}\right)^2(3+\eta^2)} \tag{2-2}$$

where ν_β is the nuclear transition frequency in the β manifold. The theoretical value is calculated with the nuclear quadrupole parameters, e^2qQ/h and η, and one of the ^{15}N transition frequencies obtained in HYSCORE experiments (0.41 MHz and 2.63 MHz; see below). The theoretical value of ν_{dq} is approximately 4.10 ± 0.14 MHz, which is comparable to the position of the broad peak.

Each of the spectra in Figure 2-1 also has a small peak around 14.3 MHz, which is almost the Larmor frequency of ^{1}H at the applied magnetic field. The position indicates that the peak is due to hydrogen atom(s) that weakly interact with the Cu(II), such as those of axially coordinated water or other remote hydrogen atom(s).[17]

On the basis of the analysis of the peaks in Figure 2-1, it is concluded that at least one histidine residue coordinates to Cu(II). Also, the almost unchanged peak positions, shapes, and intensities of the three spectra obtained with different Cu(II)-to-peptide ratios imply that the coordination environment in Aβ(1–16) is not significantly affected by the Cu(II) level. This finding is in contrast to the Cu(II)–Aβ(1–40) complex, for which the ESEEM spectrum becomes broad and heterogeneous at greater than equimolar concentrations.[44] We propose that Aβ(1–16)

has only one Cu(II)-binding site, whereas the larger peptide, Aβ(1–40), might have additional binding site(s). Syme et al.[48] have also suggested that two Cu(II)-binding sites are present in Aβ(1–28). Another possibility might be that the binding sites in Aβ(1–16) and Aβ(1–40) have different numbers of of histidine ligands. In this context, Karr et al.[4] have argued that both His13 and His14 cannot coordinate to Cu(II) in a β-sheet structure in Aβ(1–40) because the structure would be disrupted by the simultaneous coordination of two adjacent residues. It is conceivable that the Cu(II) coordination of His13 and His14 may not be restricted in Aβ(1–16) since it is soluble and highly flexible at physiological pH.

- **Direct Proof of the Cu(II) Coordination of the Three Histidine Residues (His6, His13, and His14)**

The peak positions in Figure 2-1 are similar to those for the Cu(II)-bound short peptide chain (PHGGGW) that was studied by Burns et al.[17]; ν_0, ν_- and ν_+ are 0.57, 0.90 and 1.47, respectively. Unlike the short chain PHGGGW, however, the Aβ(1–16) peptide has three histidine residues that may contribute to the ESEEM spectrum. Kosman et al.[29] showed that there may be harmonics and combination peaks between 2 and 3.5 MHz if two or more histidine residues are bound to Cu(II). Indeed, several additional peaks were clearly observed in spectral simulations that include contributions from two or three remote ^{14}N nuclei. However, the linewidths of the magnitude spectra are broad, as shown in Figure 2-1. To improve the resolution, we obtained the pure absorption spectrum by manipulating the corresponding time-domain signals with the algorithm developed by Astashkin et al.[59] The pure absorption spectum is presented in Figure 2-2.

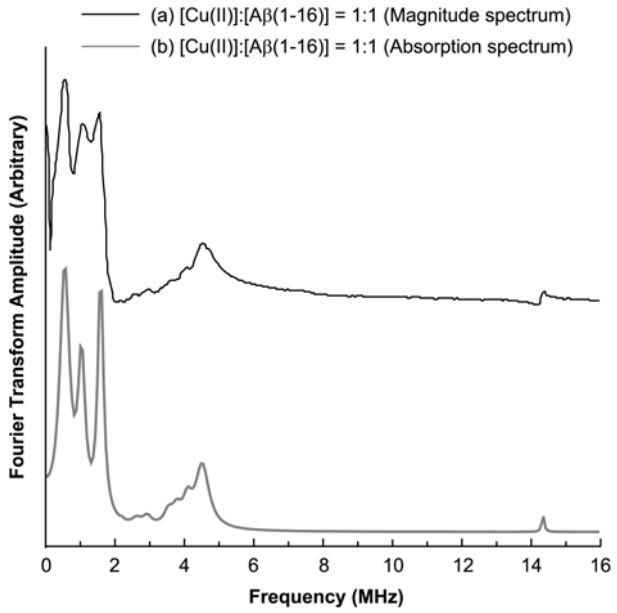

Figure 2-2. Comparison of the magnitude and absorption ESEEM spectra of the nonlabeled Aβ(1–16) peptide mixed with an equimolar amount of Cu(II). Compared with the magnitude spectra, the absorption spectra have narrower line widths, which provide clear peak separations in the histidine ESEEM region (0–10 MHz).

Even in the absorption spectrum, the peak between 2 and 3.5 MHz are not sufficiently resolved to discern harmonics or combination peaks from the baseline.

To make progress, we prepared three different singly labeled Aβ(1–16) peptide analogues that are labeled with ^{15}N at His6, His13, and His14. Then, a three-pulse ESEEM experiment was performed on the equimolar mixture of Cu(II) and each ^{15}N-labeled analogue. Figure 2-3 shows the time-domain ESEEM signals of the four Cu(II)–peptide complexes. It is known that the modulation depth in the time-domain signal increases with the number of equivalent ESEEM-active nuclei.[15] Especially, the modulation depth that is much smaller than 1 is almost directly proportional to the number of equivalent nuclei with the same frequency.[15-16] Recently, Vogt et al.[60] have determined the number of water molecules coordinated to Mn(II) by comparing modulation depths between experimental ^{2}H ESEEM spectra and simulation. In our experiments, the modulation depth in the time-domain ESEEM signals is related to the number of ^{14}N-enriched histidine residues coordinated to Cu(II). Unlike the ^{14}N NQI and double quantum transitions, the ^{15}N (I = 1/2) single-quantum transition does not meaningfully contribute to the modulation depth of time-domain signals or corresponding ESEEM spectra.[33,61-63] The comparison of the four signals in Figure 2-3 clearly shows that the nonlabeled complex has a larger modulation depth than the other three, the ^{15}N-labeled analogues, which signifies that there are more ESEEM-active ^{14}N nuclei for the Cu(II)–nonlabeled peptide complex.

To unambiguously determine the number of coordinated histidine residues, we also analyzed the integrated intensity in the corresponding ESEEM spectra. Since the integrated intensity of the ESEEM spectra is related to the modulation depth, it should decrease when one histidine residue is labeled with ^{15}N.

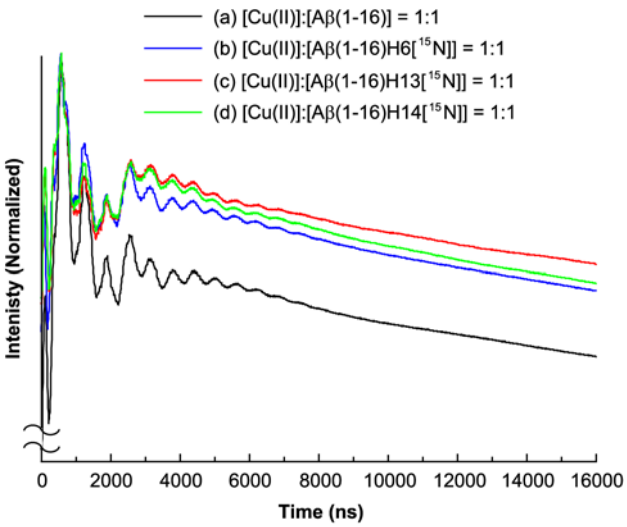

Figure 2-3. Time-domain ESEEM signals of the nonlabeled Aβ(1–16) and ^{15}N-labeled analogues mixed with an equimolar amount of Cu(II). The modulation depth of the nonlabeled complex is significantly larger than the others.

This expectation is backed by spectral simulations that include contributions from one, two, or three remote ^{14}N nuclei. Figure 2-4 shows the ESEEM spectra of the four Cu(II)–peptide complexes. Compared with the spectrum of the Cu(II)–nonlabeled peptide complex, each of the spectra of the Cu(II)–^{15}N-labeled analogues has considerably lower intensity in the histidine ESEEM region (0–10 MHz). The lower intensity of ^{15}N-labeled analogues in Figure 2-4 can be attributed to the replacement of an ESEEM-active ^{14}N nucleus with an ^{15}N nucleus as shown in the work of Burns et al.[17] The area under the curve for the histidine ESEEM region (0–10 MHz) of the nonlabeled complex is approximately 1.5 times as great as that of the ^{15}N-labeled analogues. On the other hand, the area under the curve for the ^{1}H ESEEM region (14–15 MHz) remains constant within an error range of ±3%. Since any of the ^{15}N-labeled analogues should have one fewer ESEEM-active ^{14}N nucleus, the ratio (1.5:1) is consistent with three and two contributing ^{14}N nuclei for the nonlabeled Aβ(1–16) and the ^{15}N-labeled analogues, respectively.

Whereas the three ^{14}N NQI peaks between 0 and 3 MHz display a clear difference in intensity between the nonlabeled peptide and the ^{15}N-labeled analogues, the difference in intensity of the ^{14}N double-quantum peak around 4.5 MHz is smaller. The area under the curve for the double quantum region (3–6 MHz) of the Cu(II)–nonlabeled peptide complex is approximately 1.3 times that of the ^{15}N-labeled analogues. We suspect that the use of magnitude spectra, combined with the broad linewidth and the low signal-to-noise ratio of the double quantum peak, partially explains the deviation from the expectation. The intensity of the double-quantum peak is also very sensitive to the separation between the first and second pulses.[63]

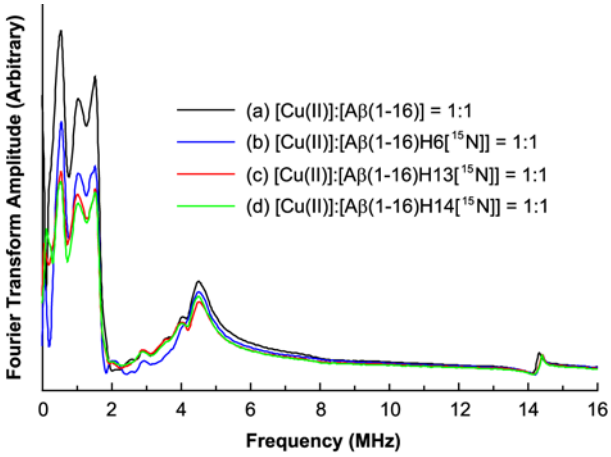

Figure 2-4. ESEEM spectra of the nonlabeled Aβ(1–16) peptide and ^{15}N-labeled analogues mixed with an equimolar amount of Cu(II). The area under the curve for the histidine ESEEM region (0–10 MHz) of the nonlabeled Aβ(1–16) complex is approximately 1.5 times that of the ^{15}N-labeled Aβ(1–16) complexes, while the four spectra have similar intensities in the ^{1}H ESEEM region (14–15 MHz).

To confirm that the three histidine residues still coordinate to Cu(II) at different Cu(II) levels, we also performed the three-pulse ESEEM experiment on the 0.25:1 mixture of Cu(II) and each ^{15}N-labeled analogue. Figure 2-5 shows the ESEEM spectra of the subequimolar mixtures of the Cu(II)–nonlabeled Aβ(1–16) peptide and the Cu(II)–^{15}N-labeled analogue complexes. When compared with the ESEEM spectra of the equimolar mixtures, shown in Figure 2-4, those of the subequimolar mixtures also reveal a similar difference in intensity between the nonlabeled peptide and the ^{15}N-labeled analogues. The peak positions are nearly identical to those for the ESEEM spectra of the equimolar mixtures and the intensity in the histidine ESEEM region (0–10 MHz) is significantly higher for the Cu(II)–nonlabeled peptide complex as in the equimolar mixtures. This points out the fact that no histidine residue is substantially preferred over the others as a ligand at a low Cu(II)-to-peptide ratio such as 0.25:1. Therefore, we conclude that the three histidine residues coordinate to Cu(II) at a range of Cu(II)-to-peptide ratios, at least from 0.25:1 to 1:1.

- **Calculation of Hyperfine Coupling Parameters by Analysis of HYSCORE Spectra.**

The interaction between each histidine residue and Cu(II) is more evident from HYSCORE experiments. In HYSCORE, the π pulse between the second and the third $\pi/2$ pulses creates the correlation between the nuclear coherences of the two different electron spin manifolds.[18,64-65] Also, the HYSCORE technique helps resolve some lines that are broadened in the ESEEM spectrum.[19,21-22] To obtain more detailed spectroscopic information about the Cu(II)–Aβ(1–16) peptide complex, HYSCORE experiments were performed on the equimolar mixture of Cu(II) and each peptide analogue.

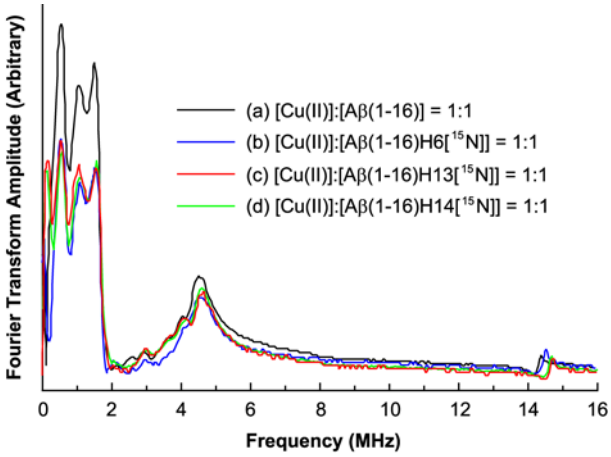

Figure 2-5. ESEEM spectra of the nonlabeled Aβ(1–16) peptide and ^{15}N-labeled analogues mixed with a subequimolar amount of Cu(II). The ratio of Cu(II) to peptide is 0.25:1. The area under the curve for the histidine ESEEM region (0–10 MHz) of the nonlabeled Aβ(1–16) complex is approximately 1.5 times that of the ^{15}N-labeled Aβ(1–16) complexes, while the four spectra have similar intensities in the ^{1}H ESEEM region (14–15 MHz).

Figure 2-6 (a) shows the HYSCORE spectrum of the Cu(II)–nonlabeled peptide complex, which contains a cross-peak around (1.5 MHz, 4.0 MHz). This peak appears due to the correlation between the ^{14}N NQI and double-quantum transition for the noncoordinating nitrogen of the histidine imidazole.[17,32] While it is also observed in the HYSCORE spectra of the Cu(II)–^{15}N-labeled peptide complexes, a new cross-peak emerges at or around (0.41 MHz, 2.63 MHz) in each of the ^{15}N-labeled analogues. The cross-peak is comparable to the ^{15}N cross-peak observed in the HYSCORE spectrum of the ^{15}N-labeled Cu(II)–HGGGW complex in terms of peak position and contour lineshape.[17,61] Moreover, the average of the two frequencies, 1.52 MHz, is close to 1.45 MHz, the Larmor frequency of ^{15}N corresponding to a magnetic field of 3360 G at which our ESEEM and HYSCORE experiments were carried out. Thus, the cross-peak is due to the correlation between the ^{15}N transitions in different electron spin manifolds. The two frequencies, ν_α and ν_β, are given by:[23,66-67]

$$\nu_\alpha = \sqrt{\left(\nu_I - \frac{A}{2}\right)^2 + \left(\frac{B}{2}\right)^2} \;;\; \nu_\beta = \sqrt{\left(\nu_I + \frac{A}{2}\right)^2 + \left(\frac{B}{2}\right)^2} \qquad (2\text{-}3)$$

where ν_I is the Larmor frequency, and A and B are the secular part and the pseudosecular part of the hyperfine interaction, respectively. The Cu(II)–Aβ(1–16) complexes show little orientation selectivity in the ESEEM spectrum at $g_\perp$ for the Cu(II), and the Cu(II)-coordinating histidine is perpendicular to the $g_\parallel$ axis.[28,32] Therefore, an axial hyperfine tensor is assumed for this system, the two frequencies, ν_α and ν_β, are related by the equation below.[20,66-68]

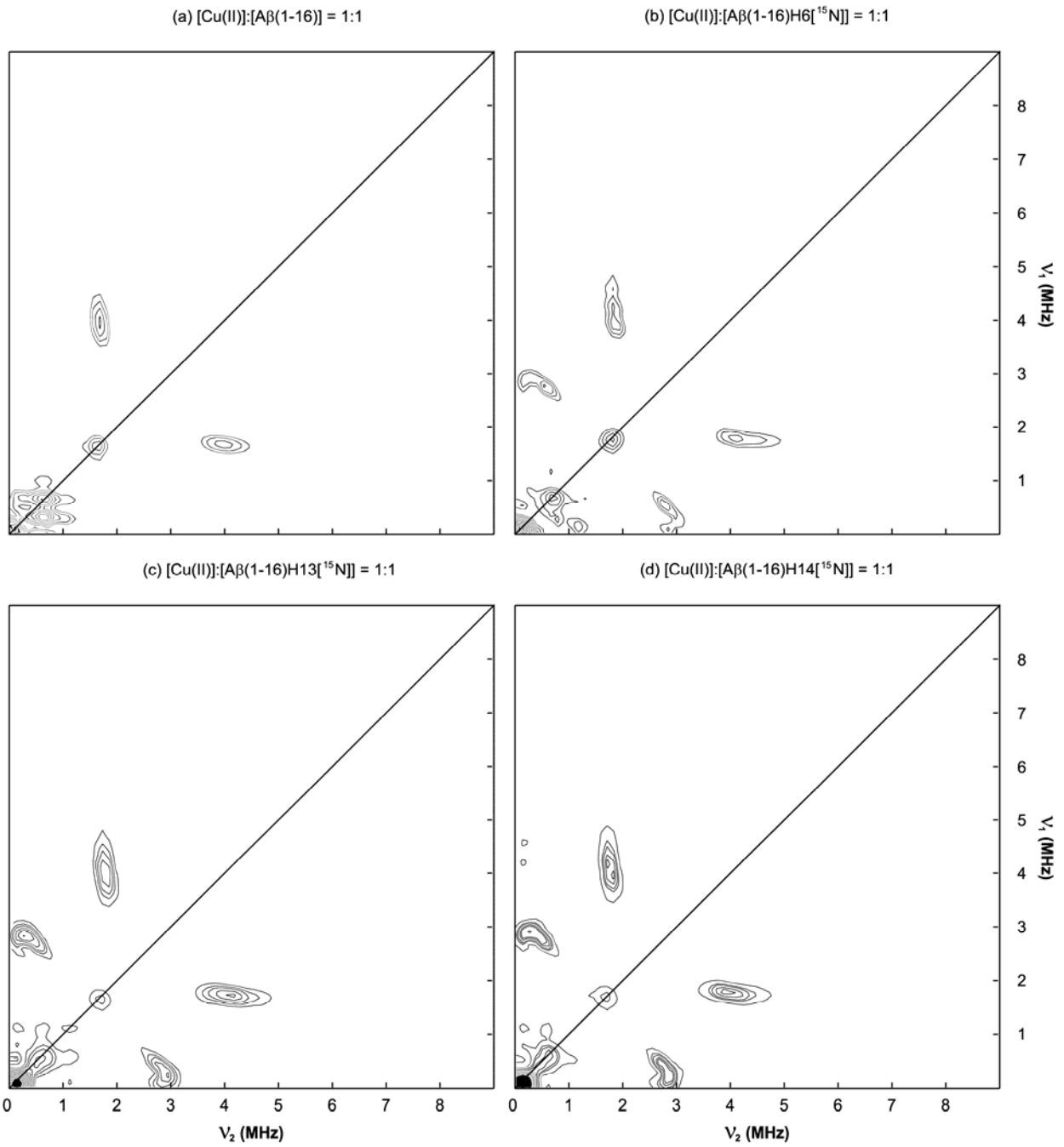

Figure 2-6. HYSCORE spectra of the nonlabeled Aβ(1–16) peptide and ^{15}N-labeled analogues mixed with an equimolar amount of Cu(II). The spectrum of the Cu(II)–nonlabeled peptide complex lacks a cross-peak at or around (0.41 MHz, 2.63 MHz) which appears in the other three spectra.

$$\nu_\alpha = Q\nu_\beta + G \tag{2-4}$$

where

$$Q = \frac{T_{\mathrm{dip}} + A_{\mathrm{iso}} - 4\nu_I}{T_{\mathrm{dip}} + A_{\mathrm{iso}} + 4\nu_I} \tag{2-5}$$

$$G = 2\nu_I \frac{4\nu_I - A_{\mathrm{iso}} + 2T_{\mathrm{dip}}^2 - A_{\mathrm{iso}}T_{\mathrm{dip}}}{T_{\mathrm{dip}} + 2A_{\mathrm{iso}} + 4\nu_I} \tag{2-6}$$

In eqs (2-5) and (2-6), A_{iso} and T_{dip} are the isotropic and the dipolar component of the hyperfine constant, respectively. Equation (2-4) accounts for the lineshape of the ^{15}N cross-peak in the contour plot: it is an elliptic or hyperbolic arc. The HYSCORE spectra of Cu(II)–Aβ(1–16)H6[^{15}N], Cu(II)–Aβ(1–16)H13[^{15}N], and Cu(II)–Aβ(1–16)H14[^{15}N], shown in Figure 2-6 (b), (c), and (d), respectively, have similar ^{15}N cross-peak positions and contour lineshapes, which indicates that the hyperfine coupling parameters for the three histidine residues are nearly identical. The Cu(II)–His13 and Cu(II)–His14 hyperfine couplings may be different because His13 and His14 are adjacent residues; therefore, the two residues are unlikely to attain similar binding conformations. Nevertheless, we were unable to detect substantial differences possibly due to the resolution of the data set. Such differences can be more quantitatively measured by the use of doubly ^{15}N-labeled peptide analogues. The two constants, Q and G, are determined to be –0.154 and 1.23 MHz^2, respectively, by plotting ν_α^2 versus ν_β^2, and A_{iso} and $|T_{\mathrm{dip}}|$ for ^{15}N are calculated to be 2.33 and 0.413 MHz, respectively. The parameters strongly suggest that the binding affinity of Cu(II)–histidine coupling in Aβ(1–16) is high because the hyperfine coupling constants are greater than those for Cu(II) complexes of imidazole derivatives that were studied by McCracken et al.[30,32] The strong hyperfine interaction may explain the submicromolar-level dissociation constant of the Cu(II)–Aβ peptide complex reported by Syme et al.[48]

2.5 SUMMARY

In this article, we elucidate the binding of Cu(II) to the three histidine residues in the Aβ(1–16) peptide with no amino acid side-chain modification or replacement of residue(s). Employing ESEEM and HYSCORE techniques with the nonlabeled Aβ(1–16) peptide and ^{15}N-labeled analogues, we reveal that ^{15}N labeling of each histidine leads to a significant change in the ESR spectra. The ESEEM spectra of the singly ^{15}N-labeled analogues exhibit lower intensities when compared with the nonlabeled Aβ(1–16) peptide. In addition, direct evidence of a strong hyperfine interaction between the Cu(II) ion and each histidine residue is obtained from the HYSCORE spectra. Our data also illustrate that the Cu(II)-binding site in Aβ(1–16) is not sensitive to the Cu(II)-to-peptide ratio, which is in contrast to the case of the Aβ(1–40) peptide.

2.6 ACKNOWLEDGMENT

This work was supported by a National Science Foundation CAREER grant (MCB 0346898). We are grateful to Drs. Sangmi Jun and Sharon Ruthstein for helpful discussions. We also thank the Peptide Synthesis Facility of the University of Pittsburgh for the peptide preparation.

3.0 SUBSTANTIAL CONTRIBUTION OF THE TWO IMIDAZOLE RINGS OF THE HIS13–HIS14 DYAD TO Cu(II) BINDING IN AMYLOID-β(1–16) AT PHYSIOLOGICAL pH AND ITS SIGNIFICANCE

Part of this work, written in collaboration with Sunil Saxena, has been published in the Journal of Physical Chemistry A, 2011, V. 115, as soon as publishable.

3.1 ABSTRACT

The interaction of the Aβ peptide with Cu(II) appears to play an important role in the etiology of Alzheimer's disease. At physiological pH, the Cu(II) coordination in Aβ is heterogeneous, and there exist at least two binding modes in which Cu(II) is coordinated by histidine residues. Electron spin resonance studies have revealed a picture of the Cu(II) binding at a higher or lower pH, where only one of the two binding modes is almost exclusively present. We describe a procedure to directly examine the coordination of Cu(II) to each histidine residue in the dominant binding mode at physiological pH. We use nonlabeled and residue-specifically ^{15}N-labeled Aβ(1–16). For quantitative analysis, the intensities of three-pulse ESEEM spectra are analyzed. Spectral simulations show that ESEEM intensities provide information about the contribution of each histidine residue. Indeed, the ESEEM experiments at pH 6.0 confirm the dominant contribution of His6 to the Cu(II) coordination as expected from the work of other

researchers. Interestingly, however, the ESEEM data obtained at pH 7.4 reveal that the contributions of the three residues to the Cu(II) coordination are in the order of His14 $\approx$ His6 $>$ His13 in the dominant binding mode. The order indicates a significant contribution from the simultaneous coordination by His13 and His14 at physiological pH, which has been underappreciated. These findings are supported by HYSCORE experiments. The simultaneous coordination by the two adjacent residues is likely to be present in a non–β-sheet structure. The coexistence of different secondary structures is possibly the molecular origin for the formation of amorphous aggregates rather than fibrils at relatively high concentrations of Cu(II). Through our approach, precise and useful information about the Cu(II) binding in Aβ(1–16) at physiological pH is obtained without any side-chain modification, amino acid residue replacement, or pH change, each of which might lead to an alteration in the peptide structure or the coordination environment.

3.2 INTRODUCTION

Amyloid-β, a naturally occurring polypeptide with 39–43 amino acid residues, is implicated in the pathogenesis of Alzheimer's disease. The aggregation of Aβ, which is normally soluble in body fluids, into insoluble deposits is a crucial pathological event in the disease. Several studies have suggested that the intermediates in the aggregation process may account for the neurotoxicity of the disease.[37-38,42,69-70] The aggregation of the polypeptide is influenced by other chemical species such as serum proteins, apolipoproteins, phospholipids, and transition metal ions.[71] In particular, some transition metal ions such as Cu(II) and Zn(II) affect the aggregation by direct coordination with the polypeptide.[72-73]

Recent research shows that Cu(II) and Zn(II) are found to be colocalized with aggregated Aβ in the brain of patients with Alzheimer's disease.[43] Also, the transition metal ions are deeply associated with the change in the secondary structure and morphology of the Aβ peptide.[74] In particular, in vitro research has revealed that, with increasing Cu(II) concentrations, amorphous aggregates become dominant over ordered fibrils.[44] While the effect of the Zn(II) binding on the aggregation and toxicity is controversial,[75-78] the coordination of Cu(II) is generally believed to increase the toxicity.[74,79-80] The role of Cu(II) as an etiological factor is, therefore, of biomedical interest.

From a molecular point of view, there has been considerable interest in determining the binding site(s) of Cu(II) in Aβ. A number of scientific approaches have revealed that histidine residues are involved in the Cu(II) coordination. Because Aβ(1–40) and Aβ(1–42), the two major forms found in the amyloid deposits, have three histidine residues, His6, His13, and His14, it has been an important issue to determine which histidine residues coordinate to Cu(II). The work performed by Karr et al.[4,45-46] suggests that Aβ(1–40) and Aβ(1–42) have essentially the same Cu(II)-binding site as shorter Aβ peptides, Aβ(1–28) and Aβ(1–16). Also, the presence of a primary Cu(II)-binding site near the N-terminus region containing the three histidine residues is accepted by researchers[47-48,81-87] even though the work of Sarell et al.[87] suggests that the two shorter Aβ peptides have a relative weak second Cu(II)-binding site. Thus, the two shorter peptides serve as good model systems to investigate the Cu(II) coordination in Aβ especially when an equimolar or subequimolar amount of Cu(II) is present with the peptide.

Despite contradictory results from some groups,[4,47] it appears to be consensual that all three histidine residues, His6, His13, and His14, coordinate to Cu(II) in the equimolar Cu(II)–Aβ(1–16) complex.[48,81-86] A number of ESR studies have, however, suggested that there exists an

equilibrium between at least two different Cu(II)-coordination environments in the equimolar complex at physiological pH.[48,82,84] Syme et al.[48] have reported that two sets of CW-ESR signals typical of type II Cu(II) complexes are detected from the mixture of Cu(II) and either Aβ(1–28) or Aβ(1–16) at a pH of 7.4. They have also shown that the component with a $g_{||}$ value of 2.26, Component I, is prevalent at a lower pH, whereas the component with a $g_{||}$ value of 2.22, Component II, is dominant at a higher pH. Drew et al.[82] have suggested Cu(II)-binding modes based on their CW-ESR and HYSCORE results. Their experimental data and simulations indicate that His6 coordinates to Cu(II) in Component I and Component II, whereas His13 and His14 simultaneously coordinate to Cu(II) in Component II, but not in Component I. The HYSCORE results of Dorlet et al.[84] have also suggested similar Cu(II)-binding modes for Component I. On the other hand, Sarell et al.[87] have argued that in both Component I and Component II, two histidine residues, one of which is His6, equatorially coordinate to Cu(II) while the other axially coordinates to Cu(II).

While most researchers propose that two histidine residues simultaneously coordinate to Cu(II) on the equatorial plane in Component I, the number of simultaneously coordinating histidine residues in Component II is controversial. Nevertheless, the binding modes suggested by these groups are consistent with one another in that His6 plays a more pivotal role in the Cu(II) coordination. However, their results may not be fully reflective of the binding modes at physiological pH because most of the experiments have been performed at a lower or higher pH.

Our group has already reported that all of the three residues are involved in the Cu(II) coordination at physiological pH, and their overall contributions are not significantly different.[81] Nevertheless, our pervious work was performed under conditions where both components

contribute to the signal. Thus, our previous results only showed the average representation of the Cu(II) coordination in Aβ(1–16), and the nature of the equilibrium was not truly appreciated.

In this context, we carefully reexamine the contribution of each histidine residue to the Cu(II) coordination in Aβ(1–16), particularly in Component I, at a pH of 7.4 by employing pulsed ESR spectroscopy and exploiting a ternary complex system. The difference between the contributions of His6, His13, and His14 to the Cu(II) coordination in Component I, the dominant component at physiological pH, is our primary interest. We are also interested in the significance of the simultaneous coordination by His13 and His14, which has been suggested to be unlikely in Component I.[82,84] To obtain information about the Cu(II) coordination in Component I, we have performed three-pulse ESEEM experiments on equimolar mixtures of Cu(II) and either Aβ(1–16) or its ^{15}N-labeled version at a relatively low magnetic field where Component II is negligible.

Intriguingly, our ESEEM results suggest that the contributions of the three histidine residues to the Cu(II) coordination in Component I are in the order of His14 $\approx$ His6 $>$ His13, which can only be explained by a significant contribution of the simultaneous Cu(II) coordination by the two imidazole rings of His13 and His14 in Component I. The observation at physiological pH is informative in that the coordination by the two adjacent residues is likely to lead to the formation of a non–β-sheet structure, which is believed to be associated with toxicity. The biochemical significance of the Cu(II) coordination by the His13–His14 dyad is further discussed in this article.

To assess the relative Cu(II)-binding affinity for each histidine residue, we have introduced a Cu(II)–diethylenetriamine (dien) complex, which is in turn mixed with nonlabeled or ^{15}N-labeled Aβ(1–16) to form a ternary complex. The ESEEM spectra of the ternary

complexes indicate that the Cu(II)-binding affinities for the three histidine residues are in the order of His14 $>$ His6 $\approx$ His13 at a pH of 7.4. The order may account for the unexpected high contribution of His14 to the Cu(II) coordination in Component I at physiological pH.

Also, a broader interpretation of our results leads to the suggestion that the contributions of the three histidine residues to the Cu(II) coordination in Component II are in the order of His13 $>$ His6 $\approx$ His14, and intermolecular bridges may form by sharing of His13 by two Cu(II) ions in Component II. All in all, our experiments are meaningful in that the interaction between Cu(II) and each histidine residue at physiological pH is traced via a simple model system.

3.3 EXPERIMENTAL SECTION

- **Peptide Synthesis and Cu(II) Complex Preparation**

Isotopically enriched [G-^{15}N]-N_{α}-Fmoc-N_{τ}-trityl-L-histidine, in which all nitrogen atoms are enriched with ^{15}N, was purchased from Cambridge Isotope Laboratory (Andover, MA). Three different analogues of the Aβ(1−16) peptide, DAEFRHDSGYEVHHQK, with an ^{15}N-labeled histidine residue at either position 6, 13, or 14 were synthesized at the Peptide Synthesis Facility of the University of Pittsburgh via the conventional solid-phase fluorenylmethoxycarbonyl chemistry.[88-89] The three ^{15}N-labeled Aβ(1−16) analogues were termed Aβ(1−16)H6[^{15}N], Aβ(1−16)H13[^{15}N], and Aβ(1−16)H14[^{15}N], respectively. Each of the analogues was characterized by high performance liquid chromatography and mass spectrometry. The nonlabeled Aβ(1−16) peptide was purchased from rPeptide (Bogart, GA). Isotopically enriched [^{63}Cu]Cl_2 was purchased from Cambridge Isotope Laboratory.

Diethylenetriamine and *N*-ethylmorpholine were purchased from Sigma–Aldrich (St. Louis, MO).

A 100 mM NEM buffer with a pH of 7.4 was prepared by mixing NEM and hydrochloric acid in 50% glycerol. Another NEM buffer with a pH of 6.0 was prepared in the same fashion. Then, 2.5 mM solutions of Aβ(1–16), Aβ(1–16)H6[^{15}N], Aβ(1–16)H13[^{15}N], and Aβ(1–16)H14[^{15}N] were prepared in the pH 7.4 NEM buffer as well as in the pH 6.0 NEM buffer. Separately, 10 mM Cu(II) stock solutions were prepared in the two buffers. For each of the Aβ(1–16) analogues, an equimolar Cu(II)–peptide mixture was prepared with a final concentration of 1.25 mM. A 6 mM solution of dien was also prepared in the pH 7.4 NEM buffer. Then, a 1.2:1 molar ratio mixture of dien and Cu(II) was prepared with a final concentration of 2.5 mM in Cu(II). For each of the Aβ(1–16) analogues, a 1.2:1:1 dien–Cu(II)–peptide mixture was prepared with a final concentration of 1.25 mM in the peptide.

- **Electron Spin Resonance Spectroscopy**

Cu(II)–peptide mixtures dissolved in the pH 7.4 buffer or in the pH 6.0 buffer and dien–Cu(II)–peptide mixtures dissolved in the pH 7.4 buffer were used for ESR experiments. A 200 μL aliquot of each Cu(II)–peptide or dien–Cu(II)–peptide mixture solution was transferred into a quartz tube with an inner diameter of 3 mm. All ESR experiments were performed on a Bruker ElexSys E580 FT/CW X-band spectrometer equipped with a Bruker ER 4118X-MD5 dielectric ring resonator. The temperature was adjusted with an Oxford ITC503 temperature controller and an Oxford CF935 dynamic continuous-flow cryostat connected to an Oxford LLT650 low-loss transfer tube.

Continuous-wave ESR experiments were carried out on the sample solutions. All CW-ESR signals were collected at 80 K with a microwave frequency of approximately 9.69 GHz. The magnetic field was generally swept from 2600 G to 3600 G for a total of 1024 data points. Other instrumental parameters include a time constant of 40.96 ms, a conversion time of 81.92 ms, a modulation amplitude of 4 G, a modulation frequency of 100 kHz, and a microwave power of 0.1993 mW. The experimentally obtained spectra were compared with the corresponding simulated spectra in Symphonia and WINEPR provided by Bruker.

Field-swept echo experiments were performed on the sample solutions at 20 K. Then, three-pulse ESEEM experiments were performed on the same sample solutions at 20 K with a conventional stimulated-echo pulse sequence of $\pi/2 - t - \pi/2 - T - \pi/2 - t -$ echo. The first pulse separation, t, was set at either 144, 192, or 200 ns, and the second pulse separation, T, was varied from either 288 or 400 ns with a step size of 16 ns for a total of 1024 points. The pulse length was 16 ns, and the magnetic field strength was fixed at one of 2800, 2950, 3100, 3226, 3350, 3360, and 3375 G; Component I of the Cu(II)–Aβ(1–16) mixtures, whether ^{15}N-labeled or not, is almost exclusively present at 2800 G at physiological pH; 2950, 3100, and 3226 G are close to the $g_{\|}$ position of the dien–Cu(II)–peptide mixtures; and 3350, 3360, and 3375 G correspond to the $g_{\perp}$ positions where the echo intensity is a maximum. In addition, a four-step phase cycle was employed to eliminate unwanted signals.[56-57] The real parts of the collected raw data were baseline-corrected and fast Fourier-transformed. Then, the final spectra were obtained as the magnitude of the Fourier transforms. Several ESR parameters for some of the experimentally obtained spectra were determined by spectral simulations based upon the methods provided by Lee et al.[24] and Stoll and Britt.[90]

Four-pulse HYSCORE experiments were performed at 20 K with a pulse sequence of $\pi/2 - t - \pi/2 - t_1 - \pi - t_2 - \pi/2 - t -$ echo. The first pulse separation, t, was set at either 144 or 200 ns, and both the second pulse separation, t_1, and the third pulse separation, t_2, were varied from either 144 or 200 ns with a step size of 16 ns for a total of either 256 or 512 points. The pulse lengths were 16 and 32 ns for $\pi/2$ and π pulses, respectively, and the magnetic field strength was fixed at approximately 3360 or 3375 G, where the echo intensity is a maximum. In addition, a four-step phase cycle was employed to eliminate unwanted signals. The real parts of the collected two-dimensional data were baseline-corrected and apodized with a Hamming window in both dimensions. Then, the processed data were zero-filled to 1024 points in both dimensions before being fast Fourier-transformed. The final spectra were obtained as the contour plots of the magnitude of the two-dimensional Fourier transforms.

3.4 RESULTS

A series of CW-ESR and pulsed ESR experiments were conducted on the nonlabeled and ^{15}N-labeled Cu(II)–Aβ(1–16) mixtures and dien–Cu(II)–Aβ(1–16) mixtures. Each of the ^{15}N-labeled Aβ(1–16) peptide analogues used here contains only one ^{15}N-enriched hisitidine residue at either His6, His13, or His14. These ^{15}N-labeled analogues are termed Aβ(1–16)H6[^{15}N], Aβ(1–16)H13[^{15}N], and Aβ(1–16)H14[^{15}N], respectively.

- **Two Components Present in the Mixture of Cu(II) and Aβ(1–16) at Physiological pH**

Continuous-wave ESR experiments were carried out on the equimolar mixture of Cu(II) and the nonlabeled Aβ(1–16) dissolved in the 100 mM NEM buffer at a pH of 7.4. Figure 3-1 shows the experimentally obtained CW-ESR spectra of the equimolar mixture and spectral simulation results. It is clear that two components are present in the mixture. The $g_{||}$ value and $A_{||}$ value of the major component (Component I) are determined to be 2.27 ± 0.005 and 171 ± 1 G, respectively, by spectral simulations. The values are consistent with a square-planar Cu(II)-coordination geometry with three nitrogen donors and one oxygen donor on the equatorial plane.[9] Similarly, the $g_{||}$ value and $A_{||}$ value of the minor component (Component II) are determined to be 2.23 ± 0.005 and 157 ± 1 G, respectively and the values are consistent with three nitrogen donors and one oxygen donor or four nitrogen donors on the equatorial plane.[9] The simulation results also show that the minor component accounts for 25–30% of the Cu(II)–peptide complex.

- **Contribution of Each Histidine Residue to the Cu(II) Coordination in Component I at Two Different pHs of 7.4 and 6.0**

Our previous work suggested that all of the three histidine residues in Aβ(1–16) contribute to a similar extent to the Cu(II) coordination at physiological pH.[81] In that work, however, three-pulse ESEEM experiments were carried out at a magnetic field of approximately 3360 G, where the ESR signal intensity reflects both Component I and Component II. Thus, our previous ESEEM results represent the average aspect of the Cu(II)–Aβ(1–16) complex at physiological pH.

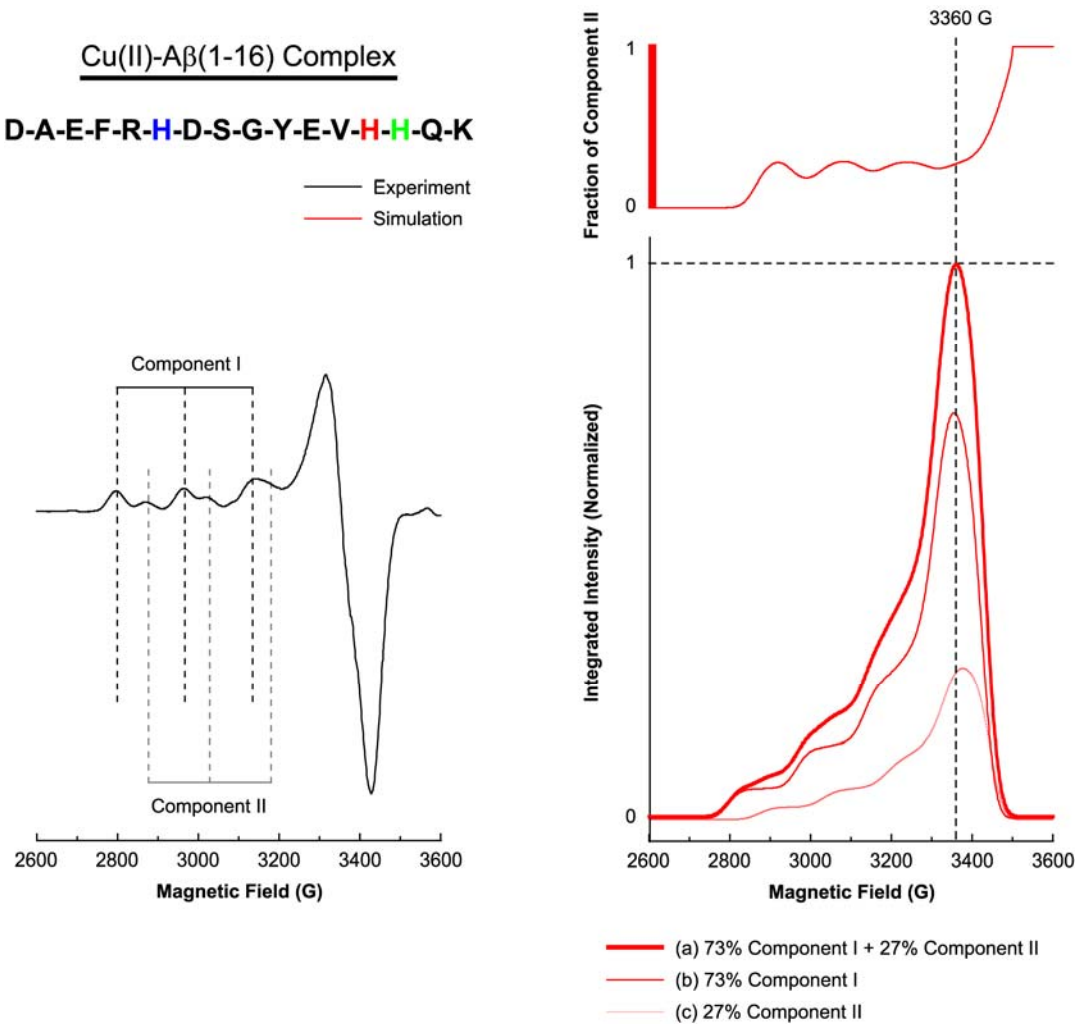

Figure 3-1. Multiple components present in the Cu(II)–Aβ(1–16) complex suggested by the experimental and simulated CW-ESR spectrum of Aβ(1–16) mixed with an equimolar amount of Cu(II). The amino acid sequence of Aβ(1–16) is illustrated with His6, His13, and His14 indicated in blue, red, and green, respectively. The experimentally obtained CW-ESR spectrum, which contains two clearly distinguished components, component I and component II, is shown at the top. The fraction of component II as a function of the magnetic field is shown at the middle. At the bottom, the curves corresponding to 73% component I, 27% component II, and the mixture thereof are shown in red, pink, and bold red, respectively. Component II

accounts for approximately a quarter of the Cu(II)–Aβ(1–16) complex at 3360 G, while there is practically no contribution of component II below 2810 G.

Figure 3-1 also shows the contribution of Component II to the overall signal intensity based on our CW-ESR simulations; Component II accounts for approximately 25% of the total signal at 3360 G. To evaluate the contribution of each histidine residue to the Cu(II) coordination exclusively in Component I without changing pH, we took advantage of a magnetic field where the contribution of Component II is negligible, as suggested by the work of Santagelo et al.[91-92] on a Cu(II)–DNA complex. As illustrated in Figure 3-1, Component II gives practically no ESR signal below 2810 G. We performed three-pulse ESEEM experiments on the equimolar mixtures of Cu(II) and the Aβ(1−16) analogues including Aβ(1−16), Aβ(1−16)H6[^{15}N], Aβ(1−16)H13[^{15}N], and Aβ(1−16)H14[^{15}N] at 2800 G.

Figure 3-2 shows the ESEEM spectrum of the nonlabeled Aβ(1−16) peptide mixed with Cu(II) at 2800 G at a pH of 7.4. The spectrum has three peaks at or around 0.55, 1.01, and 1.54 MHz. With the three ESEEM frequencies for the NQI transitions, ν_0, ν_-, and ν_+, the nuclear quadrupole parameters, e^2qQ/h and η, are determined to be 1.70 ± 0.03 MHz and 0.65 ± 0.02, respectively, which are comparable to those for Cu(II) complexes of histidine imidazole in proteins that were determined by McCracken et al.[28,30-32,93] In addition to the three peaks, each spectrum also has a broad peak around 3.8 MHz. On the basis of the analysis of the NQI frequencies and the three-pulse ESEEM and HYSCORE data obtained at 3360 G, we have concluded that the broad peak around 3.8 MHz is due to the double-quantum transition in the other electron spin manifold.

Figure 3-2 also shows the corresponding simulated spectra overlaid with the experimentally obtained spectrum. Since two histidine residues are likely to simultaneously coordinate to Cu(II) on the equatorial plane, two ESEEM-active ^{14}N nuclei are assumed to yield the best fit.

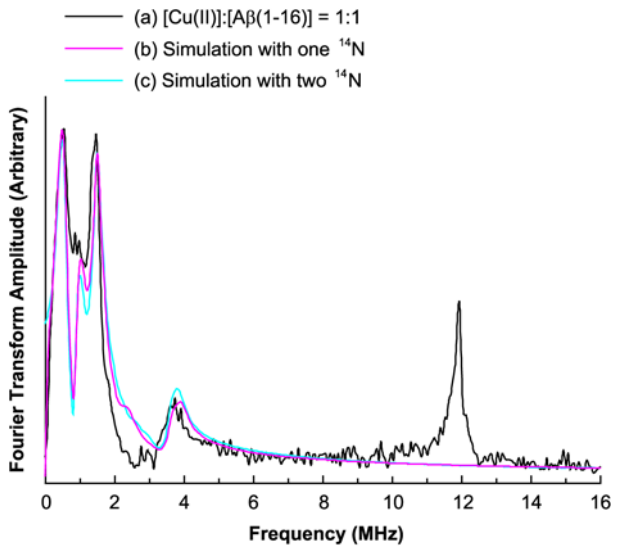

Figure 3-2. Experimentally obtained and simulated three-pulse ESEEM spectra of the isotopically nonlabeled Aβ(1–16) peptide mixed with an equimolar amount of Cu(II) at 2800 G at pH 7.4. The simulated spectra with two ESEEM-active ^{14}N nuclei are in good agreement with the experimental result.

Aside from the peaks due to ^{14}N nuclei, another peak appears around 11.9 MHz, which is almost the Larmor frequency of ^{1}H at 2800 G. The peak is attributed to the presence of hydrogen atom(s) that weakly interact with the electron spin of Cu(II).

In our work, we analyze the integrated intensity, typically between 0 and 8 MHz, in the three-pulse ESEEM spectra of the nonlabeled and ^{15}N-labeled Cu(II)–Aβ(1−16) complexes to elucidate the contributions of the three histidine residues to the Cu(II) coordination.[81] The modulation depths of the frequencies due to ESEEM-active ^{14}N nuclei decrease when some of the ^{14}N nuclei are replaced with ^{15}N because the single-quantum transition of ^{15}N nuclei does not substantially contribute to the ESEEM signal.[10,33,61-63,94] However, it is difficult to obtain the modulation depth of each frequency because there are several different frequencies attributed to ^{14}N in an ESEEM time-domain curve. Thus, instead of comparing the modulation depths, we compare the integrated intensity of the ESEEM spectrum of the nonlabeled version with that of the ^{15}N-labeled ones. Because the modulation depth of the ^{1}H-ESEEM frequency is not significantly affected by a replacement of ^{14}N with ^{15}N, the integrated intensity of the ^{1}H-ESEEM is utilized to normalize the integrated intensity of the ^{14}N-ESEEM region. Detailed calculations show that this normalized ^{14}N-ESEEM intensity is a monotonic function of the fraction of ^{14}N that is replaced with ^{15}N. The relevant equations include eqs (F-40), (F-49), and (F-59) provided in Appendix F. Also, simulations show that the normalized ^{14}N-ESEEM intensity increases by a factor of approximately 1.8 when the number of coupled ESEEM-active ^{14}N nuclei increases from one to two provided that the two nuclear spins are equivalent. Detailed explanations about the method used here are provided in Appendix F.

This analysis has been applied to the ESEEM data obtained in this work. Figure 3-3 shows the comparison of the ESEEM spectra of the nonlabeled and ^{15}N-labeled Aβ(1−16) mixed with an equimolar amount of Cu(II) at pH 7.4. The four spectra have almost identical spectral shapes including peak positions in the ^{14}N-ESEEM region below 8 MHz. The similarity in the peak shapes shown in Figure 3-3 implies that the ESEEM-active ^{14}N of each histidine residue has almost identical nuclear transition frequencies.[32] Even with the almost identical frequencies, however, possible difference in the orientation of each histidine residue might also lead to a different normalized ^{14}N-ESEEM intensity. Nevertheless, simulations show that the change in the normalized intensity by such orientational effects is within 5% of the average value for the case of a single electron spin interacting with one ^{14}N nucleus. Detailed explanations are provided in Appendix F.

As shown in Figure 3-3, it is clear that the three ESEEM spectra of the ^{15}N-labeled versions have considerably lower intensities in the ^{14}N-ESEEM region below 8 MHz, whereas all of the four spectra display nearly identical ^{1}H-ESEEM intensities at or around 11.9 MHz. At a pH of 7.4, the normalized ^{14}N-ESEEM intensity decreases by approximately 40, 20, and 40% for the Cu(II) complexes of Aβ(1−16)H6[^{15}N], Aβ(1−16)H13[^{15}N], and Aβ(1−16)H14[^{15}N], respectively, compared with the intensity of the nonlabeled version. The ESEEM spectra at 2800 G indicate that the contribution of His6 or His14 to the Cu(II) coordination in Component I is distinguishably higher than that of His13 at physiological pH. On the other hand, with the uncertainty due to the orientational effects and the error due to the baseline drift in the ESEEM spectra, it is expected that the difference between His6 and His14 may not be significant.

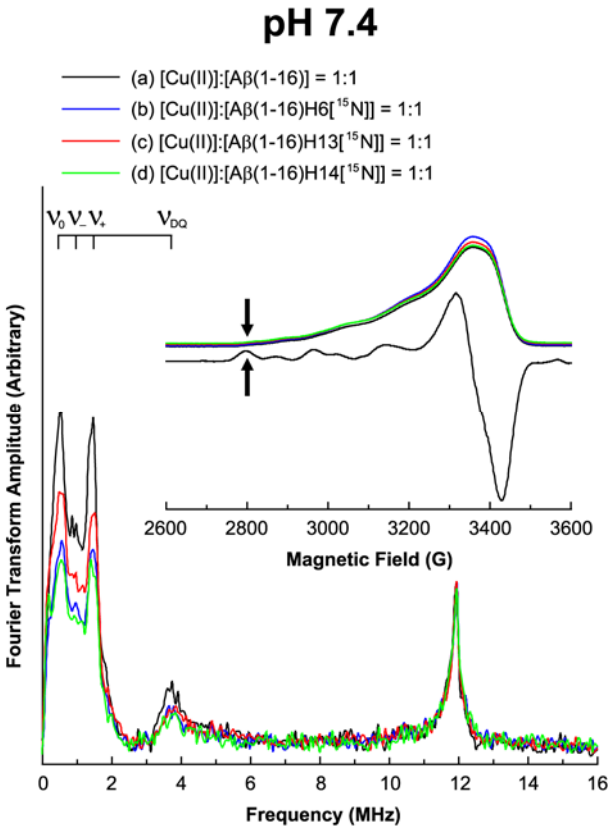

Figure 3-3. Three-pulse ESEEM and field-swept echo-detected spectra of the nonlabeled and ^{15}N-labeled Aβ(1–16) analogues mixed with an equimolar amount of Cu(II) at 2800 G at pH 7.4. The decrease in the ^{14}N-ESEEM intensity below 8 MHz is more prominent when His6 or His14 is enriched with ^{15}N. On the other hand, the ^{1}H-ESEEM intensity of each spectrum is essentially identical.

Similarly, Figure 3-4 illustrates the comparison of the ESEEM spectra of the nonlabeled and ^{15}N-labeled Aβ(1−16) mixed with an equimolar amount of Cu(II) at a pH of 6.0. The field-swept echo-detected spectra reveal that the echo is a maximum at or around 3350 G. Also, it is clear from the first derivative of the field-swept echo-detected spectrum of the nonlabeled version that Component I is almost exclusively present. The four ESEEM spectra obtained at 3350 G have almost identical spectral shapes including peak positions in the ^{14}N-ESEEM region below 8 MHz. The ESEEM spectra of the ^{15}N-labeled versions have considerably lower intensities in the ^{14}N-ESEEM region below 8 MHz, whereas all of the four spectra display nearly identical ^{1}H-ESEEM intensities at or around 14.3 MHz. The normalized ^{14}N-ESEEM intensity decreases by approximately 45, 30, and 30% for the Cu(II) complexes of Aβ(1−16)H6[^{15}N], Aβ(1−16)H13[^{15}N], and Aβ(1−16)H14[^{15}N], respectively, compared with the intensity of the nonlabeled version.

- **Affinity of Each Histidine Residue for Cu(II) Traced with the Dien–Cu(II)–Aβ(1–16) Ternary Complex**

To assess the propensity of Cu(II) to bind to each of His6, His13, and His14, we introduced a Cu(II)–dien complex, which normally forms a stable ternary complex with a monodentate ligand.[23,32]

First, we performed CW-ESR and field-swept echo experiments on the nonlabeled and ^{15}N-labeled Aβ(1−16) analogues mixed with an equimolar amount of the Cu(II)–dien complex. Figure 3-5 shows the CW-ESR spectrum of the mixture of the Cu(II)–dien complex and the nonlabeled Aβ(1−16) peptide.

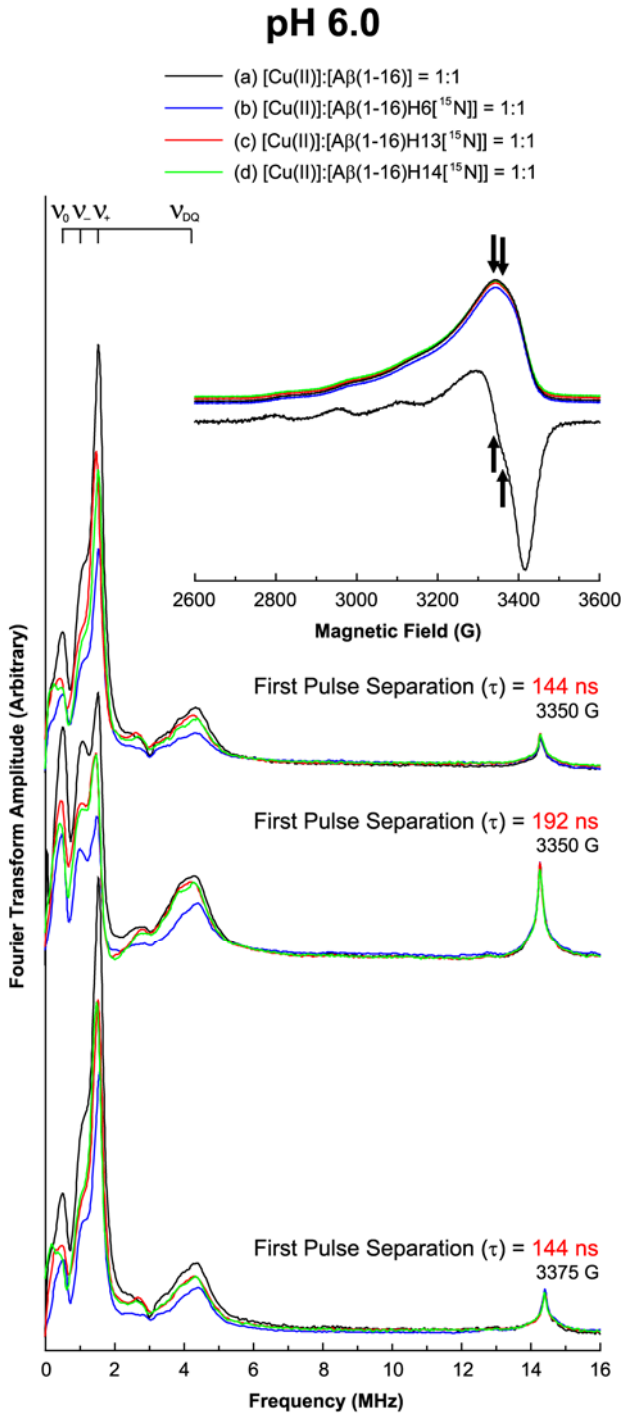

Figure 3-4. Three-pulse ESEEM and field-swept echo-detected spectra of the nonlabeled and ^{15}N-labeled Aβ(1–16) analogues mixed with an equimolar amount of Cu(II) at pH 6.0. The decrease in the ^{14}N-ESEEM intensity below 8 MHz is more prominent when His6 is enriched with ^{15}N. On the other hand, the ^{1}H-ESEEM intensity of each spectrum is essentially identical.

The $g_{||}$ and $A_{||}$ values determined by spectral simulations are 2.22 and 191 G, respectively, which are of a typical dien–Cu(II)–imidazole derivative complex with a square-planar geometry, as reported by several researchers.[23,27,32] Thus, it is certain that Cu(II) is equatorially coordinated by dien, a tridendate ligand, and one histidine residue, a monodendate ligand. Also, the presence of only one component suggests that the Cu(II) coordination by each histidine residue leads to almost identical coordination geometry.

Next, we performed three-pulse ESEEM experiments on the four mixtures at four magnetic fields: 2950, 3100, and 3226 G, which are close to the $g_{||}$ region, and 3375 G, at which the echo intensity is a maximum. Figure 3-5 also shows the ESEEM spectra of the four mixtures obtained at the four different magnetic fields. Each of the four spectra obtained at 2950 G has three relatively narrow peaks at or around 0.55, 1.03, and 1.55 MHz and a broad peak around 4.0 MHz. The three narrow peaks appear at almost the same frequencies as in the corresponding spectra obtained at the other magnetic fields, while the frequency of the broad peak changes with the magnetic field. Employing the same analysis as in the case of the Cu(II)–Aβ(1–16) complexes, we have concluded that the three peaks below 2 MHz are mainly due to the NQI transitions of ^{14}N, and the broad peak around 4.0 MHz is due to the double-quantum transition. The nuclear quadrupole parameters, e^2qQ/h and η, are determined to be 1.72 ± 0.03 MHz and 0.64 ± 0.02, respectively. The ESEEM spectra reveal that Cu(II) is coordinated by histidine in the four mixtures. Also, another peak appears at around 12.6 MHz, which is almost the Larmor frequency of ^{1}H at 2950 G. The peak is attributed to the presence of hydrogen atom(s) that weakly interact with the electron spin of Cu(II).

It is noticeable that the four spectra obtained at 2950 G have almost identical spectral shapes, including peak positions, even though the intensities of some peaks are different.

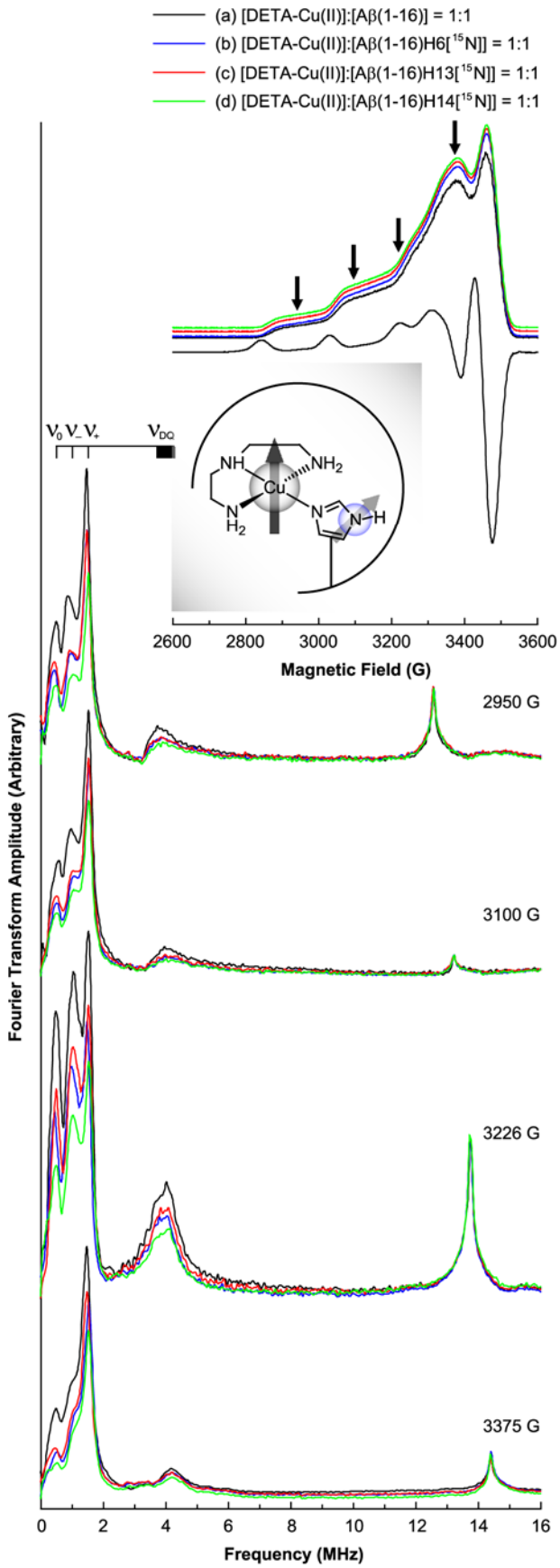
(a) [DETA-Cu(II)]:[Aβ(1-16)] = 1:1
(b) [DETA-Cu(II)]:[Aβ(1-16)H6[15N]] = 1:1
(c) [DETA-Cu(II)]:[Aβ(1-16)H13[15N]] = 1:1
(d) [DETA-Cu(II)]:[Aβ(1-16)H14[15N]] = 1:1
ν0 ν- ν+
νDQ
NH
NH2
Cu
N
H2
N
N–H
2600
2800
3000
3200
3400
3600
Magnetic Field (G)
2950 G
3100 G
3226 G
3375 G
Fourier Transform Amplitude (Arbitrary)
0
2
4
6
8
10
12
14
16
Frequency (MHz)

Figure 3-5. Three-pulse ESEEM and field-swept echo-detected spectra of the nonlabeled and ^{15}N-labeled Aβ(1–16) analogues mixed with an equimolar amount of the Cu(II)–dien complex at pH 7.4. The CW-ESR spectrum of the nonlabeled version at pH 7.4 is also presented. The CW-ESR spectrum and the field-swept echo detected spectra display characteristic features of dien–Cu(II)–imidazole ternary complexes. The decrease in the ^{14}N-ESEEM intensity below 8 MHz is most prominent when His14 is enriched with ^{15}N. On the other hand, the ^{1}H-ESEEM intensity is not significantly affected by the replacement of ^{14}N with ^{15}N.

Like the case of the Cu(II)–Aβ(1–16) complexes, the similarity in the spectral shape signifies that the ESEEM signals in the spectra are almost independent of the histidine residue that coordinates to Cu(II). However, the three ESEEM spectra of the ^{15}N-labeled versions have considerably lower intensities in the ^{14}N-ESEEM region below 8 MHz, whereas all of the four spectra display nearly identical ^{1}H-ESEEM intensities around 12.6 MHz. The normalized ^{14}N-ESEEM intensity decreases by approximately 30, 30, and 40% for the Cu(II)–dien complexes of Aβ(1–16)H6[^{15}N], Aβ(1–16)H13[^{15}N], and Aβ(1–16)H14[^{15}N], respectively, compared with the intensity of the nonlabeled version. The three-pulse ESEEM experiments performed at 3100, 3226, and 3375 G on the same samples show essentially the same trend, as illustrated in Figure 3-5. The contribution of each histidine residue to the ^{14}N-ESEEM, which is dependent on the affinity of each histidine residue for Cu(II), is in the order of His14 $>$ His6 $\approx$ His13, where the distinction between the latter two is not as clear as that between the first two. This order may explain the high contribution of His14 to the Cu(II) coordination in Component I of the Cu(II)–Aβ(1–16) complex. Therefore, it is inferred that, at physiological pH, His14 plays an important role in the major component, Component I, due to its higher affinity for Cu(II).

- **Simultaneous Coordination of Any Two Histidine Residues in the Cu(II)–Aβ(1–16) Complex Suggested by HYSCORE.**

Figure 3-6 shows the ^{14}N- and ^{15}N-ESEEM regions of the HYSCORE spectra of the equimolar mixtures of Cu(II) and the nonlabeled and ^{15}N-labeled Aβ(1–16) analogues. Each of the four spectra obtained at approximately 3360 G has a cross-peak around (1.6 MHz, 8.0 MHz). No such cross-peak is observed in the HYSCORE spectra of the dien–Cu(II)–Aβ(1–16) complexes.

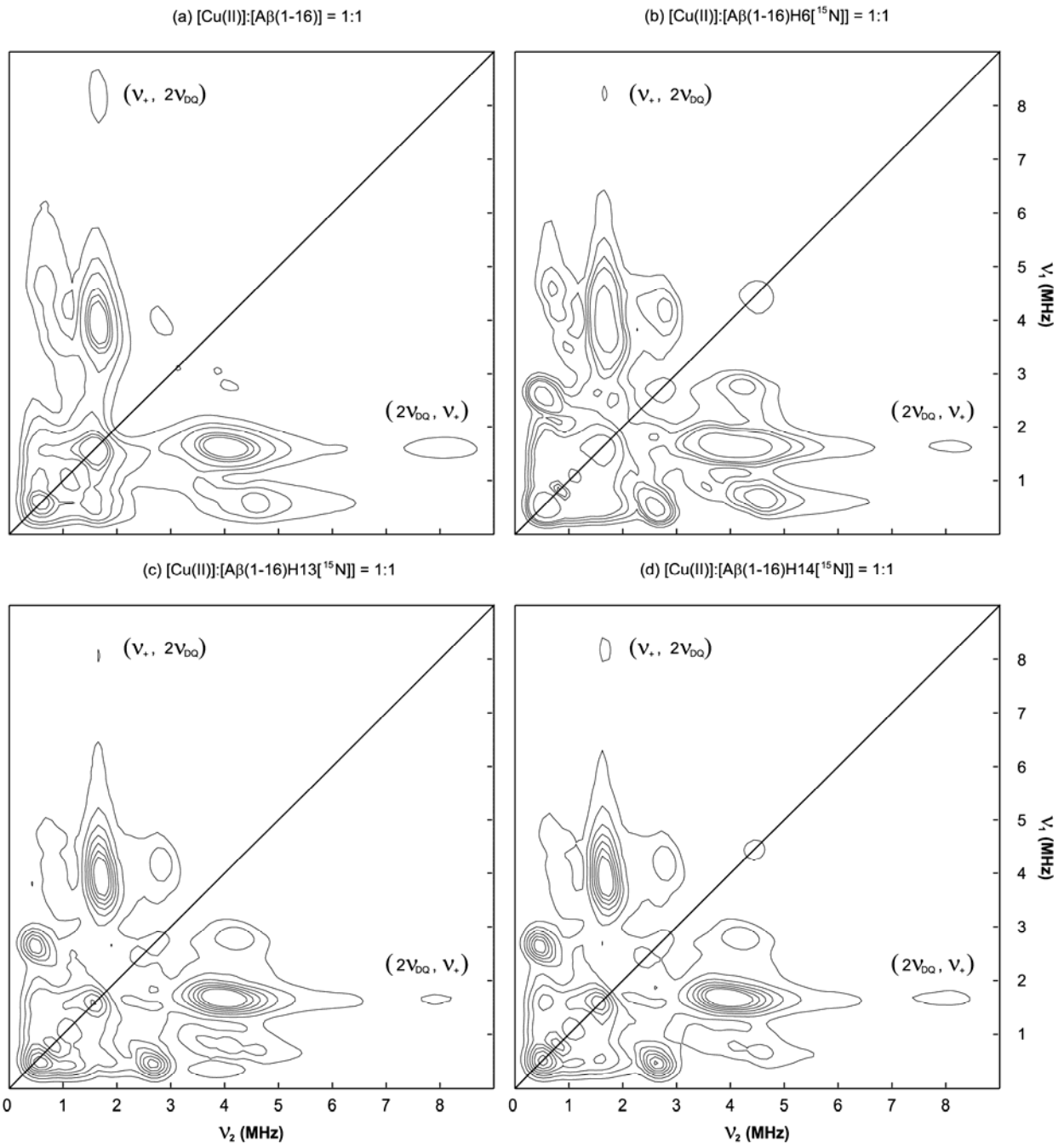

Figure 3-6. ^{14}N- and ^{15}N-ESEEM regions of the HYSCORE spectra of the nonlabeled and ^{15}N-labeled Aβ(1–16) analogues mixed with an equimolar amount of Cu(II) at 3360 G at pH 7.4. Each of the four spectra has a cross-peak around 1.6 MHz, 8.0 MHz, which indicates multiple histidine coordination.

Because the frequencies corresponding to the double-quantum transition are approximately 4.0 MHz, the cross-peak is likely to be due to the existence of two or more ^{14}N nuclei coupled with the electron spin of Cu(II). The possible appearance of a cross-peak from the correlation between a fundamental frequency at one electron spin manifold and a combination frequency at the other manifold in HYSCORE has also been proposed.[95-96] Given that the NQI and double-quantum frequencies are almost identical irrespective of the coordinated histidine residue(s), the simultaneous contributions of two ^{14}N nuclei from different histidine residues to the same electron spin system can explain the presence of the cross-peak in all of the four HYSCORE spectra.

3.5 DISCUSSION

- **Contribution of Each Histidine Residue to the Cu(II) Coordination in Component I at Two Different pHs of 7.4 and 6.0**

Our ESEEM experiments performed at a pH of 6.0 show that the contributions of the three histidine residues to the Cu(II) coordination in Component I are in the order of His6 $>$ His13 $\approx$ His14. The results at pH 6.0 are consistent with those of several other researchers including Drew et al.[82] and Dorlet et al.[84] and, thus, validate our approach. However, our ESEEM data obtained at a pH of 7.4 suggest that the contributions of the three histidine residues to the Cu(II) coordination in Component I are in the order of His14 $\approx$ His6 $>$ His13. The results at physiological pH are significant because very few researchers have emphasized the importance of His14 over His6 or His13, in the Cu(II)−Aβ(1−16) complex, and indeed several groups have suggested a dominant role of His6 in the complex.[47-48,82,84,86,97]

In fact, the CW-ESR results of Drew et al.[82] and the HYSCORE results of Dorlet et al.[84] suggest that the contribution of His6 to the Cu(II) coordination in Component I is twice as much as that of His13 or His14. To investigate Component I, however, Drew et al.[82] adjusted the pH to 6.3 or 6.9, while Dorlet et al.[84] used samples prepared at a pH of 6.5 for the same purpose. The Cu(II)-binding site(s) and involved amino acid residues for Component I are unlikely to be significantly altered by a change in the pH from 6.3 to 7.4 because the ESR parameters, including the $g_{\|}$ and $A_{\|}$ values of Component I, are found to remain almost unchanged over a wide range of pH values including 7.4.[48,84,87] Nevertheless, it has already been revealed that the pH dependence of the equilibrium between Component I and Component II in the Cu(II)−Aβ(1−28) complex is perturbed by a replacement of one histidine residue with alanine, and the extent of the perturbation is dependent on which residue is replaced.[87] Also, Ma et al.[98] have shown that the $\mathrm{p}K_a$ values of the three histidine residues are slightly different from one another and dependent on the solution conditions. Therefore, it is also probable that the Cu(II)-binding affinities of the three histidine residues change with pH, and the change is more pronounced in one residue than in another. Furthermore, the $\mathrm{p}K_a$ values reported by Ma et al.[98] are in the range of 5.9 to 7.8, which indicates that both protonated and deprotonated forms are significant, and the ratio between the two forms is sensitive to the pH value in a pH range where Component I is dominant. The lower $\mathrm{p}K_a$ value of His6 might explain its dominant contribution to the Cu(II) coordination at pH 6.0. Such considerations are compelling arguments for the examination of Cu(II) coordination at physiological pH.

Taken together, the contributions of the three histidine residues to the Cu(II) coordination suggested by our results are in the order of His14 $\approx$ His6 $>$ His13 in Component I at physiological pH. Our results, therefore, support the contention that the three histidine residues

do not equally contribute to the Cu(II) coordination in Component I, and coordinated histidine residues may be in exchange with noncoordinated histidine residues. Our ESEEM data suggest that, in Component I, all of the three residues are involved in the Cu(II) coordination, and His14 is at least as significant a contributor as His6 at physiological pH, while the contribution of His6 becomes more significant as the pH decreases.

- **Relationship between Cu(II)-Binding Affinity and Contribution to the Cu(II) Coordination in Component I**

Our ESEEM results on the Cu(II)–Aβ(1−16) complexes at 2800 G show that His6 has a significantly higher contribution in Component I than His13. On the other hand, the difference between the two histidine residues is less prominent in the dien–Cu(II)–Aβ(1−16) complex. In order to rationalize the disparity, we propose that the conformation of Component I might be more stable with His6 coordinated to Cu(II) than His13 coordinated to Cu(II) even though the affinities of the two residues for Cu(II) are similar to each other. The proposition is supported by the work of Sarell et al.[87] who have shown that a replacement of His6 with alanine reduces the Cu(II)-binding affinity of Aβ(1−28) more substantially than a replacement of His13 or His14. The ITC data of Hong et al.[97] also indicate that the Cu(II)–His6 coordination is entropically more favored than the Cu(II) coordination by His13 or His14 due to the proximity of His6 to the N-terminus, which is also likely to be involved in the Cu(II) coordination in Aβ(1−16).

On the other hand, our ESEEM results on the dien–Cu(II)–Aβ(1−16) complexes also reveal that His14 has the highest Cu(II)-binding affinity at a pH of 7.4. These findings are consistent with the work performed by Furlan et al.[99-100] who have suggested that Asp1 and His14 interact with each other by electrostatic attraction, which leads to the high metal binding

affinity of His14. In fact, the indirect involvement of the carboxylate group of Asp1 in the Cu(II) coordination of the Aβ peptide has also been proposed by Karr et al.[101] They have suggested that the carboxylate group of Asp1 participates in a hydrogen bond that stabilizes Component I at physiological pH, and the hydrogen bond is sensitive to a pH change. Considering that $\mathrm{p}K_a$ values of histidine residues are reported to be in the range of 5.9 to 7.8, it is possible that His14 is hydrogen-bonded to Asp1. Whether the interaction between Asp1 and His14 is electrostatic or hydrogen-bond-like, it is capable of affecting the Cu(II)-binding affinity of His14. Together, it is probable that the high affinity of His14 for Cu(II) explains the high contribution of the residue to the Cu(II) coordination in Component I, while the relatively high contribution of His6 in Component I is due to the overall structure of the complex.

Several researchers have suggested that two histidine residues simultaneously and intramolecularly coordinate to Cu(II) on the equatorial plane in Component I.[82-84,87] Interestingly, their suggestion is consistent with our ESEEM results. In the spectra obtained at 3375 G in Figure 3-4 and Figure 3-5, the double quantum-peak is more prominent in the nonlabeled Cu(II)–Aβ(1–16) complex at pH 6.0 than in the dien–Cu(II)–Aβ(1–16) complex, where only one histidine residue equatorially coordinates to Cu(II) at the same time. These results indicate that more than one histidine residue simultaneously coordinate to Cu(II) in at least a fraction of Component I in the Cu(II)–Aβ(1–16) complex.[30] Also, calculations show that the normalized ^{14}N-ESEEM intensity of the Cu(II)–Aβ(1–16) complex is approximately 1.7 times as great as that of the complex with dien, which indicates that approximately two histidine residues simultaneously coordinate to Cu(II) in Component I. These results are further supported by spectral simulations. More detailed information is provided in Appendix F.

Figure 3-7 illustrates the suggested Cu(II)-binding modes of Aβ(1−16) at pH 7.4 and pH 6.0. We propose that, at physiological pH, Component I is in turn made up of three different subcomponents, Subcomponent IA, IB, and IC, in each of which two histidine residues simultaneously coordinate to Cu(II) through the imidazole rings. The relative contributions of the three histidine residues are approximately 40, 20, and 40% from His6, His13, and His14, respectively. These values lead to the estimation that the subcomponent with the simultaneous coordination by His6 and His14, Subcomponent IB, accounts for approximately 60% of Component I. Each of the other two subcomponents explains about 20%. At physiological pH, Subcomponent IB accounts for 45% of overall Cu(II) complexes, including Component I and Component II, while other species are also significant.

Interestingly, Furlan et al.[99-100] have proposed that the simultaneous coordination by His6 and His14 is favored over that by His6 and His13 in the Zn(II)−Aβ(1−16) and Cu(I)−Aβ(1−16) complex. Presumably, the dominance of Subcomponent IB is due to both the high affinity of His14 and the stability provided by the Cu(II)–His6 coordination. Also, it is probable that Subcomponent IA is less favored because of the relatively lower Cu(II)-binding affinity of His13. More importantly, it is strongly suggested that Subcomponent IC is less dominant than Subcomponent IB due to the entropic penalty, but the high Cu(II)-binding affinity of His14 causes the subcomponent to be as significant as Subcomponent IA.

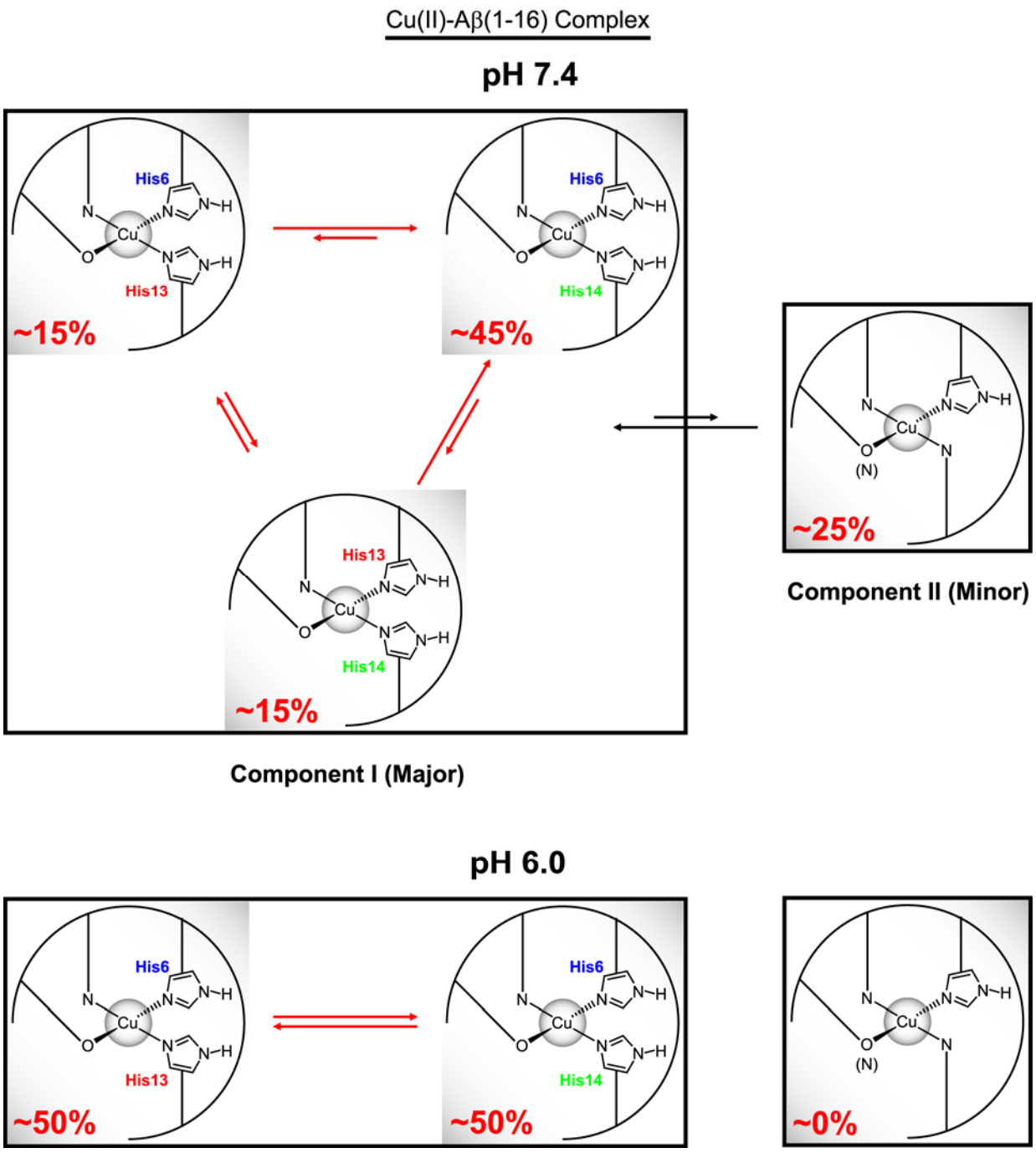

Figure 3-7. Difference in Cu(II) binding modes of Aβ(1–16) between pH 7.4 and pH 6.0 suggested by ESR spectroscopy. While His6 accounts for approximately 50% of the Cu(II)–histidine coordination in component I at pH 6.0, the contribution of His14 is at least as significant as that of His6 at pH 7.4. At pH 7.4, Component I is composed of three

subcomponents, Subcomponents IA, IB, and IC, in each of which two imidazole rings from two different histidine residues coordinate to Cu(II).

- **Simultaneous Coordination by His13 and His14 in Component I at Physiological pH and Its Biochemical Significance**

As previously mentioned, our ESEEM results suggest that the contribution of the three histidine residues to the Cu(II) coordination in Component I are in the order of His14 $\approx$ His6 $>$ His13 at physiological pH. These findings have led to the conclusion that three subcomponents, Subcomponent IA, IB, and IC, are present at physiological pH. The conclusion is also supported by the presence of the cross-peak around (1.6 MHz, 8.0 MHz) in the HYSCORE spectra of the nonlabeled and ^{15}N-labeled Cu(II)–Aβ(1−16) complexes, as illustrated in Figure 3-6. In particular, the cross-peak around (1.6 MHz, 8.0 MHz) in the HYSCORE spectrum of the Cu(II)−Aβ(1−16)H6[^{15}N] complex strongly suggests that His13 and His14 coordinate to a Cu(II) ion at the same time.

These findings are significant because the simultaneous coordination by His13 and His14 in the equatorial plane in Component I has not been appreciated by many researchers.[82,84,97] The simultaneous Cu(II) coordination by His13 and His14 through the two imidazole rings is not expected for a β-sheet structure because the two adjacent residues would be forced to be on opposite sides of the β-sheet.[4,102] Thus, the simultaneous coordination by the two residues signifies that the peptide structure is not a β-sheet near the residues in the presence of Cu(II). Recently, Ahmed et al.[103] have reported that relatively small oligomers of Aβ(1–42) with a non−β-sheet secondary structure are neurotoxic, while their conversion to protofibrils or fibrils having a β-sheet structure reduces toxicity. It is possible that the expected neurotoxicity of Cu(II) is due to inhibition of the formation of a β-sheet structure by binding to His13 and His14.

Our group has previously revealed that the in vitro morphology of the Aβ peptide depends on the Cu(II) concentration: as the Cu(II) concentration increases, the fraction of

amorphous aggregates increases, while the formation of fibrils is retarded.[44] Especially, a thioflavin-T fluorescence assay has suggested that the amount of Aβ fibrils formed in the presence of two equivalents of Cu(II) is less than half that formed at an equimolar level of Cu(II). Herein, we propose that the existence of a significant amount of Subcomponent IC leads to the dominance of amorphous aggregates in the morphology of the Aβ peptide. Figure 3-8 illustrates the formation of fibrils and amorphous aggregates and the suggested role of Subcomponent IC. With no Cu(II), soluble Aβ peptide molecules normally undergo changes in the secondary structure from the random coil to the β-sheet to form fibrils. When a substantial amount of Subcomponent IC is present with other species, however, at least some of the Aβ peptide molecules have a non–β-sheet structure.

As a consequence, the formation of fibrils is inhibited, and amorphous aggregates become more significant. It is probable that, while several factors may affect the amount of Subcomponent IC, the Cu(II)-to-peptide ratio is one of them. Also, because His6 is not equatorially involved in Subcomponent IC, its overall structure is likely to be different from that of Subcomponent IA or IB. The difference might be another factor that leads to the preference of amorphous aggregates, which are intrinsically less ordered than fibrils. Without Subcomponent IC, the fast equilibrium between Subcomponent IA and IB, whose overall structures are expected to be similar to each other, would lead to the formation of ordered fibrils.

Recently, Dong et al.[104] have shown that, in the presence of an equimolar amount of Cu(II), the fibril formation of Aβ(13–21)K16A, a mutant with intact His13 and His14, is inhibited.

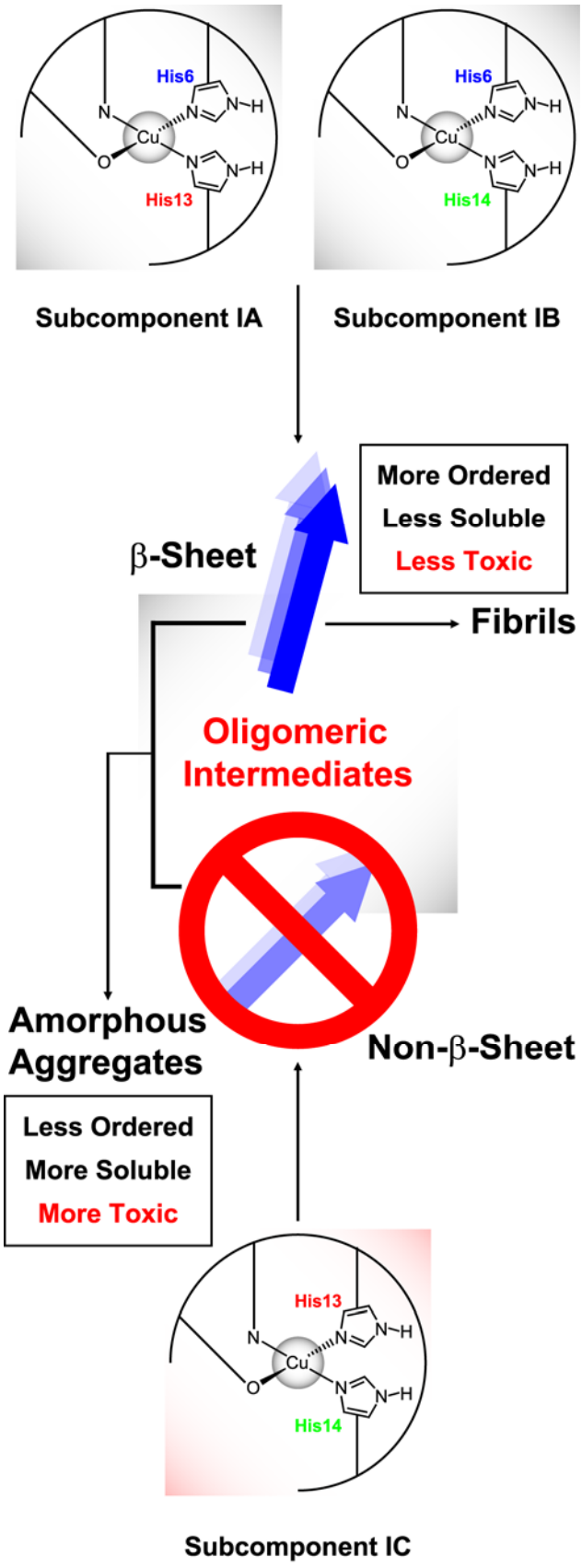
His6
His13
His6
His14
Subcomponent IA
Subcomponent IB
β-Sheet
More Ordered
Less Soluble
Less Toxic
Fibrils
Oligomeric
Intermediates
Amorphous
Aggregates
Non-β-Sheet
Less Ordered
More Soluble
More Toxic
His13
His14
Subcomponent IC

Figure 3-8. Formation of fibrils and amorphous aggregates of the Aβ peptide in the presence of Cu(II) and the suggested role of the simultaneous intramolecular coordination by two imidazole rings of His13 and His14. With a significant amount of subcomponent IC, the β-sheet and non-β-sheet structures coexist, which leads to the preference of amorphous aggregates over fibrils.

On the other hand, fibrils are observed with Ac-Aβ(13–21)H14A, a mutant with only one histidine residue. More intriguingly, they have also suggested that, in the major component of the Cu(II)–Aβ(13–21)K16A complex, only one imidazole ring from one peptide is involved in the Cu(II) coordination on the equatorial plane.[104] Their findings are consistent with our proposition in that a small but significant amount of a Cu(II) complex with two equatorially and intramolecularly bound imidazole rings can inhibit the formation of fibrils.

- **Difference in the Cu(II)–Histidine Coordination between Component I and Component II**

Our previous work suggests that when the two components are considered together, the contribution of each histidine residue is not significantly different from one another at physiological pH.[81] On the other hand, the ESEEM spectra obtained at 2800 G indicate different contributions of the three histidine residues in Component I. We surmise that the histidine residues that are less involved in Component I at a certain instance are more likely to serve as ligands in Component II. Because the contributions of the three histidine residues in Component I are in the order of His14 $\approx$ His6 $>$ His13, the contributions of those residues in Component II are likely to be in the order of His13 $>$ His6 $\approx$ His14 at physiological pH. Given that Component II only accounts for 25–30% of the overall Cu(II)–Aβ(1–16) complex, the contribution of His13 in Component II is expected to be much higher than that of His6 or His14 in Component I. Interestingly, the very high contribution of His13 in Component II occurs despite the relatively low propensity of Cu(II) to bind to His13 as shown in Figure 3-5. In fact, the amount of His13 in Component II is higher than that expected if Component II was solely intramolecular in nature and His13 was present in all complexes of Component II. We, therefore, hypothesize that the two

nitrogen atoms of the imidazole ring of His13 may coordinate to different Cu(II) ions to form intermolecular bridges in a small fraction of Component II. The possibility of bridges might explain the ESR parameters such as $g_{||}$ and $A_{||}$ values that fall into the borderline between three equatorial nitrogen donors and four equatorial nitrogen donors. In addition, the possible presence of bridges might contribute, at least to some extent, to the controversy in the Cu(II) coordination of Component II.

If all of the three imidazole rings of the three histidine residues simultaneously and intramolecularly coordinate to Cu(II) in Component II, the His13–His14 dyad provides two imidazole rings. Then, Component II would play a role similar to that of Subcomponent IC in the inhibition of the fibril formation. In fact, the cross-peak around (1.6 MHz, 8.0 MHz) in our HYSCORE spectra might be partially due to the simultaneous coordination by two histidine residues in Component II. However, more investigation is needed to obtain more precise information about the Cu(II)-coordination environment in Component II.

Regarding the overall contribution of each histidine residue to the Cu(II) coordination in the Cu(II)–Aβ(1–16) complex, some values have already been reported by other groups.[82,84,87,97] Drew et al.[82] have argued that His6, His13, and His14 account for approximately 50, 25, and 25% of the overall Cu(II)–histidine coordination at a pH of 6.3, respectively, and the contribution of each histidine residue at a pH of 8.0 is almost identical. With their data, one can expect the contributions of His6, His13, and His14 at a pH of 7.4 to be approximately 39, 31, and 31%, respectively, which is not significantly different from our previous results showing almost equal contributions of the three residues.

However, the overall contribution of each histidine residue at physiological pH expected based on the HYSCORE results of Dorlet et al.[84] appears to be inconsistent with our results. As

they suggest that only one histidine residue coordinates to Cu(II) at the same time in Component II, it is anticipated that the overall contribution of His6 is still significantly higher than that of His13 or His14 at pH 7.4, where Component I with simultaneous Cu(II) coordination by two histidine residues is dominant. We suspect that the contribution of His6 in Component I might be overestimated in their HYSCORE spectra because a cross-peak due to ^{15}N is normalized by a cross-peak due to ^{14}N, which is supposed to decrease with the increase in the contribution of ^{15}N. Nevertheless, their results are consistent with our results and those of Drew et al.[82] in that the contribution of His6 is higher than that of His13 in Component I.

3.6 SUMMARY

To obtain more precise information about Component I and Component II, both of which comprise the Cu(II)–Aβ(1–16) complex at physiological pH, we have performed three-pulse ESEEM experiments at 2800 G, where only Component I is exclusively present. The ESEEM spectra of the equimolar mixtures of Cu(II) and the nonlabeled and ^{15}N-labeled Aβ(1–16) analogues show that the contribution of His14 to the Cu(II) coordination in Component I is at least as much as that of His6, while His13 contributes significantly less than the other two residues at physiological pH. These findings are in contrast with the expectation of His6 playing a dominant role in the Cu(II) coordination in Component I at physiological pH.

The ESEEM spectra of the mixtures of the Cu(II)–dien complex and the Aβ(1–16) analogues suggest that His14 has a better Cu(II)-binding affinity than the other two residues, which may account for the higher contribution of His14 to the Cu(II) coordination in Component I. On the other hand, the contribution of His6 to the Cu(II) coordination in Component I appears

to be higher than expected from its Cu(II)-binding affinity. On the basis of our results and the data from other groups, we have suggested that there exist three different subcomponents in Component I at physiological pH. In each of the three subcomponents, two histidine residues simultaneously and intramolecularly coordinate to Cu(II) on the equatorial plane. While the Cu(II)–His6 coordination leads to a stable overall structure of Subcomponent IA (His6–His13) and IB (His6–His14), the presence of Subcomponent IC (His13–His14) may be explained by the high Cu(II)-binding affinity of His14. The existence of the simultaneous coordination by two imidazole rings is also confirmed by the appearance of the cross-peak around (1.6 MHz, 8.0 MHz) in our HYSCORE spectra.

The presence of Subcomponent IC at pH 7.4 may explain the retarded growth of fibrils and the formation of amorphous aggregates in the presence of a significant amount of Cu(II). We have proposed that the non–β-sheet nature of Subcomponent IC inhibits the formation of fibrils, and the distinct structural difference between Subcomponent IC and the other two may lead to the formation of less ordered aggregates. The proposition might explain the role of Cu(II) in the toxicity associated with the Aβ peptide, based on the consensus that small oligomers with a non–β-sheet secondary structure are neurotoxic.

In addition, we have conjectured that His13 contributes more to the Cu(II) coordination in Component II than in Component I, which would explain the negligible difference in the contribution of the three histidine residues to the Cu(II) coordination in the Aβ(1–16) complex made up of both components. Also, we suggest, from the interpretation of our results, that intermolecular bridges may form through His13 in a small fraction of Component II.

In brief, our findings are important in that the pH-dependence of the contribution of each histidine residue to the Cu(II) coordination is revealed by ESEEM spectroscopy. All of our

results help find more precise Cu(II)-binding modes by providing critical information obtained at physiological pH. Also, we provide an atomic-level insight into the formation of Aβ aggregates in the presence of Cu(II), which is believed to be an essential event in Alzheimer's disease.

3.7 ACKNOWLEDGMENT

This work was supported by a National Institutes of Health grant (5R01NS053788). We are grateful to the Peptide Synthesis Facility of the University of Pittsburgh for the peptide preparation. We also thank Dr. Sharon Ruthstein for helpful discussions.

4.0 INSIGHT INTO POTENTIAL Cu(II)-BINDING MOTIFS IN THE FOUR PSEUDOREPEATS OF TAU PROTEIN

Part of this work, written in collaboration with Sunil Saxena, has been submitted to the Journal of Physical Chemistry B.

4.1 ABSTRACT

Tau protein and Cu(II) are believed to be associated with the pathogenesis of Alzheimer's disease. However, little is known about atomic-level interactions between tau protein and Cu(II). Herein, we suggest, on the basis of ESR data, that the four pseudorepeats of tau protein in the microtubule-binding region play an important role in Cu(II) binding. We use a number of tau protein fragments in order to examine Cu(II)-binding site(s) and binding affinities. CW-ESR experiments on the four highly conserved octadecapeptides, each of which is a segment of one of the four pseudorepeats, reveal that the equimolar Cu(II) complexes of the four octadecapeptides are similar to one another in terms of the coordination environment and binding affinity. The spectra obtained with pulsed ESR techniques such as electron spin-echo envelope modulation and hyperfine sublevel correlation provide direct evidence that a histidine residue and a backbone amide group coordinate to Cu(II) in each Cu(II)–octadecapeptide complex. The results

of CW and pulsed ESR experiments on some chemically modified peptides indicate that the cysteine residues in the second and third pseudorepeats are unlikely to be involved in Cu(II) binding. On the other hand, similar experiments on tau fragments of the second pseudorepeat with different lengths lead to the conclusion that the affinity for Cu(II) decreases as the octadecapeptide is either truncated or elongated. The high Cu(II)-binding affinity of the octadecapeptide is presumably due to the N-terminal amino group stabilizing the Cu(II)–octadecapeptide complex. Finally, the ESR data for a longer tau fragment that contain two octadecapeptides suggest that the Cu(II) binding site(s) of even longer fragments of tau protein is similar to that of the octadecapeptides.

4.2 INTRODUCTION

Alzheimer's disease is the most common form of dementia. The disease is characterized by the presence of two anomalous hallmarks in the brains of patients: extracellular senile plaques and intracellular neurofibrillary tangles.[37,105] It has been reported that the senile plaques are made up of insoluble aggregates of the Aβ peptide and the neurofibrillary tangles are composed of tau protein aggregates.[106-107]

While the aggregation of the two polypeptides is linked to Alzheimer's disease, some transition metals such as copper, zinc, and iron are also believed to be involved in the neurodegenerative process of the disease.[72,86,108] Research has shown dyshomeostasis in the brain level of copper, zinc, and iron and anomaly in their metabolism in the case of Alzheimer's disease.[109] Interestingly, some studies have revealed that copper and zinc are co-localized with the Aβ deposits in the senile plaques and their local concentrations are significantly elevated in

Alzheimer's disease.[39,43] In addition, Cu(II)- or Zn(II)-induced Aβ aggregations have been reported.[110-112] Accordingly, a number of researchers are focused on elucidating the coordination chemistry of Cu(II) and Zn(II) with Aβ. In particular, our group has proposed that the morphology of Aβ aggregates changes as a function of the Cu(II)-to-peptide ratio.[44,113] By exhaustively examining Cu(II) coordination, our group has recently identified key coordination motifs that might play a role in such changes in morphology.[114] Also, several other groups have reported evidence that atomic-level interactions between Cu(II) and some specific residues of the peptide are correlated with the aggregation of the peptide and the toxic nature of Alzheimer's disease.[74,104,115]

The association of transition metal ions with the neurofibrillary tangles or their main constituent, tau protein, has only recently become relevant. Sayre et al.[116] have strongly suggested that Cu(II), Fe(II), and Fe(III) are involved in the redox reactions occurring in the neurofibrillary tangles as well as in the senile plaques. Involvement of Cu(II) in the neurofibrillary tangles, however, has been paid less attention to because the intracellular free copper level in neurons is low.[117] Nevertheless, tau in the brain has been found to contain copper and zinc.[118] Also, the dyshomeostasis of transition metal ions in Alzheimer's disease might lead to a local high concentration of copper.[119] Furthermore, the transport of tau protein through a cell membrane in the brain has been reported.[120-121] In this context, the interaction between Cu(II) and tau protein is of great interest.

Tau is a large protein that consists of up to 441 amino acid residues. In its normal state, it interacts with tubulins to promote their assembly into microtubules and stabilizes the formed microtubules.[122-123] The microtubule-binding region of tau contains three or four pseudorepeats, each of which has 31–32 amino acid residues including a highly homologous 18 amino-acid-

sequence that begins with a valine residue and ends with a PGGG sequence; the four pseudorepeats are named R1, R2, R3, and R4, respectively as illustrated in Figure 4-1.[124-125] Intriguingly, the highly conserved octadecapeptides in the pseudorepeats are also involved in Cu(II) coordination. Ma et al.[126-127] have shown that the octadecapeptide in R2 or R3 coordinates to Cu(II) and facilitates the peptide aggregation. Similarly, it has been reported that the octadecapeptide in R1 coordinates to Cu(II).[128] Also, it has been revealed that the octadecapeptide in R2 in the presence of Cu(II) can generate hydrogen peroxide as a result of a redox reaction.[129] Soragni et al.[119] have suggested, however, that a longer tau fragment containing all of the four pseudorepeats has only one Cu(II)-binding site and the binding site is present in R2 and/or R3. More recently, Mo et al.[130] have reported that the two cysteine residues and some of the histidine residues in R2 and R3 are involved in the coordination of Zn(II). A more precise picture of Cu(II) coordination is, however, yet to be established.

In this article, we assess the Cu(II) coordination of each of the octadecapeptides in R1, R2, R3, and R4 and elucidate the probable Cu(II)-coordination site(s). In order to obtain information about the Cu(II)-binding site(s) in the octadecapeptides, we have prepared cleaved and/or modified tau fragments. Then, CW and pulsed ESR experiments such as ESEEM and HYSCORE have been performed on the synthesized peptides mixed with Cu(II). We have found that a histidine residue and a backbone amide group are directly involved in the Cu(II) coordination in each of the four octadecapeptides. The Cu(II)-coordination by a backbone amide presumably helps stabilize the Cu(II)−octadecapeptide complex. In addition, our data are consistent with the results of other groups in that each of the four octadecapeptides has at least one Cu(II)-binding site.[126-128]

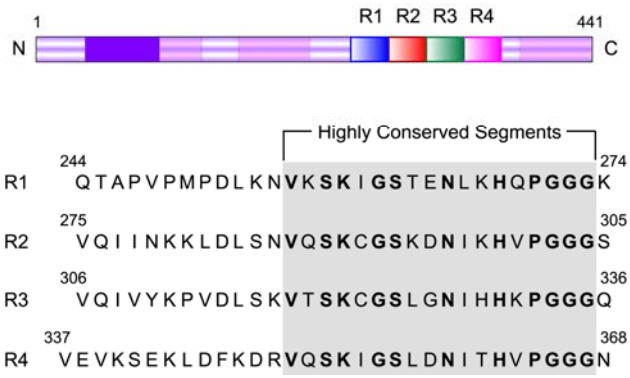

Figure 4-1. Amino acid sequences of the four pseudorepeats in the longest tau isoform. Each pseudorepeat consists of 31–32 amino acid residues and contains a highly conserved octadecapeptide, which shows >60% homology. The octadecapeptides are shaded in gray and the conserved residues are indicated in boldface.

We also suggest a Cu(II)-coordination site of longer tau fragments containing the four pseudorepeats based on analysis of our ESR results. In order to estimate the Cu(II)-binding site, we have synthesized a 49-amino-acid peptide that contains the highly conserved octadecapeptides in R2 and R3. Most of our data are consistent with the work of Soragni et al.[119] in that there is only one Cu(II)-binding site in the 49-amino-acid peptide. In addition to the consistency, our results provide more precise information about the amino acid residues that are involved in the Cu(II) coordination.

4.3 EXPERIMENTAL SECTION

- **Peptide Synthesis and Cu(II)–Peptide Complex Preparation**

A nitroxide spin-labeling agent, (1-oxyl-2,2,5,5-tetramethyl-pyrroline-3-methyl) methanethiosulfonate (MTS), was purchased from Toronto Research Chemical (North York, Ontario, Canada). Tau protein fragments as well as Aβ(1−16), DAEFRHDSGYEVHHQK, were synthesized at the Peptide Synthesis Facility of the University of Pittsburgh via the conventional solid-phase fluorenylmethoxycarbonyl chemistry.[88-89] The tau fragments include four octadecapeptides, VKSKIGSTENLKHQPGGG, VQSKCGSKDNIKHVPGGG, VTSKCGSLG-NIHHKPGGG, VQSKIGSLDNITHVPGGG, shorter sequences that contain some of the octadecapeptides, and a 49-amino acid peptide that contains the highly conserved octadecapeptides in R2 and R3, VQSKCGSKDNIKHVPGGGSVQIVYKPVDLSKVTSKCGSL-GNIHHKPGGG. In addition, some peptides were modified by either elongation to the N-terminus, acetylation at the N-terminus, or MTS spin-labeling at the cysteine residue(s). The four octadecapeptides, corresponding to Tau(256−273), Tau(287−304), Tau(318−335), and

Tau(350−367) in the longest tau isoform, were termed R1(13−30), R2(13−30), R3(13−30), and R4(14−31), respectively, for the sake of easy connotation of the relative position in each pseudorepeat. The rest of the synthesized peptides were termed in a similar fashion (see the Results and Discussion Section). Each of the synthesized peptides was characterized by high performance liquid chromatography and mass spectrometry. Isotopically enriched $[^{63}Cu]Cl_2$ was purchased from Cambridge Isotope Laboratory (Andover, MA). NEM was purchased from Sigma−Aldrich (St. Louis, MO). A 100 mM NEM buffer with a pH of 7.4 was prepared by mixing NEM and hydrochloric acid in 50% glycerol. Then, 2.5 mM solutions of tau protein fragments were prepared in the 100 mM NEM buffer. Separately, a 10 mM Cu(II) stock solution was prepared in the same buffer. Mixtures with various Cu(II)-to-peptide molar ratios such as 0.125:1, 0.25:1, 0.5:1, 1:1, 2:1, 4:1, and 8:1 were prepared with a final concentration of 1.25 mM in the peptide.

- **Electron Spin Resonance Spectroscopy**

Cu(II)−peptide mixtures either dissolved or suspended in 100 mM NEM buffer containing 50% glycerol were used for ESR experiments. A 200 μL aliquot of each Cu(II)−peptide mixture solution was transferred into a quartz tube with an inner diameter of 3 mm. All ESR experiments were performed on a Bruker ElexSys E580 FT/CW X-band Spectrometer equipped with a Bruker ER 4118X-MD5 dielectric ring resonator. The temperature was adjusted with an Oxford ITC503 temperature controller and an Oxford CF935 dynamic continuous-flow cryostat connected to an Oxford LLT650 low-loss transfer tube.

Continuous-wave ESR experiments were carried out on the sample solutions. All ESR signals were collected at 80 K with a microwave frequency of approximately 9.69 GHz. The

magnetic field was generally swept from 2600 G to 3600 G for a total of 1024 data points. Other instrumental parameters include a time constant of 40.96 ms, a conversion time of 81.92 ms, a modulation amplitude of 4 G, a modulation frequency of 100 kHz, and a microwave power of 0.1993 mW. The experimentally obtained spectra were compared with the corresponding simulated spectra in Symphonia and WINEPR provided by Bruker.

Three-pulse ESEEM experiments were performed on most of the sample solutions at 20 K with a conventional stimulated-echo pulse sequence of $\pi/2 - t - \pi/2 - T - \pi/2 - t -$ echo. The first pulse separation, t, was set at either 144 ns or 192 ns and the second pulse separation, T, was varied from 288 ns with a step size of 16 ns for a total of 1024 points. The pulse length was 16 ns and the magnetic field strength was fixed at either around 3365 G, where the echo intensity was a maximum, or around 3150 G, which corresponded to the $g_{||}$ position. In addition, a four-step phase cycle was employed to eliminate unwanted signals.[56-57] The real parts of the collected raw data were baseline-corrected and fast Fourier-transformed. Then, the final spectra were obtained as the magnitude of the Fourier transforms.

Four-pulse HYSCORE experiments were performed on some of the sample solutions at 20 K with a pulse sequence of $\pi/2 - t - \pi/2 - t_1 - \pi - t_2 - \pi/2 - t -$ echo. The first pulse separation, t, was set at 144 ns and both the second pulse separation, t_1, and the third pulse separation, t_2, were varied from 144 ns with a step size of 16 ns for a total of 512 points. The pulse lengths were 16 ns and 32 ns for $\pi/2$ and π pulses, respectively, and the magnetic field strength was fixed at approximately 3365 G, where the echo intensity was a maximum. In addition, a four-step phase cycle was employed to eliminate unwanted signals. The real parts of the collected two-dimensional data were baseline-corrected and apodized with a Hamming window in both dimensions. Then, the processed data were zero-filled to 1024 points in both

dimensions before being fast Fourier-transformed. The final spectra were obtained as the contour plots of the magnitude of the two-dimensional Fourier transforms.

4.4 RESULTS AND DISCUSSION

The longest isoform of tau, which consists of 441 amino acid residues, contains four pseudorepeats. Each pseudorepeat consists of 31–32 amino acid residues and has a highly conserved octadecapeptide that begins with a valine residue and ends with a PGGG sequence. The sequences of the pseudorepeats, R1, R2, R3, and R4, are shown in Figure 4-1. Interestingly, most of the highly conserved octadecapeptides have been found to bind Cu(II).

A series of ESR experiments were conducted on synthesized tau protein fragments, most of which contain some of the highly conserved segments of the four pseudorepeats, R1, R2, R3, and R4. The highly conserved octadecapeptides of R1, R2, R3, and R4 were termed R1(13–30), R2(13–30), R3(13–30), and R4(14–31), respectively. Similarly, other fragments with a total of 6–21 amino acid residues, all of which contain the HVPGGG sequence of R2, were termed R2(10–30), R2(11–30), R2(12–30), R2(15–30), R2(23–30), R2(24–30), and R2(25–30). The 49-amino acid peptide that contain the highly conserved octadecapeptides in R2 and R3 was named R23(13–61). The nitroxide spin-labeled versions of R2(13–30) and R3(13–30) were named R2SL(13–30) and R3SL(13–30), respectively.

- **Similarity in ESR Parameters between the Four Octadecapeptides, R1(13–30), R2(13–30), R3-(13–30), and R4(14–31): Similar Cu(II)-Binding Site(s) and Cu(II)-Binding Affinities**

The four octadecapeptides, each of which is the highly conserved segment in a pseudorepeat, were compared in terms of Cu(II) coordination by means of several ESR methods.

First, CW-ESR experiments were carried out on the octadecapeptides and Aβ(1–16), each of which was mixed with an equimolar amount of Cu(II). Figure 4-2 shows the CW-ESR spectra of the Cu(II) complexes of the octadecapeptides. The ESR spectra are similar to one another in terms of g values, A values, and linewidths. The $g_{||}$ value and $A_{||}$ value of the major component (Component 1), 2.23 ± 0.005 and 157 ± 1 G, respectively, which are determined by spectral simulations, are consistent with a square-planar Cu(II)-coordination geometry with three nitrogen donors and one oxygen donor on the equatorial plane.[9,17,50-51,53] Similarly, the $g_{||}$ value and $A_{||}$ value of the minor component (Component 2), 2.25 ± 0.005 and 183 ± 1 G, respectively, are consistent with a square-planar geometry with either three nitrogen donors and one oxygen donor or four nitrogen donors.[9,53] The simulation results also show that the minor component accounts for 5–20% of each Cu(II)–peptide complex.

It is known that the ESR signals from aqueous Cu(II) complexes are minimized in NEM buffer at a pH of 7.4.[48,50,113] Thus, comparison of the double integrals of the first derivative ESR spectra provides information about the binding affinities of the octadecapeptides. The double integrals of the spectra are similar to one another within a difference of 8%.

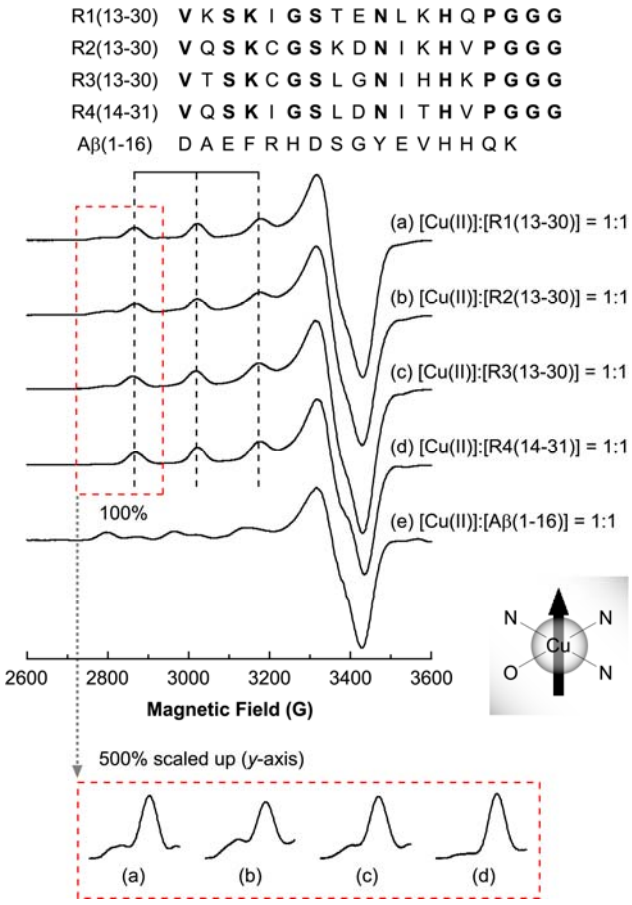

Figure 4-2. CW-ESR spectra of R1(13–30), R2(13–30), R3(13–30), R4(14–31), and Aβ(1–16) mixed with an equimolar amount of Cu(II). The amino acid sequences of the four octadecapeptides and Aβ(1–16) are illustrated with conserved residues indicated in boldface. The similarity in g values, A values as well as intensity suggests that their binding site(s) and binding affinities are comparable.

Considering that CW-ESR instrumental parameters including the microwave power and modulation amplitude are identical through all CW-ESR experiments, it is concluded that each octadecapeptide has a Cu(II)-binding affinity comparable to that of Aβ(1−16).

Next, pulsed ESR experiments such as ESEEM and HYSCORE were performed on the equimolar Cu(II) complexes as used for the CW-ESR experiments mentioned above. Figure 4-3 illustrates the three-pulse ESEEM spectra of the four Cu(II)−peptide complexes. Each of the spectra has three peaks at or around 0.55, 0.98, and 1.53 MHz. The sum of the lower two frequencies coincides with the highest one within the resolution error range of ±0.03 MHz. Also, the three peaks exhibit little field dependence. Both of these properties indicate that they are mainly due to the nuclear quadrupole interaction (NQI).[25-26,58] The three ESEEM frequencies, ν_0, ν_-, and ν_+ for the ^{14}N (I = 1) NQI transitions are given by:[58]

$$\nu_0 = \frac{e^2qQ\eta}{2h}\ ;\ \nu_- = \frac{e^2qQ(3-\eta)}{4h}\ ;\ \nu_+ = \frac{e^2qQ(3+\eta)}{4h} \qquad (4\text{-}1)$$

where e is the elementary charge, q is the z-component of the electric field gradient across the nucleus, Q is the ^{14}N nuclear quadrupole moment, η is the asymmetry parameter, and h is Planck's constant.

By comparison of the experimentally obtained frequencies with those of eq 1, the nuclear quadrupole parameters, e^2qQ/h and η, are determined to be 1.67 ± 0.03 MHz and 0.66 ± 0.02, respectively. In addition to these three peaks, each spectrum also has a peak around 4.1 MHz, which is assigned to the double quantum transition.

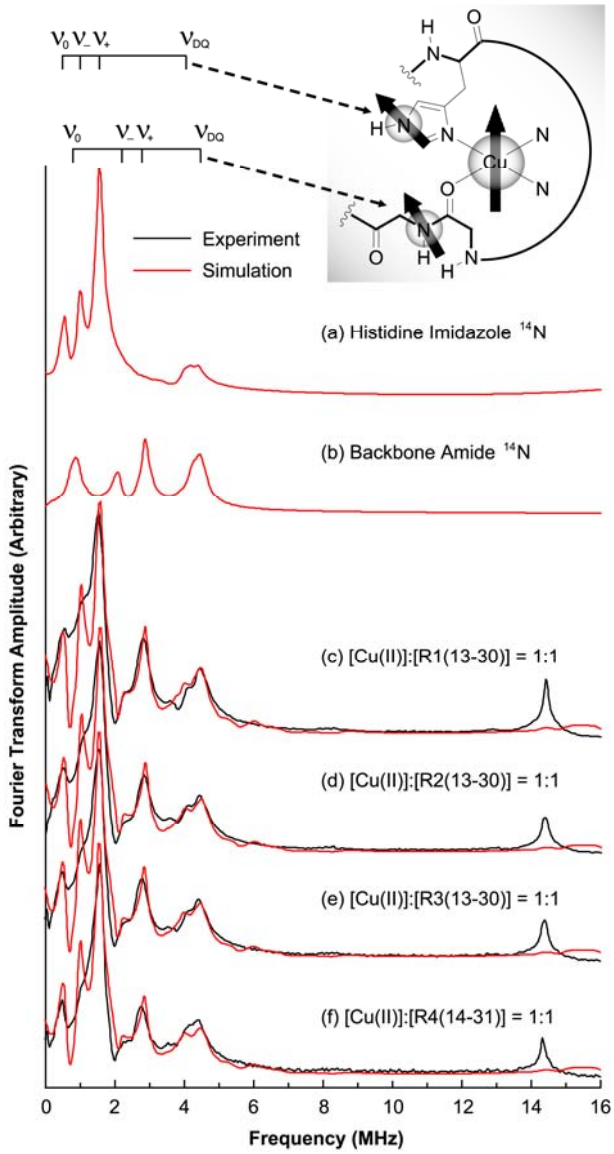

Figure 4-3. Experimentally obtained and simulated three-pulse ESEEM spectra of R1(13−30), R2(13−30), R3(13−30), and R4(14−31) mixed with an equimolar amount of Cu(II). The ESEEM frequencies at or around 0.55, 0.98, 1.53, and 4.1 MHz indicate that Cu(II) is coordinated by histidine. Also, the ESEEM frequencies at or around 0.75, 2.08, 2.80, and 4.4 MHz indicate that amide backbone is involved in the Cu(II) coordination. Accordingly, two ^{14}N nuclei, remote nitrogen of imidazole and backbone amide nitrogen are considered in the

simulations. The hyperfine interaction parameters obtained with the simulations indicate that the Cu(II) is more strongly bound to the imidazole than to the backbone amide.

The theoretical double quantum transition frequency is given by:[25]

$$\nu_{\mathrm{DQ}} = 2\sqrt{\left(\nu_I + \frac{A}{2}\right)^2 + \left(\frac{B}{2}\right)^2 + \left(\frac{e^2qQ}{4h}\right)^2 (3+\eta^2)} \qquad (4\text{-}2)$$

where ν_{DQ} is the double quantum transition frequency, ν_I is the Larmor frequency of ^{14}N, and A and B are the secular and the pseudo-secular part of the hyperfine interaction, respectively.

All of these values including the NQI and double quantum transition frequencies and the two calculated parameters are comparable to those for Cu(II) complexes of histidine imidazole in proteins that were determined by McCracken et al.[28,30-32,93] Based on the analysis of the NQI and double quantum frequencies, we have concluded that histidine imidazole coordinates to Cu(II) in all of the four complexes.

Besides the four peaks assigned to the Cu(II)–imidazole coordination, each spectrum also exhibits more peaks at or around ~0.75, 2.08, 2.80, and 4.4 MHz. These values are comparable to those for the Cu(II) coordinated by a backbone amide that were reported by Burns et al.[17] Their research has proven that the amide nitrogen of the third glycine residue in the PHGGGW sequence gives rise to three ^{14}N nuclear quadrupole transition frequencies at around ~0.80, 2.00, and 2.80 MHz. Also, they have assigned a broad peak around 4.4 MHz to the double quantum transition. The similarity between their data and our results suggests that a backbone amide in the octadecapeptide coordinates to Cu(II). With the experimentally obtained frequencies, the nuclear quadrupole parameters, e^2qQ/h and η, are determined to be 3.25 ± 0.03 MHz and 0.46 ± 0.02, respectively.

Nevertheless, which backbone amide coordinates to Cu(II) is still unclear. We initially suspected that one of the three consecutive glycine residues in the octadecapeptides is responsible for the characteristic ^{14}N-ESEEM peaks at around ~0.80, 2.00, and 2.80 MHz.

However, the ESEEM spectrum remains almost unchanged when any of the three glycine residues is labeled with ^{15}N (data not shown), which signifies that none of the three glycine residues coordinate to Cu(II). Recently, Drew et al.[83] have reported that the carbonyl oxygen of Ala2 in Aβ(1−16) directly coordinates to Cu(II) and the amide nitrogen of Glu3 is responsible for the characteristic ^{14}N-ESEEM peak at around 2.8 MHz. Considering the fact that glycine and alanine are two least bulky amino acids, one can suggest that Cu(II) is likely to be coordinated by the carbonyl oxygen of a less bulky residue than that of a bulkier one. Thus, we conjecture that the carbonyl oxygen of the other glycine residue or a serine residue in the octadecapeptide coordinates to Cu(II). The ^{15}N-labeling of each amide nitrogen would lead to a more precise conclusion.

Furthermore, spectral simulations provide information about the hyperfine interaction between the electron spin and the nuclear spin of ^{14}N. Figure 4-3 also shows the best-fit simulated spectra of the four Cu(II)–peptide complexes. The atoms that strongly coordinate to Cu(II) in the complexes of the four octadecapeptides are perpendicular to the $g_{||}$ axis and show little orientation selectivity in the ESEEM spectra when the external magnetic field is almost perpendicular to the axis.[28,32] Thus, an axial hyperfine tensor is assumed for the system and parameterized by two hyperfine constants, A_{iso} and T_{dip}, which represent the isotropic part and anisotropic part, respectively.

Our simulation results reveal that both A_{iso} and T_{dip} are larger for the remote ^{14}N nucleus, which implies that the coordination between Cu(II) and the imidazole nitrogen is stronger than that between Cu(II) and the carbonyl oxygen in the backbone. Also, the angle between the *z*-axis of the nuclear quadrupole tensor and the interspin vector has been found to be approximately 90° for all of the complexes, which indicates that the interspin vector is in the plane of the π system

containing the Cu(II)-coordinating atom and the ESEEM active atom.[32] The linewidth of the peaks below 2 MHz is narrower in the simulated spectra than in the experimentally obtained spectra. One possible explanation for the difference is the contribution of an ESEEM-active ^{14}N nucleus of Component 2 in the complexes to the ESEEM signals in the experiments. Also, it is plausible that some of the ESEEM parameters such as A_{iso} and T_{dip}, and the angle between the nuclear quadrupole axis and the interspin vector are ranges of values rather than single values.

The identity of some peaks is further confirmed by the four-pulse HYSCORE experiments. The HYSCORE spectra of the four Cu(II)–peptide complexes are illustrated in Figure 4-4. Each of the spectra contains a cross-peak around (1.6 MHz, 4.0 MHz). This peak appears owing to the correlation between the ^{14}N NQI and double quantum transition for the remote nitrogen of the Cu(II)-coordinated histidine imidazole.[17,32] Also, each spectrum displays another cross-peak around (2.8 MHz, 4.3 MHz). This peak is attributed to the correlation between the ^{14}N NQI and double quantum transition for the nearest amide nitrogen of the Cu(II)-coordinated backbone carbonyl oxygen.[17,83]

Taken together, CW and pulsed ESR experiments and simulations indicate that the four octadecapeptides, R1(13–30), R2(13–30), R3(13–30), and R4(14–31) have almost identical Cu(II)-binding site(s) and similar binding affinities for Cu(II). Especially, the ESEEM and HYSCORE results show that a histidine imidazole ring and a backbone amide coordinate to Cu(II) in the equimolar Cu(II) complexes of the four octadecapeptides.

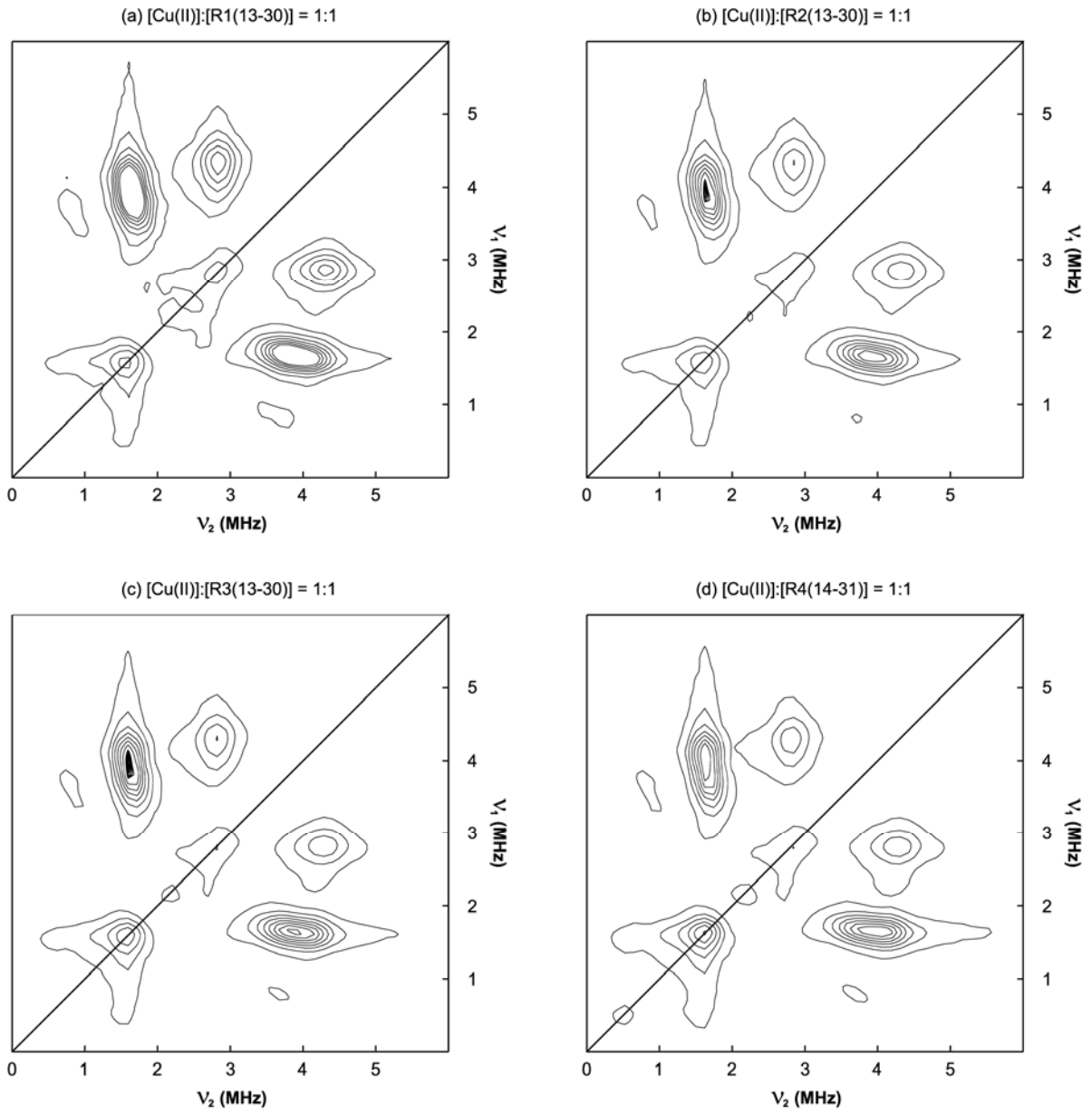

Figure 4-4. HYSCORE spectra of R1(13−30), R2(13−30), R3(13−30), and R4(14−31) mixed with an equimolar amount of Cu(II). The cross-peak around (1.6 MHz, 4.0 MHz) is ascribed to the Cu(II) ion that is coordinated by histidine. The cross-peak around (2.8 MHz, 4.3 MHz) is unique to the Cu(II)–peptide complex in which amide backbone is involved in the Cu(II) coordination.

- **Roles of Histidine Residues, Backbone Amide Groups, and N-Terminal Amino Groups in the Cu(II)-Coordination Environment**

In order to obtain more information about the Cu(II)-binding site(s), we performed CW-ESR experiments on the Cu(II) complexes of shorter tau protein fragments in the R2 pseudorepeat whose Cu(II)-binding property has already been reported by Ma et al.[127] Separately, Burns et al.[17,50-51,53] revealed that a repeated hexapeptide containing one histidine residue and three consecutive glycine residues, PHGGGW, has a good binding affinity for Cu(II) and serves as a minimal binding sequence in the prion protein. Since the CW-ESR and ESEEM parameters of the octadecapeptides are almost identical to those of the hexapeptide in the prion protein, we initially suspected that in tau protein, a hexapeptide containing one histidine residue and three consecutive glycine residues, HVPGGG, might serve as a minimal binding sequence.

Figure 4-5 shows the CW-ESR spectra of the equimolar mixtures of Cu(II) and one of tau protein fragments in the R2 pseudorepeat. Each of the fragments contains a total of 6–21 amino acid residues including the HVPGGG sequence. Unfortunately, the CW-ESR parameters of the Cu(II)–HVPGGG complex are significantly different from those of the Cu(II) complex of the corresponding octadecapeptide, VQSKCGSKDNIKHVPGGG. Also, the spectra of the Cu(II) complexes of R2(10–30), R2(11–30), R2(15–30), R2(23–30), R2(24–30), and R2(25–30) are different from one another in terms of ESR parameters and intensity. Interestingly, however, the spectra of the Cu(II) complexes of the nonadecapeptide and octadecapeptide, that is, R2(12–30) and R2(13–30), have similar ESR parameters, which indicates that only the nonadecapeptide and octadecapeptide have similar Cu(II)-binding site(s). In addition, the three longest fragments used for the experiments, R2(10–30), R2(11–30), and R2(12–30), exhibit lower Cu(II)-binding affinities than R2(13–30), that is, the octadecapeptide.

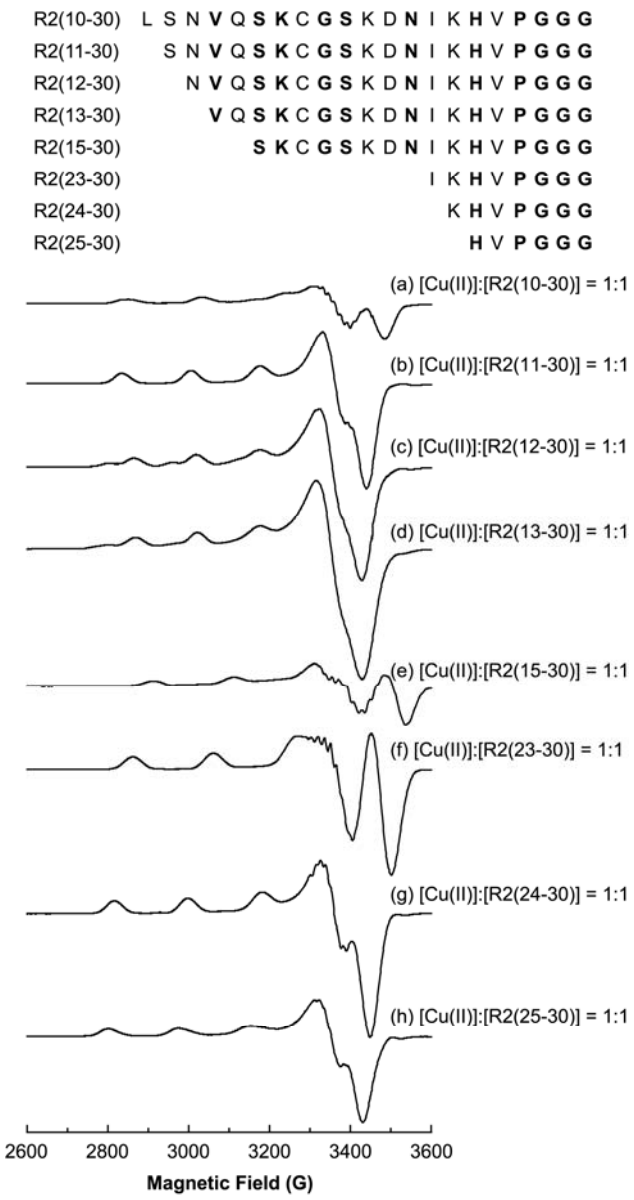

Figure 4-5. CW-ESR spectra of R2(10–30), R2(11–30), R2(12–30), R2(13–30), R2(15–30), R2(23–30), R2(24–30), and R2(25–30) mixed with an equimolar amount of Cu(II). The amino acid sequences of the eight tau fragments are illustrated with conserved residues indicated in boldface. Most spectra have different g values, A values as well as intensity, which suggests that their binding site(s) and binding affinities are different.

Taken together, the CW-ESR results indicate that while the octadecapeptide, R2(13–30), has the highest binding affinity for Cu(II), the mere existence of the octadecapeptide sequence, VQSKCGSKDNIKHVPGGG, in a peptide does not suffice for the Cu(II) coordination with a high binding affinity.

More intriguingly, the corresponding ESEEM and HYSCORE spectra of the Cu(II) complexes of the tau fragments show that the Cu(II) coordination by a backbone amide is most evident in the octadecapeptide, R2(13–30). Since the octadecapeptide appears to have a higher Cu(II)-binding affinity than any other shorter or longer fragments used in the experiments, the Cu(II) coordination by a backbone amide is likely to play an important role in stabilizing the complex. The pulsed ESR data also reveal that a histidine residue directly coordinates to Cu(II) in any fragments that contain the hexapeptide HVPGGG sequence. In fact, some peaks or cross-peaks characteristic of Cu(II)–imidazole coordination appear in the ESEEM or HYSCORE spectra of the Cu(II) complexes of the tau fragments in the R2 pseudorepeat including R2(11–30), R2(12–30), R2(15–30), R2(23–30), R2(24–30), and R2(25–30). The Cu(II) coordination by the histidine residue signifies that the histidine residue—particularly the imidazole ring—serves as an anchor for Cu(II) irrespective of the existence of other residues.

Generally, histidine and cysteine residues in a peptide are considered to have a higher affinity for Cu(II) than the other amino acid residues.[1,131-133] Ma et al.[127] have suggested the possibility that the histidine and cysteine residues in the octadecapeptide, R2(13–30), coordinate to Cu(II) based on their NMR results. Their suggestion is somewhat different from ours as the ESR parameters of the CW-ESR spectra shown in Figure 4-2 are consistent with three nitrogen donors, one oxygen donor and no sulfur donor. In order to resolve the discrepancy, we carried out CW-ESR, ESEEM, and HYSCORE experiments on the Cu(II) complexes of R2SL(13–30)

and R3SL(13–30), each of which has a nitroxide spin-label at the cysteine residue. Figure 4-6 shows that the CW-ESR spectra of the Cu(II) complexes of the spin-labeled peptides are similar to their nonlabeled counterparts except for the region where the nitroxide lines appear, which is not shown in the spectra. The similarity signifies that the free sulfhydryl group in the cysteine residue is not involved in the Cu(II) coordination because the spin-labeled octadecapeptide has no free sulfhydryl group as a disulfide bond is formed.

Figure 4-7 and Figure 4-8 illustrate the ESEEM and HYSCORE spectra of the Cu(II) complexes of the spin-labeled octadecapeptides, respectively. Each of the ESEEM spectra has four peaks at or around 0.55, 0.98, 1.53, and 4.1 MHz, which are due to the involvement of the imidazole ring in the Cu(II) coordination. Similarly, in the corresponding HYSCORE spectra, a cross-peak around (1.6 MHz, 4.0 MHz) is evident in all cases. Also, the four peaks assigned to the Cu(II)–amide coordination, that is, the peaks at or around 0.80, 2.08, 2.80, and 4.4 MHz, and the corresponding cross-peak around (2.8 MHz, 4.3 MHz) appear in each ESEEM and HYSCORE spectrum. Therefore, it is inferred that the cysteine side-chain of the octadecapeptide does not coordinate Cu(II).

Aside from histidine and cysteine, Ma et al.[126-127] have also proposed that the N-terminus coordinates to Cu(II) in the octadecapeptide. Generally, it is probable that the N-terminal amino group can directly coordinate to Cu(II) or stabilize the Cu(II)–peptide complex structure.[4,50,101] In order to obtain information about the role of the N-terminus in the tau fragments, we performed CW-ESR experiments on the acetylated versions of several tau protein fragments in the R2 pseudorepeat. Each of the fragments contains a total of 6–18 amino acid residues including the HVPGGG sequence.

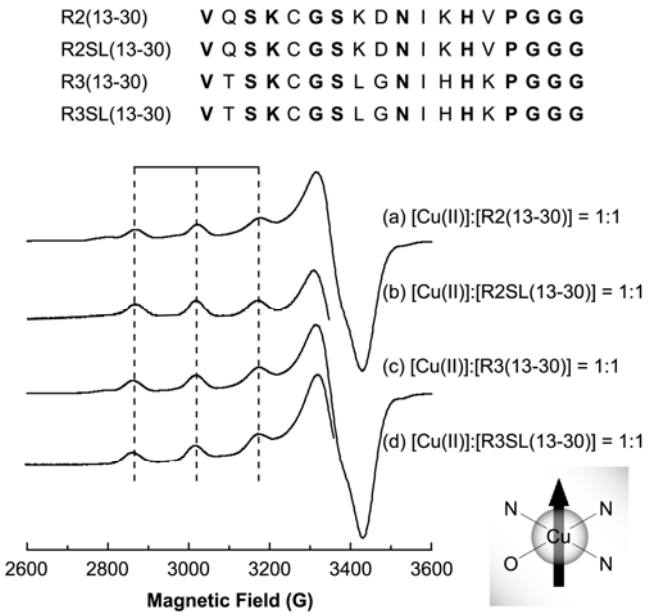

Figure 4-6. CW-ESR spectra of R2(13−30), R2SL(13−30), R3(13−30), and R3SL(13−30) mixed with an equimolar amount of Cu(II). The amino acid sequences of the four peptides are illustrated with conserved residues indicated in boldface. The similarity in g values, A values as well as intensity suggests that their binding site(s) and binding affinities are comparable.

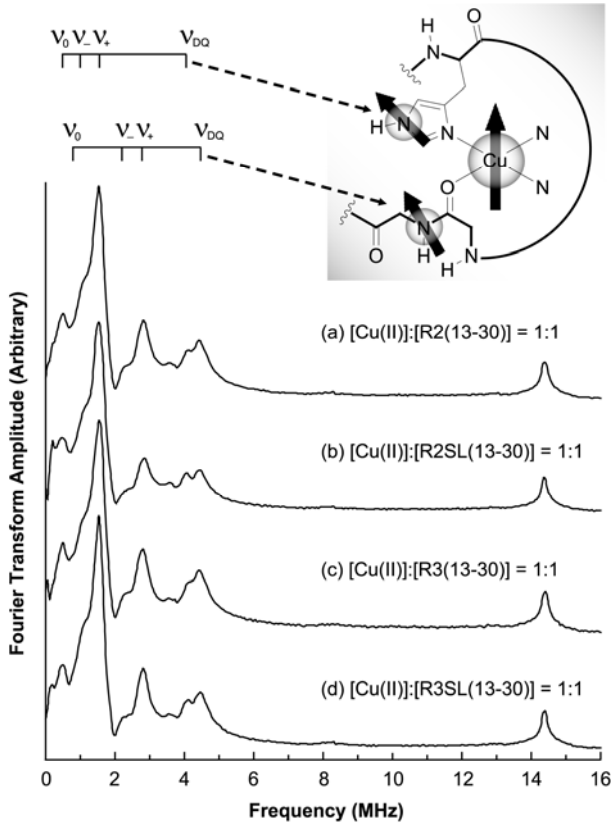

Figure 4-7. Three-pulse ESEEM spectra of R2(13−30), R2SL(13−30), R3(13−30), and R3SL(13−30) mixed with an equimolar amount of Cu(II). The ESEEM frequencies at or around 0.55, 0.98, 1.53, and 4.1 MHz indicate that Cu(II) is coordinated by histidine. Also, the ESEEM frequencies at or around 2.08, 2.80, and 4.4 MHz indicate that amide backbone is involved in the Cu(II) coordination.

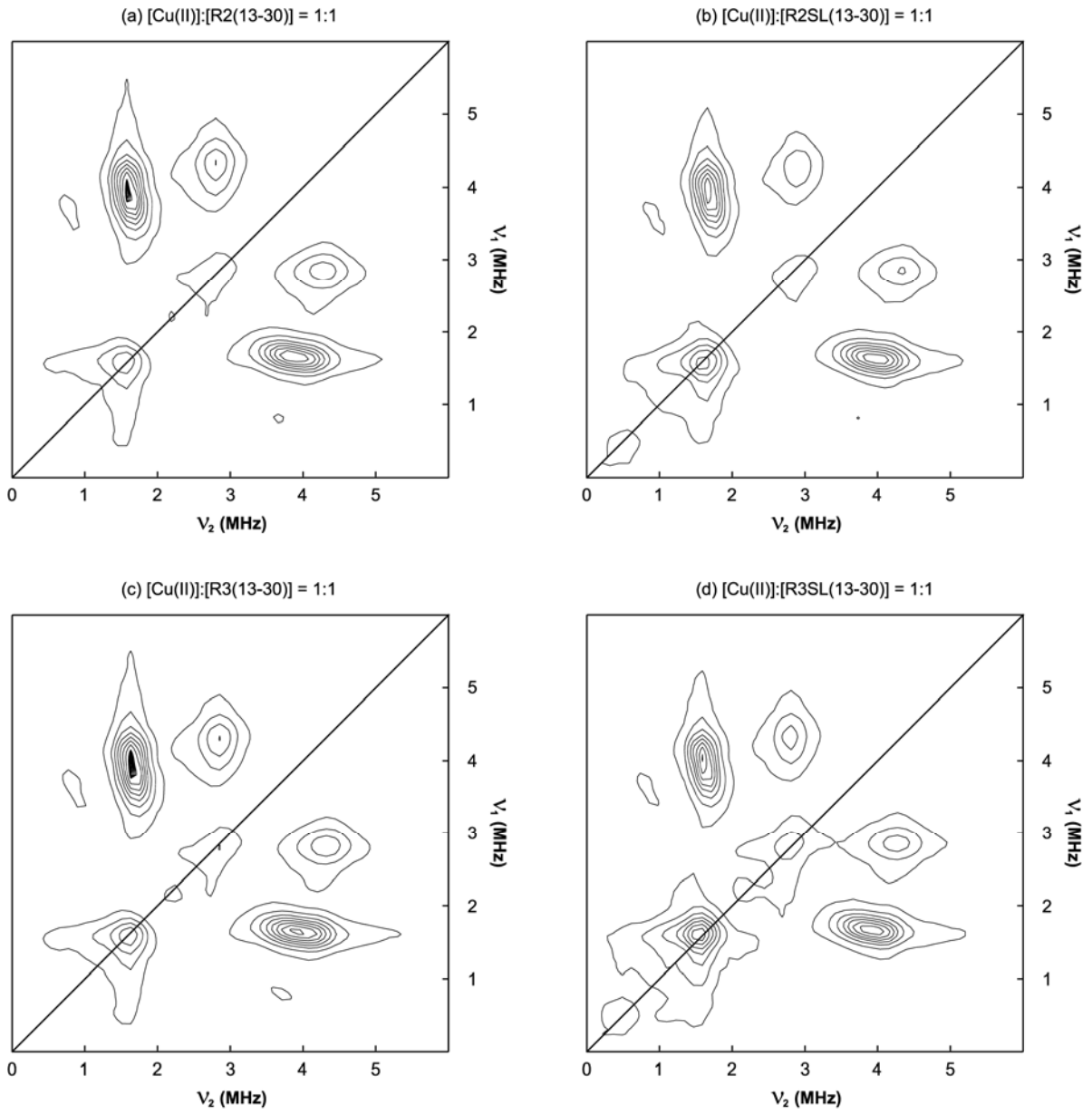

Figure 4-8. HYSCORE spectra of R2(13−30), R2SL(13−30), R3(13−30), and R3SL(13−30) mixed with an equimolar amount of Cu(II). The cross-peak around (1.6 MHz, 4.0 MHz) is ascribed to the Cu(II) ion that is coordinated by histidine. The cross-peak around (2.8 MHz, 4.3 MHz) is unique to the Cu(II)−peptide complex in which amide backbone is involved in the Cu(II) coordination.

Figure 4-9 shows that the CW-ESR spectra of the Cu(II) complexes of the acetylated tau fragments are similar to one another in terms of ESR parameters such as g values, A values, and linewidths. However, comparison of the double integrals reveals that the binding affinities of the acetylated tau fragments are much lower than their non-acetylated counterparts. The difference in binding affinity indicates that the N-terminal amino group plays a role in the Cu(II) coordination. Based on the fact that the N-terminal amino group can be protonated at a pH of 7.4, we suggest that the amino group directly coordinates to Cu(II) or stabilizes the complex structure by electrostatic interactions. Also, it is suspected that the conformation of R2(13–30) and R2(12–30), and presumably the corresponding octadecapeptides and nonadecapeptides in the other three pseudorepeats, helps the N-terminus stabilize the Cu(II)–amide coordination because the Cu(II) coordination by a backbone amide is evident only in the octadecapeptides and nonadecapeptides.

All in all, it is concluded that the Cu(II)–octadecapeptide complexes have a specific conformation that is favorable for the Cu(II) coordination, and the N-terminus plays a role in the conformation. However, the identity of some amino acid residues that coordinate to Cu(II) is yet to be elucidated.

- **Cu(II)-Binding Site(s) in the the Cu(II) Complexes of Longer Tau Fragments**

In order to compare the Cu(II) coordination to the octadecapeptides and a longer tau fragment containing two octadecapeptide, R2 and R3, we also performed CW-ESR experiments on R23(13–61) mixed with Cu(II) at Cu(II)-to-peptide molar ratios of 2:1 and 8:1 and compared the spectra with those of the equimolar mixtures of Cu(II) and either R2(13–30) or R3(13–30).

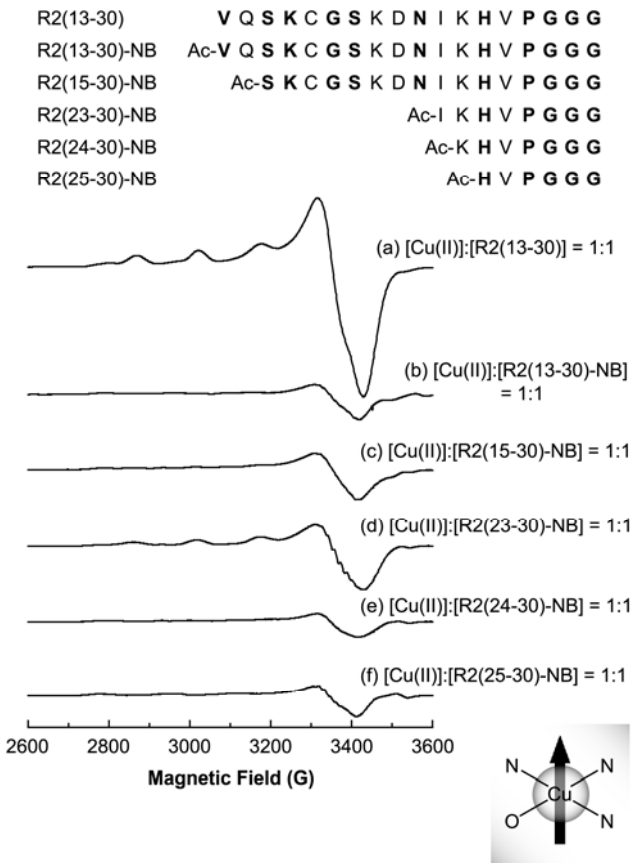

Figure 4-9. CW-ESR spectra of R2(13−30), R2(13−30)-NB, R2(15−30)-NB, R2(23−30)-NB, R2(24−30)-NB, and R2(25−30)-NB mixed with an equimolar amount of Cu(II). The amino acid sequences of the acetylated peptides are illustrated with conserved residues indicated in boldface. Most of the spectra of the tau fragments with the acetylated N-terminus have similar g values and A values. However, the intensities of the acetylated versions are significantly lower than their non-acetylated counterparts.

Figure 4-10 shows that the CW-ESR spectra of the mixtures of Cu(II) and R23(13–61) are similar to those of the equimolar mixtures in terms of ESR parameters including g values, A values, and linewidths. The similarity signifies that the longer peptide has a Cu(II)-binding site similar or identical to that of R2(13–30), R3(13–30), or probably the other two octadecapeptides. Interestingly, the intensities of the four spectra are almost the same even though two or eight equivalents of Cu(II) ions are added to the longer peptide, R23(13–61). Given the fixed CW-ESR instrumental parameters including the microwave power and modulation amplitude, the lack of significant difference in intensity suggests that the number of Cu(II)-binding sites in R23(13–61) is essentially the same as that present in either R2(13–30) or R3(13–30). Even if there is a second Cu(II)-binding site in R23(13–61), the binding affinity is in the millimolar range at best. On the assumption that the octadecapeptides have only one Cu(II)-binding site, our results support those of Soragni et al., who have found that even a longer tau fragment containing all of the four pseudorepeats coordinates to Cu(II) with a stoichiometry of 1.

In addition, we surmise that stabilization of two or more Cu(II)-coordination environments is difficult due to the intrinsic disorderedness of tau protein. A contrasting example is the prion protein, which is relatively ordered and has five or more Cu(II)-binding sites.[134] Each of the four short Cu(II)-binding sequences in the full-length prion protein, PHGGGW, displays a good binding affinity. Interestingly, however, the binding affinity decreases with the Cu(II)-to-peptide ratio ratio even in the case of the prion protein. One explanation for the decrease in the binding affinity is negative cooperativity owing to either conformation changes or increase in the positive charge.[54] The relatively small number of Cu(II)-binding site in the full-length tau protein might be partially due to negative cooperativity.

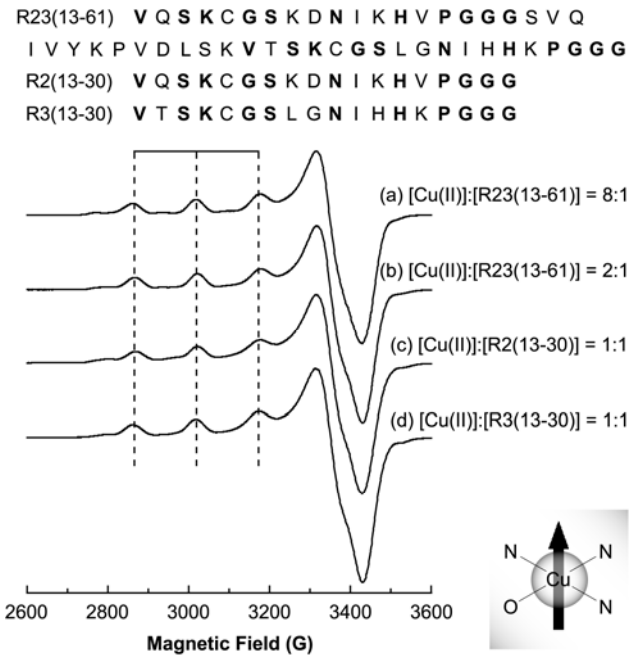

Figure 4-10. CW-ESR spectra of R23(13–61), R2(13–30), and R3(13–30) mixed with Cu(II). The amino acid sequences of the three peptides are illustrated with conserved residues indicated in boldface. All the spectra have almost identical ESR parameters such as g values and A values. Also, the double-integrated intensities of the spectra are not significantly different from one another in spite of different Cu(II)-to-peptide ratios.

Also, pulsed ESR experiments such as ESEEM and HYSCORE were performed on the Cu(II) complex of R23(13−61). The spectra reveal that at least one histidine imidazole and one backbone amide coordinate to Cu(II) in the Cu(II) complex of R23(13−61) as in the Cu(II) complex of the octadecapeptides. We suspect that the histidine residue of R2 is likely to coordinate to Cu(II) in the Cu(II)−R23(13−61) complex because the histidine residue is more proximal to the N-terminus than the other histidine residues. The N-terminal amino group may help stabilize the structure of the complex in a fashion similar to that proposed in the case of the stable Cu(II)−octadecapeptide complexes. Accordingly, it is plausible that a longer tau fragment including all of the four pseudorepeats has only one binding site with a similar coordination environment where histidine imidazole and backbone amide are involved. Also, it is anticipated that the structure is stabilized by the N-terminal amino group or similar functional groups including the amino group of a lysine residue.

Finally, it is noteworthy that a histidine residue directly coordinates to Cu(II) in any fragments that contain the hexapeptide HVPGGG sequence. On the other hand, a backbone amide coordinates to Cu(II) only in some cases. As previously mentioned, the Cu(II)–amide coordination is observed in a number of stable Cu(II) complexes of tau fragments. Therefore, in the full-length tau protein, a histidine residue and some functional groups that may stabilize a Cu(II)−amide coordination are likely to be involved in the Cu(II) coordination.

4.5 SUMMARY

In this article, we find out that each octadecapeptide in the four pseudorepeats of tau protein coordinates to Cu(II) with a binding affinity similar to that of the Aβ(1−16) peptide and provide information about the probable Cu(II) binding site(s) by employing several ESR techniques. Our CW-ESR results reveal that the four octadecapeptides have similar binding site(s). Also, our ESEEM and HYSCORE results show that a nitrogen atom of the histidine imidazole and a carbonyl oxygen of a backbone amide coordinate to Cu(II). The data from further ESR experiments on some modified tau fragments suggest that the existence of a free N-terminus along with a specific conformation is also essential to the high Cu(II)-binding affinity. In addition, we propose, on the basis of our ESR results on the 49-amino acid peptide that contains two of the four octadecapeptides, that a longer peptide with the four pseudorepeats may have Cu(II)-binding site(s) in which the functional groups involved in the Cu(II) coordination to the octadecapeptides play a crucial role. Our findings are meaningful in that they furnish an atomic-level insight into the Cu(II) coordination of tau protein, an intrinsically disordered protein.

4.6 ACKNOWLEDGMENT

This work was supported by a National Science Foundation grant (MCB 0842956). We are grateful to the Peptide Synthesis Facility of the University of Pittsburgh for the peptide preparation.

5.0 A SIMPLE METHOD TO COMPARE THE DISSOCIATION CONSTANTS OF Cu(II) COMPLEXES USING ELECTRON SPIN RESONANCE

5.1 ABSTRACT

We show that the conditional dissociation constants of some Cu(II) complexes at pH 7.4 can be precisely compared by ESR when the Cu(II) complexes are dissolved in NEM buffer. It is known that NEM has a negligibly low binding affinity for Cu(II). In our approach, the concentration of the free Cu(II) ions is determined from the solubility equilibrium of $Cu(OH)_2$ and the concentration of the Cu(II)–ligand complex is determined with the double integrals of CW-ESR spectra. When a binary complex is exclusively present, the measurable range of dissociation constants is limited by the free Cu(II) concentration at equilibrium, which depends on the signal-to-noise ratio of CW-ESR spectra. When a ternary complex as well as a binary complex is formed from a mixture of Cu(II) and a ligand, the two dissociation constants can be calculated with the experimental data including the saturation point and the molar ratio of the two types of complexes. Our approach is meaningful in that it is an entirely new application of CW-ESR to quantitatively analyze the affinities of biomolecules for Cu(II). In addition, we show that a phosphate buffer may be used to cover a wider range of dissociation constants.

5.2 INTRODUCTION

Electron spin resonance has found broad applications in physics, chemistry, and biological sciences. While pulsed ESR techniques are considered to be cutting-edge, conventional continuous-wave ESR is still widely utilized in qualitative and quantitative analysis of various chemical compounds with at least one unpaired electron.

There are numerous synthetic, semisynthetic, and natural compounds with ESR-active metal ions. In particular, Cu(II) is one of the transition metal ions that are involved in a number of synthetic complexes and biomolecules. With the relatively simple nature of spectra due to the d^9 valence electronic configuration, Cu(II) complexes are often analyzed by CW-ESR spectroscopy. The shape of a CW-ESR spectrum provides information about the identity of the sample in question. Peisach and Blumberg[9] have already shown that some CW-ESR parameters such as $g_{||}$ value and $A_{||}$ value are closely related to the type of ligands in Cu(II) complexes with a square-planar geometry. Also, the CW-ESR spectra of a number of Cu(II) complexes, whether natural or synthesized, have been used as references along with other spectroscopic data such as UV or IR spectra.[14,135-138]

The dissociation constants of a number of Cu(II)–ligand complexes are generally determined by various spectroscopic, electrochemical, or calorimetric techniques. While the intrinsic dissociation constants are more fundamental parameters, the conditional dissociation constants at various pH values, particularly those obtained at physiological pH, are also commonly obtained and used as indices that explain the relative binding affinity of complexes.[86] When the conditional dissociation constant of a Cu(II)–ligand complex is considered in lieu of the intrinsic one, all protonation equilibria regarding the ligand species are ignored.

To determine the conditional dissociation constant of a Cu(II) complex, one ought to know the concentration of the free Cu(II) ions, free ligand, and Cu(II)–ligand complex at equilibrium. Therefore, a reaction between Cu(II) and a substance other than the ligand species should be taken into account if the substance has a significant Cu(II)-binding affinity. In general, the concentrations of the Cu(II)–ligand complexes are determined by various techniques such as UV, IR, or fluorescence spectroscopy, and the concentrations of the free ligand, notwithstanding the protonation number, are often estimated with an appropriate assumption. If the concentrations of the free Cu(II) ions at equilibrium are estimated from the initial concentrations, one can obtain the apparent dissociation constant, which might be significantly different from the conditional dissociation constant.[139] While still a decent indicator of the binding affinity, the apparent dissociation constant is often misleading due to its dependency on the buffer system. For instance, the reported dissociation constants of the Cu(II)–Aβ complex range from picomolar to nanomolar.[4-8] The variation makes it difficult to assess the significance of the complexation in a biological system.

In this article, to precisely compare the conditional dissociation constant, we introduce a buffer system where the free Cu(II) concentration can be easily determined with a solubility equilibrium. The concentrations of Cu(II)–ligand complexes are determined with the double integrals of CW-ESR spectra. This method is most efficient when the dissociation constant is in the same order of magnitude as the free Cu(II) concentration. Our experimental results show that a dissociation constant of the order of 10^{-6} M can be most efficiently determined in NEM buffer. Our method is advantageous in that the conditional dissociation constants are easily compared by simple CW-ESR techniques with the use of a reference Cu(II)–ligand complex whose concentration at equilibrium is easily estimated due to its high stability.

5.3 THEORY

- **Formation of a Binary Cu(II) Complex: Cu–L**

A reaction between Cu(II) and a ligand, L, to yield a binary complex and the corresponding dissociation constant are given by:

$$\mathrm{Cu^{2+}} + \mathrm{L} \quad \rightleftarrows \quad \mathrm{Cu\text{–}L} \qquad\qquad K_{\mathrm{d}}{}^{\mathrm{c}} = \frac{[\mathrm{Cu^{2+}}]_{\mathrm{E}}[\mathrm{L}]_{\mathrm{E}}}{[\mathrm{Cu\text{–}L}]_{\mathrm{E}}} \tag{5-1}$$

where the subscripts d and E denote dissociation and equilibrium, respectively, and the superscript c denotes that the equilibrium constant is conditional, that is, dependent on pH and the $\mathrm{p}K_{\mathrm{a}}$ values of the ligand. In fact, protonated ligand species such as HL, $\mathrm{H_2L}$, and $\mathrm{H_3L}$ may be considered separately and the fraction of the protonated species, which is a function of pH and the $\mathrm{p}K_{\mathrm{a}}$ values of the ligand, is a factor that affects the conditional dissociation constant, $K_{\mathrm{d}}{}^{\mathrm{c}}$. Thus, more complicated equations are necessary to obtain the precise intrinsic dissociation constant, K_{d}. In this article, however, we only consider the conditional dissociation constant and ignore the effect of the protonation of the ligand for the sake of simplicity. In order to determine the conditional dissociation constant, the concentrations of the three species, the free Cu(II), $\mathrm{Cu^{2+}}$, the free ligand, L, and the complex, $\mathrm{Cu\text{–}L}$, at equilibrium ought to be figured out. In most cases, the concentration of the complex is determined by a spectroscopic method while the concentration of the free Cu(II) or the free ligand is calculated with some other equations.

The equations that relate the concentration of the free ligand or the free Cu(II) with that of the complex are the mass balances, which are given by:

$$[\mathrm{L}]_{\mathrm{E}} + [\mathrm{Cu\text{–}L}]_{\mathrm{E}} = [\mathrm{L}]_0 \tag{5-2}$$

$$[\mathrm{Cu^{2+}}]_{\mathrm{E}} + [\mathrm{Cu\text{–}L}]_{\mathrm{E}} = [\mathrm{Cu^{2+}}]_0 \tag{5-3}$$

where the subscript 0 denotes the initial state. Using eqs (5-2) and (5-3), one can calculate the concentration of the free ligand and the free Cu(II) at equilibrium, and therefore the equilibrium constant, provided that the concentration of the complex at equilibrium is known. The conditional dissociation constant is expressed as:

$$K_{\mathrm{d}}^{\mathrm{c}} = \frac{([\mathrm{Cu}^{2+}]_0 - [\mathrm{Cu\text{–}L}]_{\mathrm{E}})([\mathrm{L}]_0 - [\mathrm{Cu\text{–}L}]_{\mathrm{E}})}{[\mathrm{Cu\text{–}L}]_{\mathrm{E}}} \tag{5-4}$$

However, when another reaction between the free Cu(II) and other species such as the buffer exists, eq (5-3) becomes more complicated. If m molecules of buffer, B, coordinate to one Cu(II) ion to yield a relatively stable complex, the chemical reaction and the equilibrium constant are given by:

$$\mathrm{Cu}^{2+} + m\mathrm{B} \quad \rightleftarrows \quad \mathrm{Cu\text{–}B}_m \qquad\qquad \beta = \frac{[\mathrm{Cu\text{–}B}_m]_{\mathrm{E}}}{[\mathrm{Cu}^{2+}]_{\mathrm{E}}[\mathrm{B}]_{\mathrm{E}}{}^{m}} \tag{5-5}$$

where, β is the formation constant of the complex $\mathrm{Cu\text{–}B}_m$. Accordingly, the mass balance for the Cu(II) species becomes:

$$[\mathrm{Cu}^{2+}]_{\mathrm{E}} + [\mathrm{Cu\text{–}L}]_{\mathrm{E}} + [\mathrm{Cu\text{–}B}_m]_{\mathrm{E}} = [\mathrm{Cu}^{2+}]_0 \tag{5-6}$$

Plugging eq (5-6) into eq (5-1) gives a more precise equation for the conditional dissociation constant including the effect of the complex $\mathrm{Cu\text{–}B}_m$.

$$K_{\mathrm{d}}^{\mathrm{c}} = \frac{([\mathrm{Cu}^{2+}]_0 - [\mathrm{Cu\text{–}L}]_{\mathrm{E}} - [\mathrm{Cu\text{–}B}_m]_{\mathrm{E}})([\mathrm{L}]_0 - [\mathrm{Cu\text{–}L}]_{\mathrm{E}})}{[\mathrm{Cu\text{–}L}]_{\mathrm{E}}} \tag{5-7}$$

In most cases, the concentration of the complex $\mathrm{Cu\text{–}B}_m$ is ignored and the apparent dissociation constant is expressed as:

$$K_{\mathrm{d}}^{\mathrm{a}} = \frac{([\mathrm{Cu}^{2+}]_0 - [\mathrm{Cu\text{–}L}]_{\mathrm{E}})([\mathrm{L}]_0 - [\mathrm{Cu\text{–}L}]_{\mathrm{E}})}{[\mathrm{Cu\text{–}L}]_{\mathrm{E}}} \tag{5-8}$$

where the superscript a denotes that the dissociation constant is apparent. Comparing eq (5-7) to eq (5-8), one can obtain the relationship between the conditional dissociation constant, $K_{\mathrm{d}}{}^{\mathrm{c}}$, and the apparent dissociation constant, $K_{\mathrm{d}}{}^{\mathrm{a}}$.

$$K_{\mathrm{d}}^{\mathrm{a}} = K_{\mathrm{d}}^{\mathrm{c}} \frac{[\mathrm{Cu}^{2+}]_0 - [\mathrm{Cu\text{–}L}]_{\mathrm{E}}}{[\mathrm{Cu}^{2+}]_0 - [\mathrm{Cu\text{–}L}]_{\mathrm{E}} - [\mathrm{Cu\text{–}B}_m]_{\mathrm{E}}} \tag{5-9}$$

Plugging eq (5-6) into eq (5-9), one can express the apparent dissociation constant, $K_{\mathrm{d}}{}^{\mathrm{a}}$, in terms of $K_{\mathrm{d}}{}^{\mathrm{c}}$, $[\mathrm{B}]_{\mathrm{E}}$, β, and m.

$$K_{\mathrm{d}}^{\mathrm{a}} = K_{\mathrm{d}}^{\mathrm{c}}(1 + \beta[\mathrm{B}]_{\mathrm{E}}{}^{m}) \tag{5-10}$$

It is straightforward from eq (5-10) that the apparent dissociation constant increases with the formation constant of the complex $\mathrm{Cu\text{–}B}_m$, β, and the equilibrium concentration of the buffer, which is nearly the same as its initial concentration. Therefore, the formation constant, β, needs to be determined to calculate the conditional dissociation constant from the apparent dissociation constant.

If the formation constant is very small, the difference between the conditional dissociation constant and the apparent dissociation constant may be negligible. Indeed, NEM and some compounds with a similar molecular structure have a low binding affinity for Cu(II), and the comlexation between Cu(II) and these compounds may be ignored. However, the formation of the insoluble $Cu(OH)_2$ is expected. The chemical reaction and the solubility product constant, K_{sp}, are given by:

$$\mathrm{Cu}^{2+} + 2\mathrm{OH}^{-} \quad \rightleftarrows \quad \mathrm{Cu(OH)_2}\downarrow \qquad\qquad K_{\mathrm{sp}} = [\mathrm{Cu}^{2+}]_{\mathrm{E}}[\mathrm{OH}^{-}]_{\mathrm{E}}^{2} \tag{5-11}$$

Then, the mass balance for the Cu(II) species becomes:

$$[\mathrm{Cu^{2+}}]_\mathrm{E} + [\mathrm{Cu\text{–}L}]_\mathrm{E} + [\mathrm{Cu(OH)_2}]_\mathrm{P,E} = [\mathrm{Cu^{2+}}]_0 \tag{5-12}$$

where the subscript P denotes the precipitate. If the system is saturated with $Cu(OH)_2$, the concentration of the free Cu(II), $[\mathrm{Cu^{2+}}]_\mathrm{S}$, is determined by the solubility product constant, K_sp, and pH. Accordingly, eq (5-1) can be rewritten as:

$$K_\mathrm{d}{}^\mathrm{c} = \frac{[\mathrm{L}]_\mathrm{S} K_\mathrm{sp}}{[\mathrm{Cu\text{–}L}]_\mathrm{S}[\mathrm{OH^-}]_\mathrm{E}^2} \tag{5-13}$$

where the subscript S denotes that the system is saturated with $Cu(OH)_2$.

The concentration of the Cu(II)–ligand complex can be determined by ESR spectroscopy. The double integrated intensity, I, calculated for the CW-ESR spectrum of the mixture of Cu(II) and the ligand in the buffer is proportional to the concentrations of the soluble Cu(II) species.

$$I = k\left([\mathrm{Cu^{2+}}]_\mathrm{E} + [\mathrm{Cu\text{–}L}]_\mathrm{E}\right) \tag{5-14}$$

where k is a proportionality constant. Since the concentration of the free Cu(II) is low, the intensity is almost proportional to the concentration of the complex.

$$I \approx k[\mathrm{Cu\text{–}L}]_\mathrm{E} \tag{5-15}$$

When the system is saturated, the intensity becomes:

$$I_\mathrm{S} \approx k[\mathrm{Cu\text{–}L}]_\mathrm{S} \tag{5-16}$$

where the subscript S denotes the system saturated with insoluble $Cu(OH)_2$. In a special case where a ligand, $\mathrm{L_R}$, has a very low dissociation constant, the concentration of the Cu(II)–ligand

complex is expected to be nearly equal to the initial concentration of the ligand provided that at least an equimolar amount of Cu(II) is added. Then, the intensity, denotes as I_{R}, is expressed as:

$$I_{\mathrm{R}} \approx k[\mathrm{Cu}\text{–}\mathrm{L_R}]_{\mathrm{S}} \approx k[\mathrm{L_R}]_0 \tag{5-17}$$

where the subscript R denotes that the intensity is used as the reference. Using eqs (5-2), (5-16), and (5-17), one can express the conditional dissociation constant in eq (5-13) in terms of ESR intensities.

$$K_{\mathrm{d}}^{\mathrm{c}} = \left(\frac{[\mathrm{L}]_0 I_{\mathrm{R}}}{[\mathrm{L_R}]_0 I_{\mathrm{S}}} - 1 \right) \frac{K_{\mathrm{sp}}}{[\mathrm{OH^-}]_{\mathrm{E}}^2} \tag{5-18}$$

When the initial concentration of the ligand in question, $[\mathrm{L}]_0$, is the same as that of the ligand used as the reference, $[\mathrm{L_R}]_0$, eq (5-18) is simplified to:

$$K_{\mathrm{d}}^{\mathrm{c}} = \left(\frac{I_{\mathrm{R}}}{I_{\mathrm{S}}} - 1 \right) \frac{K_{\mathrm{sp}}}{[\mathrm{OH^-}]_{\mathrm{E}}^2} \tag{5-19}$$

- **Formation of a Ternary Cu(II) Complex: Cu–L_2**

We have assumed a stoichiometry of 1:1 for the reaction between Cu(II) and a ligand for the sake of simplicity. In fact, in numerous Cu(II) complexes, two or more ligand molecules simultaneously coordinate to Cu(II). Thus, several Cu(II) complexes with different numbers of ligand molecules may exist in a mixture of Cu(II) and a ligand. If a complex with a stoichiometry other than 1:1 is relatively unstable, its contribution may be neglected, which allows one to use eqs (5-18) and (5-19). However, if a stable ternary, quaternary, or higher-order complex is present along with the binary complex, more chemical reactions should be taken into account. For instance, reactions between Cu(II) and another ligand, L', with stoichiometries of 1:1 and 1:2

yield a binary complex, $\mathrm{Cu\text{–}L'}$, and a ternary complex, $\mathrm{Cu\text{–}L'_2}$, respectively. The reactions and the corresponding dissociation constants are given by:

$$\mathrm{Cu^{2+} + L' \quad \rightleftarrows \quad Cu\text{–}L'} \qquad K_\mathrm{b} = \frac{[\mathrm{Cu^{2+}}]_\mathrm{E}[\mathrm{L'}]_\mathrm{E}}{[\mathrm{Cu\text{–}L'}]_\mathrm{E}} \tag{5-20}$$

$$\mathrm{Cu^{2+} + 2L' \quad \rightleftarrows \quad Cu\text{–}L'_2} \qquad K_\mathrm{t} = \frac{[\mathrm{Cu^{2+}}]_\mathrm{E}[\mathrm{L'}]_\mathrm{E}^2}{[\mathrm{Cu\text{–}L'_2}]_\mathrm{E}} \tag{5-21}$$

where the subscripts b and t denote the binary and ternary complex, respectively. The mass balances for the ligand species and Cu(II) species are expressed as:

$$[\mathrm{L'}]_\mathrm{E} + [\mathrm{Cu\text{–}L'}]_\mathrm{E} + 2[\mathrm{Cu\text{–}L'_2}]_\mathrm{E} = [\mathrm{L'}]_0 \tag{5-22}$$

$$[\mathrm{Cu^{2+}}]_\mathrm{E} + [\mathrm{Cu\text{–}L'}]_\mathrm{E} + [\mathrm{Cu\text{–}L'_2}]_\mathrm{E} = [\mathrm{Cu^{2+}}]_0 \tag{5-23}$$

In an extreme case where the dissociation constant of the ternary complex is much smaller than that of the binary complex, that is, $K_\mathrm{t} \ll K_\mathrm{b}$, the concentration of the binary complex at equilibrium is nearly 0. With the approximation, the following equations analogous to eqs (5-16) and (5-18) are obtained.

$$I_\mathrm{S} \approx k[\mathrm{Cu\text{–}L'_2}]_\mathrm{S} \tag{5-24}$$

$$K_\mathrm{t} = \left(\frac{[\mathrm{L'}]_0^2 I_\mathrm{R}}{[\mathrm{L_R}]_0 I_\mathrm{S}} - 4[\mathrm{L'}]_0 + 4\frac{I_\mathrm{S}}{I_\mathrm{R}}[\mathrm{L_R}]_0 \right) \frac{K_\mathrm{sp}}{[\mathrm{OH^-}]_\mathrm{E}^2} \qquad \left(\frac{I_\mathrm{S}}{I_\mathrm{R}} \leqq \frac{[\mathrm{L'}]_0}{2[\mathrm{L_R}]_0} \right) \tag{5-25}$$

In case of $[\mathrm{L'}]_0 = [\mathrm{L_R}]_0$, eq (5-25) is reduced to:

$$K_\mathrm{t} = \left(\frac{I_\mathrm{R}}{I_\mathrm{S}} - 4 + \frac{4I_\mathrm{S}}{I_\mathrm{R}} \right) \frac{[\mathrm{L'}]_0 K_\mathrm{sp}}{[\mathrm{OH^-}]_\mathrm{E}^2} \qquad \left(\frac{I_\mathrm{S}}{I_\mathrm{R}} \leqq 0.5 \right) \tag{5-26}$$

As shown in eqs (5-25) and (5-26), the double integrated intensity of the CW-ESR spectrum of the mixture of Cu(II) and the ligand $\mathrm{L'}$ does not exceed half that of the mixture of

Cu(II) and the ligand L_r, which forms a very stable binary Cu(II) complex. Thus, if the titration curve of a ligand with a very high binding affinity exhibits a plateau around a Cu(II)-to-ligand molar ratio of 0.5:1, the ligand is expected to exclusively form a ternary complex with Cu(II). In the case of a competitive formation of binary and ternary complexes, however, the saturation is likely to occur beyond the half equivalence point.

- **Calculations regarding both the Binary Complex and the Ternary Complex**

Provided that n molar equivalent of Cu(II) is added to the ligand, the initial concentration of free Cu(II), $[Cu^{2+}]_0$, is simply $n[L']_0$. Also, one can express $[Cu\text{–}L']_E$ and $[Cu\text{–}L'_2]_E$ in eqs (5-22) and (5-23) in terms of $[Cu^{2+}]_E$, $[L']_E$, and either K_b or K_t by using eqs (5-20) and (5-21). Then, eqs (5-22) and (5-23) become:

$$[L']_E + \frac{[Cu^{2+}]_E[L']_E}{K_b} + \frac{2[Cu^{2+}]_E[L']_E^2}{K_t} = [L']_0 \tag{5-27}$$

$$[Cu^{2+}]_E + \frac{[Cu^{2+}]_E[L']_E}{K_b} + \frac{[Cu^{2+}]_E[L']_E^2}{K_t} = n[L']_0 \tag{5-28}$$

Solving eq (5-27) for $[L']_E$ yields an expression in terms of $[Cu^{2+}]_E$, $[L']_0$, K_b, and K_t.

$$[L']_E = -\frac{K_t}{4[Cu^{2+}]_E}\left[\frac{[Cu^{2+}]_E}{K_b} + 1 - \sqrt{\left(\frac{[Cu^{2+}]_E}{K_b} + 1\right)^2 + \frac{8[Cu^{2+}]_E[L']_0}{K_t}}\right] \tag{5-29}$$

Also, the linear relationship between n and $[L']_E$ is obtained from eqs (5-27) and (5-28).

$$n = \frac{1}{2[L']_0}\left[2[Cu^{2+}]_E + [L']_0 + \left(\frac{[Cu^{2+}]_E}{K_b} - 1\right)[L']_E\right] \tag{5-30}$$

Plugging eq (5-29) into eq (5-30) gives:

$$n = \frac{1}{2} + \frac{[\mathrm{Cu^{2+}}]_\mathrm{E}}{[\mathrm{L'}]_0} + \frac{\frac{[\mathrm{Cu^{2+}}]_\mathrm{E}}{K_\mathrm{b}} - 1}{\frac{[\mathrm{Cu^{2+}}]_\mathrm{E}}{K_\mathrm{b}} + 1 + \sqrt{\left(\frac{[\mathrm{Cu^{2+}}]_\mathrm{E}}{K_\mathrm{b}} + 1\right)^2 + \frac{8[\mathrm{Cu^{2+}}]_\mathrm{E}[\mathrm{L'}]_0}{K_\mathrm{t}}}} \tag{5-31}$$

When the system is saturated with an insoluble Cu(II) salt, the concentration of free Cu(II) ions is determined by the solubility product constant, K_{sp}, and pH. If n_S molar equivalent of Cu(II) is added at the saturation point with the concentration of free Cu(II), $[\mathrm{Cu^{2+}}]_\mathrm{S}$, the equation above can be rewritten as:

$$n_\mathrm{S} = \frac{1}{2} + \frac{[\mathrm{Cu^{2+}}]_\mathrm{S}}{[\mathrm{L'}]_0} + \frac{\frac{[\mathrm{Cu^{2+}}]_\mathrm{S}}{K_\mathrm{b}} - 1}{\frac{[\mathrm{Cu^{2+}}]_\mathrm{S}}{K_\mathrm{b}} + 1 + \sqrt{\left(\frac{[\mathrm{Cu^{2+}}]_\mathrm{S}}{K_\mathrm{b}} + 1\right)^2 + \frac{8[\mathrm{Cu^{2+}}]_\mathrm{S}[\mathrm{L'}]_0}{K_\mathrm{t}}}} \tag{5-32}$$

Once $[\mathrm{Cu^{2+}}]_\mathrm{S}$, $[\mathrm{L'}]_0$, and n_S, are either theoretically calculated or experimentally obtained, eq (5-32) can be used to relate K_b to K_t. If one of the two constants is known, the other is determined. Theoretically, one can determine the two constants by experimentally obtaining n_S values from two different sets of experiments under different conditions, that is, different $[\mathrm{L'}]_0$. However, such an approach is limited by the possible range of $[\mathrm{L'}]_0$ for ESR experiments because the dependence of n_S on $[\mathrm{L'}]_0$ may be negligibly small in many cases.

If both the binary complex and the ternary complex are present at the saturation point, the intensity is expressed as:

$$I_\mathrm{S} = I_{\mathrm{S,b}} + I_{\mathrm{S,t}} \approx k\,([\mathrm{Cu\text{–}L'}]_\mathrm{S} + [\mathrm{Cu\text{–}L'_2}]_\mathrm{S}) \tag{5-33}$$

where $I_{S,b}$ and $I_{S,t}$ denote the intensity due to the binary complex and the ternary complex, respectively. Because the intensity of the reference, I_R, is also proportional to the constant k in eq (5-17), $[Cu\text{–}L']_S$ and $[Cu\text{–}L_2']_S$ can be expressed in terms of $I_{S,b}$, $I_{S,t}$, I_R, and $[L_R]_0$.

$$[Cu\text{–}L']_S \approx \frac{I_{S,b}}{I_R}[L_R]_0 \tag{5-34}$$

$$[Cu\text{–}L_2']_S \approx \frac{I_{S,t}}{I_R}[L_R]_0 \tag{5-35}$$

Also, one can obtain another equation from eqs (5-20) and (5-21).

$$\frac{K_b^2}{K_t} = \frac{[Cu^{2+}]_S[Cu\text{–}L_2']_S}{[Cu\text{–}L']_S^2} \tag{5-36}$$

Once $[Cu\text{–}L']_S$ and $[Cu\text{–}L_2']_S$ are obtained, K_t is expressed in terms of K_b. Therefore, one can determine both K_b and K_t using eqs (5-32) and (5-36).

In the case that the formation of the ternary complex is negligible, that is, $K_t \to \infty$, eq (5-32) is simplified to:

$$n_S = \frac{[Cu^{2+}]_S}{[L']_0} + \frac{[Cu^{2+}]_S}{K_b + [Cu^{2+}]_S} \tag{5-37}$$

Given that the concentration of free Cu(II) at the saturation point is at least several orders of magnitude smaller than the initial concentration of the ligand, the equation above is further reduced to:

$$n_S = \frac{[Cu^{2+}]_S}{K_b + [Cu^{2+}]_S} \tag{5-38}$$

It is straightforward from eq (5-38) that n_S ranges from 0 to 1. In a special case where K_b is the same as $[Cu^{2+}]_S$, the saturation occurs when a half molar equivalent of Cu(II) is added.

On the other hand, if the formation of the binary complex is negligible, that is, $K_{\mathrm{b}} \to \infty$, eq (5-32) is simplified to:

$$n_{\mathrm{S}} = \frac{1}{2} + \frac{[\mathrm{Cu}^{2+}]_{\mathrm{S}}}{[\mathrm{L}']_0} - \frac{1}{1 + \sqrt{1 + \dfrac{8[\mathrm{Cu}^{2+}]_{\mathrm{S}}[\mathrm{L}']_0}{K_{\mathrm{t}}}}} \tag{5-39}$$

If a very low concentration of free Cu(II) is assumed at the saturation point, the equation above is further reduced to:

$$n_{\mathrm{S}} = \frac{1}{2} - \frac{1}{1 + \sqrt{1 + \dfrac{8[\mathrm{Cu}^{2+}]_{\mathrm{S}}[\mathrm{L}']_0}{K_{\mathrm{t}}}}} \tag{5-40}$$

Similar to the case of eq (5-38), it is clear from eq (5-40) that n_{S} ranges from 0 to 0.5. In particular, if K_{t} is the same as the product of $[\mathrm{Cu}^{2+}]_{\mathrm{S}}$ and $[\mathrm{L}']_0$, the saturation occurs when a quarter molar equivalent of Cu(II) is added.

5.4 EXPERIMENTAL SECTION

- **Cu(II) Complex Preparation**

$CuCl_2 \cdot 2H_2O$ was purchased from Sigma–Aldrich (St. Louis, MO). Ethylenediaminetetraacetic acid (EDTA), 2,6-pyridinedicarboxylic acid (2,6-PDA), glycine, tris(hydroxymethyl)aminomethane (Tris), diethylenetriamine (dien), and NEM were also purchased from Sigma–Aldrich.

A 100 mM NEM buffer with a pH of 7.4 was prepared by mixing NEM and hydrochloric acid. Then, 10 mM stock solutions of EDTA, 2,6-PDA, glycine, Tris, and dien were prepared in the 100 mM NEM buffer. Then, 0.2 mM solutions of EDTA, 2,6-PDA, glycine, Tris, and dien were prepared in the 100 mM NEM buffer by diluting the corresponding stock solutions. Separately, a 1 M Cu(II) stock solution was prepared in deionized water. An appropriate volume of the Cu(II) stock solution was added to the 0.2 mM solution of either EDTA, 2,6-PDA, glycine, Tris, or dien to give a mixture with a Cu(II)-to-ligand molar ratio of 0.1:1 through 1.2:1.

- **Electron Spin Resonance Spectroscopy**

Cu(II)–ligand mixtures with various molar ratios dissolved in the 100 mM NEM buffer were used for ESR experiments. An approximately 200 μL aliquot of each Cu(II)–ligand mixture solution was transferred into a quartz tube with an inner diameter of 3 mm. All ESR experiments were performed on a Bruker ElexSys E580 FT/CW X-band Spectrometer equipped with a Bruker ER 4118X-MD5 dielectric ring resonator. The temperature was adjusted with an Oxford ITC503 temperature controller and an Oxford CF935 dynamic continuous-flow cryostat connected to an Oxford LLT650 low-loss transfer tube. Continuous-wave ESR experiments were carried out on the sample solutions. All ESR signals were collected at 80 K with a microwave frequency of approximately 9.69 GHz. The magnetic field was generally swept from 2600 G to 3600 G for a total of 1024 data points. Other instrumental parameters include a time constant of 40.96 ms, a conversion time of 81.92 ms, a modulation amplitude of 4 G, a modulation frequency of 100 kHz, and a microwave power of 0.1993 mW. The double integral of each spectrum was obtained in the Xepr program provided by Bruker.

5.5 RESULTS

A series of CW-ESR experiments were conducted on each of the Cu(II)–ligand mixture solutions. The ligands used herein include EDTA, 2,6-PDA, glycine, Tris, and dien. The mixture solutions were prepared in 100 mM NEM buffer at a pH of 7.4.

- **ESR Intensities of the Cu(II)–Ligand Mixtures in 100 mM NEM Buffer at a pH of 7.4**

Continuous-wave ESR experiments were carried out on the mixtures of Cu(II) and EDTA in 100 mM NEM buffer at a pH of 7.4 with various molar ratios ranging from 0.1:1 to 1.2:1. Figure 5-1 shows the CW-ESR spectra and the relative double integrals of the mixtures of Cu(II) and EDTA in 100 mM NEM buffer. The intensity of the CW-ESR spectra increases with the initial Cu(II)-to-ligand ratio until the system is saturated with $Cu(OH)_2$ at around the equivalence point. Since a very low conditional dissociation constant of approximately 2×10^{-19} M is expected for the Cu(II)–EDTA complex,[140] most of the Cu(II) ions added at a subequimolar concentration bind to EDTA, which leads to a very low concentration of free Cu(II) ions. Thus, it is anticipated that the saturation occurs around the equivalence point. Assuming that all Cu(II) ions bind to EDTA at the equivalence point, we use the double integral of the CW-ESR spectrum of the equimolar mixture as the reference intensity.

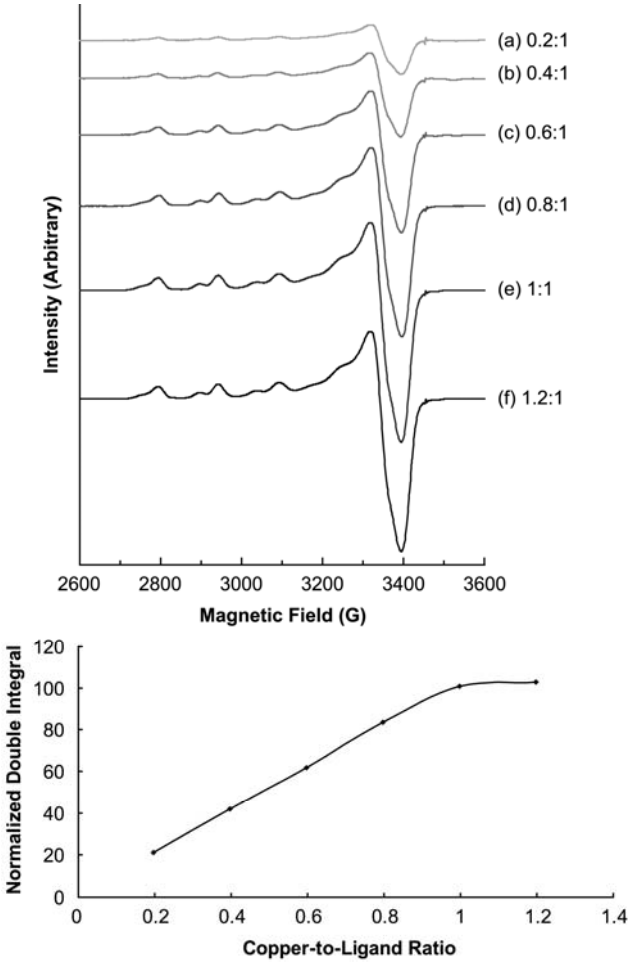

Figure 5-1. CW-ESR spectra of EDTA mixed with Cu(II) ions at various molar ratios including 0.2:1, 0.4:1, 0.6:1, 0.8:1, 1:1, and 1.2:1 in 100 mM NEM buffer and the plot of the double integral versus copper-to-peptide molar ratio. The double integral increases until it reaches its maximum at a copper-to-peptide ratio of 1:1, which signifies that nearly all Cu(II) ions added at a substoichiometrical level bind to EDTA. The results are consistent with the fact that the dissociation constant of the Cu(II)–EDTA complex is subpicomolar.

We performed CW-ESR experiments on the other samples including the mixtures of Cu(II) and either 2,6-PDA, glycine, Tris, or dien. Figure 5-2 shows the CW-ESR spectra of the mixtures of Cu(II) and 2,6-PDA and the relative double integrals. The saturation occurs at approximately 0.6 equivalent of Cu(II) and the spectral shape changes as the Cu(II)-to-ligand ratio increases. If the stoichiometry were 1:1, the titration curve with a Cu(II)-to-peptide ratio of 0.6 at the saturation point would correspond to a dissociation constant of $\sim 1 \times 10^{-6}$ M. However, the formation of a stable ternary complex along with a binary complex is known for the mixture of Cu(II) and 2,6-PDA. As shown in eqs (5-32) and (5-39), the saturation point above the half equivalence point and the change of the spectral shape, taken together, signify that two different complexes, that is, a binary complex and a ternary complex, are present. Because the difference in the spectral shape is clearly observed when the Cu(II)-to-ligand ratio changes from 0.4 to 0.6, it is probable that the ternary complex is almost exclusively present below 0.4 equivalent of Cu(II). Therefore, the binary complex accounts for no more than a third of Cu(II)–2,6-PDA complexes. If almost all 2,6-PDA molecules coordinate to Cu(II) at the saturation point, the ratio of the binary complex to the ternary complex is indeed 1:2, which means that approximately 20% of 2,6-PDA molecules coordinate to Cu(II) to form the binary complex and the rest of them form the ternary complex. Because the initial concentration of 2,6-PDA is 0.2 mM, the concentrations of the binary complex and the ternary complex are 0.04 mM and 0.08 mM, respectively. From eqs (5-32) and (5-36), the two dissociation constants, K_b and K_t, are calculated to be 3×10^{-9} M and 1×10^{-16} M^2. The experimentally obtained values are similar to the literature values, 1×10^{-9} M and 3×10^{-16} M^2.[141]

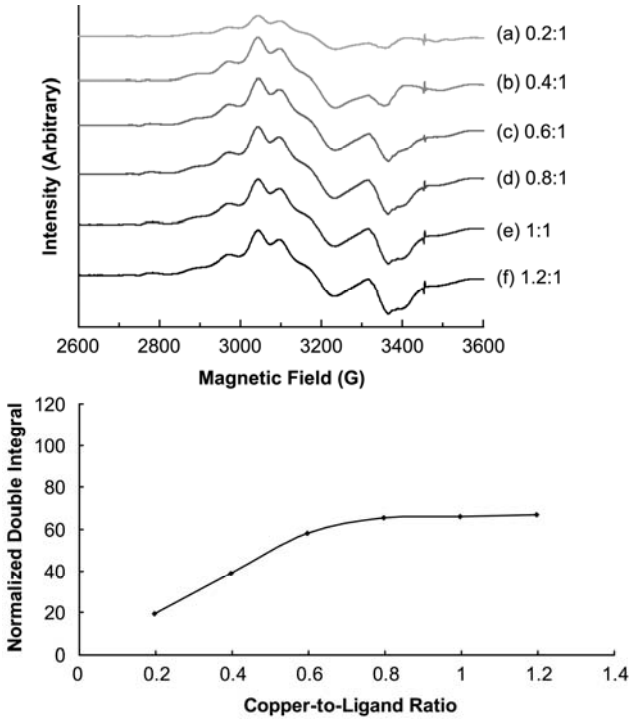

Figure 5-2. CW-ESR spectra of 2,6-PDA mixed with Cu(II) ions at various molar ratios including 0.2:1, 0.4:1, 0.6:1, 0.8:1, 1:1, and 1.2:1 in 100 mM NEM buffer and the plot of the double integral versus the copper-to-peptide molar ratio. The double integral increases until it reaches its maximum approximately at a copper-to-peptide ratio of 0.6:1. Also, a change in the spectral shape is observed as the Cu(II)-to-ligand ratio increases. The saturation point above the half equivalence point and the change in the spectral shape, taken together, indicates that two different complexes, a binary complex and a ternary complex, are present.

Figure 5-3 shows the CW-ESR spectra of the mixtures of Cu(II) and glycine and the relative double integrals. Like the case of the Cu(II)–2,6-PDA mixtures, the saturation occurs when approximately 0.6 equivalent of Cu(II). It is known that Cu(II) and glycine, a bidentate ligand, form a stable ternary complex along with a binary complex. The Cu(II)-to-ligand ratio at the saturation point, 0.6, is consistent with reported K_b and K_t values, 3×10^{-9} M and 2×10^{-16} M^2.[142]

Figure 5-4 shows the CW-ESR spectra of the mixtures of Cu(II) and Tris and the relative double integrals. The saturation occurs below 0.1 equivalent of Cu(II), which signifies that the binding affinity of Tris for Cu(II) is much lower than that of EDTA. If a stoichiometry of 1:1 is assumed, the titration curve corresponds to a dissociation constant greater than 2×10^{-5} M. In fact, the reported dissociation constant of Cu(II)–Tris complex is approximately 5×10^{-3} M.[139] However, the low signal-to-noise ratio due to the low concentration of the Cu(II)–Tris complex, the double integrals are not precise, which deters one from estimating the dissociation constant. Nevertheless, the results provide evidence that the formation of the Cu(II)–Tris complex at pH 7.4 is not as significant as that of other Cu(II) complexes such as Cu(II)–EDTA and Cu(II)–glycine.

Figure 5-5 shows the CW-ESR spectra of the mixtures of Cu(II) and dien and the relative double integrals. Like the case of the Cu(II)–EDTA mixtures, the saturation occurs at around the equivalence point, which indicates that the stoichiometry is 1:1 and the dissociation constant is very low. Because dien is a tridentate ligand, a ternary complex may be formed from a mixture of Cu(II) and dien. However, plugging reported K_b and K_t values, 1×10^{-16} M and 4×10^{-22} M, into eq (5-36), one can expect the binary complex to be dominant over the ternary complex.[143] Thus, our results are consistent with the reported values.

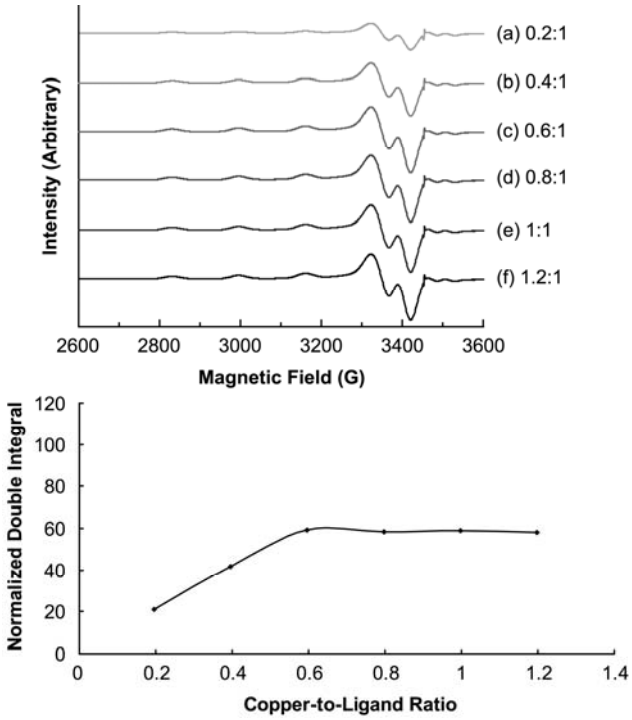

Figure 5-3. CW-ESR spectra of glycine mixed with Cu(II) ions at various molar ratios including 0.2:1, 0.4:1, 0.6:1, 0.8:1, 1:1, and 1.2:1 in 100 mM NEM buffer and the plot of the double integral versus copper-to-peptide molar ratio. The double integral increases until it reaches its maximum approximately at a copper-to-peptide ratio of 0.6:1, which is consistent with the expectation that Cu(II) and glycine form both a binary complex and a ternary complex.

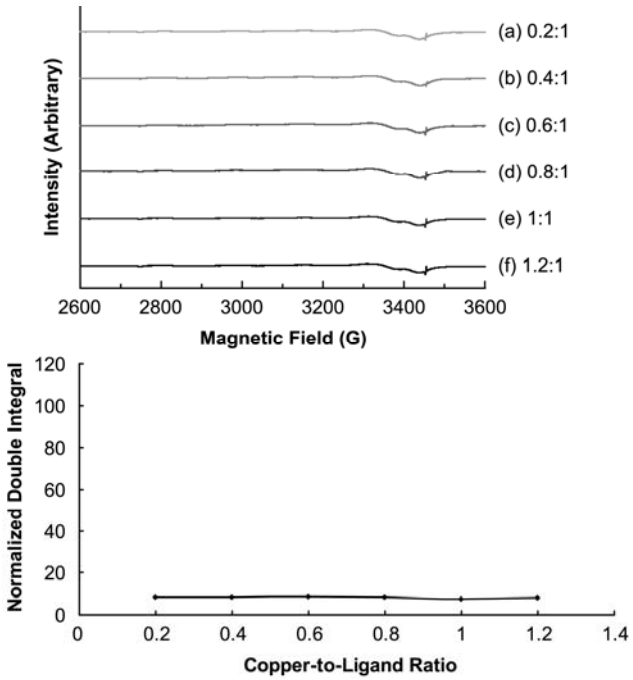

Figure 5-4. CW-ESR spectra of Tris mixed with Cu(II) ions at various molar ratios including 0.2:1, 0.4:1, 0.6:1, 0.8:1, 1:1, and 1.2:1 in 100 mM NEM buffer and the plot of the double integral versus the copper-to-peptide molar ratio. The saturation occurs below 0.1 equivalent of Cu(II), which signifies that the binding affinity of Tris for Cu(II) is very low. The results are consistent with a reported dissociation constant of ~10^{-3} M.

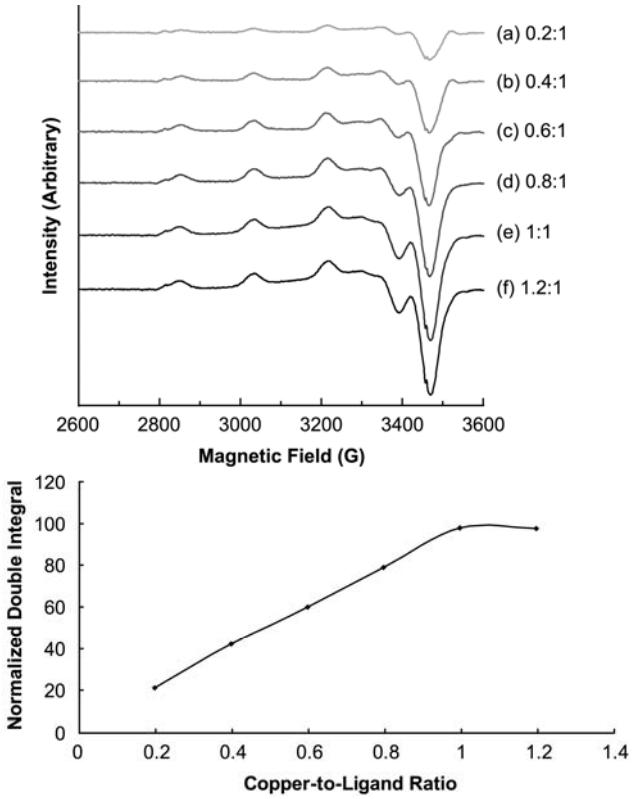

Figure 5-5. CW-ESR spectra of dien mixed with Cu(II) ions at various molar ratios including 0.2:1, 0.4:1, 0.6:1, 0.8:1, 1:1, and 1.2:1 in 100 mM phosphate buffer and the plot of the double integral versus the copper-to-peptide molar ratio. The double integral increases until it reaches its maximum at a copper-to-peptide ratio of 1:1, which signifies that the stoichiometry is 1:1 and the dissociation constant is very low.

5.6 DISCUSSION

- **Measurable Range of Dissociation Constants and Error Analysis**

In this article, the basic idea behind the determination of the conditional dissociation constant is the precise pre-determination of the free Cu(II) concentration. While the use of a solubility equilibrium enables us to know the concentration of the free Cu(II) ions at or beyond the saturation point with a certain known pH value, the measurable range of dissociation constants is limited by the free Cu(II) concentration at equilibrium.

The equation that relates the dissociation constant, $K_{\mathrm{d}}^{\mathrm{c}}$, and the ESR intensity, that is, eq (5-19), can be expressed in terms of the concentration of the free Cu(II) ions at the saturation point, $[\mathrm{Cu}^{2+}]_{\mathrm{S}}$.

$$K_{\mathrm{d}}^{\mathrm{c}} = \left(\frac{I_{\mathrm{R}}}{I_{\mathrm{S}}} - 1 \right) [\mathrm{Cu}^{2+}]_{\mathrm{S}} \tag{5-41}$$

Solving the equation for the intensity I_{S} with the logarithmic expression of the concentration and dissociation constant gives:

$$I_{\mathrm{S}} = \frac{I_{\mathrm{R}}}{1 + 10^{\mathrm{pCu} - \mathrm{p}K}} \tag{5-42}$$

where

$$\mathrm{pCu} = -\log [\mathrm{Cu}^{2+}]_{\mathrm{S}} \tag{5-43}$$

$$\mathrm{p}K = -\log K_{\mathrm{d}}^{\mathrm{c}} \tag{5-44}$$

Then, the change in intensity with respect to the change in $\mathrm{p}K$ can be considered as a measure of the sensitivity of the method. The differentiation of eq (5-42) with respect to $\mathrm{p}K$ yields:

$$\frac{dI_{\mathrm{S}}}{d\mathrm{p}K} = I_{\mathrm{R}} \ln 10 \frac{10^{\mathrm{pCu}-\mathrm{p}K}}{(1+10^{\mathrm{pCu}-\mathrm{p}K})^2} \tag{5-45}$$

It is obvious from eq (5-45) that the highest sensitivity is obtained when $\mathrm{p}K$ is the same as pCu. Also, when the error range of the intensity is assumed to be ΔI_{S}, the expected error range of $\mathrm{p}K$, denoted as $\Delta\mathrm{p}K$, is approximated to be:

$$\Delta\mathrm{p}K \approx \frac{\Delta I_{\mathrm{S}}(1+10^{\mathrm{pCu}-\mathrm{p}K})^2}{I_{\mathrm{R}} \ln 10 \cdot 10^{\mathrm{pCu}-\mathrm{p}K}} \tag{5-46}$$

In our experiments, ΔI_{S} is approximately 5% of I_{R}. Calculations show that the error range of $\mathrm{p}K$ is 0.1, 0.3, and 2.2 with a $\mathrm{pCu} - \mathrm{p}K$ value of 0, ±1, and ±2, respectively. If the allowed error range is 0.5, the measurable dissociation constant range is over 2.5 orders of magnitude and centered at the free Cu(II) concentration. In NEM buffer, the free Cu(II) concentration at the saturation point, $[\mathrm{Cu}^{2+}]_{\mathrm{S}}$, is determined by the solubility product constant for $Cu(OH)_2$ and pH as shown in eq (5-11). At a pH of 7.4, $[\mathrm{Cu}^{2+}]_{\mathrm{S}}$ is approximately 2×10^{-6} M. Because the dissociation constants of Cu(II)–EDTA and Cu(II)–Tris are approximately 2×10^{-19} M and 5×10^{-3} M, respectively, they cannot be precisely determined by our approach. A dissociation constant between 10^{-7} and 10^{-5} M would be within the measurable range.

- **Potential Use of a Phosphate Buffer System**

Because of the unavoidable errors of the double integrals of CW-ESR spectra, a dissociation constant that is several orders of magnitude greater than or smaller than the free Cu(II) concentration cannot be precisely determined. Nevertheless, the problem may be

alleviated by using another buffer system that leads to a different free Cu(II) concentration at the saturation point. For instance, a phosphate buffer system with a concentration of C_0 may be exploited. In the phosphate buffer, the mass balance of the phosphate species is given by:

$$[\mathrm{H_3PO_4}]_\mathrm{E} + [\mathrm{H_2PO_4^-}]_\mathrm{E} + [\mathrm{HPO_4^{2-}}]_\mathrm{E} + [\mathrm{PO_4^{3-}}]_\mathrm{E} = C_0 \tag{5-47}$$

Also, the relative concentrations of the phosphate species are functions of pH. With the three acid constant values, the equations relating the phosphate species with one another are given by:

$$\frac{[\mathrm{H_2PO_4^-}]_\mathrm{E}}{[\mathrm{H_3PO_4}]_\mathrm{E}} = 10^{\,\mathrm{pH}-\mathrm{p}K_\mathrm{a1}} \tag{5-48}$$

$$\frac{[\mathrm{HPO_4^{2-}}]_\mathrm{E}}{[\mathrm{H_2PO_4^-}]_\mathrm{E}} = 10^{\,\mathrm{pH}-\mathrm{p}K_\mathrm{a2}} \tag{5-49}$$

$$\frac{[\mathrm{PO_4^{3-}}]_\mathrm{E}}{[\mathrm{HPO_4^{2-}}]_\mathrm{E}} = 10^{\,\mathrm{pH}-\mathrm{p}K_\mathrm{a3}} \tag{5-50}$$

where K_a1, K_a2, and K_a3 are the first, second, and third acid dissociation constant, respectively. If the reaction between Cu(II) and the ligand L occurs in the phosphate buffer, the formation of the insoluble $Cu_3(PO_4)_2$ is anticipated due to its low solubility. The chemical equation and the solubility product constant, K'_sp, are given by:

$$3\mathrm{Cu^{2+}} + 2\mathrm{PO_4^{3-}} \quad \rightleftarrows \quad \mathrm{Cu_3(PO_4)_2}\downarrow \qquad\qquad K'_\mathrm{sp} = [\mathrm{Cu^{2+}}]_\mathrm{E}^3[\mathrm{PO_4^{3-}}]_\mathrm{E}^2 \tag{5-51}$$

Even though other reactions between Cu(II) and some other phosphate species, those between the ligand and some phosphate species, or those involving other species present in the system such as hydroxide ions and chloride ions may occur, the products of those reactions are expected to be unstable compared with the insoluble $Cu_3(PO_4)_2$.[144-145] Thus, the mass balances

for the Cu(II) species and the phosphate species are not significantly affected by those reactions. Then, the mass balances become:

$$[\mathrm{Cu^{2+}}]_\mathrm{E} + [\mathrm{Cu{-}L}]_\mathrm{E} + 3\,[\mathrm{Cu_3(PO_4)_2}]_\mathrm{P,E} = [\mathrm{Cu^{2+}}]_0 \tag{5-52}$$

$$[\mathrm{H_3PO_4}]_\mathrm{E} + [\mathrm{H_2PO_4^-}]_\mathrm{E} + [\mathrm{HPO_4^{2-}}]_\mathrm{E} + [\mathrm{PO_4^{3-}}]_\mathrm{E} + 2\,[\mathrm{Cu_3(PO_4)_2}]_\mathrm{P,E} = C_0 \tag{5-53}$$

where the subscript P denotes the precipitate.

If the concentration of the buffer, C_0, is much greater than the initial concentration of Cu(II), that is, $C_0 \gg [\mathrm{Cu^{2+}}]_0$, the presence of the insoluble $Cu_3(PO_4)_2$ does not significantly alter the concentrations of the other phosphate species. Then, the concentration of PO_4^{3-} at equilibrium is determined by the buffer concentration and pH and denoted as $P_\mathrm{E}(C_0\,, \mathrm{pH})$. If the system is saturated with $Cu_3(PO_4)_2$, the concentration of the free Cu(II), $[\mathrm{Cu^{2+}}]_\mathrm{S}$, is determined by the solubility product constant, K'_sp, and the concentration of PO_4^{3-}. Accordingly, eq (5-41) can be expressed in terms of K'_sp and $P_\mathrm{E}(C_0, \mathrm{pH})$.

$$K_\mathrm{d}{}^\mathrm{c} = \left(\frac{I_\mathrm{R}}{I_\mathrm{S}} - 1\right)\sqrt[3]{\frac{K'_\mathrm{sp}}{P_\mathrm{E}^2(C_0, \mathrm{pH})}} \tag{5-54}$$

where the subscript S denotes that the system is saturated with $Cu_3(PO_4)_2$. In the phosphate buffer, $[\mathrm{Cu^{2+}}]_\mathrm{S}$ is a function of the concentration of the buffer, C_0. Therefore, the measurable dissociation constant range also depends on the concentration of the buffer. At a pH of 7.4, approximately 2×10^{-9} M and 2×10^{-7} M free Cu(II) ions are present at the saturation point in 1 M and 1 mM phosphate buffer, respectively.[146] Thus, a dissociation constant between 10^{-10} and 10^{-6} M would be within the measurable range. We suspect that our approach is more useful to determine the conditional dissociation constant of a Cu(II)–peptide complex with a stoichiometry of 1:1, particularly if the dissociation constant is in a nanomolar range.

5.7 SUMMARY

Using simple CW-ESR techniques, we have compared the conditional dissociation constants of several Cu(II) complexes at pH 7.4. In NEM buffer system, the double integrals of the CW-ESR spectra of a ligand mixed with Cu(II) at different molar ratios provide critical information about the Cu(II)-binding affinity of the ligand in question and the binding stoichiometry. The method employed herein is particularly, albeit not exclusively, applicable to the case where the dissociation constant ranges between 10^{-7} and 10^{-5} M, and the binding stoichiometry is 1:1. Nevertheless, in the case of the formation of both a binary complex and a ternary complex, the two dissociation constants may be determined provided that the molar ratio of the two types of complexes at the saturation point is figured out. Our approach would be more precise and applicable to more Cu(II) complexes if another buffer system such as phosphate buffer were used.

5.8 ACKNOWLEDGMENT

This work was supported by a National Science Foundation grant (MCB 0842956).

6.0 OVERVIEW OF MAJOR ACHIEVEMENTS

The Aβ peptide is a naturally occurring peptide with 39–43 amino acid residues. The aggregation process of the peptide is deeply associated with the onset of Alzheimer's disease as the intermediates in the process are believed to play a critical role in the pathogenesis of the disease. The coordination of Cu(II) to the peptide helps stabilize the presumably toxic intermediates or change the morphology of aggregates. Figure 6-1 shows the microscopy images of in vitro Aβ aggregates formed at four different Cu(II) concentrations.[113] As the concentration of Cu(II) increases, amorphous aggregates become more dominant over fibrils. In this context, precise atomic-level information about the interaction between the peptide and Cu(II) may be useful to further understand fundamental aspects of the disease.

First, we have confirmed that all of the three histidine residues in Aβ(1–16) coordinate to Cu(II) using pulsed ESR. The interaction between Cu(II) and the three histidine residues, His6, His13, and His14 in the Aβ peptide has been one of the most intriguing questions. In order to assess the Cu(II) coordination of each histidine in Aβ(1–16), which has essentially the same hisitidine coordination as Aβ(1–40) and Aβ(1–42), we have introduced Aβ(1–16) analogues, in each of which a selected histidine residue is isotopically enriched with ^{15}N. ESEEM and HYSCORE spectroscopy detect the spin interaction between Cu(II) and any coordinating histidine imidazole.

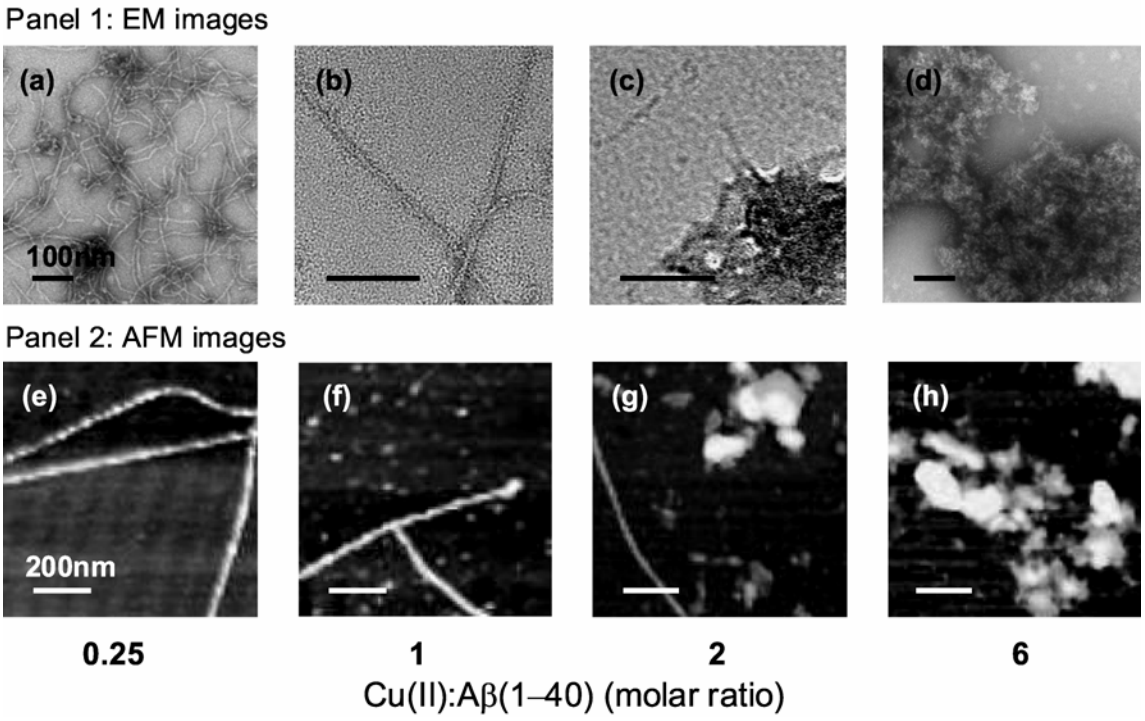

Figure 6-1. Electron microscopy images and atomic force microscopy images of Aβ aggregates formed at different Cu(II) concentrations. As the concentration of Cu(II) increases, amorphous aggregates become more dominant over fibrils.[113]

The ^{15}N nucleus has a spin of 1/2 while ^{14}N, the most abundant nitrogen isotope, is a spin-1 nucleus. Thus, an ^{15}N-labeled analogue should give a spectrum distinguishable from that of the natural Aβ peptide if Cu(II) is coordinated by the ^{15}N-labeled histidine residue. As shown in Figure 2-6, each of the three ^{15}N-labeled analogues has a new set of cross-peaks in the HYSCORE spectrum, which indicates that all of the three histidine residues coordinate to Cu(II).

We have also revealed that the simultaneous Cu(II)-coordination by the two imidazole groups in the His13–His14 dyad of Aβ(1–16) is significant at physiological pH. In fact, there exist at least two different Cu(II)-coordination environments at physiological pH suggested by CW-ESR spectroscopy as shown in Figure 3-1. Thus, the results explained above only show the average representation of Cu(II) coordination rather than the information about each component. In order to selectively examine the major component at physiological pH, we have chosen a magnetic field where only the major component contributes to the ESR signal. The ESEEM spectra of the natural and ^{15}N-labeled versions reveal that in the major component, the contribution of His13 to the Cu(II) coordination through the imidazole ring is substantially lower than that of either His6 or His14. Based on the consensus that two histidine residues simultaneously coordinate to Cu(II) in the major component, we have suggested that the major component is made up of three subcomponents: Subcomponents IA (His6–His13), IB (His6–His14), and IC (His13–His14). Figure 6-2 illustrates that Subcomponent IA, IB, and IC account for approximately 20%, 40%, and 20% of the major component, respectively.

More intriguingly, the simultaneous coordination by His13 and His14 is likely to be linked to the formation of amorphous aggregates, which are believed to be more toxic than fibrils.

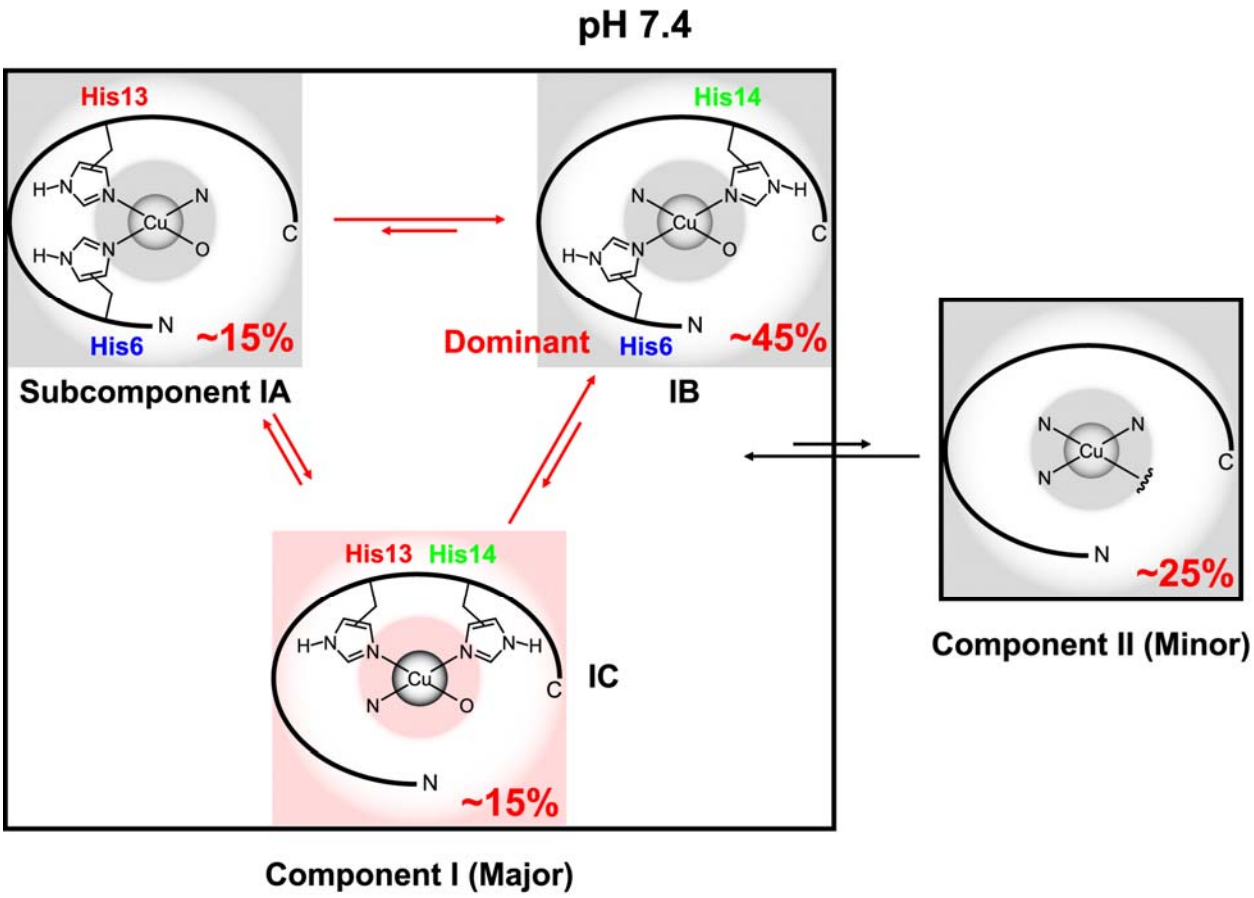

Figure 6-2. Cu(II) binding modes of Aβ(1–16) at physiological pH suggested by ESR spectroscopy. At pH 7.4, Components I and II account for approximately 75% and 25% of the Cu(II)–Aβ(1–16) complex, respectively. Component I is in turn composed of three subcomponents, Subcomponents IA, IB, and IC, in each of which the imidazole rings from two different histidine residues equatorially coordinate to Cu(II) at the same time. Subcomponents IA, IB, and IC explain approximately 15%, 45%, and 15% of the overall Cu(II) complex. In fact, the presence of Subcomponent IC has been underappreciated.

As illustrated in Figure 3-8, the ratio of fibrils to amorphous aggregates is significantly affected by the secondary structures, which are dependent on the Cu(II)-coordinating histidine residues. Through our approach, precise and useful information about the Cu(II) coordination in Aβ(1–16) at physiological pH is obtained without any side-chain modification, amino acid replacement, or pH change, each of which might lead to alteraction in the peptide structure or the coordination environment.

In addition to the research work explained above, we have helped other researchers by providing meaningful ESR data. The published and submitted papers are listed below.

List of Papers

1. Shin, B.; Saxena, S., Direct Evidence That All Three Histidine Residues Coordinate to Cu(II) in Amyloid-β_{1-16}. *Biochemistry* **2008**, *47*, 9117–9123.

2. Walczak, M. A. A.; Shin, B.; Wipf, P.; Saxena, S., An Electron Spin Resonance Analysis of the Mechanism of Pericyclic Reactions of Bicyclobutanes. *Org. Biomol. Chem.* **2009**, *7*, 2363–2366.

3. Jun, S.; Gillespie, J.; Shin, B.; Saxena, S., The Second Copper-Binding Site in a Proton-Rich Environment Interferes with the Aggregation of Amyloid-β_{1-40} into Amyloid Fibrils. *Biochemistry* **2009**, *48*, 10724–10732.

4. Shin, B.; Saxena, S., Substantial Contribution of the Two Imidazole Rings of the His13–His14 Dyad to Cu(II) Binding in Amyloid-β(1–16) at Physiological pH and Its Significance. *J. Phys. Chem. A* **2011**, *115*, available at:

http://pubs.acs.org/doi/abs/10.1021/jp200379m (As soon As Publishable).

5. Shin, B.; Saxena, S., Insight into Potential Cu(II)-Binding Motifs in the Four Pseudorepeats of Tau Protein. submitted to *J. Phys. Chem. B*.

APPENDIX A

SPIN–ORBIT COUPLING AND g-TENSOR ANISOTROPY

The spin Hamiltonian operator that describes the electron Zeeman interaction is principally made up of the terms for the interaction between the electron spin angular momentum and the external magnetic field, the interaction between the orbital angular momentum and the external magnetic field, and the spin–orbit coupling, respectively.

$$\hat{\mathcal{H}}_{\mathrm{ez}} = g_e\beta_e\mathbf{B}_0\cdot\hat{\mathbf{S}} + \beta_e\mathbf{B}_0\cdot\hat{\mathbf{L}} + \lambda\hat{\mathbf{S}}\cdot\hat{\mathbf{L}} \tag{A-1}$$

The spin–orbit coupling causes the spin and orbital wavefunctions to be modified. Using the first-order perturbation theory, one can obtain the new wavefunctions, which are given by:[11]

$$|\psi^{\pm}\rangle = N|\psi_0\rangle + \frac{1}{\sqrt{1-N^2}}\sum_{n=1}\frac{\langle\psi_n|\lambda\hat{\mathbf{S}}\cdot\hat{\mathbf{L}}|\psi_0\rangle}{E_0-E_n}|\psi_n\rangle \quad (m_S = \pm\frac{1}{2}) \tag{A-2}$$

where N is a normalization constant, $|\psi_0\rangle$ is the wavefunction at the ground state, $|\psi_n\rangle$ is the *n*th excited state, and E_0 and E_n are the energy of the ground state and the *n*th excited state, respectively. In eq (A-2), $|\psi^+\rangle$ and $|\psi^-\rangle$ are the wavefunction of the α and β electron spin manifold, respectively. Then, the first term in eq (A-1) becomes the unperturbed Zeeman

Hamiltonian with the new wavefunctions, whereas the last two terms are considered to be a perturbation. Then, eq (A-1) is simply expressed as:

$$\hat{\mathcal{H}}_{\mathrm{ez}} = \hat{\mathcal{H}}^{(0)} + \hat{\mathcal{H}}_{\mathrm{pert}} \tag{A-3}$$

Also, the energy perturbed by the spin–orbit coupling is approximately given by :

$$E_{\mathrm{pert}} = \sum_{n=1} \left(\frac{\langle\psi_0|\beta_e \mathbf{B}_0 \cdot \hat{\mathbf{L}}|\psi_n\rangle\langle\psi_n|\lambda\hat{\mathbf{S}} \cdot \hat{\mathbf{L}}|\psi_0\rangle + \langle\psi_0|\lambda\hat{\mathbf{S}} \cdot \hat{\mathbf{L}}|\psi_n\rangle\langle\psi_n|\beta_e \mathbf{B}_0 \cdot \hat{\mathbf{L}}|\psi_0\rangle}{E_0 - E_n} \right) \tag{A-4}$$

Under the high-field approximation, only the component parallel to the external magnetic field is considered. If the external magnetic field is parallel to the *z*-axis of the molecular frame, eq (A-4) is simplified to:

$$E_{\mathrm{pert}(z)} = \sum_{n=1} \left(\frac{\langle\psi_0|\beta_e B_0 \hat{L}_z|\psi_n\rangle\langle\psi_n|\lambda\hat{S}_z\hat{L}_z|\psi_0\rangle + \langle\psi_0|\lambda\hat{S}_z\hat{L}_z|\psi_n\rangle\langle\psi_n|\beta_e B_0 \hat{L}_z|\psi_0\rangle}{E_0 - E_n} \right) \tag{A-5}$$

For each electron spin manifold, that is, m_S = +1/2 or –1/2, eq (A-5) is further reduced to:

$$E_{\mathrm{pert}(z)} = 2\lambda\beta_e B_0 m_S \sum_{n=1} \left(\frac{\langle\psi_0|\hat{L}_z|\psi_n\rangle\langle\psi_n|\hat{L}_z|\psi_0\rangle}{E_0 - E_n} \right) \tag{A-6}$$

Similarly, if the external magnetic field is parallel to the *x*-axis or *y*-axis of the molecular frame, the perturbation is expressed as:

$$E_{\mathrm{pert}(x)} = 2\lambda\beta_e B_0 m_S \sum_{n=1} \left(\frac{\langle\psi_0|\hat{L}_x|\psi_n\rangle\langle\psi_n|\hat{L}_x|\psi_0\rangle}{E_0 - E_n} \right) \tag{A-7}$$

$$E_{\mathrm{pert}(y)} = 2\lambda\beta_e B_0 m_S \sum_{n=1} \left(\frac{\langle\psi_0|\hat{L}_y|\psi_n\rangle\langle\psi_n|\hat{L}_y|\psi_0\rangle}{E_0 - E_n} \right) \tag{A-8}$$

On the other hand, the Zeeman energy is expressed as:

$$E^{(0)} = g_e \beta_e B_0 m_S \tag{A-9}$$

The total energy is the summation of the two energy terms and can be expressed in terms of a new correction factor, g.

$$E = E^{(0)} + E_{\text{pert}} = g \beta_e B_0 m_S \tag{A-10}$$

As the perturbation term changes with the orientation of the external magnetic field in the molecular frame, the g-value is also perturbed. For each of the *x*-, *y*-, and *z*-direction, the g-value is expressed as:

$$g_{xx} = g_e + 2\lambda \sum_{n=1} \left(\frac{\langle \psi_0 | \hat{L}_x | \psi_n \rangle \langle \psi_n | \hat{L}_x | \psi_0 \rangle}{E_0 - E_n} \right) \tag{A-11}$$

$$g_{yy} = g_e + 2\lambda \sum_{n=1} \left(\frac{\langle \psi_0 | \hat{L}_y | \psi_n \rangle \langle \psi_n | \hat{L}_y | \psi_0 \rangle}{E_0 - E_n} \right) \tag{A-12}$$

$$g_{zz} = g_e + 2\lambda \sum_{n=1} \left(\frac{\langle \psi_0 | \hat{L}_z | \psi_n \rangle \langle \psi_n | \hat{L}_z | \psi_0 \rangle}{E_0 - E_n} \right) \tag{A-13}$$

where the subscripts *xx*, *yy*, and *zz* denote the three components in the principal axis system of the tensor.

Figure A-1 illustrates a simplified geometric interpretation of the g-tensor anisotropy with the p_z orbital. If the external magnetic field is applied along the *z*-axis of the molecular frame, the net magnetic moment associated with the electron spin angular momentum is aligned with the *z*-axis and contributes to the Zeeman energy. On the other hand, the orbital angular momentum has only *x*- and *y*-component because $\hat{L}_z | \psi_{p_z} \rangle$ is 0.

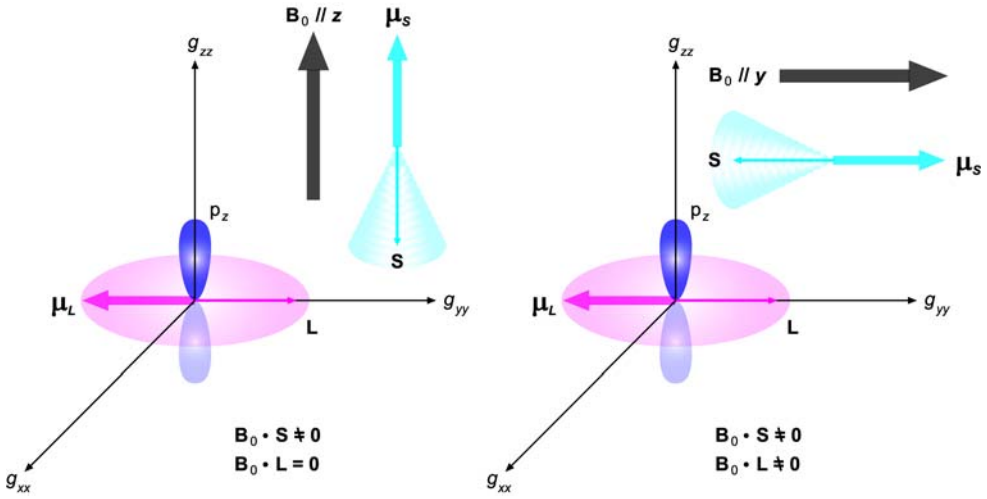

Figure A-1. Orientation of the orbital angular momentum of the p_z orbital and g-tensor anisotropy. If the external magnetic field is applied along the *z*-axis of the molecular frame, the orbital angular momentum contributes nothing to the Zeeman energy. On the other hand, if the external magnetic field is along the *y*-axis, the orbital angular momentum may have a component parallel to the direction of the external magnetic field, which leads to the contribution to the Zeeman energy.

Thus, the magnetic moment associated with the orbital angular momentum, which is perpendicular to the external magnetic field, does not contribute to the Zeeman energy. In the case where the direction of the external magnetic field coincides with the *y*-axis of the molecular frame, the net magnetic moment associated with the spin is aligned with the *y*-axis. Unlike the previous case, the dot product of the magnetic moment associated with the orbital angular momentum and the external magnetic field may be non-zero, which leads to the contribution of the orbital angular momentum to the Zeeman energy.

APPENDIX B

THEORETICAL CALCULATION OF ESEEM SIGNALS USING THE DENSITY MATRIX AND PRODUCT OPERATOR FORMALISM

In pulsed ESR, the ESR signal from the spin system at a specific time point can be mathematically calculated by estimating the net magnetization on the *xy*-plane, which is proportional to the expectation of the spin angular momentum. Since ESR experiments are performed on numerous spin ensembles, the density matrix formalism is generally used to calculate the expectation value. Also, it is often convenient to use a linear combination of product operators to describe the density matrix.

B.1 PRODUCT OPERATORS UNIQUELY USED IN ESEEM SPECTROSCOPY

The 4 × 4 spin Hamiltonian operator that describes a system with S =1/2 and I=1/2 is given by:

$$\hat{\mathcal{H}} = \beta_e \mathbf{B}_0 \cdot \tilde{\mathbf{g}} \cdot \hat{\mathbf{S}} - \beta_n \mathbf{B}_0 \cdot \tilde{\mathbf{g}}_\mathrm{n} \cdot \hat{\mathbf{I}} + \hbar \hat{\mathbf{S}} \cdot \tilde{\mathbf{A}} \cdot \hat{\mathbf{I}} \qquad \text{(B-1)}$$

where β_e is the Bohr magneton, β_n is the nuclear magneton, $\mathbf{B}_0$ is the external magnetic field, $\hbar$ is the reduced Planck constant, $\tilde{\mathbf{g}}$ and $\tilde{\mathbf{g}}_\mathrm{n}$ are the g-tensor of the electron spin and the nuclear

spin, respectively, $\tilde{\mathbf{A}}$ is the electron–nuclear hyperfine tensor, and $\hat{\mathbf{S}}$ and $\hat{\mathbf{I}}$ are the electron and nuclear spin angular momentum operator, respectively. In the lab frame, if the g-tensors of the electron spin and the nuclear spin are assumed to be isotropic, eq (B-1) can be rewritten, under the high-field approximation, as:

$$\hat{\mathcal{H}} = g\beta_e B_0 \hat{S}_z - g_n \beta_n B_0 \hat{I}_z + \hbar A_{zx} \hat{S}_z \hat{I}_x + \hbar A_{zy} \hat{S}_z \hat{I}_y + \hbar A_{zz} \hat{S}_z \hat{I}_z \tag{B-2}$$

where B_0 is the external magnetic field strength, g and g_n are the isotropic g-value for the electron spin and the nuclear spin, respectively, A_{zx}, A_{zy}, and A_{zz} are the three elements of the third row of the hyperfine tensor matrix, $\hat{S}_z$ is the *z*-component of the electron spin angular momentum operator, and $\hat{I}_x$, $\hat{I}_y$, and $\hat{I}_z$ are the *x*-, *y*-, and *z*-component of the nuclear spin angular momentum operator, respectively. While two terms, $A_{zx}\hat{S}_z\hat{I}_x$ and $A_{zy}\hat{S}_z\hat{I}_y$, contain off-diagonal elements, one can consider, for the sake of simplicity, only one of the two terms without losing generality. Then, eq (B-2) is rewritten as:

$$\hat{\mathcal{H}} = \hbar\omega_S \hat{S}_z - \hbar\omega_I \hat{I}_z + \hbar A \hat{S}_z \hat{I}_z + \hbar B \hat{S}_z \hat{I}_x \tag{B-3}$$

where

$$\hbar\omega_S = g\beta_e B_0 \;;\; \hbar\omega_I = g_n \beta B_0 \;;\; A = A_{zz} \;;\; B = \sqrt{A_{zx}^2 + A_{zy}^2} \tag{B-4}$$

In fact, the transformation from eq (B-2) to eq (B-3) is equivalent to the application of the following rotation matrix about the *z*-axis.

$$R_0 = \exp\left(-i\phi \hat{I}_z\right) \tag{B-5}$$

where

$$\phi = \tan^{-1}\left(-\frac{A_{zy}}{A_{zx}}\right) \tag{B-6}$$

In a rotating frame with a microwave frequency of ω_{mw}, the Hamiltonian becomes:

$$\hat{\mathcal{H}} = \hbar\Omega_S\hat{S}_z - \hbar\omega_I\hat{I}_z + \hbar A\hat{S}_z\hat{I}_z + \hbar B\hat{S}_z\hat{I}_x \tag{B-7}$$

where Ω_S is the (angular) frequency offset, that is, $\omega_S - \omega_{mw}$. In order to diagonalize the 4 × 4 Hamiltonian matrix, one can consider its 2 × 2 submatrices.

$$\hat{\mathcal{H}} = \begin{pmatrix} \hat{\mathcal{H}}_\alpha & O \\ O & \hat{\mathcal{H}}_\beta \end{pmatrix} \tag{B-8}$$

In eq (B-8), $\hat{\mathcal{H}}_\alpha$ and $\hat{\mathcal{H}}_\beta$ are the sub-Hamiltonian in the α and β electron spin manifold, respectively, and O is the second-order zero matrix. The two sub-Hamiltonian matrices are expressed as:

$$\hat{\mathcal{H}}_\alpha = \frac{\hbar}{2}\begin{pmatrix} \Omega_S - \omega_I + \frac{A}{2} & \frac{B}{2} \\ \frac{B}{2} & \Omega_S + \omega_I - \frac{A}{2} \end{pmatrix} \; ; \; \hat{\mathcal{H}}_\beta = -\frac{\hbar}{2}\begin{pmatrix} \Omega_S + \omega_I + \frac{A}{2} & \frac{B}{2} \\ \frac{B}{2} & \Omega_S - \omega_I - \frac{A}{2} \end{pmatrix} \tag{B-9}$$

Using appropriate rotation matrices, one can obtain the diagonalized submatrices $\hat{\mathcal{D}}_\alpha$ and $\hat{\mathcal{D}}_\beta$, which are related to $\hat{\mathcal{H}}_\alpha$ and $\hat{\mathcal{H}}_\beta$, respectively, by the following equations.

$$\hat{\mathcal{H}}_\alpha = M_\alpha\hat{\mathcal{D}}_\alpha M_\alpha^\dagger \; ; \; \hat{\mathcal{H}}_\beta = M_\beta\hat{\mathcal{D}}_\beta M_\beta^\dagger \tag{B-10}$$

where

$$\hat{\mathcal{D}}_\alpha = \frac{\hbar}{2}\begin{pmatrix} \Omega_S - \omega_\alpha & 0 \\ 0 & \Omega_S + \omega_\alpha \end{pmatrix} \; ; \; \hat{\mathcal{D}}_\beta = -\frac{\hbar}{2}\begin{pmatrix} \Omega_S + \omega_\beta & 0 \\ 0 & \Omega_S - \omega_\beta \end{pmatrix} \tag{B-11}$$

and

$$M_\alpha = \begin{pmatrix} \cos\frac{\eta_\alpha}{2} & \sin\frac{\eta_\alpha}{2} \\ -\sin\frac{\eta_\alpha}{2} & \cos\frac{\eta_\alpha}{2} \end{pmatrix} \; ; \; M_\beta = \begin{pmatrix} \cos\frac{\eta_\beta}{2} & \sin\frac{\eta_\beta}{2} \\ -\sin\frac{\eta_\beta}{2} & \cos\frac{\eta_\beta}{2} \end{pmatrix} \tag{B-12}$$

The two nuclear eigenfrequencies ω_α and ω_β are expressed in terms of ω_I, A, and B.

$$\omega_\alpha = \sqrt{\left(\omega_I - \frac{A}{2}\right)^2 + \left(\frac{B}{2}\right)^2} \; ; \; \omega_\beta = \sqrt{\left(\omega_I + \frac{A}{2}\right)^2 + \left(\frac{B}{2}\right)^2} \tag{B-13}$$

Also, the angles η_α and η_β are related to ω_I, A, and B by the following equations.

$$\eta_\alpha = \tan^{-1}\left(\frac{B}{2\omega_I - A}\right) \; ; \; \eta_\beta = \tan^{-1}\left(-\frac{B}{2\omega_I + A}\right) \tag{B-14}$$

In fact, M_α and M_β are the rotation matrix for the angle $-\eta_\alpha$ and $-\eta_\beta$, respectively, about the *y*-axis. Thus, they can be expressed in terms of 2 × 2 spin angular momentum operators.

$$M_\alpha = \exp\left(i\eta_\alpha \hat{I}_y\right) \; ; \; M_\beta = \exp\left(i\eta_\beta \hat{I}_y\right) \tag{B-15}$$

If both electron spin manifolds are considered together, the diagonalization of the 4 × 4 Hamiltonian matrix is expressed as:

$$\hat{\mathcal{H}} = R\hat{\mathcal{D}}R^\dagger \tag{B-16}$$

where

$$\hat{\mathcal{D}} = \begin{pmatrix} \hat{\mathcal{D}}_\alpha & O \\ O & \hat{\mathcal{D}}_\beta \end{pmatrix} \; ; \; R = \begin{pmatrix} M_\alpha & O \\ O & M_\beta \end{pmatrix} \tag{B-17}$$

The matrix R can be expressed in terms of 4 × 4 spin angular momentum operators.

$$R = \exp\left[i(\xi \hat{I}_y + 2\eta \hat{S}_z \hat{I}_y)\right] \tag{B-18}$$

where

$$\eta = \frac{\eta_\alpha - \eta_\beta}{2} \;;\; \xi = \frac{\eta_\alpha + \eta_\beta}{2} \tag{B-19}$$

Also, the diagonalized Hamiltonian matrix $\hat{\mathcal{D}}$ is:

$$\hat{\mathcal{D}} = \hbar\Omega_S \hat{S}_z - \hbar\omega_+ \hat{I}_z - 2\hbar\omega_- \hat{S}_z \hat{I}_z \tag{B-20}$$

where

$$\omega_+ = \frac{\omega_\alpha + \omega_\beta}{2} \;;\; \omega_- = \frac{\omega_\alpha - \omega_\beta}{2} \tag{B-21}$$

The matrix elements of the electron spin angular momentum operators used in ESEEM spectroscopy may be different from those used in most cases. As the allowed and forbidden transitions between the α and β electron spin manifold are considered, the product operators for a system with S =1/2 and I=1/2 have the following matrix elements.

$$\hat{S}_x = \frac{1}{2}\begin{pmatrix} O & M \\ M^\dagger & O \end{pmatrix} \;;\; \hat{S}_y = \frac{i}{2}\begin{pmatrix} O & -M \\ M^\dagger & O \end{pmatrix} \;;\; \hat{S}_z = \frac{1}{2}\begin{pmatrix} E_2 & O \\ O & -E_2 \end{pmatrix} \tag{B-22}$$

where the submatrix E_2 is the second-order identity matrix, and M is ${M_\alpha}^\dagger M_\beta$. Accordingly, the rotation matrices about *x*- or *y*-axis have some elements different from those used in most cases.

B.2 ESEEM SIGNAL AS A FUNCTION OF THE DENSITY MATRIX

When the magnetic field induced by microwave pulses is parallel to the *x*-axis, the resultant echo is detected on the *y*-axis. The signal detected is proportional to the *y*-component of the

magnetization, which is in turn proportional to the *y*-component of the electron spin angular momentum. Therefore, the relative signal intensity is simply given by the expectation of $\hat{S}_y$, that is, $\langle \hat{S}_y \rangle$. The expectation can be calculated with the density matrix at the echo observation time, denoted as ρ_{echo}, by the following equation.

$$\langle \hat{S}_y \rangle = \text{Tr}(\rho_{\text{echo}} \hat{S}_y) \tag{B-23}$$

In order to calculate the density matrix at the end of a time interval t, denoted as $\rho(t)$, one needs to consider the time evolution of the spin system, which can be described by:

$$\frac{d\rho(t)}{dt} = \frac{i}{\hbar} [\rho(t), \hat{\mathcal{H}}] \tag{B-24}$$

The general solution of eq (B-24) is given by:

$$\rho(t) = U(t)\, \rho(0)\, U^{\dagger}(t) \tag{B-25}$$

where $\rho(0)$ is the density matrix at the beginning of the period, and

$$U(t) = \exp\left(-\frac{i}{\hbar}\hat{\mathcal{H}}t\right) \tag{B-26}$$

In fact, $U(t)$ is a rotation matrix by which the electron spin is transformed. During a nutation period, the Hamiltonian is approximately given by:

$$\hat{\mathcal{H}}^{\text{nut}} = g\beta_e B_1(\hat{S}_x \cos\omega_{mw} + \hat{S}_y \sin\omega_{mw}) = \hbar\omega_1(\hat{S}_x \cos\omega_{mw} + \hat{S}_y \sin\omega_{mw}) \tag{B-27}$$

where B_1 is the strength of the induced magnetic field, and ω_1 is the corresponding angular frequency, also known as the Rabi frequency. In the rotating frame, eq (B-27) becomes:

$$\hat{\mathcal{H}}^{\text{nut}} = g\beta_e B_1 \hat{S}_x = \hbar\omega_1 \hat{S}_x \tag{B-28}$$

Accordingly, the rotation matrix becomes:

$$U^{\text{nut}}(t_p) = \exp\left(-i\omega_1 \hat{S}_x t_p\right) \tag{B-29}$$

where t_p is the duration of the pulse. The matrix U^{nut} rotates the electron spin by the flip angle θ_{flip}, that is, $\omega_1 t_p$, about the *x*-axis. Plugging eq (B-22) into eq (B-29) yields a more explicit expression for the matrix.

$$U^{\text{nut}}(t_p) = \hat{E}\cos\frac{\omega_1 t_p}{2} - 2i\hat{S}_x \sin\frac{\omega_1 t_p}{2} = \begin{pmatrix} E_2\cos\dfrac{\omega_1 t_p}{2} & -iM\sin\dfrac{\omega_1 t_p}{2} \\ -iM^{\dagger}\sin\dfrac{\omega_1 t_p}{2} & E_2\cos\dfrac{\omega_1 t_p}{2} \end{pmatrix} \tag{B-30}$$

On the other hand, the rotation matrix that accounts for the evolution of the system during the free-precession period t is given by:

$$U^{\text{free}}(t) = \exp\left[-i\left(\omega_S\hat{S}_z - \omega_I\hat{I}_z + A\hat{S}_z\hat{I}_z + B\hat{S}_z\hat{I}_x\right)t\right] \tag{B-31}$$

In the rotating frame, eq (B-31) becomes:

$$U^{\text{free}}(t) = \exp\left[-i\left(\Omega_S\hat{S}_z - \omega_I\hat{I}_z + A\hat{S}_z\hat{I}_z + B\hat{S}_z\hat{I}_x\right)t\right] \tag{B-32}$$

Using the diagonalized Hamiltonian matrix $\hat{\mathcal{D}}$ and the rotation matrix R, which have been defined in eq (B-16), one can rewrite eq (B-32) as:

$$U^{\text{free}}(t) = R\exp\left(-\frac{i}{\hbar}\hat{\mathcal{D}}t\right)R^{\dagger} = R\exp\left[-i\left(\Omega_S\hat{S}_z - \omega_+\hat{I}_z - \omega_-\hat{S}_z\hat{I}_z\right)t\right]R^{\dagger} \tag{B-33}$$

Plugging eq (B-17) into eq (B-33) gives a more explicit expression for the matrix.

$$U^{\text{free}}(t) = \begin{pmatrix} M_\alpha \exp\left(-\frac{i}{\hbar}\hat{\mathcal{D}}_\alpha t\right) M_\alpha^\dagger & O \\ O & M_\beta \exp\left(-\frac{i}{\hbar}\hat{\mathcal{D}}_\beta t\right) M_\beta^\dagger \end{pmatrix} \tag{B-34}$$

The density matrix of the electron spin and operations on it can be expressed in terms of some product operators. The initial density matrix at thermal equilibrium is approximately given by:

$$\rho_{\text{eq}} = \frac{1}{\text{Tr}(\hat{E})}\left(\hat{E} - \frac{\hbar\omega_S}{k_{\text{B}}T}\sigma_{\text{eq}}\right) \tag{B-35}$$

where $\hat{E}$ is the 4 × 4 identity matrix, k_{B} is the Boltzmann constant, T is the absolute temperature, and σ_{eq} is the variable part of the density matrix, which is the *z*-component of the electron spin angular momentum operator, $\hat{S}_z$, at thermal equilibrium. Since the identity operator $\hat{E}$ commutes with any matrix, one can only consider the term containing σ_{eq}. Figure B-1 illustrates changes of the density matrix through a series of time intervals during the two-pulse echo detection sequence. For the *n*th pulse, $\sigma_0(n)$, $\sigma_1(n)$, $\sigma_2(n)$, $\sigma_3(n)$, and $\sigma_4(n)$ are defined as the matrix immediately before the nutation period, immediately after the nutation period, after the transformation by the rotation matrix that diagonalizes the Hamiltonian matrix, after the free precession period, and after the back-transformation, respectively. Also, the following relationship is evident.

$$\rho_i(n) = \frac{1}{\text{Tr}(\hat{E})}\left(\hat{E} - \frac{\hbar\omega_S}{k_{\text{B}}T}\sigma_i(n)\right) \quad (i = 0,\ 1,\ 2,\ 3,\ 4) \tag{B-36}$$

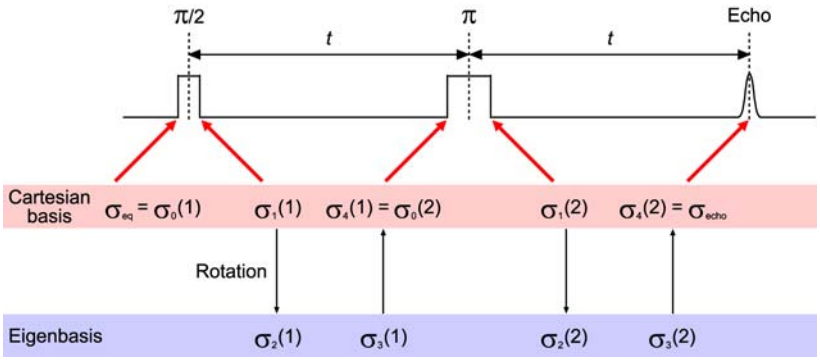

Figure B-1. Changes of the density matrix through a series of time intervals during the two-pulse echo detection sequence. The initial density matrix at thermal equilibrium and the final density matrix at the echo observation time are denoted as σ_{eq} and σ_{echo}, respectively. The density matrix immediately before and after a pulse are denoted as σ_0 and σ_1, respectively. The density matrix in the eigenbasis immediately before and after the free precession are denoted as σ_2 and σ_3, respectively. The numbers 1 and 2 in the parentheses denote the first and second pulse, respectively.

From this point, the variable part of the density matrix, that is, $\sigma_i(n)$, is used in lieu of the whole matrix and simply denoted as the density matrix.

B.3 ESEEM SIGNAL IN THE TWO-PULSE HAHN ECHO SEQUENCE

In the two-pulse sequence for the generation of a Hahn echo, a $\pi/2$ pulse and a π pulse are applied with a separation of t. The two-pulse ESEEM signal detected on the echo observation time is expressed as:

$$V_{2p}(t) = \mathrm{Tr}[\sigma_{\mathrm{echo}}(t)\hat{S}_y] = \mathrm{Tr}[U_{2p}(t)\sigma_{\mathrm{eq}}U_{2p}^{\dagger}(t)\hat{S}_y] \tag{B-37}$$

where

$$U_{2p}(t) = U^{\mathrm{free}}(t)\,U^{\mathrm{nut}}(t_\pi)\,U^{\mathrm{free}}(t)\,U^{\mathrm{nut}}(t_{\pi/2}) \tag{B-38}$$

In eq (B-38), the subscripts $\pi/2$ and π denote the flip angles.

At the thermal equilibrium state, the density matrix is the *z*-component of the electron spin angular momentum operator, which is the initial density matrix before the first pulse. The nutation during the first $\pi/2$ pulse is simply expressed as:

$$\sigma_{\mathrm{eq}} = \sigma_0(1) = \hat{S}_z \xrightarrow{(\pi/2)_x} -\hat{S}_y = \sigma_1(1) \tag{B-39}$$

where the subscript *x* denotes the rotation about the *x*-axis. Then, the transformation by the rotation matrix that diagonalizes the 4 × 4 Hamiltonian matrix is performed.

$$\sigma_1(1) = -\hat{S}_y \xrightarrow{\xi\hat{I}_y} \xrightarrow{2\eta\hat{S}_z\hat{I}_y} -\hat{S}_y\cos\eta + \hat{S}_x\hat{I}_y\sin\eta = \sigma_2(1) \tag{B-40}$$

Next, the evolution during the first free precession period t is expressed in terms of the diagonalized Hamiltonian matrix $\hat{\mathcal{D}}$.

$$\begin{aligned}
&\sigma_2(1) \xrightarrow{\Omega_S t\hat{S}_z} \xrightarrow{-\omega_+ t\hat{I}_z} \xrightarrow{-2\omega_- t\hat{S}_z\hat{I}_z} \\
&-\hat{S}_y\cos\eta\cos\omega_- t\cos\Omega_S t + \hat{S}_x\cos\eta\cos\omega_- t\sin\Omega_S t \\
&+2\hat{S}_x\hat{I}_x\sin\eta\sin\omega_+ t\cos\Omega_S t + 2\hat{S}_y\hat{I}_x\sin\eta\sin\omega_+ t\sin\Omega_S t \\
&+2\hat{S}_x\hat{I}_y\sin\eta\cos\omega_+ t\cos\Omega_S t + 2\hat{S}_y\hat{I}_y\sin\eta\cos\omega_+ t\sin\Omega_S t \\
&-2\hat{S}_x\hat{I}_z\cos\eta\sin\omega_- t\cos\Omega_S t - 2\hat{S}_y\hat{I}_z\cos\eta\sin\omega_- t\sin\Omega_S t = \sigma_3(1)
\end{aligned} \tag{B-41}$$

Finally, the back-transformation by the rotation matrix is performed.

$$\begin{aligned}
&\sigma_3(1) \xrightarrow{-\xi\hat{I}_y} \xrightarrow{-2\eta\hat{S}_z\hat{I}_y} \\
&(-\hat{S}_y\cos\Omega_S t + \hat{S}_x\sin\Omega_S t)(\cos^2\eta\cos\omega_- t + \sin^2\eta\cos\omega_+ t) \\
&+(2\hat{S}_x\hat{I}_x\cos\Omega_S t + 2\hat{S}_y\hat{I}_x\sin\Omega_S t)(\cos\eta\sin\xi\sin\omega_- t + \sin\eta\cos\xi\sin\omega_+ t) \\
&+(2\hat{S}_x\hat{I}_y\cos\Omega_S t + 2\hat{S}_y\hat{I}_y\sin\Omega_S t)(\sin\eta\cos\eta\cos\omega_+ t - \sin\eta\cos\eta\cos\omega_- t) \\
&+(2\hat{S}_x\hat{I}_z\cos\Omega_S t + 2\hat{S}_y\hat{I}_z\sin\Omega_S t)(\sin\eta\sin\xi\sin\omega_+ t - \cos\eta\cos\xi\sin\omega_- t) = \sigma_4(1)
\end{aligned} \tag{B-42}$$

Similarly, for the second pulse, a π pulse, the final density matrix is obtained as follows:

$$\begin{aligned}
&\sigma_4(1) = \sigma_0(2) \xrightarrow{(\pi)_x} \sigma_1(2) \xrightarrow{\xi\hat{I}_y} \xrightarrow{2\eta\hat{S}_z\hat{I}_y} \sigma_2(2) \xrightarrow{\Omega_S t\hat{S}_z} \xrightarrow{-\omega_+ t\hat{I}_z} \xrightarrow{-2\omega_- t\hat{S}_z\hat{I}_z} \\
&\sigma_3(2) \xrightarrow{-\xi\hat{I}_y} \xrightarrow{-2\eta\hat{S}_z\hat{I}_y} \hat{S}_y[1 - 2\sin^2\eta\cos^2\eta(\cos\omega_+ t - \cos\omega_- t)^2] \\
&+2\hat{S}_x\hat{I}_x[2\sin\eta\cos\eta(\cos\eta\cos\xi\sin\omega_+ t - \sin\eta\sin\xi\sin\omega_- t)(\cos\omega_+ t - \cos\omega_- t)] \\
&+2\hat{S}_x\hat{I}_y[2\sin\eta\cos\eta(\cos^2\eta\cos\omega_+ t + \sin^2\eta\cos\omega_- t)(\cos\omega_+ t - \cos\omega_- t)] \\
&+2\hat{S}_x\hat{I}_z[2\sin\eta\cos\eta(\cos\eta\sin\xi\sin\omega_+ t + \sin\eta\cos\xi\sin\omega_- t)(\cos\omega_+ t - \cos\omega_- t)] = \sigma_4(2) = \sigma_{\text{echo}}
\end{aligned} \tag{B-43}$$

The coefficient of $\hat{S}_y$ in eq (B-43) is the real part of the conventional two-pulse ESEEM signal and denoted as $V_{2p}(t)$, which can be expressed in terms of ω_α and ω_β as follows:

$$
\begin{aligned}
V_{2p}(t) &= 1 - \frac{k}{2}(1 - \cos\omega_\alpha t)(1 - \cos\omega_\beta t) \\
&= 1 - \frac{k}{4}[2 - 2\cos\omega_\alpha t - 2\cos\omega_\beta t + \cos(\omega_\alpha + \omega_\beta)t + \cos(\omega_\alpha - \omega_\beta)t]
\end{aligned}
\tag{B-44}
$$

where k is the modulation depth parameter and given by:

$$
k = 4\sin^2\eta\cos^2\eta = \sin^2 2\eta = \left(\frac{\omega_I B}{\omega_\alpha \omega_\beta}\right)^2 \tag{B-45}
$$

It is straightforward from eq (B-44) that the two-pulse ESEEM signal is made up of the non-oscillating part with an amplitude of $1 - (k/2)$ and the oscillating part with the two fundamental frequencies and their sum and difference. The modulation at either fundamental frequency has an amplitude of $k/2$, while the modulation with the sum or difference frequency has an amplitude of $k/4$ with the inverted phase. In fact, the echo intensity is also affected by relaxation processes that cause an exponential decay characterized by the phase memory time T_{m}. Then, the signal is expressed as:

$$
V_{2p}^{\exp}(t) = \exp\left(-\frac{2t}{T_{\mathrm{m}}}\right) V_{2p}(t) \tag{B-46}
$$

B.4 ESEEM SIGNAL IN THE THREE-PULSE STIMULATED ECHO SEQUENCE

In the three-pulse sequence for the generation of a stimulated echo, three $\pi/2$ pulses are applied. The separation between the second and third pulse, T, is incremented while the separation between the first and second pulse, t, is often fixed. The three-pulse ESEEM signal detected on the echo observation time is expressed as:

$$V_{3p}(t) = \mathrm{Tr}[\sigma_{\mathrm{echo}}(t)\hat{S}_y] = \mathrm{Tr}[U_{3p}(t)\sigma_{\mathrm{eq}}U_{3p}^{\dagger}(t)\hat{S}_y] \tag{B-47}$$

where

$$U_{3p}(t) = U^{\mathrm{free}}(t)\,U^{\mathrm{nut}}(t_{\pi/2})\,U^{\mathrm{free}}(T)\,U^{\mathrm{nut}}(t_{\pi/2})\,U^{\mathrm{free}}(t)\,U^{\mathrm{nut}}(t_{\pi/2}) \tag{B-48}$$

For the first pulse, the evolution of the spin system is essentially the same as in the two-pulse sequence for the generation of a Hahn echo and described by:

$$\begin{aligned}
&\sigma_{\mathrm{eq}} = \sigma_0(1_3) = \hat{S}_z \xrightarrow{(\pi/2)_x} \sigma_1(1_3) \xrightarrow{\xi\hat{I}_y} \xrightarrow{2\eta\hat{S}_z\hat{I}_y} \sigma_2(1_3) \xrightarrow{\Omega_S t\hat{S}_z} \xrightarrow{-\omega_+ t\hat{I}_z} \xrightarrow{-2\omega_- t\hat{S}_z\hat{I}_z} \\
&\sigma_3(1_3) \xrightarrow{-\xi\hat{I}_y} \xrightarrow{-2\eta\hat{S}_z\hat{I}_y} \hat{S}_y[1 - 2\sin^2\eta\cos^2\eta(\cos\omega_+ t - \cos\omega_- t)^2] \\
&+ 2\hat{S}_x\hat{I}_x[2\sin\eta\cos\eta(\cos\eta\cos\xi\sin\omega_+ t - \sin\eta\sin\xi\sin\omega_- t)(\cos\omega_+ t - \cos\omega_- t)] \\
&+ 2\hat{S}_x\hat{I}_y[2\sin\eta\cos\eta(\cos^2\eta\cos\omega_+ t + \sin^2\eta\cos\omega_- t)(\cos\omega_+ t - \cos\omega_- t)] \\
&+ 2\hat{S}_x\hat{I}_z[2\sin\eta\cos\eta(\cos\eta\sin\xi\sin\omega_+ t + \sin\eta\cos\xi\sin\omega_- t)(\cos\omega_+ t - \cos\omega_- t)] = \sigma_4(1_3)
\end{aligned} \tag{B-49}$$

where the subscript 3 denotes that the three-pulse sequence is applied.

The second pulse is another $\pi/2$ pulse, which leads to a number of terms that are not seen in the two-pulse sequence. The evolution is described by:

$$\begin{aligned}
&\sigma_4(1_3) = \sigma_0(2_3) \xrightarrow{(\pi/2)_x} \sigma_1(2_3) \xrightarrow{\xi\hat{I}_y} \xrightarrow{2\eta\hat{S}_z\hat{I}_y} \sigma_2(2_3) \xrightarrow{\Omega_S T\hat{S}_z} \xrightarrow{-\omega_+ T\hat{I}_z} \xrightarrow{-2\omega_- T\hat{S}_z\hat{I}_z} \\
&\sigma_3(2_3) \xrightarrow{-\xi\hat{I}_y} \xrightarrow{-2\eta\hat{S}_z\hat{I}_y} \hat{S}_x A_{x1} + \hat{S}_y A_{y1} + \hat{S}_z A_{z1} + 2\hat{S}_x\hat{I}_x A_{xx} + 2\hat{S}_x\hat{I}_y A_{xy} + 2\hat{S}_x\hat{I}_z A_{xz} \\
&\qquad + 2\hat{S}_y\hat{I}_x A_{yx} + 2\hat{S}_y\hat{I}_y A_{yy} + 2\hat{S}_y\hat{I}_z A_{yz} + 2\hat{S}_z\hat{I}_x A_{zx} + 2\hat{S}_z\hat{I}_y A_{zy} + 2\hat{S}_z\hat{I}_z A_{zz} \\
&\qquad + \hat{I}_x A_{1x} + \hat{I}_y A_{1y} + \hat{I}_z A_{1z} = \sigma_4(2_3)
\end{aligned} \tag{B-50}$$

where $A_{mn}\,(m = x,\ y,\ z,\ 1\ ;\ \ n = x,\ y,\ z,\ 1)$ is the coefficient of the operator $\hat{S}_m\hat{I}_n$, as $\hat{S}_1$ and $\hat{I}_1$ are the identity operator $\hat{E}$. Especially, the coefficients of $\hat{S}_x$, $\hat{S}_y$, and $\hat{S}_z$ are:

$$
\begin{aligned}
A_{x1} = {} & (\sin^2\eta\cos\omega_+t + \cos^2\eta\cos\omega_-t)(\sin^2\eta\cos\omega_+T + \cos^2\eta\cos\omega_-T)\sin\Omega_St\cos\Omega_ST \\
& + [\sin^2\eta\cos^2\eta(\cos\omega_+t - \cos\omega_-t)(\cos\omega_+T - \cos\omega_-T) \\
& - \sin^2\eta\sin\omega_+t\sin\omega_+T - \cos^2\eta\sin\omega_-t\sin\omega_-T]\cos\Omega_St\sin\Omega_ST
\end{aligned}
\tag{B-51}
$$

$$
\begin{aligned}
A_{y1} = {} & (\sin^2\eta\cos\omega_+t + \cos^2\eta\cos\omega_-t)(\sin^2\eta\cos\omega_+T + \cos^2\eta\cos\omega_-T)\sin\Omega_St\sin\Omega_ST \\
& - [\sin^2\eta\cos^2\eta(\cos\omega_+t - \cos\omega_-t)(\cos\omega_+T - \cos\omega_-T) \\
& - \sin^2\eta\sin\omega_+t\sin\omega_+T - \cos^2\eta\sin\omega_-t\sin\omega_-T]\cos\Omega_St\cos\Omega_ST
\end{aligned}
\tag{B-52}
$$

$$
A_{z1} = -(\sin^2\eta\cos\omega_+t + \cos^2\eta\cos\omega_-t)\cos\Omega_St \tag{B-53}
$$

For the third $\pi/2$ pulse, the final density matrix is obtained as follows:

$$
\begin{aligned}
& \sigma_4(2_3) = \sigma_0(3_3) \xrightarrow{(\pi/2)_x} \sigma_1(3_3) \xrightarrow{\xi\hat{I}_y} \xrightarrow{2\eta\hat{S}_z\hat{I}_y} \sigma_2(3_3) \xrightarrow{\Omega_St\hat{S}_z} \xrightarrow{-\omega_+t\hat{I}_z} \xrightarrow{-2\omega_-t\hat{S}_z\hat{I}_z} \\
& \sigma_3(3_3) \xrightarrow{-\xi\hat{I}_y} \xrightarrow{-2\eta\hat{S}_z\hat{I}_y} \hat{S}_xB_{x1} + \hat{S}_yB_{y1} + \hat{S}_zB_{z1} + 2\hat{S}_x\hat{I}_xB_{xx} + 2\hat{S}_x\hat{I}_yB_{xy} + 2\hat{S}_x\hat{I}_zB_{xz} \\
& \qquad + 2\hat{S}_y\hat{I}_xB_{yx} + 2\hat{S}_y\hat{I}_yB_{yy} + 2\hat{S}_y\hat{I}_zB_{yz} + 2\hat{S}_z\hat{I}_xB_{zx} + 2\hat{S}_z\hat{I}_yB_{zy} + 2\hat{S}_z\hat{I}_zB_{zz} \\
& \qquad + \hat{I}_xB_{1x} + \hat{I}_yB_{1y} + \hat{I}_zB_{1z} = \sigma_4(3_3) = \sigma_{\text{echo}}
\end{aligned}
\tag{B-54}
$$

where B_{mn} $(m = x,\ y,\ z,\ 1\ ;\ \ n = x,\ y,\ z,\ 1)$ is the coefficient of the operator $\hat{S}_m\hat{I}_n$, used in the same fashion as in eq (B-50). Especially, the coefficients of $\hat{S}_x$, $\hat{S}_y$, and $\hat{S}_z$ are:

$$
\begin{aligned}
B_{x1} = {} & \{\sin^2\eta\cos^2\eta\,[2\sin\omega_+t\sin\omega_-t\sin\omega_+T\sin\omega_-T \\
& - \sin\omega_+t\cos\omega_-t\sin\omega_+T\cos\omega_-T - \cos\omega_+t\sin\omega_-t\cos\omega_+T\sin\omega_-T \\
& + \sin\omega_+t(2\cos\omega_+t - \cos\omega_-t)\sin\omega_+T\cos\omega_-T + \sin\omega_-t(2\cos\omega_-t - \cos\omega_+t)\cos\omega_+T\sin\omega_-T \\
& + 2(\cos\omega_+t\cos\omega_-t - \cos^2\omega_+t - \cos^2\omega_-t + 1)\cos\omega_+T\cos\omega_-T] \\
& + (\sin^4\eta\sin^2\omega_+t + \cos^4\eta\sin^2\omega_-t) - (\sin^2\eta\cos\omega_+t + \cos^2\eta\cos\omega_-t)^2\}\,\mathbf{\sin\Omega_St\cos\Omega_St} \\
& + \{(\sin^2\eta\cos\omega_+t + \cos^2\eta\cos\omega_-t)^2(\sin^2\eta\cos\omega_+T + \cos^2\eta\cos\omega_-T) \\
& - (\sin^2\eta\sin^2\omega_+t\cos\omega_+T + \cos^2\eta\sin^2\omega_-t\cos\omega_-T) \\
& + \sin^2\eta\cos^2\eta\,[(\cos\omega_+t - \cos\omega_-t)^2(\cos^2\eta\cos\omega_+T + \sin^2\eta\cos\omega_-T) \\
& - 2(\cos\omega_+t - \cos\omega_-t)(\sin\omega_+t\sin\omega_+T - \sin\omega_-t\sin\omega_-T)]\}\,\mathbf{\sin\Omega_St\cos\Omega_St\cos\Omega_ST} \\
& + \{(\sin^2\eta\cos\omega_+t + \cos^2\eta\cos\omega_-t)[\sin^2\eta\cos^2\eta(\cos\omega_+t - \cos\omega_-t)(\cos\omega_+T - \cos\omega_-T) \\
& - \sin^2\eta\sin\omega_+t\sin\omega_+T - \cos^2\eta\sin\omega_-t\sin\omega_-T]\}\,\mathbf{(\cos^2\Omega_St - \sin^2\Omega_St)\sin\Omega_ST}
\end{aligned}
\tag{B-55}
$$

$$
\begin{aligned}
B_{y1} = &\{ \sin^2\eta\cos^2\eta\,[2\sin\omega_+t\sin\omega_-t\sin\omega_+T\sin\omega_-T \\
&-\sin\omega_+t\cos\omega_-t\sin\omega_+T\cos\omega_-T-\cos\omega_+t\sin\omega_-t\cos\omega_+T\sin\omega_-T \\
&+\sin\omega_+t(2\cos\omega_+t-\cos\omega_-t)\sin\omega_+T\cos\omega_-T+\sin\omega_-t(2\cos\omega_-t-\cos\omega_+t)\cos\omega_+T\sin\omega_-T \\
&+2(\cos\omega_+t\cos\omega_-t-\cos^2\omega_+t-\cos^2\omega_-t+1)\cos\omega_+T\cos\omega_-T] \\
&+(\sin^4\eta\sin^2\omega_+t+\cos^4\eta\sin^2\omega_-t)\}\,\mathbf{\sin^2\Omega_S t}+\{(\sin^2\eta\cos\omega_+t+\cos^2\eta\cos\omega_-t)^2\}\,\mathbf{\cos^2\Omega_S t} \\
&+\{(\sin^2\eta\cos\omega_+t+\cos^2\eta\cos\omega_-t)^2(\sin^2\eta\cos\omega_+T+\cos^2\eta\cos\omega_-T)\}\,\mathbf{\sin^2\Omega_S t\cos\Omega_S T} \\
&+\{(\sin^2\eta\sin^2\omega_+t\cos\omega_+T+\cos^2\eta\sin^2\omega_-t\cos\omega_-T) \\
&-\sin^2\eta\cos^2\eta\,[(\cos\omega_+t-\cos\omega_-t)^2(\cos^2\eta\cos\omega_+T+\sin^2\eta\cos\omega_-T) \\
&-2(\cos\omega_+t-\cos\omega_-t)(\sin\omega_+t\sin\omega_+T-\sin\omega_-t\sin\omega_-T)]\}\,\mathbf{\cos^2\Omega_S t\cos\Omega_S T} \\
&+\{(\sin^2\eta\cos\omega_+t+\cos^2\eta\cos\omega_-t)[\sin^2\eta\cos^2\eta(\cos\omega_+t-\cos\omega_-t)(\cos\omega_+T-\cos\omega_-T) \\
&-\sin^2\eta\sin\omega_+t\sin\omega_+T-\cos^2\eta\sin\omega_-t\sin\omega_-T]\}\,\mathbf{2\sin\Omega_S t\cos\Omega_S t\sin\Omega_S T}
\end{aligned}
\tag{B-56}
$$

$$
\begin{aligned}
B_{z1} = &\{(\sin^2\eta\cos\omega_+t+\cos^2\eta\cos\omega_-t)(\sin^2\eta\cos\omega_+T+\cos^2\eta\cos\omega_-T)\}\,\mathbf{\sin\Omega_S t\sin\Omega_S T} \\
&+\{\sin^2\eta\sin\omega_+t\sin\omega_+T+\cos^2\eta\sin\omega_-t\sin\omega_-T \\
&-\sin^2\eta\cos^2\eta(\cos\omega_+t-\cos\omega_-t)(\cos\omega_+T-\cos\omega_-T)\}\,\mathbf{\cos\Omega_S t\cos\Omega_S T}
\end{aligned}
\tag{B-57}
$$

In eqs (B-55), (B-56), and (B-57), the sine and cosine functions of $\Omega_S t$ and $\Omega_S T$ and their products can be evaluated by the integration over a range of Ω_S, weighted by a distribution function. Since the distribution of the frequency offset is expressed by an even function such as a sinc function or a Gaussian function within the excitation bandwidth, the weighted averages of $\sin\Omega_S t\cos\Omega_S t$, $\sin\Omega_S t\cos\Omega_S t\cos\Omega_S T$, $\sin^2\Omega_S t\cos\Omega_S T$, and $\cos^2\Omega_S t\cos\Omega_S T$ are 0. Therefore, the coefficient of $\hat{S}_x$ becomes 0.

If the pulse separation T is much longer than the maximum pulse length, the weighted averages of $\cos\Omega_S T$, $\cos\Omega_S(T\pm t)$, and $\cos\Omega_S(T\pm 2t)$ tend to 0. More detailed calculations are provided in Appendix C. Then, the coefficient of $\hat{S}_z$ also becomes 0, and the coefficient of $\hat{S}_y$ is simplified to:

$$
\begin{aligned}
B_{y1} = \{ & \sin^2\eta\cos^2\eta\,[2\sin\omega_+t\sin\omega_-t\sin\omega_+T\sin\omega_-T \\
& - \sin\omega_+t\cos\omega_-t\sin\omega_+T\cos\omega_-T - \cos\omega_+t\sin\omega_-t\cos\omega_+T\sin\omega_-T \\
& + \sin\omega_+t(2\cos\omega_+t - \cos\omega_-t)\sin\omega_+T\cos\omega_-T + \sin\omega_-t(2\cos\omega_-t - \cos\omega_+t)\cos\omega_+T\sin\omega_-T \\
& + 2(\cos\omega_+t\cos\omega_-t - \cos^2\omega_+t - \cos^2\omega_-t + 1)\cos\omega_+T\cos\omega_-T] \\
& + (\sin^4\eta\sin^2\omega_+t + \cos^4\eta\sin^2\omega_-t)\}\,\mathbf{\sin^2\Omega_S t} + \{(\sin^2\eta\cos\omega_+t + \cos^2\eta\cos\omega_-t)^2\}\,\mathbf{\cos^2\Omega_S t}
\end{aligned}
\tag{B-58}
$$

Using trigonometric identities, one can rewrite eq (B-58) as:

$$
\begin{aligned}
B_{y1} = & \frac{1}{2}\{(\sin^2\eta\cos\omega_+t + \cos^2\eta\cos\omega_-t)^2 + (\sin^4\eta\sin^2\omega_+t + \cos^4\eta\sin^2\omega_-t) \\
& + \sin^2\eta\cos^2\eta\,[2\sin\omega_+t\sin\omega_-t\sin\omega_+T\sin\omega_-T \\
& - \sin\omega_+t\cos\omega_-t\sin\omega_+T\cos\omega_-T - \cos\omega_+t\sin\omega_-t\cos\omega_+T\sin\omega_-T \\
& + \sin\omega_+t(2\cos\omega_+t - \cos\omega_-t)\sin\omega_+T\cos\omega_-T + \sin\omega_-t(2\cos\omega_-t - \cos\omega_+t)\cos\omega_+T\sin\omega_-T \\
& + 2(\cos\omega_+t\cos\omega_-t - \cos^2\omega_+t - \cos^2\omega_-t + 1)\cos\omega_+T\cos\omega_-T]\} \\
& + \frac{1}{2}\{(\sin^2\eta\cos\omega_+t + \cos^2\eta\cos\omega_-t)^2 - (\sin^4\eta\sin^2\omega_+t + \cos^4\eta\sin^2\omega_-t) \\
& - \sin^2\eta\cos^2\eta\,[2\sin\omega_+t\sin\omega_-t\sin\omega_+T\sin\omega_-T \\
& - \sin\omega_+t\cos\omega_-t\sin\omega_+T\cos\omega_-T - \cos\omega_+t\sin\omega_-t\cos\omega_+T\sin\omega_-T \\
& + \sin\omega_+t(2\cos\omega_+t - \cos\omega_-t)\sin\omega_+T\cos\omega_-T + \sin\omega_-t(2\cos\omega_-t - \cos\omega_+t)\cos\omega_+T\sin\omega_-T \\
& + 2(\cos\omega_+t\cos\omega_-t - \cos^2\omega_+t - \cos^2\omega_-t + 1)\cos\omega_+T\cos\omega_-T]\}\,\mathbf{\cos 2\Omega_S t} \\
= & \frac{1}{2}\{V_{3p}(t,\,T)\} + \frac{1}{2}\{V_{3p}^{\mathrm{v}}(t,\,T)\}\,\mathbf{\cos 2\Omega_S t}
\end{aligned}
\tag{B-59}
$$

The terms in the first pair of braces, denoted as $V_{3p}(t,\,T)$, contribute to the normal stimulated echo, whereas those in the second pair of braces, denoted as $V_{3p}^{\mathrm{v}}(t,\,T)$, are the components of the virtual echo, which would form a real echo at the time $T - t$ after the second pulse.[147] The two parts can be expressed in terms of ω_α and ω_β as follows:

$$
V_{3p}(t,\,T) = 1 - \frac{k}{4}\{(1-\cos\omega_\alpha t)[1-\cos\omega_\beta(T+t)] + (1-\cos\omega_\beta t)[1-\cos\omega_\alpha(T+t)]\}
\tag{B-60}
$$

$$
\begin{aligned}
V_{3p}^{\mathrm{v}}(t,\,T) = & \frac{k}{2}(1-\cos\omega_\alpha t\cos\omega_\beta t) + \cos\omega_\alpha t\cos\omega_\beta t + (\cos^2\eta - \sin^2\eta)\sin\omega_\alpha t\sin\omega_\beta t \\
& - \frac{k}{4}\{(1-\cos\omega_\alpha t)[1+\cos\omega_\beta(T+t)] + (1-\cos\omega_\beta t)[1+\cos\omega_\alpha(T+t)]\}
\end{aligned}
$$

(B-61)

where k is the modulation depth parameter defined in eq (B-45).

When the pulse separation t is much longer than the maximum pulse length, the weighted average of $\cos 2\Omega_S t$, denoted as $\langle \cos 2\Omega_S t \rangle$, tends to 0, which means that there is practically no effect of the virtual echo. However, if the pulse separation t is relatively short or a long, selective pulse is applied, the virtual echo may not be negligible. In the extreme case of $\langle \cos 2\Omega_S t \rangle$ tending to 1, the terms containing $\cos^2 \Omega_S t$ in eq (B-58) would account for the echo signal as the weighted averages of $\sin^2 \Omega_S t$ and $\cos^2 \Omega_S t$ are expected to be 0 and 1, respectively. Then, the echo would not modulate with the pulse separation T. In reality, $\langle \cos 2\Omega_S t \rangle$ is much less than 1 and often close to 0. Thus, the stimulated echo is usually detected with a modulation depth proportional to $\sin^2 \eta \cos^2 \eta$. Nevertheless, the contribution from the virtual echo might reduce the modulation depth if $\langle \cos 2\Omega_S t \rangle$ is not negligibly small.

Unlike the two-pulse ESEEM signal, the three-pulse ESEEM signal has no modulation at the sum or difference frequency. The amplitude of the modulation at a fundamental frequency depends on the other fundamental frequency as well as the modulation depth parameter k. In a special case where $1 - \cos \omega_\alpha t$ or $1 - \cos \omega_\beta t$ becomes 0, the modulation at a frequency of ω_α or ω_β vanishes.

Another difference from the two-pulse ESEEM signal is relaxation processes. During the interval T, relaxation is dependent primarily on the phase memory time of the nuclear spin, $T_{\mathrm{m}}^{(\mathrm{n})}$, which is usually in the order of the longitudinal relaxation time of the electron spin, T_1.[147] The signal including the relaxation is expressed as:

$$V_{3p}^{\exp}(t, T) = \exp\left(-\frac{2t}{T_{\mathrm{m}}}\right) \exp\left(-\frac{T}{T_{\mathrm{m}}^{(\mathrm{n})}}\right) V_{3p}(t, T) \qquad \text{(B-62)}$$

B.5 HYSCORE SIGNAL IN THE FOUR-PULSE STIMULATED ECHO SEQUENCE

In the four-pulse HYSCORE sequence, a π pulse is inserted between the second and the third $\pi/2$ pulse in the three-pulse stimulated echo sequence. The final density matrix can be calculated in a manner similar to that used in the three-pulse ESEEM sequence. The signal expressed in terms of ω_α and ω_β is given by:

$$V_{4p}(t,\,t_1,\,t_2) = 1 - \frac{k}{4}\Big\{3 - \cos\omega_\alpha t - \cos\omega_\beta t - \sin^2\eta\cos(\omega_\alpha+\omega_\beta)t - \cos^2\eta\cos(\omega_\alpha-\omega_\beta)t$$
$$+ K_\alpha(t)\Big[\cos\omega_\alpha\Big(\frac{t}{2}+t_1\Big) + \cos\omega_\alpha\Big(\frac{t}{2}+t_2\Big)\Big] + K_\beta(t)\Big[\cos\omega_\beta\Big(\frac{t}{2}+t_1\Big) + \cos\omega_\beta\Big(\frac{t}{2}+t_2\Big)\Big]$$
$$- 2\sin\frac{\omega_\alpha}{2}t\sin\frac{\omega_\beta}{2}t\cos^2\eta\Big[\cos\Big(\frac{\omega_\alpha+\omega_\beta}{2}t+\omega_\alpha t_1+\omega_\beta t_2\Big) + \cos\Big(\frac{\omega_\alpha+\omega_\beta}{2}t+\omega_\beta t_1+\omega_\alpha t_2\Big)\Big]$$
$$+ 2\sin\frac{\omega_\alpha}{2}t\sin\frac{\omega_\beta}{2}t\sin^2\eta\Big[\cos\Big(\frac{\omega_\alpha-\omega_\beta}{2}t+\omega_\alpha t_1-\omega_\beta t_2\Big) + \cos\Big(\frac{\omega_\beta-\omega_\alpha}{2}t+\omega_\beta t_1-\omega_\alpha t_2\Big)\Big]\Big\} \tag{B-63}$$

where

$$K_\alpha(t) = \cos^2\eta\cos\Big(\omega_\beta - \frac{\omega_\alpha}{2}\Big)t + \sin^2\eta\cos\Big(\omega_\beta + \frac{\omega_\alpha}{2}\Big)t - \cos\frac{\omega_\alpha}{2}t \tag{B-64}$$

$$K_\beta(t) = \cos^2\eta\cos\Big(\omega_\alpha - \frac{\omega_\beta}{2}\Big)t + \sin^2\eta\cos\Big(\omega_\alpha + \frac{\omega_\beta}{2}\Big)t - \cos\frac{\omega_\beta}{2}t \tag{B-65}$$

In eq (B-63), the terms containing a cosine function of $\omega_\alpha t_1 \pm \omega_\beta t_2$ or $\omega_\beta t_1 \pm \omega_\alpha t_2$ account for the appearance of cross-peaks in the two-dimensional Fourier transform of the HYSCORE signal. During the intervals t_1 and t_2, relaxation is dependent primarily on the phase memory time of the nuclear spin, $T_{\mathrm{m}}^{(\mathrm{n})}$, as in the case of the three-pulse sequence.[147] Then, the signal including the relaxation is expressed as:

$$V_{4p}^{\exp}(t,\,t_1,\,t_2) = \exp\left(-\frac{2t}{T_{\mathrm{m}}}\right)\exp\left(-\frac{t_1+t_2}{T_{\mathrm{m}}^{(\mathrm{n})}}\right)V_{4p}(t,\,t_1,\,t_2) \tag{B-66}$$

B.6 ESEEM SIGNAL IN THE CONVENTIONAL DQC SEQUENCE

The conventional double quantum coherence (DQC) pulse sequence is made up of six pulses and pulse separations. The sequence is illustrated in Figure B-2. First, the density matrix immediately before the second pulse is obtained in the same manner as in the two-pulse echo detection sequence.

$$\sigma_{\mathrm{eq}} = \sigma_0(1) = \hat{S}_z \xrightarrow{(\pi/2)_x} \sigma_1(1) \xrightarrow{\xi \hat{I}_y} \xrightarrow{2\eta \hat{S}_z \hat{I}_y} \sigma_2(1) \xrightarrow{\Omega_S t_p \hat{S}_z} \xrightarrow{-\omega_+ t_p \hat{I}_z} \xrightarrow{-2\omega_- t_p \hat{S}_z \hat{I}_z} \rightarrow$$
$$\sigma_3(1) \xrightarrow{-\xi \hat{I}_y} \xrightarrow{-2\eta \hat{S}_z \hat{I}_y} (-\hat{S}_y \cos \Omega_S t_p + \hat{S}_x \sin \Omega_S t_p)(\cos^2 \eta \cos \omega_- t_p + \sin^2 \eta \cos \omega_+ t_p)$$
$$+ (2\hat{S}_x \hat{I}_x \cos \Omega_S t_p + 2\hat{S}_y \hat{I}_x \sin \Omega_S t_p)(\cos \eta \sin \xi \sin \omega_- t_p + \sin \eta \cos \xi \sin \omega_+ t_p)$$
$$+ (2\hat{S}_x \hat{I}_y \cos \Omega_S t_p + 2\hat{S}_y \hat{I}_y \sin \Omega_S t_p)(\sin \eta \cos \eta \cos \omega_+ t_p - \sin \eta \cos \eta \cos \omega_- t_p)$$
$$+ (2\hat{S}_x \hat{I}_z \cos \Omega_S t_p + 2\hat{S}_y \hat{I}_z \sin \Omega_S t_p)(\sin \eta \sin \xi \sin \omega_+ t_p - \cos \eta \cos \xi \sin \omega_- t_p) = \sigma_4(1) \tag{B-67}$$

Similarly, for the second pulse, a π pulse, the density matrix after the back-transformation is obtained as follows:

$$\sigma_4(1) = \sigma_0(2) \xrightarrow{(\pi)_x} \sigma_1(2) \xrightarrow{\xi \hat{I}_y} \xrightarrow{2\eta \hat{S}_z \hat{I}_y} \sigma_2(2) \xrightarrow{\Omega_S t_p \hat{S}_z} \xrightarrow{-\omega_+ t_p \hat{I}_z} \xrightarrow{-2\omega_- t_p \hat{S}_z \hat{I}_z} \rightarrow$$
$$\sigma_3(2) \xrightarrow{-\xi \hat{I}_y} \xrightarrow{-2\eta \hat{S}_z \hat{I}_y} \hat{S}_y[1 - 2\sin^2 \eta \cos^2 \eta (\cos \omega_+ t_p - \cos \omega_- t_p)^2]$$
$$+ 2\hat{S}_x \hat{I}_x [2 \sin \eta \cos \eta (\cos \eta \cos \xi \sin \omega_+ t_p - \sin \eta \sin \xi \sin \omega_- t_p)(\cos \omega_+ t_p - \cos \omega_- t_p)]$$
$$+ 2\hat{S}_x \hat{I}_y [2 \sin \eta \cos \eta (\cos^2 \eta \cos \omega_+ t_p + \sin^2 \eta \cos \omega_- t_p)(\cos \omega_+ t_p - \cos \omega_- t_p)]$$
$$+ 2\hat{S}_x \hat{I}_z [2 \sin \eta \cos \eta (\cos \eta \sin \xi \sin \omega_+ t_p + \sin \eta \cos \xi \sin \omega_- t_p)(\cos \omega_+ t_p - \cos \omega_- t_p)] = \sigma_4(2) \tag{B-68}$$

The coefficient of $\hat{S}_y$ in eq (B-68) is the real part of the conventional two-pulse ESEEM signal and denoted as V_y. In the same fashion, the coefficients of $2\hat{S}_x \hat{I}_x$, $2\hat{S}_x \hat{I}_y$, and $2\hat{S}_x \hat{I}_z$ are denoted as V_{xx}, V_{xy}, and V_{xz}, respectively. The coefficients are functions of t_p.

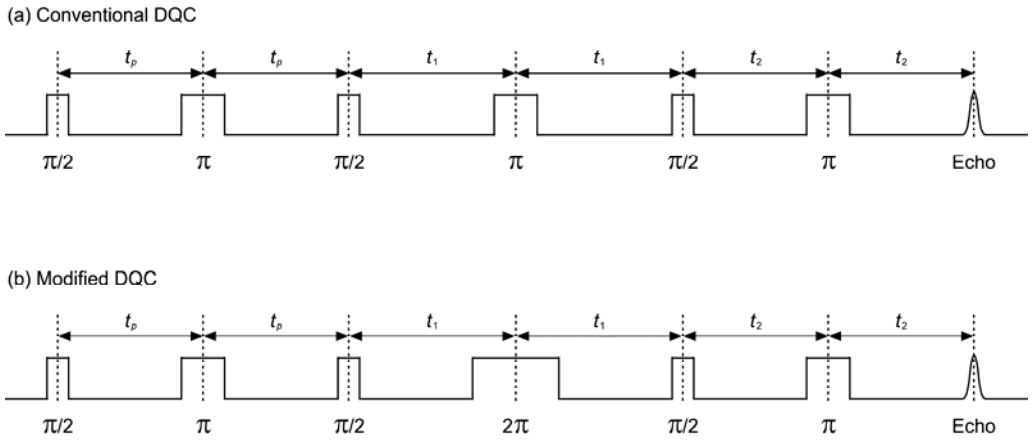

Figure B-2. Conventional and modified DQC pulse sequences. In the modified DQC, the fourth pulse is a 2π pulse instead of a π pulse, which is conventionally used to refocus spins with different frequency offsets. Thus, the echo signal is a function of the frequency offset in the modified DQC.

For the third pulse, another $\pi/2$ pulse, the density matrix immediately before the next pulse is obtained as follows:

$$\begin{aligned}
&\sigma_4(2)=\sigma_0(3)\xrightarrow{(\pi/2)_x}\sigma_1(3)\xrightarrow{\xi\hat{I}_y}\xrightarrow{2\eta\hat{S}_z\hat{I}_y}\sigma_2(3)\xrightarrow{\Omega_S t_1\hat{S}_z}\xrightarrow{-\omega_+ t_1\hat{I}_z}\xrightarrow{-2\omega_- t_1\hat{S}_z\hat{I}_z}\\
&\sigma_3(3)\xrightarrow{-\xi\hat{I}_y}\xrightarrow{-2\eta\hat{S}_z\hat{I}_y}\sigma_4(3)=\hat{S}_zV_y\\
&+(\hat{S}_y\cos\Omega_S t_1-\hat{S}_x\sin\Omega_S t_1)\cdot\\
&\quad[V_{x1}\sin\eta\sin\omega_+ t_1+V_{x2}\cos\eta\sin\omega_- t_1-V_{xy}\sin\eta\cos\eta\cos\omega_+ t_1+V_{xy}\sin\eta\cos\eta\cos\omega_- t_1]\\
&+(2\hat{S}_x\hat{I}_x\cos\Omega_S t_1+2\hat{S}_y\hat{I}_x\sin\Omega_S t_1)\cdot\\
&\quad[V_{x1}\cos\xi\cos\omega_+ t_1+V_{x2}\sin\xi\cos\omega_- t_1+V_{xy}\cos\eta\cos\xi\sin\omega_+ t_1-V_{xy}\sin\eta\sin\xi\sin\omega_- t_1]\\
&-(2\hat{S}_x\hat{I}_y\cos\Omega_S t_1+2\hat{S}_y\hat{I}_y\sin\Omega_S t_1)\cdot\\
&\quad[V_{x1}\cos\eta\sin\omega_+ t_1-V_{x2}\sin\eta\sin\omega_- t_1-V_{xy}\cos^2\eta\cos\omega_+ t_1-V_{xy}\sin^2\eta\cos\omega_- t_1]\\
&+(2\hat{S}_x\hat{I}_z\cos\Omega_S t_1+2\hat{S}_y\hat{I}_z\sin\Omega_S t_1)\cdot\\
&\quad[V_{x1}\sin\xi\cos\omega_+ t_1-V_{x2}\cos\xi\cos\omega_- t_1+V_{xy}\cos\eta\sin\xi\sin\omega_+ t_1+V_{xy}\sin\eta\cos\xi\sin\omega_- t_1]
\end{aligned}\tag{B-69}$$

where

$$\begin{aligned}
V_{x1}&=V_{xx}\cos\xi+V_{xz}\sin\xi\\
&=\sin 2\eta\cos\eta\sin\omega_+ t_p(\cos\omega_+ t_p-\cos\omega_- t_p)
\end{aligned}\tag{B-70}$$

$$\begin{aligned}
V_{x2}&=V_{xx}\sin\xi-V_{xz}\cos\xi\\
&=-\sin 2\eta\sin\eta\sin\omega_- t_p(\cos\omega_+ t_p-\cos\omega_- t_p)
\end{aligned}\tag{B-71}$$

The fourth pulse for the conventional DQC is a π pulse. The density matrix immediately before the next pulse is obtained as follows:

$$\begin{aligned}
&\sigma_4(3)=\sigma_0(4)\xrightarrow{(\pi)_x}\sigma_1(4)\xrightarrow{\xi\hat{I}_y}\xrightarrow{2\eta\hat{S}_z\hat{I}_y}\sigma_2(4)\xrightarrow{\Omega_S t_1\hat{S}_z}\xrightarrow{-\omega_+ t_1\hat{I}_z}\xrightarrow{-2\omega_- t_1\hat{S}_z\hat{I}_z}\\
&\sigma_3(4)\xrightarrow{-\xi\hat{I}_y}\xrightarrow{-2\eta\hat{S}_z\hat{I}_y}\hat{S}_zW_z+\hat{S}_yW_y+2\hat{S}_x\hat{I}_xW_{xx}+2\hat{S}_x\hat{I}_yW_{xy}+2\hat{S}_x\hat{I}_zW_{xz}=\sigma_4(4)
\end{aligned}\tag{B-72}$$

where

$$W_z=-V_y\tag{B-73}$$

$$
\begin{aligned}
W_y = &-\frac{1}{2}V_{xy}\sin 2\eta(\cos 2\eta+1)\cos^2\omega_+t_1 - \frac{1}{2}V_{xy}\sin 2\eta(\cos 2\eta-1)\cos^2\omega_-t_1 \\
&+ V_{xy}\sin 2\eta\cos 2\eta\cos\omega_+t_1\cos\omega_-t_1 \\
&+ V_{x1}\sin\eta(\cos 2\eta+1)\sin\omega_+t_1\cos\omega_+t_1 - V_{x2}\cos\eta(\cos 2\eta-1)\sin\omega_-t_1\cos\omega_-t_1 \\
&- V_{x1}\sin 2\eta\cos\eta\sin\omega_+t_1\cos\omega_-t_1 - V_{x2}\sin 2\eta\sin\eta\sin\omega_-t_1\cos\omega_+t_1
\end{aligned}
\tag{B-74}
$$

$$
\begin{aligned}
W_{xx} = &\, V_{x1}\cos\xi(\cos 2\eta+1)\cos^2\omega_+t_1 - V_{x2}\sin\xi(\cos 2\eta-1)\cos^2\omega_-t_1 \\
&+ (V_{x1}\sin\xi + V_{x2}\cos\xi)\sin 2\eta\sin\omega_+t_1\sin\omega_-t_1 - (V_{x1}\cos\xi - V_{x2}\sin\xi)\cos 2\eta \\
&+ V_{xy}(\cos 2\eta+1)\cos\eta\cos\xi\sin\omega_+t_1\cos\omega_+t_1 + V_{xy}(\cos 2\eta-1)\sin\eta\sin\xi\sin\omega_-t_1\cos\omega_-t_1 \\
&+ V_{xy}\sin 2\eta\sin\eta\cos\xi\sin\omega_+t_1\cos\omega_-t_1 - V_{xy}\sin 2\eta\cos\eta\sin\xi\sin\omega_-t_1\cos\omega_+t_1
\end{aligned}
\tag{B-75}
$$

$$
\begin{aligned}
W_{xy} = &\, V_{xy}\cos^2\eta(\cos 2\eta+1)\cos^2\omega_+t_1 - V_{xy}\sin^2\eta(\cos 2\eta-1)\cos^2\omega_-t_1 \\
&+ V_{xy}\sin^2 2\eta\cos\omega_+t_1\cos\omega_-t_1 - V_{xy} \\
&- V_{x1}\cos\eta(\cos 2\eta+1)\sin\omega_+t_1\cos\omega_+t_1 - V_{x2}\sin\eta(\cos 2\eta-1)\sin\omega_-t_1\cos\omega_-t_1 \\
&- V_{x1}\sin\eta\sin 2\eta\sin\omega_+t_1\cos\omega_-t_1 + V_{x2}\cos\eta\sin 2\eta\sin\omega_-t_1\cos\omega_+t_1
\end{aligned}
\tag{B-76}
$$

$$
\begin{aligned}
W_{xz} = &\, V_{x1}\sin\xi(\cos 2\eta+1)\cos^2\omega_+t_1 + V_{x2}\cos\xi(\cos 2\eta-1)\cos^2\omega_-t_1 \\
&- (V_{x1}\cos\xi - V_{x2}\sin\xi)\sin 2\eta\sin\omega_+t_1\sin\omega_-t_1 - (V_{x1}\sin\xi + V_{x2}\cos\xi)\cos 2\eta \\
&+ V_{xy}(\cos 2\eta+1)\cos\eta\sin\xi\sin\omega_+t_1\cos\omega_+t_1 - V_{xy}(\cos 2\eta-1)\sin\eta\cos\xi\sin\omega_-t_1\cos\omega_-t_1 \\
&+ V_{xy}\sin 2\eta\sin\eta\sin\xi\sin\omega_+t_1\cos\omega_-t_1 + V_{xy}\sin 2\eta\cos\eta\cos\xi\sin\omega_-t_1\cos\omega_+t_1
\end{aligned}
\tag{B-77}
$$

It is obvious that W_y, W_{xx}, W_{xy}, and W_{xz} are functions of t_p and t_1 as V_{x1}, V_{x2}, and V_{xy} are functions of t_p.

For the fifth pulse, the other $\pi/2$ pulse, the evolution of the system is described by:

$$\sigma_4(4)=\sigma_0(5)\xrightarrow{(\pi/2)_x}\sigma_1(5)\xrightarrow{\xi\hat{I}_y}\xrightarrow{2\eta\hat{S}_z\hat{I}_y}\sigma_2(5)\xrightarrow{\Omega_S t_2\hat{S}_z}\xrightarrow{-\omega_+ t_2\hat{I}_z}\xrightarrow{-2\omega_- t_2\hat{S}_z\hat{I}_z}$$
$$\sigma_3(5)\xrightarrow{-\xi\hat{I}_y}\xrightarrow{-2\eta\hat{S}_z\hat{I}_y}\sigma_4(5)=$$
$$\begin{aligned}
&-V_y[(-\hat{S}_y\cos\Omega_S t_2+\hat{S}_x\sin\Omega_S t_2)(\cos^2\eta\cos\omega_- t_2+\sin^2\eta\cos\omega_+ t_2)\\
&\quad+(2\hat{S}_x\hat{I}_x\cos\Omega_S t_2+2\hat{S}_y\hat{I}_x\sin\Omega_S t_2)(\cos\eta\sin\xi\sin\omega_- t_2+\sin\eta\cos\xi\sin\omega_+ t_2)\\
&\quad+(2\hat{S}_x\hat{I}_y\cos\Omega_S t_2+2\hat{S}_y\hat{I}_y\sin\Omega_S t_2)(\sin\eta\cos\eta\cos\omega_+ t_2-\sin\eta\cos\eta\cos\omega_- t_2)\\
&\quad+(2\hat{S}_x\hat{I}_z\cos\Omega_S t_2+2\hat{S}_y\hat{I}_z\sin\Omega_S t_2)(\sin\eta\sin\xi\sin\omega_+ t_2-\cos\eta\cos\xi\sin\omega_- t_2)]+\hat{S}_z W_y\\
&+(\hat{S}_y\cos\Omega_S t_2-\hat{S}_x\sin\Omega_S t_2)\cdot\\
&\quad[W_{x1}\sin\eta\sin\omega_+ t_2+W_{x2}\cos\eta\sin\omega_- t_2-W_{xy}\sin\eta\cos\eta\cos\omega_+ t_2+W_{xy}\sin\eta\cos\eta\cos\omega_- t_2]\\
&+(2\hat{S}_x\hat{I}_x\cos\Omega_S t_2+2\hat{S}_y\hat{I}_x\sin\Omega_S t_2)\cdot\\
&\quad[W_{x1}\cos\xi\cos\omega_+ t_2+W_{x2}\sin\xi\cos\omega_- t_2+W_{xy}\cos\eta\cos\xi\sin\omega_+ t_2-W_{xy}\sin\eta\sin\xi\sin\omega_- t_2]\\
&-(2\hat{S}_x\hat{I}_y\cos\Omega_S t_2+2\hat{S}_y\hat{I}_y\sin\Omega_S t_2)\cdot\\
&\quad[W_{x1}\cos\eta\sin\omega_+ t_2-W_{x2}\sin\eta\sin\omega_- t_2-W_{xy}\cos^2\eta\cos\omega_+ t_2-W_{xy}\sin^2\eta\cos\omega_- t_2]\\
&+(2\hat{S}_x\hat{I}_z\cos\Omega_S t_2+2\hat{S}_y\hat{I}_z\sin\Omega_S t_2)\cdot\\
&\quad[W_{x1}\sin\xi\cos\omega_+ t_2-W_{x2}\cos\xi\cos\omega_- t_2+W_{xy}\cos\eta\sin\xi\sin\omega_+ t_2+W_{xy}\sin\eta\cos\xi\sin\omega_- t_2]
\end{aligned}\tag{B-78}$$

where

$$\begin{aligned}
W_{x1}&=W_{xx}\cos\xi+W_{xz}\sin\xi\\
&=V_{x1}(\cos 2\eta+1)\cos^2\omega_+ t_1+V_{x2}\sin 2\eta\sin\omega_+ t_1\sin\omega_- t_1-V_{x1}\cos 2\eta\\
&\quad+V_{xy}(\cos 2\eta+1)\cos\eta\sin\omega_+ t_1\cos\omega_+ t_1+V_{xy}\sin 2\eta\sin\eta\sin\omega_+ t_1\cos\omega_- t_1
\end{aligned}\tag{B-79}$$

$$\begin{aligned}
W_{x2}&=W_{xx}\sin\xi-W_{xz}\cos\xi\\
&=V_{x2}(\cos 2\eta-1)\cos^2\omega_- t_1+V_{x1}\sin 2\eta\sin\omega_+ t_1\sin\omega_- t_1+V_{x2}\cos 2\eta\\
&\quad+V_{xy}(\cos 2\eta-1)\sin\eta\sin\omega_- t_1\cos\omega_- t_1-V_{xy}\sin 2\eta\cos\eta\sin\omega_- t_1\cos\omega_+ t_1
\end{aligned}\tag{B-80}$$

For the sixth pulse, the final density matrix is obtained as follows:

$$\sigma_4(5)=\sigma_0(6)\xrightarrow{(\pi)_x}\sigma_1(6)\xrightarrow{\xi\hat{I}_y}\xrightarrow{2\eta\hat{S}_z\hat{I}_y}\sigma_2(6)\xrightarrow{\Omega_S t_2\hat{S}_z}\xrightarrow{-\omega_+ t_2\hat{I}_z}\xrightarrow{-2\omega_- t_2\hat{S}_z\hat{I}_z}$$
$$\sigma_3(6)\xrightarrow{-\xi\hat{I}_y}\xrightarrow{-2\eta\hat{S}_z\hat{I}_y}\hat{S}_z X_z+\hat{S}_y X_y+2\hat{S}_x\hat{I}_x X_{xx}+2\hat{S}_x\hat{I}_y X_{xy}+2\hat{S}_x\hat{I}_z X_{xz}=\sigma_4(6)=\sigma_{\text{echo}}\tag{B-81}$$

where

$$X_z=-W_y\tag{B-82}$$

$$
\begin{aligned}
X_y = &-V_y[1 - 2\sin^2\eta\cos^2\eta(\cos\omega_+t_2 - \cos\omega_-t_2)^2] \\
&- \frac{1}{2}W_{xy}\sin 2\eta(\cos 2\eta + 1)\cos^2\omega_+t_2 - \frac{1}{2}W_{xy}\sin 2\eta(\cos 2\eta - 1)\cos^2\omega_-t_2 \\
&+ W_{xy}\sin 2\eta\cos 2\eta\cos\omega_+t_2\cos\omega_-t_2 \\
&+ W_{x1}\sin\eta(\cos 2\eta + 1)\sin\omega_+t_2\cos\omega_+t_2 - W_{x2}\cos\eta(\cos 2\eta - 1)\sin\omega_-t_2\cos\omega_-t_2 \\
&- W_{x1}\sin 2\eta\cos\eta\sin\omega_+t_2\cos\omega_-t_2 - W_{x2}\sin 2\eta\sin\eta\sin\omega_-t_2\cos\omega_+t_2
\end{aligned}
\tag{B-83}
$$

$$
\begin{aligned}
X_{xx} = &-V_y[2\sin\eta\cos\eta(\cos\eta\cos\xi\sin\omega_+t_2 - \sin\eta\sin\xi\sin\omega_-t_2)(\cos\omega_+t_2 - \cos\omega_-t_2)] \\
&+ W_{x1}\cos\xi(\cos 2\eta + 1)\cos^2\omega_+t_2 - W_{x2}\sin\xi(\cos 2\eta - 1)\cos^2\omega_-t_2 \\
&+ (W_{x1}\sin\xi + W_{x2}\cos\xi)\sin 2\eta\sin\omega_+t_2\sin\omega_-t_2 - (W_{x1}\cos\xi - W_{x2}\sin\xi)\cos 2\eta \\
&+ W_{xy}(\cos 2\eta + 1)\cos\eta\cos\xi\sin\omega_+t_2\cos\omega_+t_2 + W_{xy}(\cos 2\eta - 1)\sin\eta\sin\xi\sin\omega_-t_2\cos\omega_-t_2 \\
&+ W_{xy}\sin 2\eta\sin\eta\cos\xi\sin\omega_+t_2\cos\omega_-t_2 - W_{xy}\sin 2\eta\cos\eta\sin\xi\sin\omega_-t_2\cos\omega_+t_2
\end{aligned}
\tag{B-84}
$$

$$
\begin{aligned}
X_{xy} = &-V_y[2\sin\eta\cos\eta(\cos^2\eta\cos\omega_+t_2 + \sin^2\eta\cos\omega_-t_2)(\cos\omega_+t_2 - \cos\omega_-t_2)] \\
&+ W_{xy}\cos^2\eta(\cos 2\eta + 1)\cos^2\omega_+t_2 - W_{xy}\sin^2\eta(\cos 2\eta - 1)\cos^2\omega_-t_2 \\
&+ W_{xy}\sin^2 2\eta\cos\omega_+t_2\cos\omega_-t_2 - W_{xy} \\
&- W_{x1}\cos\eta(\cos 2\eta + 1)\sin\omega_+t_2\cos\omega_+t_2 - W_{x2}\sin\eta(\cos 2\eta - 1)\sin\omega_-t_2\cos\omega_-t_2 \\
&- W_{x1}\sin\eta\sin 2\eta\sin\omega_+t_2\cos\omega_-t_2 + W_{x2}\cos\eta\sin 2\eta\sin\omega_-t_2\cos\omega_+t_2
\end{aligned}
\tag{B-85}
$$

$$
\begin{aligned}
X_{xz} = &-V_y[2\sin\eta\cos\eta(\cos\eta\sin\xi\sin\omega_+t_2 + \sin\eta\cos\xi\sin\omega_-t_2)(\cos\omega_+t_2 - \cos\omega_-t_2)] \\
&+ W_{x1}\sin\xi(\cos 2\eta + 1)\cos^2\omega_+t_2 + W_{x2}\cos\xi(\cos 2\eta - 1)\cos^2\omega_-t_2 \\
&- (W_{x1}\cos\xi - W_{x2}\sin\xi)\sin 2\eta\sin\omega_+t_2\sin\omega_-t_2 - (W_{x1}\sin\xi + W_{x2}\cos\xi)\cos 2\eta \\
&+ W_{xy}(\cos 2\eta + 1)\cos\eta\sin\xi\sin\omega_+t_2\cos\omega_+t_2 - W_{xy}(\cos 2\eta - 1)\sin\eta\cos\xi\sin\omega_-t_2\cos\omega_-t_2 \\
&+ W_{xy}\sin 2\eta\sin\eta\sin\xi\sin\omega_+t_2\cos\omega_-t_2 + W_{xy}\sin 2\eta\cos\eta\cos\xi\sin\omega_-t_2\cos\omega_+t_2
\end{aligned}
\tag{B-86}
$$

The coefficient of $\hat{S}_y$ in eq (B-81), that is, X_y, is the real part of the ESEEM signal of the conventional DQC, and it is a function of t_p, t_1, and t_2.

B.7 ESEEM SIGNAL IN THE MODIFIED DQC SEQUENCE

In the modified DQC, the fourth pulse is a 2π pulse, which prevents the spins with different frequency offsets from refocusing. As a result, the density matrix becomes a function of the frequency offset Ω_S. The sequence is illustrated in Figure B-2.

For the first three pulses, the evolution of the spin system is the same as in the conventional DQC. The evolution for the fourth pulse, the 2π pulse, is described by:

$$\begin{aligned}\sigma_4(3) = \sigma_0(4') \xrightarrow{(2\pi)_x} \sigma_1(4') \xrightarrow{\xi\hat{I}_y} \xrightarrow{2\eta\hat{S}_z\hat{I}_y} \sigma_2(4') \xrightarrow{\Omega_S t_1\hat{S}_z} \xrightarrow{-\omega_+ t_1\hat{I}_z} \xrightarrow{-2\omega_- t_1\hat{S}_z\hat{I}_z} \\ \sigma_3(4') \xrightarrow{-\xi\hat{I}_y} \xrightarrow{-2\eta\hat{S}_z\hat{I}_y} \hat{S}_z W'_z + (\hat{S}_y\cos 2\Omega_S t_1 - \hat{S}_x \sin 2\Omega_S t_1)W'_y \\ + (2\hat{S}_x\hat{I}_x\cos 2\Omega_S t_1 + 2\hat{S}_y\hat{I}_x \sin 2\Omega_S t_1)W'_{xx} \\ + (2\hat{S}_x\hat{I}_y\cos 2\Omega_S t_1 + 2\hat{S}_y\hat{I}_y \sin 2\Omega_S t_1)W'_{xy} \\ + (2\hat{S}_x\hat{I}_z\cos 2\Omega_S t_1 + 2\hat{S}_y\hat{I}_z \sin 2\Omega_S t_1)W'_{xz} = \sigma_4(4')\end{aligned} \tag{B-87}$$

where

$$W'_z = V_y \tag{B-88}$$

$$\begin{aligned}W'_y = {} & V_{x1}\sin\xi\sin 2\omega_+ t_1 + V_{x2}\cos\xi\sin 2\omega_- t_1 \\ & - V_{xy}\cos\eta\sin\xi\cos\omega_+ t_1 + V_{xy}\sin\eta\cos\xi\cos\omega_- t_1\end{aligned} \tag{B-89}$$

$$\begin{aligned}W'_{xx} = {} & V_{x1}\cos\xi\cos 2\omega_+ t_1 + V_{x2}\sin\xi\cos 2\omega_- t_1 \\ & + V_{xy}\cos\eta\cos\xi\sin 2\omega_+ t_1 - V_{xy}\sin\eta\sin\xi\sin 2\omega_- t_1\end{aligned} \tag{B-90}$$

$$\begin{aligned}W'_{xy} = {} & -V_{x1}\cos\xi\sin 2\omega_+ t_1 + V_{x2}\sin\xi\sin 2\omega_- t_1 \\ & + V_{xy}\cos\eta\cos\xi\cos 2\omega_+ t_1 + V_{xy}\sin\eta\sin\xi\cos 2\omega_- t_1\end{aligned} \tag{B-91}$$

$$\begin{aligned}W'_{xz} = {} & V_{x1}\sin\xi\cos 2\omega_+ t_1 - V_{x2}\cos\xi\cos 2\omega_- t_1 \\ & + V_{xy}\cos\eta\sin\xi\sin 2\omega_+ t_1 + V_{xy}\sin\eta\cos\xi\sin 2\omega_- t_1\end{aligned} \tag{B-92}$$

The prime symbol denotes that the modified DQC pulse sequence is applied. It is clear that W'_y, W'_{xx}, W'_{xy}, and W'_{xz} are functions of t_p and t_1 as V_{x1}, V_{x2}, and V_{xy} are functions of t_p.

In eq (B-87), $\sin 2\Omega_S t_1$ and $\cos 2\Omega_S t_1$ can be evaluated by the integration over a range of Ω_S, weighted by a distribution function. The distribution of the frequency offset may be expressed by an even function such as a sinc function or a Gaussian function within the excitation bandwidth. Then, the weighted average of $\sin 2\Omega_S t_1$ is 0 because the probability

distribution function is even, and the sine function is odd. Thus, the density matrix $\sigma_4(4')$ is simplified to:

$$\sigma_4(4') = \hat{S}_z W'_z + (\hat{S}_y W'_y + 2\hat{S}_x \hat{I}_x W'_{xx} + 2\hat{S}_x \hat{I}_y W'_{xy} + 2\hat{S}_x \hat{I}_z W'_{xz}) \cos 2\Omega_S t_1 \qquad \text{(B-93)}$$

Since the last two pulses of the modified DQC are identical to those of the conventional version, the density matrix can be expressed in the same manner. The density matrix immediately before the sixth pulse is:

$$\begin{aligned}
\sigma_4(5') = {} & V_y[(-\hat{S}_y \cos\Omega_S t_2 + \hat{S}_x \sin\Omega_S t_2)(\cos^2\eta \cos\omega_- t_2 + \sin^2\eta \cos\omega_+ t_2) \\
& + (2\hat{S}_x \hat{I}_x \cos\Omega_S t_2 + 2\hat{S}_y \hat{I}_x \sin\Omega_S t_2)(\cos\eta \sin\xi \sin\omega_- t_2 + \sin\eta \cos\xi \sin\omega_+ t_2) \\
& + (2\hat{S}_x \hat{I}_y \cos\Omega_S t_2 + 2\hat{S}_y \hat{I}_y \sin\Omega_S t_2)(\sin\eta \cos\eta \cos\omega_+ t_2 - \sin\eta \cos\eta \cos\omega_- t_2) \\
& + (2\hat{S}_x \hat{I}_z \cos\Omega_S t_2 + 2\hat{S}_y \hat{I}_z \sin\Omega_S t_2)(\sin\eta \sin\xi \sin\omega_+ t_2 - \cos\eta \cos\xi \sin\omega_- t_2)] \\
& + \hat{S}_z W'_y \cos 2\Omega_S t_1 + (\hat{S}_y \cos\Omega_S t_2 - \hat{S}_x \sin\Omega_S t_2) \cos 2\Omega_S t_1 \cdot \\
& \quad [W'_{x1} \sin\eta \sin\omega_+ t_2 + W'_{x2} \cos\eta \sin\omega_- t_2 - W'_{xy} \sin\eta \cos\eta \cos\omega_+ t_2 + W'_{xy} \sin\eta \cos\eta \cos\omega_- t_2] \\
& + (2\hat{S}_x \hat{I}_x \cos\Omega_S t_2 + 2\hat{S}_y \hat{I}_x \sin\Omega_S t_2) \cos 2\Omega_S t_1 \cdot \\
& \quad [W'_{x1} \cos\xi \cos\omega_+ t_2 + W'_{x2} \sin\xi \cos\omega_- t_2 + W'_{xy} \cos\eta \cos\xi \sin\omega_+ t_2 - W'_{xy} \sin\eta \sin\xi \sin\omega_- t_2] \\
& - (2\hat{S}_x \hat{I}_y \cos\Omega_S t_2 + 2\hat{S}_y \hat{I}_y \sin\Omega_S t_2) \cos 2\Omega_S t_1 \cdot \\
& \quad [W'_{x1} \cos\eta \sin\omega_+ t_2 - W'_{x2} \sin\eta \sin\omega_- t_2 - W'_{xy} \cos^2\eta \cos\omega_+ t_2 - W'_{xy} \sin^2\eta \cos\omega_- t_2] \\
& + (2\hat{S}_x \hat{I}_z \cos\Omega_S t_2 + 2\hat{S}_y \hat{I}_z \sin\Omega_S t_2) \cos 2\Omega_S t_1 \cdot \\
& \quad [W'_{x1} \sin\xi \cos\omega_+ t_2 - W'_{x2} \cos\xi \cos\omega_- t_2 + W'_{xy} \cos\eta \sin\xi \sin\omega_+ t_2 + W'_{xy} \sin\eta \cos\xi \sin\omega_- t_2]
\end{aligned} \qquad \text{(B-94)}$$

where

$$\begin{aligned}
W'_{x1} &= W'_{xx} \cos\xi + W'_{xz} \sin\xi \\
&= V_{x1} \cos 2\omega_+ t_1 + V_{xy} \cos\eta \sin 2\omega_+ t_1
\end{aligned} \qquad \text{(B-95)}$$

$$\begin{aligned}
W'_{x2} &= W'_{xx} \sin\xi - W'_{xz} \cos\xi \\
&= V_{x2} \cos 2\omega_- t_1 - V_{xy} \sin\eta \sin 2\omega_- t_1
\end{aligned} \qquad \text{(B-96)}$$

The final density matrix for the sixth pulse in the modified DQC is:

$$\sigma_4(6') = \sigma_{\text{echo}} = \hat{S}_z X'_z + \hat{S}_y X'_y + 2\hat{S}_x \hat{I}_x X'_{xx} + 2\hat{S}_x \hat{I}_y X'_{xy} + 2\hat{S}_x \hat{I}_z X'_{xz} \qquad \text{(B-97)}$$

where

$$X'_z = -W'_y \cos 2\Omega_S t_1 \tag{B-98}$$

$$\begin{aligned} X'_y = {} & V_y[1 - 2\sin^2\eta\cos^2\eta(\cos\omega_+ t_2 - \cos\omega_- t_2)^2] \\ & - \cos 2\Omega_S t_1 \,[\frac{1}{2}W'_{xy}\sin 2\eta(\cos 2\eta + 1)\cos^2\omega_+ t_2 + \frac{1}{2}W'_{xy}\sin 2\eta(\cos 2\eta - 1)\cos^2\omega_- t_2 \\ & - W'_{xy}\sin 2\eta\cos 2\eta\cos\omega_+ t_2\cos\omega_- t_2 \\ & - W'_{x1}\sin\eta(\cos 2\eta + 1)\sin\omega_+ t_2\cos\omega_+ t_2 + W'_{x2}\cos\eta(\cos 2\eta - 1)\sin\omega_- t_2\cos\omega_- t_2 \\ & + W'_{x1}\sin 2\eta\cos\eta\sin\omega_+ t_2\cos\omega_- t_2 + W'_{x2}\sin 2\eta\sin\eta\sin\omega_- t_2\cos\omega_+ t_2] \end{aligned} \tag{B-99}$$

$$\begin{aligned} X'_{xx} = {} & V_y[2\sin\eta\cos\eta(\cos\eta\cos\xi\sin\omega_+ t_2 - \sin\eta\sin\xi\sin\omega_- t_2)(\cos\omega_+ t_2 - \cos\omega_- t_2)] \\ & + \cos 2\Omega_S t_1 \,[W'_{x1}\cos\xi(\cos 2\eta + 1)\cos^2\omega_+ t_2 - W'_{x2}\sin\xi(\cos 2\eta - 1)\cos^2\omega_- t_2 \\ & + (W'_{x1}\sin\xi + W'_{x2}\cos\xi)\sin 2\eta\sin\omega_+ t_2\sin\omega_- t_2 - (W'_{x1}\cos\xi - W'_{x2}\sin\xi)\cos 2\eta \\ & + W'_{xy}(\cos 2\eta + 1)\cos\eta\cos\xi\sin\omega_+ t_2\cos\omega_+ t_2 + W'_{xy}(\cos 2\eta - 1)\sin\eta\sin\xi\sin\omega_- t_2\cos\omega_- t_2 \\ & + W'_{xy}\sin 2\eta\sin\eta\cos\xi\sin\omega_+ t_2\cos\omega_- t_2 - W'_{xy}\sin 2\eta\cos\eta\sin\xi\sin\omega_- t_2\cos\omega_+ t_2] \end{aligned} \tag{B-100}$$

$$\begin{aligned} X'_{xy} = {} & V_y[2\sin\eta\cos\eta(\cos^2\eta\cos\omega_+ t_2 + \sin^2\eta\cos\omega_- t_2)(\cos\omega_+ t_2 - \cos\omega_- t_2)] \\ & + \cos 2\Omega_S t_1 \,[W'_{xy}\cos^2\eta(\cos 2\eta + 1)\cos^2\omega_+ t_2 - W'_{xy}\sin^2\eta(\cos 2\eta - 1)\cos^2\omega_- t_2 \\ & + W'_{xy}\sin^2 2\eta\cos\omega_+ t_2\cos\omega_- t_2 - W'_{xy} \\ & - W'_{x1}\cos\eta(\cos 2\eta + 1)\sin\omega_+ t_2\cos\omega_+ t_2 - W'_{x2}\sin\eta(\cos 2\eta - 1)\sin\omega_- t_2\cos\omega_- t_2 \\ & - W'_{x1}\sin\eta\sin 2\eta\sin\omega_+ t_2\cos\omega_- t_2 + W'_{x2}\cos\eta\sin 2\eta\sin\omega_- t_2\cos\omega_+ t_2] \end{aligned} \tag{B-101}$$

$$\begin{aligned} X'_{xz} = {} & V_y[2\sin\eta\cos\eta(\cos\eta\sin\xi\sin\omega_+ t_2 + \sin\eta\cos\xi\sin\omega_- t_2)(\cos\omega_+ t_2 - \cos\omega_- t_2)] \\ & + \cos 2\Omega_S t_1 \,[W'_{x1}\sin\xi(\cos 2\eta + 1)\cos^2\omega_+ t_2 + W'_{x2}\cos\xi(\cos 2\eta - 1)\cos^2\omega_- t_2 \\ & - (W'_{x1}\cos\xi - W'_{x2}\sin\xi)\sin 2\eta\sin\omega_+ t_2\sin\omega_- t_2 - (W'_{x1}\sin\xi + W'_{x2}\cos\xi)\cos 2\eta \\ & + W'_{xy}(\cos 2\eta + 1)\cos\eta\sin\xi\sin\omega_+ t_2\cos\omega_+ t_2 - W'_{xy}(\cos 2\eta - 1)\sin\eta\cos\xi\sin\omega_- t_2\cos\omega_- t_2 \\ & + W'_{xy}\sin 2\eta\sin\eta\sin\xi\sin\omega_+ t_2\cos\omega_- t_2 + W'_{xy}\sin 2\eta\cos\eta\cos\xi\sin\omega_- t_2\cos\omega_+ t_2] \end{aligned} \tag{B-102}$$

The coefficient of $\hat{S}_y$ in eq (B-98), that is, X'_y, is the real part of the ESEEM signal of the modified DQC, and it is a function of t_p, t_1, t_2, and Ω_S. In eq (B-100), if t_1 is long, the weighted average of $\cos 2\Omega_S t_1$ is so close to 0 that one can ignore the terms that have $\cos 2\Omega_S t_1$. Then, the ESEEM signal is simplified to:

$$X_y'(0) = V_y[1 - 2\sin^2\eta\cos^2\eta(\cos\omega_+ t_2 - \cos\omega_- t_2)^2]$$
$$= [1 - 2\sin^2\eta\cos^2\eta(\cos\omega_+ t_p - \cos\omega_- t_p)^2][1 - 2\sin^2\eta\cos^2\eta(\cos\omega_+ t_2 - \cos\omega_- t_2)^2] \quad \text{(B-103)}$$

More precise calculations are provided in Appendix C.

APPENDIX C

CALCULATION OF THE WEIGHTED AVERAGES OF TERMS CONTAINING FREQUENCY OFFSETS

A number of terms encountered in the calculation of ESEEM signal have the frequency offset Ω_S. Since the frequency offset has a distribution, terms containing the frequency offset can be evaluated by the integration over a range of Ω_S, weighted by a distribution function. In particular, the weighted averages of $\sin 2\Omega_S t$ and $\cos 2\Omega_S t$ are given by:[147]

$$\langle \sin 2\Omega_S t \rangle = \int_{-\mathrm{EBW}}^{\mathrm{EBW}} \sin 2\Omega_S t P(\Omega_S) d\Omega_S \ ; \ \langle \cos 2\Omega_S t \rangle = \int_{-\mathrm{EBW}}^{\mathrm{EBW}} \cos 2\Omega_S t P(\Omega_S) d\Omega_S \qquad \text{(C-1)}$$

where $P(\Omega_S)$ is the probability distribution function of the frequency offset, and EBW and –EBW are the upper limit and the lower limit of the excitation range in the angular frequency unit, respectively. In general, the probability distribution function $P(\Omega_S)$ is an even function. Therefore, the weighted averages of $\sin 2\Omega_S t$ is 0 while that of $\cos 2\Omega_S t$ depends on the distribution function.

C.1 APPROXIMATION USING A SINC FUNCTION

If the distribution of the frequency offset can be described by a sinc function, the probability distribution function is given by:

$$P_{\text{sinc}}(\Omega_S) = k_{\text{sinc}} \frac{\sin \Omega_S t_m}{\Omega_S} \tag{C-2}$$

where t_m is the longest pulse length, and k_{sinc} is the normalization factor as shown below.

$$k_{\text{sinc}} = \left(\int_{-\frac{\pi}{t_m}}^{\frac{\pi}{t_m}} \frac{\sin \Omega_S t_m}{\Omega_S} d\Omega_S \right)^{-1} \tag{C-3}$$

The excitation bandwidth is the reciprocal of the longest pulse length t_m, and the excitation range is assumed to be between $-1/(2t_m)$ and $1/(2t_m)$ in the frequency domain, which corresponds to between $-\pi/t_m$ and π/t_m in the angular frequency domain. Then, the weighted average of $\cos 2\Omega_S t$ is given by:

$$\langle \cos 2\Omega_S t \rangle = \int_{-\frac{\pi}{t_m}}^{\frac{\pi}{t_m}} \cos 2\Omega_S t P_{\text{sinc}}(\Omega_S) d\Omega_S = k_{\text{sinc}} \int_{-\frac{\pi}{t_m}}^{\frac{\pi}{t_m}} \frac{\sin \Omega_S t_m \cos 2\Omega_S t}{\Omega_S} d\Omega_S \tag{C-4}$$

Using the sine integral, one can express the weighted average in terms of t_m and t.

$$\langle \cos 2\Omega_S t \rangle = 2k_{\text{sinc}} \left[\text{Si}\left(\frac{2t + t_m}{t_m} \pi \right) - \text{Si}\left(\frac{2t - t_m}{t_m} \pi \right) \right] \tag{C-5}$$

If the pulse separation t is much longer than the longest pulse length t_m, the weighted average tends to 0.

C.2 APPROXIMATION USING A GAUSSIAN FUNCTION WITH A FINITE EXCITATION BANDWIDTH

If a Gaussian function is assumed, the probability distribution function is given by:

$$P_{\text{gauss}}(\Omega_S) = k_{\text{gauss}} \exp\left(-\frac{n^2 \Omega_S^2 t_m^2}{2\pi^2}\right) \tag{C-6}$$

where k_{gauss} is the normalization factor as shown below.

$$k_{\text{gauss}} = \left[\int_{-\frac{\pi}{t_m}}^{\frac{\pi}{t_m}} \exp\left(-\frac{n^2 \Omega_S^2 t_m^2}{2\pi^2}\right) d\Omega_S\right]^{-1} \tag{C-7}$$

In eq (C-6), n describes the linewidth of the Gaussian distribution function. For instance, if n is 2, the probability within the excitation bandwidth is approximately 0.95, and if n is 3, the probability is greater than 0.99. In the same fashion as in eqs (C-3) and (C-4), the excitation range is assumed to be between $-\pi/t_m$ and π/t_m in the angular frequency domain. Then, the weighted average of $\cos 2\Omega_S t$ is given by:

$$\langle \cos 2\Omega_S t \rangle = \int_{-\frac{\pi}{t_m}}^{\frac{\pi}{t_m}} \cos 2\Omega_S t P_{\text{gauss}}(\Omega_S) d\Omega_S = k_{\text{gauss}} \int_{-\frac{\pi}{t_m}}^{\frac{\pi}{t_m}} \cos 2\Omega_S t \exp\left(-\frac{n^2 \Omega_S^2 t_m^2}{2\pi^2}\right) d\Omega_S \tag{C-8}$$

Using the error function, one can express the weighted average in terms of t_m, t, and n.

$$\langle \cos 2\Omega_S t \rangle = \frac{k_{\text{gauss}} \sqrt{\pi^3}}{\sqrt{2}\, n t_m} \exp\left(-\frac{2\pi^2 t^2}{n^2 t_m^2}\right) \left[\text{erf}\left(\frac{n^2 t_m + 2\pi i t}{\sqrt{2} n t_m}\right) + \text{erf}\left(\frac{n^2 t_m - 2\pi i t}{\sqrt{2} n t_m}\right)\right] \tag{C-9}$$

If the pulse separation t is much longer than the longest pulse length t_m, the weighted average tends to 0.

C.3 APPROXIMATION USING A GAUSSIAN FUNCTION WITH AN INFINITE EXCITATION BANDWIDTH

If the excitation bandwidth is infinite with a Gaussian distribution of the frequency offset, the normalization factor in eq (C-7) becomes:

$$k_{\text{gauss}} = \left[\int_{-\infty}^{\infty} \exp\left(-\frac{n^2\Omega_S^2 t_m^2}{2\pi^2}\right) d\Omega_S\right]^{-1} = \frac{nt_m}{\sqrt{2\pi^3}} \tag{C-10}$$

Accordingly, the probability distribution function becomes:

$$P_{\text{gauss}}(\Omega_S) = \frac{nt_m}{\sqrt{2\pi^3}} \exp\left(-\frac{n^2\Omega_S^2 t_m^2}{2\pi^2}\right) \tag{C-11}$$

Since the excitation bandwidth is infinite, the weighted average of $\cos 2\Omega_S t_1$ is given by:

$$\langle \cos 2\Omega_S t \rangle = \int_{-\infty}^{\infty} \cos 2\Omega_S t P_{\text{gauss}}(\Omega_S) d\Omega_S = \frac{nt_m}{\sqrt{2\pi^3}} \int_{-\infty}^{\infty} \cos 2\Omega_S t \exp\left(-\frac{n^2\Omega_S^2 t_m^2}{2\pi^2}\right) d\Omega_S \tag{C-12}$$

The Gaussian integral in eq (C-12) is simplified to:

$$\langle \cos 2\Omega_S t \rangle = \exp\left(-\frac{2\pi^2 t^2}{n^2 t_m^2}\right) \tag{C-13}$$

Like the case of a finite excitation bandwidth, if the pulse separation t is much longer than the longest pulse length t_m, the weighted average approaches 0.

APPENDIX D

PRODUCT RULE OF ESEEM SIGNALS

With multiple nuclear spins coupled to the electron spin system, the Hamiltonian in eq (B-7) becomes:

$$\hat{\mathcal{H}}^{(N)} = \hbar\Omega_S\hat{S}_z - \hbar\sum_{i=1}^{N}\omega_{Ii}\hat{I}_{iz} + \hbar\hat{S}_z\sum_{i=1}^{N}\left(A_i\hat{I}_{iz} + B_i\hat{I}_{ix}\right) \tag{D-1}$$

where N is the number of coupled nuclear spins. In order to diagonalize the Hamiltonian in eq (D-1), whose dimension is $2^{N+1} \times 2^{N+1}$, one can consider its $2^N \times 2^N$ submatrices, $\hat{\mathcal{H}}_\alpha^{(N)}$ and $\hat{\mathcal{H}}_\beta^{(N)}$.

$$\hat{\mathcal{H}}^{(N)} = \begin{pmatrix} \hat{\mathcal{H}}_\alpha^{(N)} & O \\ O & \hat{\mathcal{H}}_\beta^{(N)} \end{pmatrix} \tag{D-2}$$

In eq (D-2), O is the 2^Nth-order zero matrix. In each of the α and β submatrices, the nuclear Hamiltonian can be considered to be the Kronecker (tensor) sum of N different 2 × 2 nuclear Hamiltonian matrices.

$$
\begin{aligned}
\hat{\mathcal{H}}_{\alpha}^{(N)} &= \frac{\hbar}{2}\Omega_S E_{2^N} + \hat{\mathcal{H}}_{1\alpha} \otimes E_{2^{N-1}} + E_2 \otimes \hat{\mathcal{H}}_{2\alpha} \otimes E_{2^{N-2}} + \cdots + E_{2^{N-1}} \otimes \hat{\mathcal{H}}_{N\alpha} \\
&= \frac{\hbar}{2}\Omega_S E_{2^N} + \sum_{i=1}^{N} E_{2^{i-1}} \otimes \hat{\mathcal{H}}_{i\alpha} \otimes E_{2^{N-i}} \\
\hat{\mathcal{H}}_{\beta}^{(N)} &= -\frac{\hbar}{2}\Omega_S E_{2^N} + \hat{\mathcal{H}}_{1\beta} \otimes E_{2^{N-1}} + E_2 \otimes \hat{\mathcal{H}}_{2\beta} \otimes E_{2^{N-2}} + \cdots + E_{2^{N-1}} \otimes \hat{\mathcal{H}}_{N\beta} \\
&= -\frac{\hbar}{2}\Omega_S E_{2^N} + \sum_{i=1}^{N} E_{2^{i-1}} \otimes \hat{\mathcal{H}}_{i\beta} \otimes E_{2^{N-i}}
\end{aligned}
\tag{D-3}
$$

where E_{2^K} is the 2^Kth-order identity matrix, and $\hat{\mathcal{H}}_{i\alpha}$ and $\hat{\mathcal{H}}_{i\beta}$ are the 2×2 nuclear Hamiltonian matrix for ith nuclear spin in the α and β electron spin manifold, respectively.

To diagonalize each nuclear Hamiltonian matrix in the α or β submatrix, one can consider N rotation matrices that may be different from one another. In analogy to eq (B-10), $\hat{\mathcal{H}}_{i\alpha}$ and $\hat{\mathcal{H}}_{i\beta}$ are related to the diagonalized matrices $\hat{\mathcal{D}}_{i\alpha}$ and $\hat{\mathcal{D}}_{i\beta}$ by the following equations.

$$
\hat{\mathcal{H}}_{i\alpha} = M_{i\alpha}\hat{\mathcal{D}}_{i\alpha}M_{i\alpha}^{\dagger} \;;\; \hat{\mathcal{H}}_{i\beta} = M_{i\beta}\hat{\mathcal{D}}_{i\beta}M_{i\beta}^{\dagger} \tag{D-4}
$$

Plugging eq (D-4) into eq (D-3) yields:

$$
\begin{aligned}
\hat{\mathcal{H}}_{\alpha}^{(N)} &= \frac{\hbar}{2}\Omega_S E_{2^N} + \left(\prod_{i=1}^{N} \otimes M_{i\alpha}\right)\left[\sum_{i=1}^{N}(E_{2^{i-1}} \otimes \hat{\mathcal{D}}_{i\alpha} \otimes E_{2^{N-i}})\right]\left(\prod_{i=1}^{N} \otimes M_{i\alpha}^{\dagger}\right) \\
\hat{\mathcal{H}}_{\beta}^{(N)} &= -\frac{\hbar}{2}\Omega_S E_{2^N} + \left(\prod_{i=1}^{N} \otimes M_{i\beta}\right)\left[\sum_{i=1}^{N}(E_{2^{i-1}} \otimes \hat{\mathcal{D}}_{i\beta} \otimes E_{2^{N-i}})\right]\left(\prod_{i=1}^{N} \otimes M_{i\beta}^{\dagger}\right)
\end{aligned}
\tag{D-5}
$$

where

$$
\prod_{i=1}^{N} \otimes \Gamma_i \overset{\text{def}}{=} \Gamma_1 \otimes \Gamma_2 \otimes \cdots \otimes \Gamma_N \tag{D-6}
$$

Finally, the two $2^N \times 2^N$ submatrices $\hat{\mathcal{H}}_{\alpha}^{(N)}$ and $\hat{\mathcal{H}}_{\beta}^{(N)}$ are diagonalized as follows:

$$\hat{\mathcal{H}}_{\alpha}^{(N)} = M_{\alpha}^{(N)} \hat{\mathcal{D}}_{\alpha}^{(N)} M_{\alpha}^{(N)\dagger} \; ; \; \hat{\mathcal{H}}_{\beta}^{(N)} = M_{\beta}^{(N)} \hat{\mathcal{D}}_{\beta}^{(N)} M_{\beta}^{(N)\dagger} \tag{D-7}$$

where

$$\begin{aligned} M_{\alpha}^{(N)} &= \prod_{i=1}^{N} \otimes M_{i\alpha} \; ; \; \hat{\mathcal{D}}_{\alpha}^{(N)} = \frac{\hbar}{2} \Omega_S E_{2^N} + \sum_{i=1}^{N} (E_{2^{i-1}} \otimes \hat{\mathcal{D}}_{i\alpha} \otimes E_{2^{N-i}}) \\ M_{\beta}^{(N)} &= \prod_{i=1}^{N} \otimes M_{i\beta} \; ; \; \hat{\mathcal{D}}_{\beta}^{(N)} = -\frac{\hbar}{2} \Omega_S E_{2^N} + \sum_{i=1}^{N} (E_{2^{i-1}} \otimes \hat{\mathcal{D}}_{i\beta} \otimes E_{2^{N-i}}) \end{aligned} \tag{D-8}$$

Also, the exponential function for $\hat{\mathcal{D}}_{\alpha}^{(N)}$ or $\hat{\mathcal{D}}_{\beta}^{(N)}$ can be expressed as:

$$\begin{aligned} \exp\left(-\frac{i}{\hbar} \hat{\mathcal{D}}_{\alpha}^{(N)} t\right) &= \exp\left(-\frac{i}{2} \Omega_S t\right) \prod_{i=1}^{N} \otimes \exp\left(-\frac{i}{\hbar} \hat{\mathcal{D}}_{i\alpha} t\right) \\ \exp\left(-\frac{i}{\hbar} \hat{\mathcal{D}}_{\beta}^{(N)} t\right) &= \exp\left(\frac{i}{2} \Omega_S t\right) \prod_{i=1}^{N} \otimes \exp\left(-\frac{i}{\hbar} \hat{\mathcal{D}}_{i\beta} t\right) \end{aligned} \tag{D-9}$$

Similarly, the electron spin angular momentum operators can be expressed as:

$$\hat{S}_x = \frac{1}{2} \begin{pmatrix} O & M^{(N)} \\ M^{(N)\dagger} & O \end{pmatrix} \; ; \; \hat{S}_y = \frac{i}{2} \begin{pmatrix} O & -M^{(N)} \\ M^{(N)\dagger} & O \end{pmatrix} \; ; \; \hat{S}_z = \frac{1}{2} \begin{pmatrix} E_{2^N} & O \\ O & -E_{2^N} \end{pmatrix} \tag{D-10}$$

where $M^{(N)}$ is $M_{\alpha}^{(N)\dagger} M_{\beta}^{(N)}$. Eventually, the elements of the density matrix and rotation matrices can be expressed as the Kronecker (tensor) products of the corresponding elements of some 2×2 matrices.

For the two-pulse ESEEM sequence, the final signal with only one coupled nuclear spin is given by:

$$V_{2p}(t) = \mathrm{Tr}[Y(t)] \tag{D-11}$$

where $Y(t)$ is the final density matrix multiplied by the *y*-component of the spin angular momentum operator, that is, $\sigma_{\mathrm{echo}}(t)\hat{S}_y$. With N coupled nuclear spins, the signal becomes:

$$V_{2p}^{(N)}(t) = \mathrm{Tr}[Y^{(N)}(t)] = \mathrm{Tr}\left[\prod_{i=1}^{N} \otimes Y_i(t)\right] = \prod_{i=1}^{N} \mathrm{Tr}[Y_i(t)] = \prod_{i=1}^{N} V_{2p,\,i}(t) \qquad \text{(D-12)}$$

where the superscript (N) denotes that all N nuclear spins are considered, and subscript i denotes that only the ith nuclear spin is considered.

When only one nuclear spin is coupled to the system, the final signal for the three-pulse ESEEM sequence is the sum of signals from two different pathways and given by:

$$V_{3p}(t,\,T) = \frac{1}{2}\mathrm{Tr}[Y_\alpha(t) + Y_\beta(t)] \qquad \text{(D-13)}$$

where $Y_\alpha(t)$ and $Y_\beta(t)$ are the contribution to $Y(t)$ from the α and β pathway, respectively. Then, the signal with N coupled nuclear spins is expressed as:

$$\begin{aligned} V_{3p}^{(N)}(t,\,T) &= \frac{1}{2}\mathrm{Tr}[Y_\alpha^{(N)}(t,\,T) + Y_\beta^{(N)}(t,\,T)] = \frac{1}{2}\mathrm{Tr}\left[\prod_{i=1}^{N} \otimes Y_{i\alpha}(t,\,T) + \prod_{i=1}^{N} \otimes Y_{i\beta}(t,\,T)\right] \\ &= \frac{1}{2}\left\{\prod_{i=1}^{N} \mathrm{Tr}[Y_{i\alpha}(t,\,T)] + \prod_{i=1}^{N} \mathrm{Tr}[Y_{i\beta}(t,\,T)]\right\} = \frac{1}{2}\left[\prod_{i=1}^{N} V_{3p,\,i\alpha}(t,\,T) + \prod_{i=1}^{N} V_{3p,\,i\beta}(t,\,T)\right] \end{aligned} \qquad \text{(D-14)}$$

Similarly, the product rule for the four-pulse HYSCORE signal with multiple nuclei is given by:

$$
\begin{aligned}
V_{4p}^{(N)}(t,\, t_1,\, t_2) &= \frac{1}{2}\mathrm{Tr}[Y_{\alpha}^{(N)}(t,\, t_1,\, t_2) + Y_{\beta}^{(N)}(t,\, t_1,\, t_2)] \\
&= \frac{1}{2}\mathrm{Tr}\left[\prod_{i=1}^{N} \otimes Y_{i\alpha}(t,\, t_1,\, t_2) + \prod_{i=1}^{N} \otimes Y_{i\beta}(t,\, t_1,\, t_2)\right] \\
&= \frac{1}{2}\left\{\prod_{i=1}^{N} \mathrm{Tr}[Y_{i\alpha}(t,\, t_1,\, t_2)] + \prod_{i=1}^{N} \mathrm{Tr}[Y_{i\beta}(t,\, t_1,\, t_2)]\right\} \\
&= \frac{1}{2}\left[\prod_{i=1}^{N} V_{4p,\, i\alpha}(t,\, t_1,\, t_2) + \prod_{i=1}^{N} V_{4p,\, i\beta}(t,\, t_1,\, t_2)\right]
\end{aligned}
\tag{D-15}
$$

APPENDIX E

NUCLEAR QUADRUPOLE TENSOR AND ITS PRINCIPAL AXIS SYSTEM

The spin Hamiltonian operator that describes a system with S=1/2 and I=1 is 6 × 6 in dimension and given by:

$$\hat{\mathcal{H}} = \beta_e \mathbf{B}_0 \cdot \tilde{\mathbf{g}} \cdot \hat{\mathbf{S}} - \beta_n \mathbf{B}_0 \cdot \tilde{\mathbf{g}}_n \cdot \hat{\mathbf{I}} + \hbar \hat{\mathbf{S}} \cdot \tilde{\mathbf{A}} \cdot \hat{\mathbf{I}} + \hbar \hat{\mathbf{I}} \cdot \tilde{\mathbf{Q}} \cdot \hat{\mathbf{I}} \tag{E-1}$$

where $\mathbf{Q}$ is the nuclear quadrupole tensor. If the g-tensors of the electron spin and the nuclear spin are assumed to be isotropic, eq (E-1) can be rewritten as:

$$\hat{\mathcal{H}} = g\beta_e \mathbf{B}_0 \cdot \hat{\mathbf{S}} - g_n \beta_n \mathbf{B}_0 \cdot \hat{\mathbf{I}} + \hbar \hat{\mathbf{S}} \cdot \tilde{\mathbf{A}} \cdot \hat{\mathbf{I}} + \hbar \hat{\mathbf{I}} \cdot \tilde{\mathbf{Q}} \cdot \hat{\mathbf{I}} \tag{E-2}$$

The 3 × 3 sub-Hamiltonian matrices in the α and β electron spin manifolds are expressed, under the high-field approximation, as:

$$\begin{aligned} \hat{\mathcal{H}}_\alpha &= \frac{\hbar}{2}\Omega_S E_3 - \hbar\omega_I \mathbf{m} \cdot \hat{\mathbf{I}} + \frac{\hbar}{2}\mathbf{m} \cdot \tilde{\mathbf{A}} \cdot \hat{\mathbf{I}} + \hbar \hat{\mathbf{I}} \cdot \tilde{\mathbf{Q}} \cdot \hat{\mathbf{I}} \\ \hat{\mathcal{H}}_\beta &= -\frac{\hbar}{2}\Omega_S E_3 - \hbar\omega_I \mathbf{m} \cdot \hat{\mathbf{I}} - \frac{\hbar}{2}\mathbf{m} \cdot \tilde{\mathbf{A}} \cdot \hat{\mathbf{I}} + \hbar \hat{\mathbf{I}} \cdot \tilde{\mathbf{Q}} \cdot \hat{\mathbf{I}} \end{aligned} \tag{E-3}$$

where E_3 is the third-order identity matrix, and $\mathbf{m}$ is the unit vector along the direction of the external magnetic field. The third term in either electron manifold describes the hyperfine interaction and can be rewritten as:

$$\hat{\mathcal{H}}_{\mathrm{hf}\alpha} = \frac{\hbar}{2}\mathbf{m}\cdot\tilde{\mathbf{A}}\cdot\hat{\mathbf{I}} = \frac{\hbar}{2}A_{\mathrm{iso}}\,\mathbf{m}\cdot\hat{\mathbf{I}} + \frac{\hbar}{2}T_{\mathrm{dip}}\left[\mathbf{m}\cdot\hat{\mathbf{I}} - 3\frac{(\mathbf{m}\cdot\mathbf{r})(\hat{\mathbf{I}}\cdot\mathbf{r})}{r^2}\right]$$
$$\hat{\mathcal{H}}_{\mathrm{hf}\beta} = -\frac{\hbar}{2}\mathbf{m}\cdot\tilde{\mathbf{A}}\cdot\hat{\mathbf{I}} = -\frac{\hbar}{2}A_{\mathrm{iso}}\,\mathbf{m}\cdot\hat{\mathbf{I}} - \frac{\hbar}{2}T_{\mathrm{dip}}\left[\mathbf{m}\cdot\hat{\mathbf{I}} - 3\frac{(\mathbf{m}\cdot\mathbf{r})(\hat{\mathbf{I}}\cdot\mathbf{r})}{r^2}\right] \quad \text{(E-4)}$$

where

$$T_{\mathrm{dip}} = -\frac{\mu_0 g\beta g_n\beta_n}{4\hbar\pi r^3} \quad \text{(E-5)}$$

In eqs (E-4) and (E-5), A_{iso} is the isotropic component of the hyperfine tensor, $\mathbf{r}$ is the electron–nuclear interspin vector, r is the interspin distance, and μ_0 is the vacuum permeability. Introducing $\mathbf{n}$, the unit vector along the direction of the interspin vector, one can simplify eq (E-4) to:

$$\hat{\mathcal{H}}_{\mathrm{hf}\alpha} = \frac{\hbar}{2}(A_{\mathrm{iso}} + T_{\mathrm{dip}})\mathbf{m}\cdot\hat{\mathbf{I}} - \frac{3}{2}\hbar T_{\mathrm{dip}}(\mathbf{m}\cdot\mathbf{n})(\hat{\mathbf{I}}\cdot\mathbf{n})$$
$$\hat{\mathcal{H}}_{\mathrm{hf}\beta} = -\frac{\hbar}{2}(A_{\mathrm{iso}} + T_{\mathrm{dip}})\mathbf{m}\cdot\hat{\mathbf{I}} + \frac{3}{2}\hbar T_{\mathrm{dip}}(\mathbf{m}\cdot\mathbf{n})(\hat{\mathbf{I}}\cdot\mathbf{n}) \quad \text{(E-6)}$$

In eq (E-3), the second and third terms are considered together after eq (E-6) is plugged into eq (E-3). Then, eq (E-3) becomes:

$$\hat{\mathcal{H}}_{\alpha} = \frac{\hbar}{2}\Omega_S E_3 + \hat{\mathcal{H}}_{n\alpha} = \frac{\hbar}{2}\Omega_S E_3 + \hbar\mathbf{\Lambda}_{\alpha}\cdot\hat{\mathbf{I}} + \hbar\hat{\mathbf{I}}\cdot\tilde{\mathbf{Q}}\cdot\hat{\mathbf{I}}$$
$$\hat{\mathcal{H}}_{\beta} = -\frac{\hbar}{2}\Omega_S E_3 + \hat{\mathcal{H}}_{n\beta} = -\frac{\hbar}{2}\Omega_S E_3 + \hbar\mathbf{\Lambda}_{\beta}\cdot\hat{\mathbf{I}} + \hbar\hat{\mathbf{I}}\cdot\tilde{\mathbf{Q}}\cdot\hat{\mathbf{I}} \quad \text{(E-7)}$$

where $\hat{\mathcal{H}}_{n\alpha}$ and $\hat{\mathcal{H}}_{n\beta}$ denote the nuclear Hamiltonian matrix in the α and β electron spin manifold, respectively, and

$$\begin{aligned}\boldsymbol{\Lambda}_\alpha &= \left(\frac{A_{\mathrm{iso}}}{2} + \frac{T_{\mathrm{dip}}}{2} - \omega_I\right)\mathbf{m} - \frac{3}{2}T_{\mathrm{dip}}(\mathbf{m}\cdot\mathbf{n})\mathbf{n} = \omega_{m\alpha}\mathbf{m} + \omega_{n\alpha}\mathbf{n} \\ \boldsymbol{\Lambda}_\beta &= -\left(\frac{A_{\mathrm{iso}}}{2} + \frac{T_{\mathrm{dip}}}{2} + \omega_I\right)\mathbf{m} + \frac{3}{2}T_{\mathrm{dip}}(\mathbf{m}\cdot\mathbf{n})\mathbf{n} = \omega_{m\beta}\mathbf{m} + \omega_{n\beta}\mathbf{n}\end{aligned} \tag{E-8}$$

In the nuclear quadrupole axis, each of the vectors $\mathbf{m}$ and $\mathbf{n}$ can be determined by two angles, the colatitude and the azimuthal angle. Accordingly, the *x*-, *y*-, and *z*-component of the vectors $\boldsymbol{\Lambda}_\alpha$ and $\boldsymbol{\Lambda}_\beta$ are expressed as:

$$\begin{pmatrix} \Lambda_{x\alpha} & \vdots & \Lambda_{x\beta} \\ \Lambda_{y\alpha} & \vdots & \Lambda_{y\beta} \\ \Lambda_{z\alpha} & \vdots & \Lambda_{z\beta} \end{pmatrix} = \begin{pmatrix} \omega_{m\alpha}\sin\theta\cos\phi + \omega_{n\alpha}\sin\beta\cos\gamma & \vdots & \omega_{m\beta}\sin\theta\cos\phi + \omega_{n\beta}\sin\beta\cos\gamma \\ \omega_{m\alpha}\sin\theta\sin\phi + \omega_{n\alpha}\sin\beta\sin\gamma & \vdots & \omega_{m\beta}\sin\theta\sin\phi + \omega_{n\beta}\sin\beta\sin\gamma \\ \omega_{m\alpha}\cos\theta + \omega_{n\alpha}\cos\beta & \vdots & \omega_{m\beta}\cos\theta + \omega_{n\beta}\cos\beta \end{pmatrix} \tag{E-9}$$

The dot product of the two vectors $\mathbf{m}$ and $\mathbf{n}$ is expressed in terms of those angles as follows:

$$\mathbf{m}\cdot\mathbf{n} = \cos\alpha = \sin\theta\cos\phi\sin\beta\cos\gamma + \sin\theta\sin\phi\sin\beta\sin\gamma + \cos\theta\cos\beta \tag{E-10}$$

where α is the angle between the two vectors $\mathbf{m}$ and $\mathbf{n}$, that is, between the external magnetic field and the interspin vector, θ and ϕ are the colatitude and the azimuthal angle of the external magnetic field with respect to the principal axis system of the nuclear quadrupole tensor, respectively, and β and γ are the colatitude and the azimuthal angle of the interspin vector with respect to the principal axis system, respectively. Figure E-1 illustrates the principal axes of the nuclear quadrupole tensor and the relationship between vectors and angles.

In general, the nuclear Hamiltonian matrices in terms of the basis of the pure nuclear quadrupole states, $|T_x\rangle$, $|T_y\rangle$, and $|T_z\rangle$, are given by:[24]

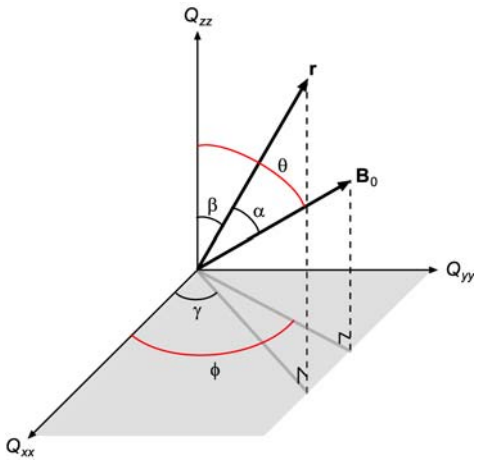

Figure E-1. Vectors and angles in the principal axis system of the nuclear quadrupole tensor. The angle between the electron–nuclear interspin vector **r** and the external magnetic field $\mathbf{B}_0$ can be expressed in terms of their colatitudes and azimuthal angles.

$$\hat{\mathcal{H}}_{n\alpha} = \hbar \begin{pmatrix} \frac{e^2qQ(1-\eta)}{4\hbar} & \Lambda_{z\alpha} & i\Lambda_{y\alpha} \\ \Lambda_{z\alpha} & \frac{e^2qQ(1+\eta)}{4\hbar} & \Lambda_{x\alpha} \\ -i\Lambda_{y\alpha} & \Lambda_{x\alpha} & -\frac{e^2qQ}{2\hbar} \end{pmatrix} ; \hat{\mathcal{H}}_{n\beta} = \hbar \begin{pmatrix} \frac{e^2qQ(1-\eta)}{4\hbar} & \Lambda_{z\beta} & i\Lambda_{y\beta} \\ \Lambda_{z\beta} & \frac{e^2qQ(1+\eta)}{4\hbar} & \Lambda_{x\beta} \\ -i\Lambda_{y\beta} & \Lambda_{x\beta} & -\frac{e^2qQ}{2\hbar} \end{pmatrix} \quad \text{(E-11)}$$

where e is the electron charge, q is the *z*-component of the electric field gradient across the nucleus, Q is the nuclear quadrupole moment of the nucleus, and η is the asymmetry parameter. Finally, one can obtain each element of the 6 × 6 Hamiltonian using eq (E-7) through eq (E-11).

APPENDIX F

NUMBER OF HISTIDINE RESIDUES THAT SIMULTANEOUSLY COORDINATE TO Cu(II)

A comparison of the ESEEM spectra of the nonlabeled Cu(II)–Aβ(1–16) complex and nonlabeled dien–Cu(II)–Aβ(1–16) complex at 3375 G provides information about the number of histidine residues simultaneously coordinating to Cu(II) in Component I. Figure F-1 shows the comparison between the ESEEM spectra of the nonlabeled Cu(II)–Aβ(1–16) complex at pH 6.0 and the nonlabeled dien–Cu(II)–Aβ(1–16) complex at pH 7.4.

In general, the ratio of the integrated intensity of the double-quantum region (2–8 MHz) to that of the NQI region (0–2 MHz) increases with the number of equivalent ESEEM-active ^{14}N nuclei coupled in an electron spin system.[30] The double-quantum peak is more prominent in the Cu(II)–Aβ(1–16) complex at pH 6.0 than in the dien–Cu(II)–Aβ(1–16) complex, where only one histidine residue equatorially coordinates to Cu(II) at the same time. These results indicate that more than one histidine residue simultaneously coordinate to Cu(II) in at least a fraction of Component I in the Cu(II)–Aβ(1–16) complex.

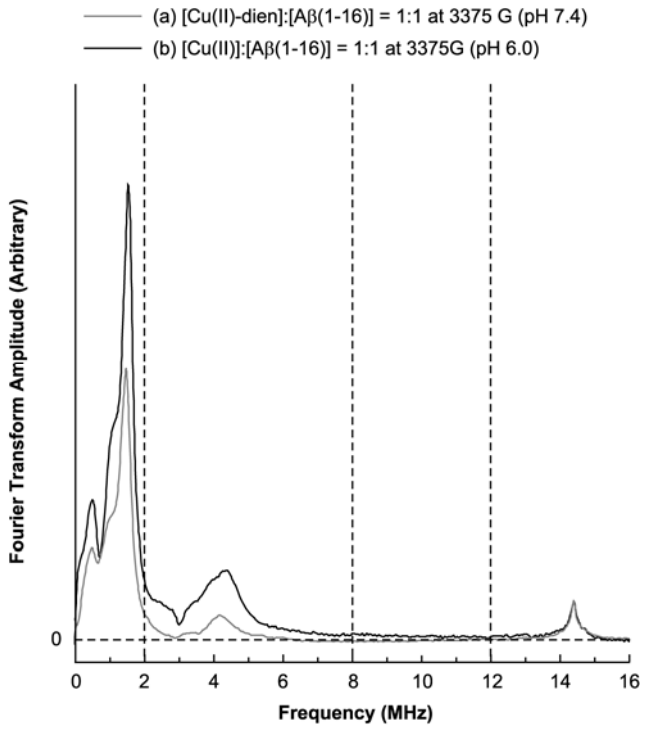

Figure F-1. Comparison of the NQI region (0–2 MHz), DQ region (2–8 MHz), and ^{1}H-ESEEM region (12–16 MHz) between the ESEEM spectra of the nonlabeled Aβ(1–16) peptide mixed with an equimolar amount of Cu(II) at pH 6.0 and the nonlabeled peptide mixed with an equimolar amount of the Cu(II)–dien complexes at pH 7.4. The vertical dashed lines separate the NQI region, DQ region, and ^{1}H-ESEEM region. The ^{14}N-ESEEM intensity normalized by the ^{1}H-ESEEM intensity provides information about the number of histidine residues that simultaneously coordinate to Cu(II) in Component I.

A similar approach is possible by comparing the normalized ^{14}N-ESEEM intensities with each other. Calculations reveal that the normalized ^{14}N-ESEEM intensity of the Cu(II)–Aβ(1–16) complex is approximately 1.7 times as much as that of the complex with dien, which signifies that approximately two histidine residues simultaneously coordinate to Cu(II) in Component I.

The consistent results by both approaches indicate that the normalized ^{14}N-ESEEM intensity of the ESEEM spectrum of a Cu(II) complex can provide critical information about the number of equivalent ^{14}N nuclei coupled to an electron spin system when the ESEEM spectrum of a ternary Cu(II) complex with a tridentate ligand such as dien is used as a reference. The two spectra have almost identical spectral shapes including peak positions in the ^{14}N-ESEEM region below 8 MHz and in the ^{1}H-ESEEM region around 14.4 MHz. The similarity in the peak shapes implies that the ESEEM-active nuclei of both complexes have almost identical nuclear transition frequencies.

F.1 MODULATION DEPTHS OF ^{14}N FREQUENCIES IN ESEEM

- **Relative Modulation Depth (Case I: One Nitrogen Coupled to an Electron Spin System)**

For a system with an electron spin of one half, the three-pulse ESEEM time-domain signal obtained by a conventional stimulated-echo pulse sequence of $\pi/2 - t - \pi/2 - T - \pi/2 - t$ – echo is given by:[10]

$$V(t, T) = \frac{1}{2}\left[V^{\alpha}(t, T) + V^{\beta}(t, T)\right] \tag{F-1}$$

where the signal in the α electron spin manifold is expressed as:

$$V^{\alpha}(t, T) = 1 - \frac{k}{2}(1 - \cos\omega_{\beta}t)[1 - \cos\omega_{\alpha}(t + T)] \tag{F-2}$$

The constant k is the modulation depth parameter, and ω_{α} and ω_{β} are the nuclear spin transition frequency in the α and β electron spin manifold, respectively. The signal in the β electron spin manifold can be expressed in the same fashion. Introducing new symbols, one can simplify eq (F-2).[94]

$$\begin{aligned} V^{\alpha}(t, T) &= 1 - K^{\alpha}(1 - S^{\alpha}) \\ &= 1 - K^{\alpha} + K^{\alpha}S^{\alpha} \end{aligned} \tag{F-3}$$

where

$$K^{\alpha}(t) = \frac{k}{2}(1 - \cos\omega_{\beta}t) \tag{F-4}$$

$$S^{\alpha}(t\,, T) = \cos\omega_{\alpha}(t + T) \tag{F-5}$$

In eq (F-3) the first two terms are the zero-frequency part, which is independent of T, while the last term is the oscillating part. When two or more nuclear spins are considered in the same electron spin system, the ESEEM signal is expressed by the product rule.[10,148]

$$V(t, T) = \frac{1}{2}\left[\prod_{i=1}^{N} V_i^{\alpha}(t, T) + \prod_{i=1}^{N} V_i^{\beta}(t, T)\right] \quad (i = 1, 2, 3, \cdots, N) \tag{F-6}$$

where $V_i^{\alpha}(t\,, T)$ and $V_i^{\beta}(t\,, T)$ are the contribution of the *i*th nuclear spin to the total signal in the α and β electron spin manifold, respectively, and N is the number of coupled nuclei. If one ^{14}N nuclear spin and one ^{1}H nuclear spin are coupled to an electron spin, the total signal is:

$$V_{14,1}(t,\,T) = \frac{1}{2}\Big[V^{\alpha}_{14}(t,\,T)V^{\alpha}_{1}(t,\,T) + V^{\beta}_{14}(t,\,T)V^{\beta}_{1}(t,\,T)\Big] \tag{F-7}$$

where the subscripts 14 and 1 denote the ^{14}N spin and the ^{1}H spin, respectively. For a weakly coupled ^{1}H nucleus, $V^{\alpha}_{1}(t\,,T)$ and $V^{\beta}_{1}(t\,,T)$ are almost identical, which leads to a deeper modulation at one frequency. Then, using eq (F-3), one can rewrite eq (F-7) as:

$$V_{14,1}(\tau\,,T) = \frac{1}{2}\Big[(1 - K^{\alpha}_{14} + K^{\alpha}_{14}S^{\alpha}_{14}) + (1 - K^{\beta}_{14} + K^{\beta}_{14}S^{\beta}_{14})\Big](1 - K_1 + K_1S_1) \tag{F-8}$$

where

$$K_1 = K^{\alpha}_{1} = K^{\beta}_{1} \tag{F-9}$$

$$S_1 = S^{\alpha}_{1} = S^{\beta}_{1} \tag{F-10}$$

Expansion of eq (F-8) gives an equation that contains the zero-frequency part and the oscillating part with several different frequencies.

$$V_{14,1}(t\,,T) = A + BS^{\alpha}_{14} + CS^{\beta}_{14} + DS_1 + ES^{\alpha}_{14}S_1 + FS^{\beta}_{14}S_1 \tag{F-11}$$

where

$$A = \Big(1 - \frac{K^{\alpha}_{14} + K^{\beta}_{14}}{2}\Big)(1 - K_1) \tag{F-12}$$

$$B = \frac{K^{\alpha}_{14}(1 - K_1)}{2} \tag{F-13}$$

$$C = \frac{K^{\beta}_{14}(1 - K_1)}{2} \tag{F-14}$$

$$D = K_1\Big(1 - \frac{K^{\alpha}_{14} + K^{\beta}_{14}}{2}\Big) \tag{F-15}$$

$$E = \frac{K^{\alpha}_{14}K_1}{2} \tag{F-16}$$

$$F = \frac{K^{\beta}_{14} K_1}{2} \tag{F-17}$$

The first term is the zero-frequency part, the second and third terms are the oscillations due to the ^{14}N nuclear spin, the four term is the oscillation due to the ^{1}H nucleus. The fifth and sixth terms are the oscillations due to the combination of the two nuclear spins. It is straightforward that the modulation depths of the second, third, and fourth term are proportional to their coefficients, B, C, and D, respectively. Particularly, the ratio of B to D is expressed as:

$$B/D = \frac{K^{\alpha}_{14}(1 - K_1)}{K_1(2 - K^{\alpha}_{14} - K^{\beta}_{14})} \tag{F-18}$$

The ratio B/D is the relative modulation depth of an ^{14}N nuclear transition frequency in the α electron spin manifold, which is normalized by that of the ^{1}H transition frequency. Similarly, the ratio C/D is the relative modulation depth of the corresponding transition frequency in the β electron spin manifold.

- **Relative Modulation Depth (Case II: Two Equivalent Nitrogen Nuclei)**

In the case that two equivalent ^{14}N nuclear spins and one ^{1}H nuclear spin are coupled to the same electron spin, the total signal becomes:

$$V_{14,14,1}(t, T) = \frac{1}{2}\left[[V^{\alpha}_{14}(t, T)]^2 V^{\alpha}_{1}(t, T) + [V^{\beta}_{14}(t, T)]^2 V^{\beta}_{1}(t, T)\right] \tag{F-19}$$

Then, eq (F-19) can be rewritten in the same manner as eq (F-7).

$$V_{14,14,1}(t, T) = \frac{1}{2}\left[(1 - K^{\alpha}_{14} + K^{\alpha}_{14} S^{\alpha}_{14})^2 + (1 - K^{\beta}_{14} + K^{\beta}_{14} S^{\beta}_{14})^2\right](1 - K_1 + K_1 S_1) \tag{F-20}$$

Like eq (F-8), expansion of eq (F-20) gives an equation that contains the zero-frequency part and the oscillating part. The coefficient of the term containing S^{α}_{14}, B_2, is expressed as:

$$B_2 = K^{\alpha}_{14}(1 - K^{\alpha}_{14})(1 - K_1) \tag{F-21}$$

where the subscript 2 denotes two equivalent ^{14}N spins. Considering the fact that $(S^{\alpha}_{14})^2$ and $(S^{\beta}_{14})^2$ contribute to the zero-frequency part, one can also calculate the coefficient of the term containing S_1, D_2.

$$D_2 = \frac{K_1}{4}\left[2\,(1 - K^{\alpha}_{14})^2 + (K^{\alpha}_{14})^2 + 2\,(1 - K^{\beta}_{14})^2 + (K^{\beta}_{14})^2\right] \tag{F-22}$$

Finally, the ratio of B_2 to D_2 is expressed as:

$$B_2/D_2 = \frac{4K^{\alpha}_{14}(1 - K^{\alpha}_{14})(1 - K_1)}{K_1\left[2\,(1 - K^{\alpha}_{14})^2 + (K^{\alpha}_{14})^2 + 2\,(1 - K^{\beta}_{14})^2 + (K^{\beta}_{14})^2\right]} \tag{F-23}$$

The ratios B/D and B_2/D_2 represent the relative modulation depth of an ^{14}N nuclear transition frequency in the α electron spin manifold, which is normalized by that of the ^{1}H transition frequency in the case of one and two coupled ^{14}N, respectively. The relative modulation depth of the ^{14}N nuclear transition frequency increases with an additional ^{14}N nucleus and the factor of increase is given by:

$$F(2\ ^{14}\mathrm{N}/1\ ^{14}\mathrm{N}) = \frac{B_2/D_2}{B/D} = \frac{4(1 - K^{\alpha}_{14})(2 - K^{\alpha}_{14} - K^{\beta}_{14})}{2\,(1 - K^{\alpha}_{14})^2 + (K^{\alpha}_{14})^2 + 2\,(1 - K^{\beta}_{14})^2 + (K^{\beta}_{14})^2} \tag{F-24}$$

If K^{α}_{14} and K^{β}_{14} are much smaller than 1, the factor converges to 2.

Next, if one of the two ^{14}N nuclei is replaced with ^{15}N, the coupled nuclei in the electron spin system are one ^{14}N nuclear spin, one ^{15}N nuclear spin, and one ^{1}H nuclear spin. Then, the total signal becomes:

$$V_{14,15,1}(t,T) = \frac{1}{2}\Big[V^{\alpha}_{14}(t,T)\,V^{\alpha}_{15}(t,T)\,V^{\alpha}_{1}(t,T) + V^{\beta}_{14}(t,T)\,V^{\beta}_{15}(t,T)\,V^{\beta}_{1}(t,T)\Big] \quad \text{(F-25)}$$

where the subscript 15 denotes the ^{15}N spin. In the case that the modulation of ^{15}N is significantly shallower than that of ^{14}N and ^{1}H, V^{α}_{15} and V^{β}_{15} are almost 1. Thus, the time-domain signal appears as if one ^{14}N and one ^{1}H nuclear spin were coupled.

$$V_{14,15,1}(t,T) \approx \frac{1}{2}\Big[V^{\alpha}_{14}(t,T)\,V^{\alpha}_{1}(t,T) + V^{\beta}_{14}(t,T)\,V^{\beta}_{1}(t,T)\Big] = V_{14,1}(t,T) \quad \text{(F-26)}$$

- **Relative Modulation Depth (Case III: Two Non-Equivalent Nitrogen Nuclei)**

In the case that two non-equivalent ^{14}N nuclear spins and one ^{1}H nuclear spin are coupled to the same electron spin, the total signal becomes:

$$V_{14,14',1}(t,T) = \frac{1}{2}\Big[V^{\alpha}_{14}(t,T)\,V^{\alpha}_{14'}(t,T)\,V^{\alpha}_{1}(t,T) + V^{\beta}_{14}(t,T)\,V^{\beta}_{14'}(t,T)\,V^{\beta}_{1}(t,T)\Big] \quad \text{(F-27)}$$

where the subscripts 14 and 14' denote two distinguishable ^{14}N spins. Then, eq (F-27) can be rewritten in the same manner as eqs (F-7) and (F-19).

$$V_{14,14',1}(t,T) = \frac{1}{2}(1 - K_1 + K_1 S_1)$$
$$\Big[(1 - K^{\alpha}_{14} + K^{\alpha}_{14}S^{\alpha}_{14})(1 - K^{\alpha}_{14'} + K^{\alpha}_{14'}S^{\alpha}_{14'}) + (1 - K^{\beta}_{14} + K^{\beta}_{14}S^{\beta}_{14})(1 - K^{\beta}_{14'} + K^{\beta}_{14'}S^{\beta}_{14'})\Big] \quad \text{(F-28)}$$

Like eqs (F-8) and (F-20), expansion of eq (F-28) gives an equation that contains the zero-frequency part and the oscillating part. The sum of the coefficients of the terms containing either S^{α}_{14} or $S^{\alpha}_{14'}$, $B_{2'}$, is expressed as:

$$B_{2'} = \frac{1}{2}(K^{\alpha}_{14} + K^{\alpha}_{14'} - 2K^{\alpha}_{14}K^{\alpha}_{14'})(1 - K_1) \tag{F-29}$$

where the subscript 2' denotes two distinguishable ^{14}N spins. One can also calculate the coefficient of the term containing S_1, $D_{2'}$.

$$D_{2'} = \frac{K_1}{2}\Big[(1 - K^{\alpha}_{14})(1 - K^{\alpha}_{14'}) + (1 - K^{\beta}_{14})(1 - K^{\beta}_{14'})\Big] \tag{F-30}$$

Finally, the ratio of $B_{2'}$ to $D_{2'}$ is expressed as:

$$B_{2'}/D_{2'} = \frac{(K^{\alpha}_{14} + K^{\alpha}_{14'} - 2K^{\alpha}_{14}K^{\alpha}_{14'})(1 - K_1)}{K_1[(1 - K^{\alpha}_{14})(1 - K^{\alpha}_{14'}) + (1 - K^{\beta}_{14})(1 - K^{\beta}_{14'})]} \tag{F-31}$$

The ratio $B_{2'}/D_{2'}$ represents the sum of the relative modulation depths of the transition frequencies of the two non-equivalent ^{14}N nuclei in the α electron spin manifold, which is normalized by the modulation depth of the ^{1}H transition frequency. The sum of the relative modulation depths, $B_{2'}/D_{2'}$, is greater than B/D, the relative modulation depth of the ^{14}N nuclear transition frequency in the case of one coupled ^{14}N. The ratio of $B_{2'}/D_{2'}$ to B/D is given by:

$$\begin{aligned} F(2'\ {}^{14}\mathrm{N}/1\ {}^{14}\mathrm{N}) &= \frac{B_{2'}/D_{2'}}{B/D} \\ &= \frac{(K^{\alpha}_{14} + K^{\alpha}_{14'} - 2K^{\alpha}_{14}K^{\alpha}_{14'})(2 - K^{\alpha}_{14} - K^{\beta}_{14})}{K^{\alpha}_{14}[(1 - K^{\alpha}_{14})(1 - K^{\alpha}_{14'}) + (1 - K^{\beta}_{14})(1 - K^{\beta}_{14'})]} \end{aligned} \tag{F-32}$$

where 2' denotes two non-equivalent ^{14}N spins. If K^{α}_{14}, $K^{\alpha}_{14'}$, K^{β}_{14}, and$K^{\beta}_{14'}$ are much smaller than 1, eq (F-32) becomes:

$$F(2'\ {}^{14}\mathrm{N}/1\ {}^{14}\mathrm{N}) = 1 + \frac{K^{\alpha}_{14'}}{K^{\alpha}_{14}} \tag{F-33}$$

Therefore, in the case of two non-equivalent ^{14}N nuclear spins and one ^{1}H nuclear spin coupled to the same electron spin system, a comparison of relative modulations depths, which is similar to that made in the case of two equivalent ^{14}N nuclear spins, is still meaningful when the modulation depths of the different frequencies are considered together. Particularly, if K^{α}_{14} and $K^{\alpha}_{14'}$ in eq [S-33] are identical, the ratio becomes 2.

F.2 CHANGE IN THE MODULATION DEPTHS OF ^{14}N FREQUENCIES BY REPLACEMENT OF ^{14}N WITH ^{15}N

- **Decrease in Relative Modulation Depth (Case I: One Nitrogen Nucleus)**

In a system where one ^{14}N nuclear spin and one ^{1}H nuclear spin are coupled to the electron spin, if a fraction of ^{14}N is replaced with ^{15}N, the signal becomes:

$$V^{m}_{14,15,1}(t, T) = m\, V_{15,1}(t, T) + (1 - m)\, V_{14,1}(t, T) \tag{F-34}$$

where m is the fraction of ^{14}N substituted with ^{15}N and

$$V_{14,1}(t, T) = \frac{1}{2}\left[V^{\alpha}_{14}(t, T)\, V^{\alpha}_{1}(t, T) + V^{\beta}_{14}(t, T)\, V^{\beta}_{1}(t, T)\right] \tag{F-35}$$

$$V_{15,1}(t, T) = \frac{1}{2}\left[V^{\alpha}_{15}(t, T)\, V^{\alpha}_{1}(t, T) + V^{\beta}_{15}(t, T)\, V^{\beta}_{1}(t, T)\right] \tag{F-36}$$

Assuming that V^{α}_{15} and V^{β}_{15} are almost 1, one can rewrite eq (F-36) as:

$$\begin{aligned} V_{15,1}(t, T) &= \frac{1}{2}\Big[V^{\alpha}_{1}(t, T) + V^{\beta}_{1}(t, T)\Big] \\ &= 1 - K_1 + K_1 S_1 \end{aligned} \tag{F-37}$$

Similarly, eq (F-35) can be expressed in terms of K^{α}_{14}, S^{α}_{14}, K^{β}_{14}, and S^{β}_{14}. Thus, expansion of eq (F-34) gives an equation that contains the zero-frequency part and the oscillating part. The coefficient of the term containing S^{α}_{14}, $B^{m}_{14\text{–}15}$, is:

$$B^{m}_{14\text{–}15} = \frac{(1-m)K^{\alpha}_{14}(1-K_1)}{2} \tag{F-38}$$

where the subscript 14–15 denotes the replacement of ^{14}N with ^{15}N. Also, the coefficient of the term containing S_1, $D^{m}_{14\text{–}15}$, is:

$$D^{m}_{14\text{–}15} = K_1\Big[1 - \frac{(1-m)(K^{\alpha}_{14} + K^{\beta}_{14})}{2}\Big] \tag{F-39}$$

The ratio of $B^{m}_{14\text{–}15}$ to $B^{m}_{14\text{–}15}$ is expressed as:

$$B^{m}_{14\text{–}15}/D^{m}_{14\text{–}15} = \frac{(1-m)K^{\alpha}_{14}(1-K_1)}{K_1[2-(1-m)(K^{\alpha}_{14} + K^{\beta}_{14})]} \tag{F-40}$$

Finally, one can calculate the decrease in the relative modulation depth of the ^{14}N nuclear transition frequency by comparing $B^{m}_{14\text{–}15}/D^{m}_{14\text{–}15}$ with $B^{0}_{14\text{–}15}/D^{0}_{14\text{–}15}$, that is, B/D in eq (F-18).

$$F(m\ ^{15}\mathrm{N}/0\ ^{15}\mathrm{N}) = \frac{B^{m}_{14\text{–}15}/D^{m}_{14\text{–}15}}{B/D} = \frac{(1-m)[2-(K^{\alpha}_{14} + K^{\beta}_{14})]}{2-(1-m)(K^{\alpha}_{14} + K^{\beta}_{14})} \tag{F-41}$$

It is evident that the decrease in the relative modulation depth of the ^{14}N nuclear transition frequency is greater than that in the fraction of ^{14}N. If K^{α}_{14} and K^{β}_{14} are much smaller than 1, the factor converges to $1 - m$, which is the fraction of ^{14}N. For example, if the K^{α}_{14} and K^{β}_{14} values are approximately 0.15, eq (F-41) becomes:

$$F(m\ ^{15}\mathrm{N}/0\ ^{15}\mathrm{N}) = \frac{1.70\,(1-m)}{1.70 + 0.30\,m} \tag{F-42}$$

In the case of a 33% replacement of ^{14}N with ^{15}N, the ratio $F(m\ ^{15}\mathrm{N}/0\ ^{15}\mathrm{N})$ is approximately 0.63, which indicates that the relative modulation depth of the ^{14}N transition frequency decreases by 37%, 4% greater than expected from the fraction of replacement.

- **Decrease in Relative Modulation Depth (Case II: Two Equivalent Nitrogen Nuclei)**

One may consider another system where two equivalent ^{14}N nuclear spins and one ^{1}H nuclear spin are coupled to the same electron spin. If a fraction of either ^{14}N is replaced with ^{15}N, the signal becomes:

$$V^{n}_{14,14,15,1}(t,\,T) = n\,V_{14,15,1}\,(t,\,T) + (1-n)\,V_{14,14,1}(t,\,T) \tag{F-43}$$

where n is the fraction of ^{14}N substituted with ^{15}N and

$$V_{14,14,1}(t,\,T) = \frac{1}{2}\Big[[V^{\alpha}_{14}(t,\,T)]^2\,V^{\alpha}_{1}(t,\,T) + [V^{\beta}_{14}(t,\,T)]^2\,V^{\beta}_{1}(t,\,T)\Big] \tag{F-44}$$

$$V_{14,15,1}(t,\,T) = \frac{1}{2}\Big[V^{\alpha}_{14}(t,\,T)\,V^{\alpha}_{15}(t,\,T)\,V^{\alpha}_{1}(t,\,T) + V^{\beta}_{14}(t,\,T)\,V^{\beta}_{15}(t,\,T)\,V^{\beta}_{1}(t,\,T)\Big] \tag{F-45}$$

Assuming that V^{α}_{15} and V^{β}_{15} are almost 1, one can rewrite eq (F-45) as:

$$V_{14,15,1}(t,\,T) = \frac{1}{2}\Big[V^{\alpha}_{14}(t,\,T)\,V^{\alpha}_{1}(t,\,T) + V^{\beta}_{14}(t,\,T)\,V^{\beta}_{1}(t,\,T)\Big] \tag{F-46}$$

Expansion of eq (F-43) gives an equation that contains the zero-frequency part and the oscillating part. The coefficient of the term containing S^{α}_{14}, $B^{n}_{14\text{–}15}$, is:

$$B^{n}_{14\text{–}15} = \frac{K^{\alpha}_{14}(1-K_1)}{2}\Big[2(1-n)(1-K^{\alpha}_{14})+n\Big] \tag{F-47}$$

Also, the coefficient of the term containing S_1, $D^{n}_{14\text{–}15}$, is:

$$D^{n}_{14\text{–}15} = \frac{K_1}{4}\Big[3(1-n)[(K^{\alpha}_{14})^2+(K^{\beta}_{14})^2]+2(n-2)(K^{\alpha}_{14}+K^{\beta}_{14})+4\Big] \tag{F-48}$$

The ratio of $B^{n}_{14\text{–}15}$ to $D^{n}_{14\text{–}15}$ is expressed as:

$$B^{n}_{14\text{–}15}/D^{n}_{14\text{–}15} = \frac{2K^{\alpha}_{14}(1-K_1)[2(1-n)(1-K^{\alpha}_{14})+n]}{K_1\big[3(1-n)[(K^{\alpha}_{14})^2+(K^{\beta}_{14})^2]+2(n-2)(K^{\alpha}_{14}+K^{\beta}_{14})+4\big]} \tag{F-49}$$

As already shown in eq (F-41), one can calculate the decrease in the relative modulation depth of the ^{14}N nuclear transition frequency by comparing $B^{n}_{14\text{–}15}/D^{n}_{14\text{–}15}$ with $B^{0}_{14\text{–}15}/D^{0}_{14\text{–}15}$, that is, B_2/D_2 in eq (F-23).

$$\begin{aligned} F(n\ ^{15}\mathrm{N}/0\ ^{15}\mathrm{N}) &= \frac{B^{n}_{14\text{–}15}/D^{n}_{14\text{–}15}}{B_2/D_2} \\ &= \frac{[2(1-n)(1-K^{\alpha}_{14})+n]\big[3[(K^{\alpha}_{14})^2+(K^{\beta}_{14})^2]-4(K^{\alpha}_{14}+K^{\beta}_{14})+4\big]}{2(1-K^{\alpha}_{14})\big[3(1-n)[(K^{\alpha}_{14})^2+(K^{\beta}_{14})^2]+2(n-2)(K^{\alpha}_{14}+K^{\beta}_{14})+4\big]} \end{aligned} \tag{F-50}$$

If n is 1, eq (F-50) becomes:

$$F(1\ ^{15}\mathrm{N}/0\ ^{15}\mathrm{N}) = \frac{2\,(1-K^{\alpha}_{14})^2+(K^{\alpha}_{14})^2+2\,(1-K^{\beta}_{14})^2+(K^{\beta}_{14})^2}{4(1-K^{\alpha}_{14})(2-K^{\alpha}_{14}-K^{\beta}_{14})} \tag{F-51}$$

In fact, the right-hand side of eq (F-51) is the reciprocal of eq (F-24), which explains the increase in the relative modulation depth of the ^{14}N nuclear transition frequency with an additional ^{14}N

nucleus. On the other hand, if K^{α}_{14} and K^{β}_{14} are much smaller than 1, the factor converges to $1-(n/2)$, which is the fraction of ^{14}N. If the K^{α}_{14} and K^{β}_{14} values are approximately 0.15, eq (F-50) becomes:

$$F(n\ ^{15}\mathrm{N}/0\ ^{15}\mathrm{N}) = \frac{2.94\,(1-0.70\,n)}{1.70\,(2.94+0.47\,n)} \tag{F-52}$$

In the case that two-thirds of either ^{14}N is replaced with ^{15}N, the ratio $F(n\ ^{15}\mathrm{N}/0\ ^{15}\mathrm{N})$ is approximately 0.66, which indicates that the relative modulation depth of the ^{14}N transition frequency decreases by 34%. Since two-thirds of either ^{14}N means one third of the entire ^{14}N nuclei, the decrease by 34% is similar to the fraction of replacement.

- **Decrease in Relative Modulation Depth (Case III: Two Non-Equivalent Nitrogen Nuclei)**

One may also consider a third system where two distinguishable ^{14}N nuclear spins and one ^{1}H nuclear spin are coupled to the same electron spin. If a fraction of either ^{14}N is replaced with ^{15}N, the signal becomes:

$$V^{p}_{14,14',15,1}(t,T) = p\,V_{14,15,1}(t,T) + (1-p)\,V_{14,14',1}(t,T) \tag{F-53}$$

where p is the fraction of ^{14}N replaced with ^{15}N and

$$V_{14,14',1}(t,T) = \frac{1}{2}\Big[V^{\alpha}_{14}(t,T)\,V^{\alpha}_{14'}(t,T)\,V^{\alpha}_{1}(t,T) + V^{\beta}_{14}(t,T)\,V^{\beta}_{14'}(t,T)\,V^{\beta}_{1}(t,T)\Big] \tag{F-54}$$

$$V_{14,15,1}(t,T) = \frac{1}{2}\Big[V^{\alpha}_{14}(t,T)\,V^{\alpha}_{15}(t,T)\,V^{\alpha}_{1}(t,T) + V^{\beta}_{14}(t,T)\,V^{\beta}_{15}(t,T)\,V^{\beta}_{1}(t,T)\Big] \tag{F-55}$$

Assuming that V^{α}_{15} and V^{β}_{15} are almost 1, one can rewrite eq (F-55) as:

$$V_{14,15,1}(t,T) = \frac{1}{2}\Big[V^{\alpha}_{14}(t,T)\,V^{\alpha}_{1}(t,T) + V^{\beta}_{14}(t,T)\,V^{\beta}_{1}(t,T)\Big] \tag{F-56}$$

Expansion of eq (F-53) gives an equation that contains the zero-frequency part and the oscillating part. The sum of the coefficients of the terms containing either S^{α}_{14} or $S^{\alpha}_{14'}$, $B^{p}_{14\text{–}15}$, is:

$$B^{p}_{14\text{–}15} = \frac{1-K_1}{2}\left[K^{\alpha}_{14} + (1-p)K^{\alpha}_{14'} - 2(1-p)K^{\alpha}_{14}K^{\alpha}_{14'}\right] \tag{F-57}$$

Also, the coefficient of the term containing S_1, $D^{p}_{14\text{–}15}$, is:

$$D^{p}_{14\text{–}15} = \frac{K_1}{2}\left[(1-p)(K^{\alpha}_{14}K^{\alpha}_{14'} + K^{\beta}_{14}K^{\beta}_{14'} - K^{\alpha}_{14'} - K^{\beta}_{14'}) - (K^{\alpha}_{14} + K^{\beta}_{14}) + 2\right] \tag{F-58}$$

The ratio of $B^{p}_{14\text{–}15}$ to $D^{p}_{14\text{–}15}$ is expressed as:

$$B^{p}_{14\text{–}15}/D^{p}_{14\text{–}15} = \frac{(1-K_1)[K^{\alpha}_{14} + (1-p)K^{\alpha}_{14'} - 2(1-p)K^{\alpha}_{14}K^{\alpha}_{14'}]}{K_1[(1-p)(K^{\alpha}_{14}K^{\alpha}_{14'} + K^{\beta}_{14}K^{\beta}_{14'} - K^{\alpha}_{14'} - K^{\beta}_{14'}) - (K^{\alpha}_{14} + K^{\beta}_{14}) + 2]} \tag{F-59}$$

As already shown in eqs (F-41) and (F-50), one can calculate the decrease in the sum of the relative modulation depths of the ^{14}N nuclear transition frequencies by comparing $B^{p}_{14\text{–}15}/D^{p}_{14\text{–}15}$ with $B^{0}_{14\text{–}15}/D^{0}_{14\text{–}15}$, that is, $B_{2'}/D_{2'}$ in eq (F-31).

$$F(p\ ^{15}\mathrm{N}/0\ ^{15}\mathrm{N}) = \frac{B^{p}_{14\text{–}15}/D^{p}_{14\text{–}15}}{B_{2'}/D_{2'}}$$
$$= \frac{[K^{\alpha}_{14} + (1-p)K^{\alpha}_{14'} - 2(1-p)K^{\alpha}_{14}K^{\alpha}_{14'}][(1-K^{\alpha}_{14})(1-K^{\alpha}_{14'}) + (1-K^{\beta}_{14})(1-K^{\beta}_{14'})]}{(K^{\alpha}_{14} + K^{\alpha}_{14'} - 2K^{\alpha}_{14}K^{\alpha}_{14'})[(1-p)(K^{\alpha}_{14}K^{\alpha}_{14'} + K^{\beta}_{14}K^{\beta}_{14'} - K^{\alpha}_{14'} - K^{\beta}_{14'}) - (K^{\alpha}_{14} + K^{\beta}_{14}) + 2]} \tag{F-60}$$

If p is 1, eq (F-60) becomes:

$$F(1\ ^{15}\mathrm{N}/0\ ^{15}\mathrm{N}) = \frac{K^{\alpha}_{14}[(1-K^{\alpha}_{14})(1-K^{\alpha}_{14'}) + (1-K^{\beta}_{14})(1-K^{\beta}_{14'})]}{(K^{\alpha}_{14} + K^{\alpha}_{14'} - 2K^{\alpha}_{14}K^{\alpha}_{14'})(2 - K^{\alpha}_{14} - K^{\beta}_{14})} \tag{F-61}$$

The right-hand side of eq (F-61) is the reciprocal of eq (F-32), which explains the increase in the sum of the relative modulation depths of the ^{14}N nuclear transition frequencies with an additional ^{14}N nucleus that is distinguishable from the other ^{14}N nucleus. On the other hand, if K^{α}_{14}, $K^{\alpha}_{14'}$, K^{β}_{14}, and $K^{\beta}_{14'}$ are much smaller than 1, the factor converges to $1 - pq/(q+1)$, where q is the ratio of $K^{\alpha}_{14'}$ to K^{α}_{14}. If the K^{α}_{14}, $K^{\alpha}_{14'}$, K^{β}_{14}, and $K^{\beta}_{14'}$ values are assumed to be 0.150, eq (F-60) becomes:

$$F(p\ ^{15}\mathrm{N}/0\ ^{15}\mathrm{N}) = \frac{1.445\,(0.255 - 0.105\,p)}{0.255\,(1.445 + 0.255\,p)} \tag{F-62}$$

In the case that two-thirds of either ^{14}N is replaced with ^{15}N, the ratio $F(p\ ^{15}\mathrm{N}/0\ ^{15}\mathrm{N})$ is approximately 0.649, which indicates that the sum of the relative modulation depths of the ^{14}N transition frequencies decreases by 35.1%. Since two-thirds of either ^{14}N means one third of the entire ^{14}N nuclei, the decrease by 35.1% is similar to the fraction of replacement, which is approximately 33.3%.

F.3 USE OF DEFINITE INTEGRALS INSTEAD OF MODULATION DEPTHS

Since an ESEEM time-domain signal may contain modulations at several different frequencies, it is often difficult to obtain the modulation depths of some frequencies. The modulation at each frequency can be expressed as the product of a constant and a damped oscillating function. Also, it has already been shown that the coefficient of the damped oscillating function depends on the fraction of a certain type of nucleus replaced, f. Therefore, a general three-pulse ESEEM signal with l different frequencies is given by:

$$V(t,\, T,\, f) = K_0(t,\, f)\, S_0(T) + \sum_{i=1}^{l} K_i(t,\, f)\, S_i(t,\, T) \;\; (i = 1,\, 2,\, 3,\, \cdots,\, l) \qquad \text{(F-63)}$$

where K_i $(i = 0,\, 1,\, 2,\, \cdots,\, l)$ and S_i $(i = 1,\, 2,\, 3,\, \cdots,\, l)$ are the amplitude parameter and the damped oscillating function of the modulation at *i*th frequency, ω_i, respectively, and S_0 is a decay function. The ratio of the modulation depth of the frequency ω_a to that of the frequency ω_b is K_a/K_b. Then, the Fourier transform of $V(t,\, T,\, f)$ with respect to T is given by:

$$\mathcal{V}(t,\, \omega,\, f) = K_0(t,\, f)\, \mathcal{S}_0(\omega) + \sum_{i=1}^{l} K_i(t,\, f)\, \mathcal{S}_i(t,\, \omega) \;\; (i = 1,\, 2,\, 3,\, \cdots,\, l) \qquad \text{(F-64)}$$

where $\mathcal{S}_i$ $(i = 0,\, 1,\, 2,\, \cdots,\, l)$ is the Fourier transform of S_i. For each i $(i = 1,\, 2,\, 3,\, \cdots,\, l)$, the definite integral of the function $\mathcal{S}_i(t,\, \omega)$ through the spectral bandwidth in the (angular) frequency domain is considered and denoted as $\mathcal{I}_i(t)$.

$$\mathcal{I}_i(t) = \int_{-\omega_{BW}}^{\omega_{BW}} \mathcal{S}_i(t,\, \omega)\, dw \qquad \text{(F-65)}$$

where ω_{BW} and $-\omega_{BW}$ are the upper limit and the lower limit of the spectral bandwidth, respectively. Since the function $\mathcal{S}_i(t,\, \omega)$ is peaked at a specific frequency of ω_i, the integral from $\omega_i - \delta\omega_i$ to $\omega_i + \delta\omega_i$ with an appropriate $\delta\omega_i$ can account for a significant portion of the integral $\mathcal{I}_i(t)$. If an absorptive Lorentzian curve with a full-width at half maximum of Γ_i is assumed, the integral $\mathcal{I}_i(t)$ is independent of τ and expressed as:

$$\mathcal{A}_i = \int_{-\omega_{BW}}^{\omega_{BW}} \frac{2\Gamma_i}{4(\omega - \omega_i)^2 + {\Gamma_i}^2}\, d\omega = \tan^{-1}\left[\frac{2(\omega_{BW} + \omega_i)}{\Gamma_i}\right] + \tan^{-1}\left[\frac{2(\omega_{BW} - \omega_i)}{\Gamma_i}\right] \qquad \text{(F-66)}$$

In eq (F-66), $\mathcal{A}_i$ is used in lieu of $\mathcal{I}_i$ to denote the absorptive Lorentzian. Similarly, the integral between $\omega_i - \delta\omega_i$ and $\omega_i + \delta\omega_i$, $\mathcal{A}_i^{\delta\omega_i}$, is:

$$\mathcal{A}_i^{\delta\omega_i} = 2\tan^{-1}\left(\frac{2\delta\omega_i}{\Gamma_i}\right) \tag{F-67}$$

It is obvious that the ratio of $\mathcal{A}_i^{\delta\omega_i}$ to $\mathcal{A}_i$ is larger with a smaller Γ_i value. Calculations show that the ratio, $\mathcal{A}_i^{\delta\omega_i}/\mathcal{A}_i$, is greater than 0.8, 0.9, and 0.95 with a $\delta\omega_i$ value of 1.5, 2.9, and 5.3 MHz, respectively, provided that a Γ_i value of 1 MHz and a spectral bandwidth of 62.5 MHz are assumed. Also, it is noteworthy that the ratio $\mathcal{A}_i^{\delta\omega_i}/\mathcal{A}_i$ is a function of ω_i, $\delta\omega_i$, Γ_i, and ω_{BW}.

Even though the absorptive Lorentzian lineshape leads to a better resolved spectrum, a magnitude spectrum is more generally obtained due to the phase difference. If a peak with a full-width at half maximum of Γ_i in a magnitude spectrum is considered, the integral $\mathcal{I}_i(t)$ is given by:

$$\begin{aligned}\mathcal{M}_i &= \int_{-\omega_{BW}}^{\omega_{BW}} \frac{2\sqrt{3}}{\sqrt{12(\omega-\omega_i)^2+{\Gamma_i}^2}}\,d\omega \\ &= \ln\left[\frac{\left[\sqrt{12(\omega_{BW}+\omega_i)^2+{\Gamma_i}^2}+2\sqrt{3}(\omega_{BW}+\omega_i)\right]\left[\sqrt{12(\omega_{BW}-\omega_i)^2+{\Gamma_i}^2}+2\sqrt{3}(\omega_{BW}-\omega_i)\right]}{{\Gamma_i}^2}\right]\end{aligned} \tag{F-68}$$

In eq (F-68), $\mathcal{M}_i$ is used to denote the magnitude spectrum. Likewise, the integral between $\omega_i - \delta\omega_i$ and $\omega_i + \delta\omega_i$, $\mathcal{M}_i^{\delta\omega_i}$, is:

$$\mathcal{M}_i^{\delta\omega_i} = 2\ln\left(\frac{\sqrt{12{\delta\omega_i}^2+{\Gamma_i}^2}+2\sqrt{3}\,\delta\omega_i}{\Gamma_i}\right) \tag{F-69}$$

Like $\mathcal{A}_i^{\delta\omega_i}/\mathcal{A}_i$, the ratio of $\mathcal{M}_i^{\delta\omega_i}$ to $\mathcal{M}_i$ is larger with a smaller Γ_i value and a function of ω_i, $\delta\omega_i$, Γ_i, and ω_{BW}. Calculations show that the ratio, $\mathcal{M}_i^{\delta\omega_i}/\mathcal{M}_i$, is greater than 0.5, 0.6, 0.7, and

0.8 with a $\delta\omega_i$ value of 2.1 3.6, 6.2, and 10.7 MHz, respectively, provided that a Γ_i value of 1 MHz and a spectral bandwidth of 62.5 MHz are assumed.

In eq (F-63), the relative modulation depth of the frequency ω_a, which is defined as the modulation depth of the frequency ω_a normalized by the that of the frequency ω_b, is denoted as $K_a(t,\, f)/K_b(t,\, f)$. According to eqs (F-64) and (F-65), the integrals of the frequencies ω_a and ω_b in the (angular) frequency domain are expressed as $K_a(t,\, f)\,\mathcal{I}_a(t)$ and $K_b(t,\, f)\,\mathcal{I}_b(t)$, respectively. Since magnitude spectra are obtained in our experiments, the integrals can be rewritten as $K_a(t,\, f)\,\mathcal{M}_a$ and $K_b(t,\, f)\,\mathcal{M}_b$, respectively. Then, the relative integral of the frequency ω_a, which is defined as the integral of the frequency ω_a normalized by the integral of the frequency ω_b, is $K_a(t,\, f)\,\mathcal{M}_a/K_b(t,\, f)\,\mathcal{M}_b$.

If no ^{14}N nucleus is replaced with ^{15}N, the fraction of ^{15}N, f, is 0. The relative modulation depth of the frequency ω_a in the time domain becomes $K_a(t,\, 0)/K_b(t,\, 0)$ and its relative integral in the (angular) frequency domain becomes $K_a(t,\, 0)\,\mathcal{M}_a/K_b(t,\, 0)\,\mathcal{M}_b$. As already shown in eqs (F-41) and (F-50), one can calculate the decrease in the relative modulation depth of the frequency ω_a by comparing $K_a(t,\, f)/K_b(t,\, f)$ with $K_a(t,\, 0)/K_b(t,\, 0)$.

$$F_K(f\ {}^{15}\mathrm{N}/0\ {}^{15}\mathrm{N}) = \frac{K_a(t,\, f)/K_b(t,\, f)}{K_a(t,\, 0)/K_b(t,\, 0)} \tag{F-70}$$

where the subscript K denotes the comparison of modulation depths. Similarly, the decrease in the relative integral of the frequency is calculated by comparing $K_a(t,\, f)\,\mathcal{M}_a/K_b(t,\, f)\,\mathcal{M}_b$ with $K_a(t,\, 0)\,\mathcal{M}_a/K_b(t,\, 0)\,\mathcal{M}_b$.

$$F_I(f\ {}^{15}\mathrm{N}/0\ {}^{15}\mathrm{N}) = \frac{K_a(t,\, f)\,\mathcal{M}_a/K_b(t,\, f)\,\mathcal{M}_b}{K_a(t,\, 0)\,\mathcal{M}_a/K_b(t,\, 0)\,\mathcal{M}_b} = \frac{K_a(t,\, f)/K_b(t,\, f)}{K_a(t,\, 0)/K_b(t,\, 0)} \tag{F-71}$$

where the subscript I denotes the comparison of integrals. It is concluded from eq (F-71) that the decrease in the relative integral is the same as that in the modulation depth. Also, if the integral between $\omega_a - \delta\omega_a$ and $\omega_a + \delta\omega_a$, $\mathcal{M}_a^{\delta\omega_a}$, and the integral between $\omega_b - \delta\omega_b$ and $\omega_b + \delta\omega_b$, $\mathcal{M}_b^{\delta\omega_b}$, are used instead of $\mathcal{M}_a$ and $\mathcal{M}_b$, respectively, the decrease in the new relative integral of the frequency is expressed as:

$$F_I^{\delta}(f\ ^{15}\mathrm{N}/0\ ^{15}\mathrm{N}) = \frac{K_a(t,\ f)\,\mathcal{M}_a^{\delta\omega_a}/K_b(t,\ f)\,\mathcal{M}_b^{\delta\omega_b}}{K_a(t,\ 0)\,\mathcal{M}_a^{\delta\omega_a}/K_b(t,\ 0)\,\mathcal{M}_b^{\delta\omega_b}} = \frac{K_a(t,\ f)/K_b(t,\ f)}{K_a(t,\ 0)/K_b(t,\ 0)} \qquad \text{(F-72)}$$

where the superscript δ denotes the integral over a part of the spectral bandwidth. Therefore, the comparison of the integrals over a part of the spectral bandwidth can be used for the same purpose.

In fact, the relatively broad lineshape of magnitude spectra might cause significant overlaps of two or more peaks in some frequency regions. In addition, magnitude spectra essentially have cross-term errors. A large difference in frequencies may alleviate these problems. We use the ^{14}N transition frequencies ranging approximately from 0.5 MHz to 5 MHz and the transition frequency of a weakly coupled ^{1}H nuclear spin, whose Larmor frequency ranges between 11 MHz and 15.5 MHz with a magnetic field swept from 2600 G to 3600 G. Calculations reveal that when the difference in two frequencies and the full-width at half maximum are assumed to be 10 MHz and 1 MHz, respectively, the intensity of one magnitude Lorentizan line at the peak of the other magnitude Lorentzian line is less than 2.9% the intensity at its own peak.

F.4 CALCULATION OF THE DEFINITE INTEGRALS OF SOME SIMULATED THREE-PULSE ESEEM SPECTRA

Figure F-2 illustrates the simulated three-pulse ESEEM spectra of two systems with different numbers of coupled ^{14}N nuclear spins. One ^{14}N nuclear spin and one weakly coupled ^{1}H nuclear spin are assumed for the spectrum in gray whereas two equivalent ^{14}N nuclei and one weakly coupled ^{1}H nucleus are for the spectrum in black.nce an ESEEM time-domain

When the nuclear quadrupole interaction (NQI) region and DQ region of the ^{14}N-ESEEM are considered together, the normalized ^{14}N-ESEEM intensity of the system with two ^{14}N nuclear spins is approximately 1.78 times as much as that of the system with only one ^{14}N. The approximately 11% deviation from 2 may be explained by the modulation depths that are not small enough to ignore. However, when the NQI region of the ^{14}N-ESEEM, which is between 0 and 2 MHz, or the DQ region, which is roughly between 2 and 8 MHz, is considered separately, the ratio between the two normalized ^{14}N-ESEEM intensities changes. In eq (F-24), the ratio $F(2\ {}^{14}\mathrm{N}/1\ {}^{14}\mathrm{N})$ depends on the modulation depths of the frequencies in both electron spin manifolds. Also, it is expected from the equation that the ratio $F(2\ {}^{14}\mathrm{N}/1\ {}^{14}\mathrm{N})$ is smaller for the electron spin manifold with the deeper modulation than the other electron spin manifold. For weakly coupled ^{14}N nuclear spins, the frequencies in the α manifold have deeper modulations than those in the β manifold as the former and the latter correspond to the NQI transition and the DQ transition, respectively. In our simulations, the ratios for the NQI region and the DQ region are 1.57 and 2.23, respectively, which is consistent with the expectation.

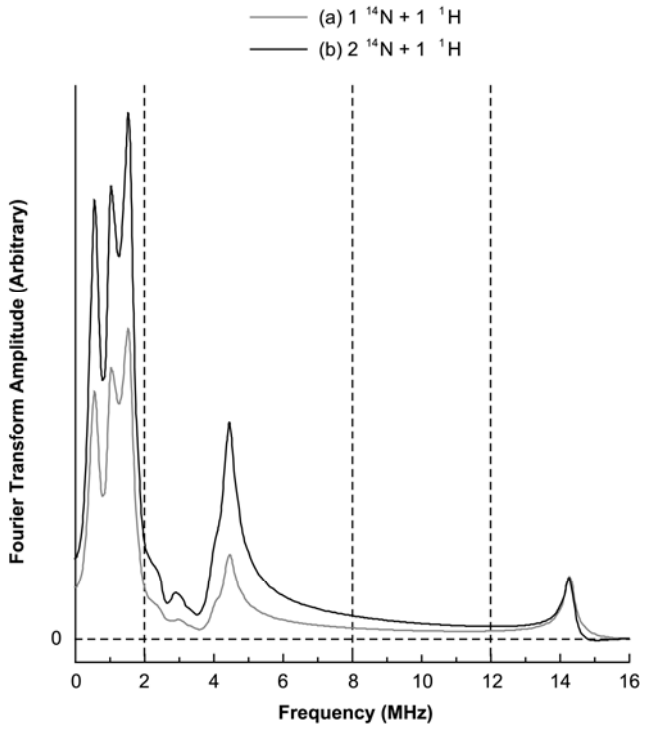

Figure F-2. Simulated three-pulse ESEEM spectra of an electron spin system to which one ^{14}N and one ^{1}H nuclear spin are coupled and another electron spin system to which two equivalent ^{14}N nuclear spins and one ^{1}H nuclear spin are coupled. The vertical dashed lines separate the NQI region (0–2 MHz), DQ region (2–8 MHz), and ^{1}H-ESEEM region (12–16 MHz).

The negative deviation from 2 is possibly due to the deeper modulations of the frequencies in the α manifold while the positive deviation from 2 may be accounted for by some combinations or harmonics of the fundamental NQI transition frequencies.

To assess the contribution of each histidine residue to the Cu(II) coordination in the Cu(II)–Aβ(1–16) and dien–Cu(II)–Aβ(1–16) complexes, we compare the decrease in the normalized ^{14}N-ESEEM intensity caused by replacing ^{14}N of either His6, His13, or His14 with ^{15}N. It is assumed that the ESEEM-active ^{14}N nuclei of all the three residues have almost identical ESEEM parameters including e^2qQ/h, η, A_{iso}, and $|T|$ because there is little difference in the spectral shape between the nonlabeled versions and their ^{15}N-labeled counterparts irrespective of which residue is ^{15}N-enriched. Thus, one can consider the ESEEM-active ^{14}N nuclei of the three residues to be equivalent, which means that the frequencies and their modulation depths attributed to the three residues are essentially identical to one another.

Our simulations reveal that the spectral shape of the three-pulse ESEEM spectrum may depend on the Euler angles between the quadrupole tensor and the hyperfine tensor when the other NQI and hyperfine parameters are identical. In the Cu(II)–Aβ(1–16) complex, the Euler angles of the ESEEM-active ^{14}N nuclei of two different histidine residues might be different because the two residues simultaneously coordinate to Cu(II). Nevertheless, only little difference in the angles or little dependency of the spectral shape on the angles is expected between the two simultaneously Cu(II)-coordinated histidine residues because the shapes of the experimentally obtained spectra are not significantly different from one another. Figure F-3 shows the difference in spectral shape due to different Euler angles. While the three NQI frequencies remain identical, the double-quantum frequency is affected by the angles.

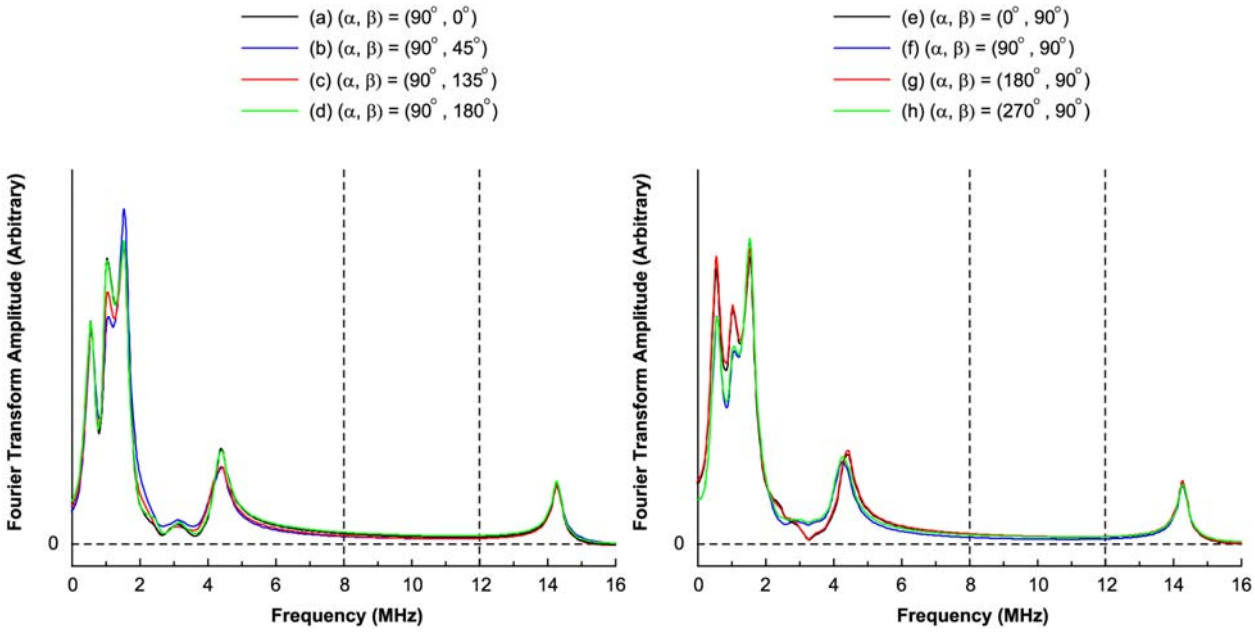

Figure F-3. Simulated three-pulse ESEEM spectra of an electron spin system to which one ^{14}N and one ^{1}H nuclear spin are coupled with different Euler angles. The vertical dashed lines separate the ^{14}N-ESEEM region (0–8 MHz) and ^{1}H-ESEEM region (12–16 MHz).

Interestingly, the normalized ^{14}N-ESEEM intensity varies only within 5% of the average value in spite of the different spectral shapes due to the different Euler angles. Therefore, if the difference in the normalized ^{14}N-ESEEM intensity between two of the three ^{15}N-labeled Cu(II)–Aβ(1–16) complexes is larger than the expected deviation, it is probable that the difference results, at least partially, from the different contributions of the two histidine residues.

BIBLIOGRAPHY

1. Rickard, G. A.; Gomez-Balderas, R.; Brunelle, P.; Raffa, D. F.; Rauk, A. Binding Affinities for Models of Biologically Available Potential Cu(II) Ligands Relevant to Alzheimer's Disease: An ab Initio Study. *J. Phys. Chem. A* **2005**, *109*, 8361–8370.

2. Klein, W. L.; Stine, W. B.; Teplow, D. B. Small Assemblies of Unmodified Amyloid β-Protein are the Proximate Neurotoxin in Alzheimer's Disease. *Neurobiol. Aging* **2004**, *25*, 569–580.

3. Tabner, B. J.; El-Agnaf, O. M. A.; Turnbull, S.; German, M. J.; Paleologou, K. E.; Hayashi, Y.; Cooper, L. J.; Fullwood, N. J.; Allsop, D. Hydrogen Peroxide Is Generated during the Very Early Stages of Aggregation of the Amyloid Peptides Implicated in Alzheimer Disease and Familial British Dementia. *J. Biol. Chem.* **2005**, *280*, 35789–35792.

4. Karr, J. W.; Akintoye, H.; Kaupp, L. J.; Szalai, V. A. N-Terminal Deletions Modify the Cu^{2+} Binding Site in Amyloid-β. *Biochemistry* **2005**, *44*, 5478–5487.

5. Ma, Q.-F.; Hu, J.; Wu, W.-H.; Liu, H.-D.; Du, J.-T.; Fu, Y.; Wu, Y.-W.; Lei, P.; Zhao, Y.-F.; Li, Y.-M. Characterization of Copper Binding to the Peptide Amyloid-beta(1–16) Associated with Alzheimer's Disease. *Biopolymers* **2006**, *83*, 20–31.

6. Guilloreau, L.; Damian, L.; Coppel, Y.; Mazarguil, H.; Winterhalter, M.; Faller, P. Structural and Thermodynamical Properties of CuII Amyloid-β16/28 Complexes Associated with Alzheimer's Disease. *J. Biol. Inorg. Chem.* **2006**, *11*, 1024–1038.

7. Hong, L.; Bush, W. D.; Hatcher, L. Q.; Simon, J. Determining Thermodynamic Parameters from Isothermal Calorimetric Isotherms of the Binding of Macromolecules to Metal Cations Originally Chelated by a Weak Ligand. *J. Phys. Chem. B* **2007**, *112*, 604–611.

8. Hatcher, L. Q.; Hong, L.; Bush, W. D.; Carducci, T.; Simon, J. D. Quantification of the Binding Constant of Copper(II) to the Amyloid-Beta Peptide. *J. Phys. Chem. B* **2008**, *112*, 8160–8164.

9. Peisach, J.; Blumberg, W. E. Structural Implications Derived from the Analysis of Electron Paramagnetic Resonance Spectra of Natural and Artificial Copper Proteins. *Arch. Biochem. Biophys.* **1974**, *165*, 691–708.

10. Mims, W. B. Envelope Modulation in Spin-Echo Experiments. *Phys. Rev. B* **1972**, *5*, 2409–2419.

11. Weil, J. A.; Bolton, J. R., Electron Paramagnetic Resonance: Elementary Theory and Practical Applications. Second ed.; John Wiley & Sons, Inc.: Hoboken, New Jersey, **2007**.

12. Gauerke, E. S. J.; Campbell, M. L. A Simple, Systmatic Method for Determining J levels for J–J Coupling. *J. Chem. Educ.* **1994**, *71*, 457–463.

13. Slichter, C. P., Principles of Magnetic Resonance. Third ed.; Springer-Verlag: Heidelberg, Germany, **1978**.

14. Savelieff, M. G.; Wilson, T. D.; Elias, Y.; Nilges, M. J.; Garner, D. K.; Lu, Y. Experimental Evidence for a Link among Cupredoxins: Red, Blue, and Purple Copper Transformations in Nitrous Oxide Reductase. *Proc. Natl. Acad. Sci. U.S.A.* **2008**, *105*, 7919–7924.

15. Kevan, L.; Bowman, M. K.; Narayana, P. A.; Boeckman, R. K.; Yudanov, V. F.; Tsvetkov, Y. D. Electron Spin Echo Envelope Modulation of Trapped Radicals in Disordered Glassy Systems: Application to the Molecular Structure around Excess Electrons in gamma-Irradiated 2-Methyltetrahydrofuran glass. *J. Chem. Phys.* **1975**, *63*, 409–416.

16. Mims, W. B.; Davis, J. L. Proton Modulation of the Electron Spin Echo Envelope in a Nd^{3+}: Aquo Glass. *J. Chem. Phys.* **1976**, *64*, 4836–4846.

17. Burns, C. S.; Aronoff-Spencer, E.; Dunham, C. M.; Lario, P.; Avdievich, N. I.; Antholine, W. E.; Olmstead, M. M.; Vrielink, A.; Gerfen, G. J.; Peisach, J.; Scott, W. G.; Millhauser, G. L. Molecular Features of the Copper Binding Sites in the Octarepeat Domain of the Prion Protein. *Biochemistry* **2002**, *41*, 3991–4001.

18. Höfer, P.; Grupp, A.; Nebenführ, H.; Mehring, M. Hyperfine Sublevel Correlation (HYSCORE) Spectroscopy: A 2D ESR Investigation of the Squaric Acid Radical. *Chem. Phys. Lett.* **1986**, *132*, 279–282.

19. Ponti, A.; Schweiger, A. Nuclear Coherence-Transfer Echoes in Pulsed EPR. *J. Chem. Phys.* **1995**, *102*, 5207–5219.

20. Höfer, P. Distortion-Free Electron-Spin-Echo Envelope-Modulation Spectra of Disordered Solids Obtained from Two-Dimensional and Three-Dimensional HYSCORE Experiments. *J. Magn. Reson. Series A* **1994**, *111*, 77–86.

21. Kofman, V.; Shane, J. J.; Dikanov, S. A.; Bowman, M. K.; Libman, J.; Shanzer, A.; Goldfarb, D. Coordination of Cu(II) to Lipophilic Bis-hydroxamate Binders As Studied by One- and Two-Dimensional Electron Spin Echo Spectroscopy. *J. Am. Chem. Soc.* **1995**, *117*, 12771–12778.

22. Kofman, V.; Farver, O.; Pecht, I.; Goldfarb, D. Two-Dimensional Pulsed EPR Spectroscopy of the Copper Protein Azurin. *J. Am. Chem. Soc.* **1996**, *118*, 1201–1206.

23. Mims, W. B.; Peisach, J. The Nuclear Modulation Effect in Electron Spin Echoes for Complexes of Cu^{2+} and Imidazole with ^{14}N and ^{15}N. *J. Chem. Phys.* **1978**, *69*, 4921–4930.

24. Lee, H.-I.; Doan, P. E.; Hoffman, B. M. General Analysis of ^{14}N (I = 1) Electron Spin Echo Envelope Modulation. *J. Magn. Reson.* **1999**, *140*, 91–107.

25. Flanagan, H. L.; Singel, D. J. Analysis of ^{14}N ESEEM Patterns of Randomly Oriented Solids. *J. Chem. Phys.* **1987**, *87*, 5606–5616.

26. Flanagan, H. L.; Gerfen, G. J.; Singel, D. J. Multifrequency Electron Spin-Echo Envelope Modulation: The Determination of Nitro Group ^{14}N Hyperfine and Quadrupole Interactions of DPPH in Frozen Solution. *J. Chem. Phys.* **1988**, *88*, 20–24.

27. Gerfen, G. J.; Singel, D. J. Determination of Hyperfine Interaction Matrix Principal Values and Principal Axis Orientations in an Orientationally Disordered Solid: A Multifrequency Electron Spin Echo Envelope Modulation Study of Nitrogen-15 in a Copper(II)–^{15}N–Imidazole Complex. *J. Chem. Phys.* **1994**, *100*, 4127–4137.

28. McCracken, J.; Peisach, J.; Dooley, D. M. Cu(II) Coordination Chemistry of Amine Oxidases: Pulsed EPR Studies of Histidine Imidazole, Water, and Exogenous Ligand Coordination. *J. Am. Chem. Soc.* **1987**, *109*, 4064–4072.

29. Kosman, D. J.; Peisach, J.; Mims, W. B. Pulsed Electron Paramagnetic Resonance Studies of the Copper(II) Site in Galactose Oxidase. *Biochemistry* **1980**, *19*, 1304–1308.

30. McCracken, J.; Pember, S.; Benkovic, S. J.; Villafranca, J. J.; Miller, R. J.; Peisach, J. Electron Spin-Echo Studies of the Copper Binding Site in Phenylalanine Hydroxylase from Chromobacterium violaceum. *J. Am. Chem. Soc.* **1988**, *110*, 1069–1074.

31. McCracken, J.; Desai, P. R.; Papadopoulos, N. J.; Villafranca, J. J.; Peisach, J. Electron Spin-Echo Studies of the Copper(II) Binding Sites in Dopamine β-Hydroxylase. *Biochemistry* **1988**, *27*, 4133–4137.

32. Jiang, F.; McCracken, J.; Peisach, J. Nuclear Quadrupole Interactions in Copper(II)-Diethylenetriamine-Substituted Imidazole Complexes and in Copper(II) Proteins. *J. Am. Chem. Soc.* **1990**, *112*, 9035–9044.

33. McCracken, J.; Peisach, J.; Cote, C. E.; McGuirl, M. A.; Dooley, D. M. Pulsed EPR Studies of the Semiquinone State of Copper-Containing Amine Oxidases. *J. Am. Chem. Soc.* **1992**, *114*, 3715–3720.

34. McLaurin, J.; Chakrabartty, A. Membrane Disruption by Alzheimer β-Amyloid Peptides Mediated through Specific Binding to Either Phospholipids or Gangliosides. *J. Biol. Chem.* **1996**, *271*, 26482–26489.

35. Walsh, D. M.; Lomakin, A.; Benedek, G. B.; Condron, M. M.; Teplow, D. B. Amyloid β-Protein Fibrillogenesis. *J. Biol. Chem.* **1997**, *272*, 22364–22372.

36. Lambert, M. P., et al. Diffusible, Nonfibrillar Ligands Derived from Aβ1–42 Are Potent Central Nervous System Neurotoxins. *Proc. Natl. Acad. Sci. U.S.A.* **1998**, *95*, 6448–6453.

37. Hardy, J.; Selkoe, D. J. The Amyloid Hypothesis of Alzheimer's Disease: Progress and Problems on the Road to Therapeutics. *Science* **2002**, *297*, 353–356.

38. Carrotta, R.; Manno, M.; Bulone, D.; Martorana, V.; Biagio, P. L. S. Protofibril Formation of Amyloid β-Protein at Low pH via a Non-cooperative Elongation Mechanism. *J. Biol. Chem.* **2005**, *280*, 30001–30008.

39. Lovell, M. A.; Robertson, J. D.; Teesdale, W. J.; Campbell, J. L.; Markesbery, W. R. Copper, Iron and Zinc in Alzheimer's Disease Senile Plaques. *J. Neurol. Sci.* **1998**, *158*, 47–52.

40. Huang, X., et al. Cu(II) Potentiation of Alzheimer Aβ Neurotoxicity: Correlation with Cell-Free Hydrogen Peroxide Production and Metal Reduction. *J. Biol. Chem.* **1999**, *274*, 37111–37116.

41. Bush, A. I. Metal Complexing Agents as Therapies for Alzheimer's Disease. *Neurobiol. Aging* **2002**, *23*, 1031–1038.

42. Kirkitadze, M. D.; Bitan, G.; Teplow, D. B. Paradigm Shifts in Alzheimer's Disease and Other Neurodegenerative Disorders: The Emerging Role of Oligomeric Assemblies. *J. Neurosci. Res.* **2002**, *69*, 567–577.

43. Miller, L. M.; Wang, Q.; Telivala, T. P.; Smith, R. J.; Lanzirotti, A.; Miklossy, J. Synchrotron-Based Infrared and X-ray Imaging Shows Focalized Accumulation of Cu and Zn Co-localized with β-Amyloid Deposits in Alzheimer's Disease. *J. Struct. Biol.* **2006**, *155*, 30–37.

44. Jun, S.; Saxena, S. The Aggregated State of Amyloid-beta Peptide In Vitro Depends on Cu^{2+} Ion Concentration. *Angew. Chem., Int. Ed.* **2007**, *46*, 3959–3961.

45. Karr, J. W.; Kaupp, L. J.; Szalai, V. A. Amyloid-β Binds Cu^{2+} in a Mononuclear Metal Ion Binding Site. *J. Am. Chem. Soc.* **2004**, *126*, 13534–13538.

46. Karr, J. W.; Szalai, V. A. Cu(II) Binding to Monomeric, Oligomeric, and Fibrillar Forms of the Alzheimer's Disease Amyloid-β Peptide. *Biochemistry* **2008**, *47*, 5006–5016.

47. Kowalik-Jankowska, T.; Ruta, M.; Wisniewska, K.; Lankiewicz, L. Coordination Abilities of the 1–16 and 1–28 Fragments of β-Amyloid Peptide towards Copper(II) Ions: A Combined Potentiometric and Spectroscopic Study. *J. Inorg. Biochem.* **2003**, *95*, 270–282.

48. Syme, C. D.; Nadal, R. C.; Rigby, S. E. J.; Viles, J. H. Copper Binding to the Amyloid-β (Aβ) Peptide Associated with Alzheimer's Disease. *J. Biol. Chem.* **2004**, *279*, 18169–18177.

49. Raffa, D. F.; Rauk, A. Molecular Dynamics Study of the Beta Amyloid Peptide of Alzheimer's Disease and Its Divalent Copper Complexes. *J. Phys. Chem. B* **2007**, *111*, 3789–3799.

50. Aronoff-Spencer, E.; Burns, C. S.; Avdievich, N. I.; Gerfen, G. J.; Peisach, J.; Antholine, W. E.; Ball, H. L.; Cohen, F. E.; Prusiner, S. B.; Millhauser, G. L. Identification of the Cu^{2+} Binding Sites in the N-Terminal Domain of the Prion Protein by EPR and CD Spectroscopy. *Biochemistry* **2000**, *39*, 13760–13771.

51. Burns, C. S.; Aronoff-Spencer, E.; Legname, G.; Prusiner, S. B.; Antholine, W. E.; Gerfen, G. J.; Peisach, J.; Millhauser, G. L. Copper Coordination in the Full-Length, Recombinant Prion Protein. *Biochemistry* **2003**, *42*, 6794–6803.

52. Millhauser, G. L. Copper Binding in the Prion Protein. *Acc. Chem. Res.* **2004**, *37*, 79–85.

53. Chattopadhyay, M.; Walter, E. D.; Newell, D. J.; Jackson, P. J.; Aronoff-Spencer, E.; Peisach, J.; Gerfen, G. J.; Bennett, B.; Antholine, W. E.; Millhauser, G. L. The Octarepeat Domain of the Prion Protein Binds Cu(II) with Three Distinct Coordination Modes at pH 7.4. *J. Am. Chem. Soc.* **2005**, *127*, 12647–12656.

54. Walter, E. D.; Chattopadhyay, M.; Millhauser, G. L. The Affinity of Copper Binding to the Prion Protein Octarepeat Domain: Evidence for Negative Cooperativity. *Biochemistry* **2006**, *45*, 13083–13092.

55. Atwood, C. S.; Scarpa, R. C.; Huang, X.; Moir, R. D.; Jones, W. D.; Fairlie, D. P.; Tanzi, R. E.; Bush, A. I. Characterization of Copper Interactions with Alzheimer Amyloid β Peptides. *J. Neurochem.* **2000**, *75*, 1219–1233.

56. Fauth, J. M.; Schweiger, A.; Braunschweiler, L.; Forrer, J.; Ernst, R. R. Elimination of Unwanted Echoes and Reduction of Dead Time in Three-Pulse Electron Spin-Echo Spectroscopy. *J. Magn. Reson.* **1986**, *66*, 74–85.

57. Gemperle, C.; Aebli, G.; Schweiger, A.; Ernst, R. R. Phase Cycling in Pulse EPR. *J. Magn. Reson.* **1990**, *88*, 241–256.

58. Dikanov, S. A.; Tsvetkov, Y. D.; Bowman, M. K.; Astashkin, A. V. Parameters of Quadrupole Coupling of ^{14}N Nuclei in Chlorophyll a Cations Determined by the Electron Spin Echo Method. *Chem. Phys. Lett.* **1982**, *90*, 149–153.

59. Astashkin, A. V.; Kawamori, A. A New Fourier-Transformation-Based Algorithm for Data Filtering and Extrapolation. *J. Magn. Reson. Series A* **1995**, *112*, 24–29.

60. Vogt, M.; Lahiri, S.; Hoogstraten, C. G.; Britt, R. D.; DeRose, V. J. Coordination Environment of a Site-Bound Metal Ion in the Hammerhead Ribozyme Determined by ^{15}N and ^{2}H ESEEM Spectroscopy. *J. Am. Chem. Soc.* **2006**, *128*, 16764–16770.

61. Lai, A.; Flanagan, H. L.; Singel, D. J. Multifrequency Electron Spin Echo Envelope Modulation in S=1/2, I=1/2 systems: Analysis of the Spectral Amplitudes, Line Shapes, and Linewidths. *J. Chem. Phys.* **1988**, *89*, 7161–7166.

62. Tang, X. S.; Diner, B. A.; Larsen, B. S.; Gilchrist, M. L.; Lorigan, G. A.; Britt, R. D. Identification of Histidine at the Catalytic Site of the Photosynthetic Oxygen-Evolving Complex. *Proc. Natl. Acad. Sci. U.S.A.* **1994**, *91*, 704–708.

63. Singh, V.; Zhu, Z.; Davidson, V. L.; McCracken, J. Characterization of the Tryptophan Tryptophyl-Semiquinone Catalytic Intermediate of Methylamine Dehydrogenase by Electron Spin−Echo Envelope Modulation Spectroscopy. *J. Am. Chem. Soc.* **2000**, *122*, 931–938.

64. Goldfarb, D.; Fauth, J. M.; Tor, Y.; Shanzer, A. Study of Copper(II) Binding to Chiral Tripodal Ligands by Electron Spin Echo Spectroscopy. *J. Am. Chem. Soc.* **1991**, *113*, 1941–1948.

65. Pöppl, A.; Kevan, L. A Practical Strategy for Determination of Proton Hyperfine Interaction Parameters in Paramagnetic Transition Metal Ion Complexes by Two-Dimensional HYSCORE Electron Spin Resonance Spectroscopy in Disordered Systems. *J. Phys. Chem.* **1996**, *100*, 3387–3394.

66. Dikanov, S. A.; Bowman, M. K. Cross-Peak Lineshape of Two-Dimensional ESEEM Spectra in Disordered S = 1/2 , I = 1/2 Spin Systems. *J. Magn. Reson. Series A* **1995**, *116*, 125–128.

67. Dikanov, S. A.; Tyryshkin, A. M.; Bowman, M. K. Intensity of Cross-Peaks in Hyscore Spectra of S = 1/2, I = 1/2 Spin Systems. *J. Magn. Reson.* **2000**, *144*, 228–242.

68. Käss, H.; Rautter, J.; Bönigk, B.; Höfer, P.; Lubitz, W. 2D ESEEM of the ^{15}N-Labeled Radical Cations of Bacteriochlorophyll a and of the Primary Donor in Reaction Centers of Rhodobacter sphaeroides. *J. Phys. Chem.* **1995**, *99*, 436–448.

69. Haass, C.; Selkoe, D. J. Soluble Protein Oligomers in Neurodegeneration: Lessons from the Alzheimer's Amyloid β-peptide. *Nat. Rev. Mol. Cell Biol.* **2007**, *8*, 101–112.

70. Crouch, P. J.; Harding, S.-M. E.; White, A. R.; Camakaris, J.; Bush, A. I.; Masters, C. L. Mechanisms of Aβ Mediated Neurodegeneration in Alzheimer's Disease. *Int. J. Biochem. Cell Biol.* **2008**, *40*, 181–198.

71. McLaurin, J.; Yang, D. S.; Yip, C. M.; Fraser, P. E. Review: Modulating Factors in Amyloid-β Fibril Formation. *J. Struct. Biol.* **2000**, *130*, 259–270.

72. Bush, A. I. The Metallobiology of Alzheimer's Disease. *Trends Neurosci.* **2003**, *26*, 207–214.

73. Talmard, C.; Guilloreau, L.; Coppel, Y.; Mazarguil, H.; Faller, P. Amyloid-Beta Peptide Forms Monomeric Complexes With Cu^{II} and Zn^{II} Prior to Aggregation. *ChemBioChem* **2007**, *8*, 163–165.

74. Faller, P. Copper and Zinc Binding to Amyloid-beta: Coordination, Dynamics, Aggregation, Reactivity and Metal-Ion Transfer. *ChemBioChem* **2009**, *10*, 2837–2845.

75. Cuajungco, M. P.; Fagét, K. Y. Zinc Takes the Center Stage: Its Paradoxical Role in Alzheimer's Disease. *Brain Res. Rev.* **2003**, *41*, 44–56.

76. Garai, K.; Sahoo, B.; Kaushalya, S. K.; Desai, R.; Maiti, S. Zinc Lowers Amyloid-β Toxicity by Selectively Precipitating Aggregation Intermediates. *Biochemistry* **2007**, *46*, 10655–10663.

77. Talmard, C.; Leuma Yona, R.; Faller, P. Mechanism of Zinc(II)-Promoted Amyloid Formation: Zinc(II) Binding Facilitates the Transition from the Partially α-Helical Conformer to Aggregates of Amyloid β Protein(1–28). *J. Biol. Inorg. Chem.* **2009**, *14*, 449–455.

78. Miller, Y.; Ma, B.; Nussinov, R. Zinc Ions Promote Alzheimer Aβ Aggregation via Population Shift of Polymorphic States. *Proc. Natl. Acad. Sci. U.S.A.* **2010**, *107*, 9490–9495.

79. Huang, X.; Atwood, C. S.; Hartshorn, M. A.; Multhaup, G.; Goldstein, L. E.; Scarpa, R. C.; Cuajungco, M. P.; Gray, D. N.; Lim, J.; Moir, R. D.; Tanzi, R. E.; Bush, A. I. The Aβ Peptide of Alzheimer's Disease Directly Produces Hydrogen Peroxide through Metal Ion Reduction. *Biochemistry* **1999**, *38*, 7609–7616.

80. Dai, X.; Sun, Y.; Gao, Z.; Jiang, Z. Copper Enhances Amyloid-β Peptide Neurotoxicity and non β-Aggregation: A Series of Experiments Conducted upon Copper-Bound and Copper-Free Amyloid-β Peptide. *J. Mol. Neurosci.* **2010**, *41*, 66–73.

81. Shin, B.-k.; Saxena, S. Direct Evidence That All Three Histidine Residues Coordinate to Cu(II) in Amyloid-β_{1-16}. *Biochemistry* **2008**, *47*, 9117–9123.

82. Drew, S. C.; Noble, C. J.; Masters, C. L.; Hanson, G. R.; Barnham, K. J. Pleomorphic Copper Coordination by Alzheimer's Disease Amyloid-β Peptide. *J. Am. Chem. Soc.* **2009**, *131*, 1195–1207.

83. Drew, S. C.; Masters, C. L.; Barnham, K. J. Alanine-2 Carbonyl is an Oxygen Ligand in Cu^{2+} Coordination of Alzheimer's Disease Amyloid-β Peptide — Relevance to N-Terminally Truncated Forms. *J. Am. Chem. Soc.* **2009**, *131*, 8760–8761.

84. Dorlet, P.; Gambarelli, S.; Faller, P.; Hureau, C. Pulse EPR Spectroscopy Reveals the Coordination Sphere of Copper(II) Ions in the 1–16 Amyloid-beta Peptide: A Key Role of the First Two N-Terminus Residues. *Angew. Chem. Int. Ed.* **2009**, *48*, 9273–9276.

85. Hureau, C.; Coppel, Y.; Dorlet, P.; Solari, P. L.; Sayen, S.; Guillon, E.; Sabater, L.; Faller, P. Deprotonation of the Asp1–Ala2 Peptide Bond Induces Modification of the Dynamic Copper(II) Environment in the Amyloid-beta Peptide near Physiological pH. *Angew. Chem. Int. Ed.* **2009**, *48*, 9522–9525.

86. Faller, P.; Hureau, C. Bioinorganic Chemistry of Copper and Zinc Ions Coordinated to Amyloid-β Peptide. *Dalton Trans.* **2009**, 1080–1094.

87. Sarell, C. J.; Syme, C. D.; Rigby, S. E. J.; Viles, J. H. Copper(II) Binding to Amyloid-β Fibrils of Alzheimer's Disease Reveals a Picomolar Affinity: Stoichiometry and Coordination Geometry Are Independent of Aβ Oligomeric Form. *Biochemistry* **2009**, *48*, 4388–4402.

88. Merrifield, R. B. Solid Phase Peptide Synthesis. I. The Synthesis of a Tetrapeptide. *J. Am. Chem. Soc.* **1963**, *85*, 2149–2154.

89. Fields, G. B.; Nobel, R. L. Solid Phase Peptide Synthesis Utilizing 9-Fluourenylmethoxycarbonyl Amino Acid. *Int. J. Pept. Protein Res.* **1990**, *35*, 161–214.

90. Stoll, S.; Britt, R. D. General and Efficient Simulation of Pulse EPR Spectra. *Phys. Chem. Chem. Phys.* **2009**, *11*, 6614–6625.

91. Santangelo, M.; Medina-Molner, A.; Schweiger, A.; Mitrikas, G.; Spingler, B. Structural Analysis of Cu(II) Ligation to the 5′-GMP Nucleotide by Pulse EPR Spectroscopy. *J. Biol. Inorg. Chem.* **2007**, *12*, 767–775.

92. Santangelo, M. G.; Antoni, P. M.; Spingler, B.; Jeschke, G. Can Copper(II) Mediate Hoogsteen Base-Pairing in a Left-Handed DNA Duplex? A Pulse EPR Study. *ChemPhysChem* **2010**, *11*, 599–606.

93. Magliozzo, R. S.; Bubacco, L.; McCracken, J.; Jiang, F.; Beltramini, M.; Salvato, B.; Peisach, J. Cu(II) Coordination in Arthropod and Mollusk Green Half-Methemocyanins Analyzed by Electron Spin-Echo Envelope Modulation Spectroscopy. *Biochemistry* **1995**, *34*, 1513–1523.

94. Stoll, S.; Calle, C.; Mitrikas, G.; Schweiger, A. Peak Suppression in ESEEM Spectra of Multinuclear Spin Systems. *J. Magn. Reson.* **2005**, *177*, 93–101.

95. Hubrich, M.; Jeschke, G.; Schweiger, A. The Generalized Hyperfine Sublevel Coherence Transfer Experiment in One and Two Dimensions. *J. Chem. Phys.* **1996**, *104*, 2172–2184.

96. Jeschke, G.; Rakhmatullin, R.; Schweiger, A. Sensitivity Enhancement by Matched Microwave Pulses in One- and Two-Dimensional Electron Spin Echo Envelope Modulation Spectroscopy. *J. Magn. Reson.* **1998**, *131*, 261–271.

97. Hong, L.; Carducci, T. M.; Bush, W. D.; Dudzik, C. G.; Millhauser, G. L.; Simon, J. D. Quantification of the Binding Properties of Cu^{2+} to the Amyloid Beta Peptide: Coordination Spheres for Human and Rat Peptides and Implication on Cu^{2+}-Induced Aggregation. *J. Phys. Chem. B* **2010**, *114*, 11261–11271.

98. Ma, K.; Clancy, E. L.; Zhang, Y.; Ray, D. G.; Wollenberg, K.; Zagorski, M. G. Residue-Specific pKa Measurements of the β-Peptide and Mechanism of pH-Induced Amyloid Formation. *J. Am. Chem. Soc.* **1999**, *121*, 8698–8706.

99. Furlan, S.; La Penna, G. Modeling of the Zn^{2+} Binding in the 1–16 Region of the Amyloid β Peptide Involved in Alzheimer's Disease. *Phys. Chem. Chem. Phys.* **2009**, *11*, 6468-6481.

100. Furlan, S.; Hureau, C.; Faller, P.; La Penna, G. Modeling the Cu^{+} Binding in the 1−16 Region of the Amyloid-β Peptide Involved in Alzheimer's Disease. *J. Phys. Chem. B* **2010**, *114*, 15119–15133.

101. Karr, J. W.; Szalai, V. A. Role of Aspartate-1 in Cu(II) Binding to the Amyloid-β Peptide of Alzheimer's Disease. *J. Am. Chem. Soc.* **2007**, *129*, 3796–3797.

102. Morgan, D. M.; Dong, J.; Jacob, J.; Lu, K.; Apkarian, R. P.; Thiyagarajan, P.; Lynn, D. G. Metal Switch for Amyloid Formation: Insight into the Structure of the Nucleus. *J. Am. Chem. Soc.* **2002**, *124*, 12644–12645.

103. Ahmed, M.; Davis, J.; Aucoin, D.; Sato, T.; Ahuja, S.; Aimoto, S.; Elliott, J. I.; Van Nostrand, W. E.; Smith, S. O. Structural Conversion of Neurotoxic Amyloid-β1–42 Oligomers to Fibrils. *Nat. Struct. Mol. Biol.* **2010**, *17*, 561–567.

104. Dong, J.; Canfield, J. M.; Mehta, A. K.; Shokes, J. E.; Tian, B.; Childers, W. S.; Simmons, J. A.; Mao, Z.; Scott, R. A.; Warncke, K.; Lynn, D. G. Engineering Metal Ion Coordination To Regulate Amyloid Fibril Assembly and Toxicity. *Proc. Natl. Acad. Sci. U.S.A.* **2007**, *104*, 13313–13318.

105. Mendelkow, E. Alzheimer's Disease: The Tangled Tale of Tau. *Nature* **1999**, *402*, 588–589.

106. Masters, C. L.; Simms, G.; Weinman, N. A.; Multhaup, G.; McDonald, B. L.; Beyreuther, K. Amyloid Plaque Core Protein in Alzheimer Disease and Down Syndrome. *Proc. Natl. Acad. Sci. U.S.A.* **1985**, *82*, 4245–4249.

107. Wischik, C. M.; Novak, M.; Thøgersen, H. C.; Edwards, P. C.; Runswick, M. J.; Jakes, R.; Walker, J. E.; Milstein, C.; Roth, M.; Klug, A. Isolation of a Fragment of Tau Derived from the Core of the Paired Helical Filament of Alzheimer Disease. *Proc. Natl. Acad. Sci. U.S.A.* **1988**, *85*, 4506–4510.

108. Hung, Y.; Bush, A.; Cherny, R. Copper in the Brain and Alzheimer's Disease. *J. Biol. Inorg. Chem.* **2010**, *15*, 61–76.

109. Smith, D. G.; Cappai, R.; Barnham, K. J. The Redox Chemistry of the Alzheimer's Disease Amyloid β peptide. *Biochim. Biophys. Acta, Biomembr.* **2007**, *1768*, 1976–1990.

110. Bush, A. I.; Pettingell, W. H.; Multhaup, G.; Paradis, M. D.; Vonsattel, J.-P.; Gusella, J. F.; Beyreuther, K.; Masters, C. L.; Tanzi, R. E. Rapid Induction of Alzheimer Aβ Amyloid Formation by Zinc. *Science* **1994**, *265*, 1464–1467.

111. Huang, X.; Atwood, C. S.; Moir, R. D.; Hartshorn, M. A.; Vonsattel, J.-P.; Tanzi, R. E.; Bush, A. I. Zinc-Induced Alzheimer's Aβ1–40 Aggregation Is Mediated by Conformational Factors. *J. Biol. Chem.* **1997**, *272*, 26464–26470.

112. Atwood, C. S.; Moir, R. D.; Huang, X.; Scarpa, R. C.; Bacarra, N. M. E.; Romano, D. M.; Hartshorn, M. A.; Tanzi, R. E.; Bush, A. I. Dramatic Aggregation of Alzheimer Aβ by Cu(II) Is Induced by Conditions Representing Physiological Acidosis. *J. Biol. Chem.* **1998**, *273*, 12817–12826.

113. Jun, S.; Gillespie, J. R.; Shin, B.-k.; Saxena, S. The Second Cu(II)-Binding Site in a Proton-Rich Environment Interferes with the Aggregation of Amyloid-β(1−40) into Amyloid Fibrils. *Biochemistry* **2009**, *48*, 10724–10732.

114. Shin, B.-k.; Saxena, S. Substantial Contribution of the Two Imidazole Rings of the His13–His14 Dyad to Cu(II) Binding in Amyloid-β(1–16) at Physiological pH and Its Significance. *J. Phys. Chem. A* **2011**, *115*, in press.

115. Hou, L.; Shao, H.; Zhang, Y.; Li, H.; Menon, N. K.; Neuhaus, E. B.; Brewer, J. M.; Byeon, I.-J. L.; Ray, D. G.; Vitek, M. P.; Iwashita, T.; Makula, R. A.; Przybyla, A. B.; Zagorski, M. G. Solution NMR Studies of the Aβ(1−40) and Aβ(1−42) Peptides Establish that the Met35 Oxidation State Affects the Mechanism of Amyloid Formation. *J. Am. Chem. Soc.* **2004**, *126*, 1992−2005.

116. Sayre, L. M.; Perry, G.; Harris, P. L. R.; Liu, Y.; Schubert, K. A.; Smith, M. A. In Situ Oxidative Catalysis by Neurofibrillary Tangles and Senile Plaques in Alzheimer's Disease. *J. Neurochem.* **2000**, *74*, 270–279.

117. Rae, T. D.; Schmidt, P. J.; Pufahl, R. A.; Culotta, V. C.; O'Halloran, T. V. Undetectable Intracellular Free Copper: The Requirement of a Copper Chaperon for Superoxide Dismutase. *Science* **1999**, *284*, 805–808.

118. Becker, J. S.; Zoriy, M.; Przybylski, M.; Becker, J. S. Study of Formation of Cu- and Zn-Containing Tau Protein Using Isotopically-Enriched Tracers by LA–ICP–MS and MALDI–FTICR–MS. *J. Anal. At. Spectrom.* **2007**, *22*, 63–68.

119. Soragni, A.; Zambelli, B.; Mukrasch, M. D.; Biernat, J.; Jeganathan, S.; Griesinger, C.; Ciurli, S.; Mandelkow, E.; Zweckstetter, M. Structural Characterization of Binding of Cu(II) to Tau Protein. *Biochemistry* **2008**, *47*, 10841–10851.

120. Gómez-Ramos, A.; Díaz-Hernández, M.; Cuadros, R.; Hernández, F.; Avila, J. Extracellular Tau Is Toxic to Neuronal Cells. *FEBS Lett.* **2006**, *580*, 4842–4850.

121. Clavaguera, F.; Bolmont, T.; Crowther, R. A.; Abramowski, D.; Frank, S.; Probst, A.; Fraser, G.; Stalder, A. K.; Beibel, M.; Staufenbiel, M.; Jucker, M.; Goedert, M.; Tolnay, M. Transmission and Spreading of Tauopathy in Transgenic Mouse Brain. *Nat. Cell Biol.* **2009**, *11*, 909–913.

122. Cleveland, D. W.; Hwo, S.-Y.; Kirschner, M. W. Purification of Tau, a Microtubule-Associated Protein That Induces Assembly of Microtubules from Purified Tubulin. *J. Mol. Biol.* **1977**, *116*, 207–225.

123. Drubin, D. G.; Kirschner, M. W. Tau Protein Function in Living Cells. *J. Cell Biol.* **1986**, *103*, 2739–2746.

124. Butner, K. A.; Kirschner, M. W. Tau Protein Binds to Microtubules through a Flexible Array of Distributed Weak Sites. *J. Cell Biol.* **1991**, *115*, 717–730.

125. Gustke, N.; Trinczek, B.; Biernat, J.; Mandelkow, E. M.; Mandelkow, E. Domains of tau Protein and Interactions with Microtubules. *Biochemistry* **1994**, *33*, 9511–9522.

126. Ma, Q.-F.; Li, Y.-M.; Du, J.-T.; Kanazawa, K.; Nemoto, T.; Nakanishi, H.; Zhao, Y.-F. Binding of Copper (II) Ion to an Alzheimer's Tau Peptide As Revealed by MALDI-TOF MS, CD, and NMR. *Biopolymers* **2005**, *79*, 74–85.

127. Ma, Q.; Li, Y.; Du, J.; Liu, H.; Kanazawa, K.; Nemoto, T.; Nakanishi, H.; Zhao, Y. Copper Binding Properties of a Tau Peptide Associated with Alzheimer's Disease Studied by CD, NMR, and MALDI-TOF MS. *Peptides* **2006**, *27*, 841–849.

128. Zhou, L.-X.; Du, J.-T.; Zeng, Z.-Y.; Wu, W.-H.; Zhao, Y.-F.; Kanazawa, K.; Ishizuka, Y.; Nemoto, T.; Nakanishi, H.; Li, Y.-M. Copper (II) Modulates in vitro Aggregation of a Tau Peptide. *Peptides* **2007**, *28*, 2229–2234.

129. Su, X.-Y.; Wu, W.-H.; Huang, Z.-P.; Hu, J.; Lei, P.; Yu, C.-H.; Zhao, Y.-F.; Li, Y.-M. Hydrogen Peroxide Can Be Generated by Tau in the Presence of Cu(II). *Biochem. Biophys. Res. Commun.* **2007**, *358*, 661–665.

130. Mo, Z.-Y.; Zhu, Y.-Z.; Zhu, H.-L.; Fan, J.-B.; Chen, J.; Liang, Y. Low Micromolar Zinc Accelerates the Fibrillization of Human Tau via Bridging of Cys-291 and Cys-322. *J. Biol. Chem.* **2009**, *284*, 34648–34657.

131. Lu, Y.; Gralla, E. B.; Roe, J. A.; Valentine, J. S. The Redesign of a Type 2 into a Type 1 Copper Protein: Construction and Characterization of Yeast Copper–Zinc Superoxide Dismutase Mutants. *J. Am. Chem. Soc.* **1992**, *114*, 3560–3562.

132. Andrew, C. R.; Yeom, H.; Valentine, J. S.; Karlsson, B. G.; van Pouderoyen, G.; Canters, G. W.; Loehr, T. M.; Sanders-Loehr, J.; Bonander, N. Raman Spectroscopy as an Indicator of Cu–S Bond Length in Type 1 and Type 2 Copper Cysteinate Proteins. *J. Am. Chem. Soc.* **1994**, *116*, 11489–11498.

133. Kozlowski, H.; Kowalik-Jankowska, T.; Jezowska-Bojczuk, M. Chemical and Biological Aspects of Cu^{2+} Interactions with Peptides and Aminoglycosides. *Coord. Chem. Rev.* **2005**, *249*, 2323–2334.

134. Brown, D. R.; Guantieri, V.; Grasso, G.; Impellizzeri, G.; Pappalardo, G.; Rizzarelli, E. Copper(II) Complexes of Peptide Fragments of the Prion Protein. Conformation Changes Induced by Copper(II) and the Binding Motif in C-terminal Protein Region. *J. Inorg. Biochem.* **2004**, *98*, 133−143.

135. Buglyó, P.; Kiss, T.; Dyba, M.; Jezowska-Bojczuk, M.; Kozlowski, H.; Bouhsina, S. Complexes of Aminophosphonates–10. Copper(II) Complexes of Phosphonic Derivatives of Iminodiacetate and Nitrilotriacetate. *Polyhedron* **1997**, *16*, 3447–3454.

136. Park, G.; Tomlinson, J. T.; Melvin, M. S.; Wright, M. W.; Day, C. S.; Manderville, R. A. Zinc and Copper Complexes of Prodigiosin: Implications for Copper-Mediated Double-Strand DNA Cleavage. *Org. Lett.* **2003**, *5*, 113–116.

137. Matsuno, M.; Itoh, T.; Hirai, K.; Tomioka, H. Preparation of Sterically Congested Diphenyldiazomethanes Having a Pyridine Ligand and Magnetic Characterization of Photoproducts of Their 2:1 Copper Complexes. *J. Org. Chem.* **2005**, *70*, 7054–7064.

138. Zhou, Y.; Liu, K.; Li, J.-Y.; Fang, Y.; Zhao, T.-C.; Yao, C. Visualization of Nitroxyl in Living Cells by a Chelated Copper(II) Coumarin Complex. *Org. Lett.* **2011**, *13*, 1290–1293.

139. Rózga, M.; Kłoniecki, M.; Dadlez, M.; Bal, W. A Direct Determination of the Dissociation Constant for the Cu(II) Complex of Amyloid β 1−40 Peptide. *Chem. Res. Toxicol.* **2010**, *23*, 336−340.

140. Martell Arthur, E., The Chelate Effect. In *Werner Centennial*, American Chemical Society: 1967; Vol. 62, pp 272–294.

141. Grenthe, I. Stability Relationships Among the Rare Earth Dipicolinates. *J. Am. Chem. Soc.* **1961**, *83*, 360–364.

142. Izatt, R. M.; Christensen, J. J.; Kothari, V. Acid Dissociation Constant, Formation Constant, Enthalpy, and Entropy Values for Some Copper(II)-α-Amino Acid Systems in Aqueous Solution. *Inorg. Chem.* **1964**, *3*, 1565–1567.

143. Walker, J. K.; Nakon, R. On the Differing Acidities of Tri- vs. Tetradentate Copper(II) Chelates and Its Effects on Their Catalytic Properties. *Inorg. Chim. Acta* **1981**, *55*, 135–140.

144. Ramette, R. W.; Fan, G. Copper(II) Chloride Complex Equilibrium Constants. *Inorg. Chem.* **1983**, *22*, 3323–3326.

145. Byrne, R. H.; van der Weijden, C. H.; Kester, D. R.; Zuehlke, R. W. Evaluation of the $CuCl^{+}$ Stability Constant and Molar Absorptivity in Aqueous Media. *J. Solution Chem.* **1983**, *12*, 581–596.

146. Somasundrum, M.; Kirtikara, K.; Tanticharoen, M. Amperometric Determination of Hydrogen Peroxide by Direct and Catalytic Reduction at a Copper Electrode. *Anal. Chim. Acta* **1996**, *319*, 59–70.

147. Schweiger, A.; Jeschke, G., Principles of Pulse Electron Paramagnetic Resonance. Oxford University Press: Oxford, United Kingdom, **2001**.

148. Dikanov, S. A.; Shubin, A. A.; Parmon, V. N. Modulation Effects in the Electron Spin Echo Resulting from Hyperfine Interaction with a Nucleus of an Arbitrary Spin. *J. Magn. Reson.* **1981**, *42*, 474–487.